To the Graduate Council:

I am submitting herewith a dissertation written by Mehdi Bolorizadeh entitled "The Effects of Fast Secondary Electrons on Low voltage Electron Beam Lithography." I have examined the final paper copy of this dissertation for form and content and recommend that it be accepted in partial fulfillment of the requirements for the degree of Doctor of Philosophy, with a major in Physics.

E. Ward Plummer, Major Professor

We have read this
dissertation and recommend
its acceptance:

Accepted for the Council:

Interim Dean of Graduate Studies

Thesis
2006b
.B63

The Effects of Fast Secondary Electrons on Low voltage Electron Beam Lithography

A Dissertation
Presented for the
Doctor of Philosophy Degree
The University of Tennessee, Knoxville

Mehdi Bolorizadeh
December 2006

Copyright © 2006 by Mehdi Bolorizadeh
All rights reserved.

Acknowledgements

During the years of my dissertation I had the great fortune of to work with exceptional scientists and educators, my research advisor Professor David C. Joy and my academic advisor Professor E. Ward Plummer. I cannot thank them enough for all their guidance, leadership and input I received and the opportunities they have opened up for me. They made what would otherwise be ordinary, become exciting. I am fortunate to have Professor Michael W. Guidry and Professor Hanno H. Weitering on my committee for their ideas and suggestions. I had the pleasure of working together with a group of enthusiastic young scientists. I am thankful to all the past and present members of Professor Joy's, Plummer's, and Rack's groups. In special, Dr. Jing He, Xiaohu Tang, Dr. Satya, Dr. Wei Li, Yinghong Lin, Dr. Young Choi, Dr. Jason Fowler, Dr. Steven Randolph, Kiran Jaladhi, Sachin Deo, Satyavani Bari, and Ranjan Ramachandra. I am thankful to Dr. John Dunlap, Jennifer Trollinger, Thomas Enck, Levi Greenwood for sharing their assistance. I am thankful to the technicians at the Physics Department's electronic shop and the Material Science's Machine shop for their ideas, suggestions and work. My deepest thanks go to my wife Allison and my parents, Mitra and Mohammad Agha for their trust, encouragement, and support in so many ways.

Abstract

In 1981 Prof. Sir Alec Broers suggested that the spatial limit of direct writing electron beam lithography (DWEBL) would be limited to ~10 nm by the laterally scattered fast secondary electrons (FSE) even in atomically thin resist. Experiments and simulations have been carried out to quantify the contribution of FSE to the energy deposition that results in exposure of the resist over high beam energies. One possible solution to this restriction would be to use low energy electrons.

To examine Broers' hypothesis in low voltage electron beam lithography (EBL), studies in the low energy range on the effects of FSE were performed. Commonly used resists such as PMMA were employed, and the results were compared to those from conventional high voltage exposure. DWEBL was performed in a Schottky field emission gun scanning electron microscope (SEM), used in cathode-lens mode for low voltage operation. The exposure characteristics and sensitivity of the system at these energies have been investigated using Monte Carlo simulation methods. An improved model that describes electron energy losses and a parameterized point spread function of the electron energy distribution process in a solid material has been developed. Using the dose distribution of a source spread function, the patterning ability and ultimate resolution can be predicted correctly. Saturation doses were calculated at low energies, which would give a useful condition to target for routine exposure because it ensures the critical dimensions will not be affected by any random changes in beam intensity.

Table of Contents

Chapter 1 1
1. Introduction 1
1.1. Motivation 1
1.2. Objective 3
1.3. Outline 4
Chapter 2 5
2. Electron Beam Lithography 5
2.1. Introduction 5
2.2. Electron Beam Lithography Systems 6
2.2.1. Scanning Electron Beam Systems 7
2.2.2. Scanning Strategies 13
2.3. Advantages and Disadvantages of EBL 14
2.4. Resists in Electron Beam Lithography 15
2.5. Applications of Electron Beam Lithography 17
Chapter 3 18
3. Interaction of electron with matter 18
3.1. Introduction 18
3.2. General Kinematics of the Collision 19
3.3. Definitions 21
3.3.1. Secondary, Fast Secondary, and Back Scattered Electrons 21
3.3.2. Bosons and Fermions 24
3.4. Elastically scattered electrons 26
3.4.1. General Formulas 29
3.4.2. Atomic Models 31
3.4.3. Diffraction Effects 33
3.4.4. Electron Channeling 35
3.4.5. Phonon Scattering 37
3.5. Inelastic Collision (Inelastically Rearranged Electrons) 37
3.5.1. Atomic Models for Ionization 42
3.5.2. Solid State Effects 58
Chapter 4 62
4. Electron Beam Resist 62
4.1. Introduction 62
4.2. Contrast 64
4.3. Profile Modeling 64
4.4. Development Model 65
4.5. Molecular Weight of PMMA 65
Chapter 5 74
5. Interaction of Ions with Matter 74
5.1. Introduction 74
5.2. Kinematics of Ion-Matter Interactions 75
5.3. Elastic Scattering of Ions from Matter 77
5.3.1. Rutherford Back Scattering (RBS) 77

5.4. Secondary Electron Production 79
5.4.1. Atomic Models 79
5.4.2. Low Energy Ions 89
5.5. Ion-Solid Interaction 90
5.5.1. Stopping of Ions 92
5.5.2. Key Data to Compare Between Secondary Electrons Generated by an Electron Bean and an Ion Beam 97
5.6. X-ray Fluorescence in an Ion-Atom Interaction 105
5.6.1. Bremsstrahlung 105
5.6.2. Characteristic X-rays 105
5.7. Secondary Ion Emission 107
Chapter 6 108
6. Experimental and Simulation Techniques 108
6.1. Experiment 108
6.1.1. Low Voltage EBL Experiment Setup 108
6.1.2. Sample Preparation 116
6.1.3. Developing Process and Liftoff 128
6.1.4. Different Resist Thicknesses 129
6.1.5. Probe Sizes 130
6.1.6. Critical dose and resolution test 132
6.1.7. Charging effects 132
6.1.8. Resist Thickness Effects 132
6.1.9. Dot Arrays 133
6.1.10. Shot Noise 136
6.2. Simulation 137
6.2.1. Monte Carlo Simulation 137
Chapter 7 152
7. Conclusion 152
List of References 154
Appendices 168
Appendix A 169
Appendix B 171
Appendix C 173
Vita 217

List of Tables

Table 2-1: A list of electron gun filaments and their physical properties. 11
Table 2-2: A few common e-beam resists and some of their characteristic parameters at 20keV incident. 16
Table 3-1: k values for a few elements. 60
Table 5-1: Comparison between SEM and SIM as the electron/ion beam energy increases. 104
Table 6-1: Experiment Flowchart. 108
Table 6-2: Hotplate process problems. 128
Table 6-3: Minimum probe size achievable at a working distance of 5 mm using the Hitachi S-4300 SE/N with an aperture of 20 μm. 131
Table 6-4: An array of dots with a 170nm pitch was patterned on a 45 nm and an 85 nm thick layer of PMMA, with beam energies 1, 2, and 25 keV. 133
Table 6-5: Electron Interaction Volume. Model 1 does not include the FSE. Model 2 is equal to Model 1 + FSE. The red volume is caused by secondary and fast secondary electrons. 148

List of Figures

Figure 2-1: Evolution of EBL. 6
Figure 2-2: Electron beam lithography strategies. The red branches are the writing strategies used in this thesis. 7
Figure 2-3: Schematic of pixel exposure (a) Gaussian round beam (b) shaped beam.. 8
Figure 2-4: A simplified diagram of an e-beam exposure system. 10
Figure 2-5: A schematic of the electron optics' geometry. The electron beam at the intersection point is magnified to show the parameters used. 10
Figure 2-6: A schematic of raster and vector scanning 13
Figure 2-7: Schematics of positive and negative resists reaction to e-beam and resist development. 16
Figure 3-1: A schematic diagram of the processes involved in the electron with matter interaction. 20
Figure 3-2: The general kinematics of an electron colliding with the target's electron. The kinematic representation here is applicable to the bound electrons as well as free electrons from the target. $\mathbf{k}_0$ and $\mathbf{k}_{se}$ are in the plane shown, and all the vectors are drawn in polar coordinates $\left(\hat{r},\hat{\theta},\hat{\varphi}\right)$. $\mathbf{k}=\mathbf{k}_0-\mathbf{k}_{se}$. θ_{se} & θ_s, are the polar angles between $\mathbf{k}_0$ & $\mathbf{k}_{se}$ and $\mathbf{k}_0$ & $\mathbf{k}_s$ respectively 21
Figure 3-3: The energy variation of the secondary electron cross section for the electron-water collision[51] (W is the secondary electron's kinetic energy). 23
Figure 3-4: The angular distribution of the secondary electrons as a function of scattering angle θ ($\theta=\pi/2-\alpha$) is plotted for different ejection energy for the primary electrons of 500eV, in the electron-water collision. +, Ref[51].; ○, Ref[52] 24
Figure 3-5: An overview of the total electron scattering data for Ne. σ_t: solid line was drawn on the basis of the average data presented in references[53, 57-59]. σ_e: ○, Ref.[53]; Δ, Ref.[60]; •, Ref.[61]; ×, Ref.[53]; σ_{exc}: ○, Ref.[62]; ×, Ref[60]. 27
Figure 3-6: Schematics of the processes involved in the elastic scattering of an electron from an atom or molecule. The atom or molecule may be a part of a gaseous target or solid sample. The impact parameter, b, and the scattered angle, θ, are also shown. 28
Figure 3-7: The "scaled" angular distribution, $(a_0/2\gamma Z)^2\,(d\sigma/d\Omega)$, of the elastically scattered electrons with atoms assuming different r_0, is plotted against the relative momentum transfer, $2q/\hbar k_0$. 32
Figure 3-8: Schematic diagrams of the two types of Bloch wave present in a simple cubic crystal at the exact Bragg-reflecting orientation, assuming two-beam conditions. The Bloch wave intensities are shown at the top of the diagram, in relation to the planes of reflecting atoms. (After Hirsch *el al.,* 1977, but following a more recent numbering scheme) 36
Figure 3-9: Schematics of the processes involved in the inelastic scattering of an electron from (a) an atom/molecule including BSE, (b) X-rays from Silicon, and

(c) a solid. Again, the atom or molecule may be a part of a gaseous target or solid sample. 39
Figure 3-10: The total K-shell cross sections under the Bethe formula is plotted against the incident energy for Ar, Ni, Y, Ag, and Ba..... 49
Figure 3-11: The angular distribution of the Mott inelastic cross sections of Silicon for 20, 75, and 100 eV normal incident electrons..... 52
Figure 3-12: Electron impact ionization cross section of H_2O as a function of electron energy. The experimental data points are from[117] (filled squares),[118] (open diamonds), [51] (open inverted triangles), and [119] (open squares). The thick solid line represents the present DM calculation, the thin solid line denotes the BEB calculation[120], the dashed line refers to the calculation of Khare and co-workers[103], and the open circles connected by a solid line denote the calculation of Saksena et al.[121, 122]..... 57
Figure 4-1: PMMA monomer. Carbon, Oxygen, and Hydrogen atoms are shown with Blue, red, and grey balls respectively. (This sketch was drawn using PCMODEL)..... 62
Figure 4-2: Geometry of methyl methacrylate after optimization of the total energy of the molecule..... 63
Figure 4-3: In PMMA the scission process dominates the cross link process (The scission and cross link processes are shown with thick and narrow arrows respectively)..... 63
Figure 4-4: Solubility rate of PMMA as a function of energy dissipation in the polymer for two different solvents: 40% MIK / 60% IPA and pure MIK. The open circles and triangles denote exposure by a 20 keV electron beam, and the closed circles exposure by a 10 keV electron beam[141] 66
Figure 4-5: Film thickness removed as a function of the develoment time for the several values of the incident electron density N for a 0.3 μm thick film of PMMA. (a) is for exposure by 10 keV electrons and development in 40% MIK, 60% IPA, and (b) is for exposure by 20 keV electrons and development is pure MIK. The circles and dots are experimental results and the solid curves are theoretical calculations based upon the solubility rate of Figure 4-4. 68
Figure 4-6: Cell-removal model. The contours shown are ones calculated for a simulated electron beam exposure. The numbers shown at the centers of the cells are the times (T) of dissolution of the cells. The contours are interpolated from these numbers. The time and distances shown have been normalized by use of a rate function $R(x,y) =$ Larger of $\left[\left(10 - x^2(1+\frac{y}{8})^{-1} \text{ or } 0.5\right)\right]$ (units/time step). 69
Figure 4-7: Ray tracing algorithms. (a)Etch ray is referred at a boundary between regions having etch rates R and R+dR according to Snell's law. The effective refractive index for the resist is $n_R = \frac{\text{Maximum Etch Rate}}{\text{Local Etch Rate}} = \frac{R_{max}}{R}$. (b) Rays are started at the surface and the contour joining their endpoints after a given time (etch front). 71

Figure 4-8: Algorithm for the string model. (a) The advancement of a point by a distance Δx in a time Δt is along the bisector of the angle between the segments of the line at point $P_n(t)$. The distance $\Delta x=\Delta t.R(P_n(t))$, where R is the rate. All points along the string are advanced in this manner. (b) The string where a point is about to be eliminated. The segment length is S and the minimum allowed value is S_{min}. (c) The string after change that eliminated one point..... 72
Figure 5-1: A schematic diagram of the processes involved in the interaction of primary ions with matter. (The nuclear reactions are not shown and are not of concern, especially for low energy ions.) 76
Figure 5-2: The general kinematics of the interaction of ions that involves the target's nucleus, excluding nuclear reactions, is quite simple and it could be discussed in the context of elastic scattering and Rutherford Back Scattering (RBS)..... 78
Figure 5-3: The angular and energy distribution (DDCS) of the ionization cross section are plotted as a function of secondary electron energy for 0.5 MeV H+ on H2..... 82
Figure 5-4: The energy and angular distribution of electrons ejected in the collision of 150 keV H^+ on H_2O.[173] 83
Figure 5-5: Double differential cross section; i.e. the cross sections differential in the scattering angle and the energy of the secondary electrons, is plotted against the ejected electron energy for the impact of 150 keV H^0 on He. Dotted line shows the singly differential cross sections, integrated over all angles, in m^2/eV on the same numerical scale. 84
Figure 5-6: Differential cross sections in energy is plotted against the energy of ejected electron for the collision of 20-150 keV H^0 on H_2O.[175] 85
Figure 5-7: The doubly differential ionization cross sections for the collision of 150-keV H^0 and H^+ impact and 100-eV electron impact on Helium. Electron ejected at 10° relative to the beam[169]. T is the energy of the "equivalent electron" to the projectile. The annotation in the figure is wrong about the energy of primary electron..... 86
Figure 5-8: Doubly differential cross sections for the ejecting electrons in the collision of 150 keV primaries are plotted against the ejected electron energies scaled by the equivalent electron energies. The ordinate is the cross sections for neutral divided by similar cross sections for ions. Here, W is the energy of the ejected electron and T is the "equivalent electron" energy..... 87
Figure 5-9: Doubly differential cross sections for the ejected electrons in the collision of 150 keV primaries are plotted against the ejected electron energies scaled by the equivalent electron energies. The ordinate is the cross sections for neutral divided by similar cross sections for ions. Here, W is the energy of the ejected electron and T is the "equivalent electron" energy..... 88
Figure 5-10: The doubly differential cross sections for the ionization of Benzene plotted against the ejected electron energies for the 2.0 MeV H^+ projectiles[177]. 89
Figure 5-11: Doubly differential cross sections for secondary electrons by 15-keV protons from water vapor as a function of angle of ejection for various ejection energies. Error bars on some data points show the error due to statistical fluctuations in the count..... 91

Figure 5-12: Doubly differential cross sections for secondary electrons by 150 keV protons from water vapor as a function of ejection energy for various angles of ejection. 91
Figure 5-13: High-energy electronic stopping of a proton in Ni from quantum mechanical (Bathe-Bloch) and classical (Bohr) calculations. The predictions are compared to semi-empirical data from the SRIM-2000 package . The energy of the Bohr Criterion is indicated at the lower left..... 94
Figure 5-14: As in Figure 5-13, but for Ge ions colliding with Si. Note the different scales used. The energy of the Bohr Criterion is indicated at the lower left. 94
Figure 5-15: Nuclear stopping power as function of the reduced energy for Thomas-Fermi screening according to an exact calculation based on Fermi-Dirac screening function (solid line) and the Matsunami approximation (dotted line), with high- and low-energy limits (dashed-dotted and dashed line, respectively). The x- and y- axis are represented in a relative scale. 95
Figure 5-16: Nuclear (dotted line), electronic (SRIM package, solid line, and equation (5,11), corrected by fitting factor of 1.2, dashed line) and total stopping (thin solid line) cross section versus ion energy, for germanium in silicon. 95
Figure 5-17: As Figure 5-16, but for hydrogen in nickel. The Lindhard-Scharff electronic stopping has been corrected by a fitting factor of 1.3. Note the different scales. 96
Figure 5-18: The stopping power of He^+ ions on different solids as a function of ion energy which is calculated by SRIM-2000 package. 96
Figure 5-19: Topographic secondary electron (SE) yield data for 3 keV Ar+ ions and electrons. In both cases the beam current was the same. 97
Figure 5-20: iSE Yield Curve of Ar beam at different energies on Cu, Ag, Al, and Au solid targets. 99
Figure 5-21: Ion SE yield vs Z_2 (target) for 30 keV He^+ and Ar^+ incident ion beams. 99
Figure 5-22: Compare iSE and SP as a function of Z1 and Z2..... 100
Figure 5-23: Ion SE yield vs Z_1 (projectile) for solid Ag, C, Cr, and Al targets. 30keV ion -beam has been used. 100
Figure 5-24: Total SE yield data for quartz (SiO_2). The black solid line represents the eSE and the blue dashed lines represents the iSE produced by an He^+ ion beam. 101
Figure 5-25: N(E) Eletron emission spectrum Fe at 1keV e-beam using a PHI680 SAM with CMA..... 103
Figure 5-26: eSE spectrum – Fe at 1keV. The peak SE emission energy is ~6eV depending on surface state. The FWHM width of the SE peak is about 15eV. Dynamic range 0-50eV is ~ 7 103
Figure 5-27: iSE spectra from Fe Ar+ vs keV. SE peak energy similar to eSE but peak is very narrow (few eV) Dynamic range from 0 to 50eV is ~ 10^5..... 104
Figure 5-28: X-ray fluorescence emission in the interaction of 15 keV ions with a Be surface. The target was bombarded at an angle of 60° with respect to the normal. (After, Sharodi, Yu.A. Bandurin and Pop) 106

Figure 5-29: X-ray energy-dispersive spectroscopy spectra acquired for 100's from standard K968 using a 30 keV, 20 nA Ga^+ beam with a focused ion beam (solid line) and a 15 keV electron beam with a scanning electron microscope (dashed line) as the primary source[187] 107
Figure 6-1: Schematics of the experimental set up, known as cathode lens mode, to measure the true landing energy of the electron beam on the specimen. 110
Figure 6-2: Smiley face in the top left corner is an RGB bitmap image. When zoomed in, it might look like the big smiley face to the right. Every square represents a pixel. Three adjacent pixels whose colors are constructed by adding the values for red, green and blue are shown. 111
Figure 6-3: The raster image in the left is read by the pattern generator. As shown in this figure, the threshold level is defined and the output of the e-beam writer would look like the right image (only in black and white). 112
Figure 6-4: Magnification is defined by these parameters: Lx & Ly, dimensions in pixels; $0 < V_x$ & $V_y < 10$, dimensions in volts 113
Figure 6-5: (a) Shows the AO voltage of the pattern generator to the DBC in the case when the e-beam of the SEM is scanning the largest field that consists of four parallel scan lines pointing in the positive x direction as shown in part b..... 114
Figure 6-6: CEE® Model 100CB, which consists of a programmable spinner and a hotplate 116
Figure 6-7: A schematic of ramp rate. 119
Figure 6-8: A schematic of the closed bowl of the spinner. 120
Figure 6-9: Spin speed vs. film thickness for different solutions of PMMA in Aerosal. The number following the letter "A" is the percentage of PMMA in the Aerosal + PMMA solution. 121
Figure 6-10: The above charts show the film thickness dependence on spin speed, spin time, and exhaust rate. 122
Figure 6-11: Non uniform temperature zones in a convection oven. 124
Figure 6-12: (a) Hard Contact Hotplate Chuck (b) Soft Contact Hotplate Chuck (c) Proximity Hotplate Chuck. The arrows are representative of the forces applied to the wafer 125
Figure 6-13: Cee® exhaust cover above the hotplate. The wafer was placed at the end of the hotplate to be at a fare distance for the air turbulence. 127
Figure 6-14: A schematic of evaporation and sputtering in the lift-off process. 129
Figure 6-15: Using Kenway-Cliff numerical ray-tracing simulations of electron arrivals with 131
Figure 6-16: Seven 51 × 51 square dot arrays are drawn. From left to right the beam dose is decreased. At the end of each lithography, the beam is parked. 134
Figure 6-17: The dots are not properly developed. This is mainly because the resist is not uniform over the wafer. 134
Figure 6-18: The EBL is done on a 50 nm thick PMMA on Silicon at 2 kV. The white bar represents the scale. 135
Figure 6-19: The EBL is done on a 50 nm thick PMMA on Silicon at 1 kV. The white bar represents the scale. 135

Figure 6-20: An example of an underdeveloped process. The white bar represents the scale..... 136
Figure 6-21: The pattern was written on a 32 nm thick PMMA with a 3 kV e-beam. ~10 nm Cr was evaporated and lift-off at the end. The LWR was measured with regards to the red circle of 8 nm diameter. 137
Figure 6-22: LWR versus the linewidth for different PMMA thicknesses. The pattern s were drawn using a 1 kV e-beam. 138
Figure 6-23: LWR versus the linewidth for different PMMA thicknesses. Pattern s were drawn using a 2 kV e-beam..... 139
Figure 6-24: Trajectory plot of 5 keV electron beam entering a PMMA layer 45 nm in thickness. Primary trajectories are shown in light dashed lines and the fast secondaries are shown in dark solid lines. 142
Figure 6-25: Radial energy distributions of a point source beam in a PMMA resist layer. (a) 5 keV incident beam, 100 nm thickness. (b) 1 keV incident beam, 10 nm thickness. (c) 0.5 keV incident beam, 4 nm thickness. 142
Figure 6-26: Peak energy density deposited in PMMA as a function of the incident beam energy (The data are from 10^5 trajectories with relative error < 1%). 144
Figure 6-27: The radial energy deposited per volume plots for a point source beam in a free standing PMMA resist slab. Both models 1 and 2 are compared for incident beam energies of 100 and 25 kV on a 2000 and 500 nm thick resist respectively. The energy color bar in the center is explained in section 6.2.1.2. 145
Figure 6-28: The radial energy deposited per volume plots for a point source beam in a free standing PMMA resist slab. Both models 1 and 2 are compared for incident beam energies of 5 and 2 kV on a 100 and 20 nm thick resist respectively. The energy color bar in the center is explained in section 6.2.1.2. 146
Figure 6-29: The radial energy deposited per volume plots for a point source beam in a free standing PMMA resist slab. Both models 1 and 2 are compared for incident beam energies of 1 and 0.5 kV on a 10 and 4 nm thick resist respectively. The energy color bar in the center is explained in section 6.2.1.2. 147
Figure 6-30: It consists of a three dimensional and a contour plot which has been drawn in Mathematica 5.0. The EBL is done on a 20 nm thick PMMA on Silicon at 3 kV..... 149
Figure 6-31: Feature diameter in PMMA as a function of incident dose for a point source electron beam with energies of 1 keV onto 10 nm thick PMMA and 0.5 keV onto 4nm thick PMMA respectively. The dose error, which is caused by shot noise is $\frac{1}{\sqrt{N}}$. 151

Figure A-1: E-beam throughput trend in wafers/hr and pixels/sec for IBM's EL systems, as contrasted with the trends in wafer and pixel size (*at 50% density). 169

List of Symbols

a_0	Born Radius
A	Atomic Mass
A	Area (Irradiation Area)
A_C	Constant in Richardson–Dushman's Equation, 120 A/cm^{2}K^2
B	Brightness
B_E	Binding Energy (of the ejected electron)
b	Impact Parameter
C_c	Chromatic Aberration Constant
C_s	Spherical Aberration Constant
d	Diameter
$d\sigma/d_$	Differential Cross Section with respect to _
D	Dose
$D_{Critical}$	Critical Dose
D_E	Absorbed Energy Density (eV/cm^3)
$D_{E,threshold}$	Threshold Absorbed Energy Density
D_p	Sensitivity of the Positive Resist
D_n	Sensitivity of the Negative Resist
D^i_g	Interface Gel Dose
e	Proton's Charge
eV	Electron Volts
E_0	Primary Electron's Kinetic Energy, Incident Kinetic Energy
$\overline{E_0}$	Average of E_0
E_F	Fermi Energy
E_L	Landing Kinetic Energy
E_r	Recoil Energy
E_S	Internal Secondary Electron's Kinetic Energy
E_W	Work Function Energy
f	Scattering Amplitude (Factor)
F_a	Atomic Form Factor
F	Elastic Form Factor
$f_{nl}(\mathrm{v})$	Velocity Distribution of Electron in the State *n,l.*
$F_f(\mathbf{q})$	Inelastic Form Factor Related to the Final State *f,*
f_s	Structure Factor
$f(w)$	Oscillator Strength
g	Number of Scission Events Per eV
g_{crit}	Development (energy / unit volume)
g_{nl}	Weighting Factor
$\hbar$	Plank's Constant
I	Ionization Energy

I_1	First Ionization Energy
I_b	Beam Current
J	Current Density (A/cm^2)
J_b	Beam Current Density (A/cm^2)
J_C	Cathode Current Density (A/cm^2)
$\mathbf{k}_0$	Primary Electron Wave Number Vector
$\mathbf{k}_s$	Scattered Electron Wave Number Vector
k_B	Boltzmann's Constant, 8.6×10^{-5} eV/K
$\mathbf{k}_{se}$	Secondary Electron Wave Number Vector
keV	Kilo Electron Volts
m	Electron's Reduced Rest Mass
$\mathrm{m_e}$	Electron's Rest Mass
M_a	Average Molecular Weight After Exposure
M_b	Average Molecular Weight Before Exposure
n_a	Number of Atoms/Molecules per Unit Volume of the Sample
N_A	Au
N_n	Number of Electrons in Shell n
N_{nl}	Number of Electrons in Subshell n,l
$\mathbf{q}$	Recoil Momentum
r_0	Screening Radius
$\langle r_{nl} \rangle$	Mean Square Radius of Electron in the (n,l) Subshell
R	Pseudouniform Random Number
R_y	Rydberg Energy (13.6 eV)
$\mathbf{R}$	Position Operator
$\lvert r \rangle$	Spatial Wave Function, Spatial Ket
S	Stopping Power
S_{nl}	Nominal Stopping Power Associated with the State nl.
S	Spin Operator
$\lvert s \rangle$	Spin Wave Function, Spin Ket
t	Time
t	Crystal Thickness
T	Absolute temperature (K)
T_D	Debye Temperature
u	Reduced Energy, $u = E_0/I$
U	Reduced Energy, $U = E_0/E_{nl}$ for subshell energy of E_{nl}
U_{int}	Reduced Potential for the Interaction
v	Speed
$V(r)$	Interaction Potential
V_0^i	Imaginary Potential
V_0^p	Phonon Contribution to the Imaginary Potential

Z	The Total Number of Protons in the Nucleus
α	Convergence Angle
α	"absorption coefficient" of the secondaries
β	Screening Parameter (in Rutherford's equation)
γ	Relativistic Factor
γ_n	Contrast (Negative Resists)
γ_p	Contrast (Positive Resists)
ΔE	Energy Lost in the Collision
$\overline{\Delta E}$	Average Energy Lost in the Collision
δ	Secondary Electron's Yield
ε	Energy Transfer ΔE Normalized to E
ε_c	Cut-off value of ε
η	Backscatter Coefficient
θ	Polar Angle Relative to the Incident Beam
θ_B	Bragg Angle
λ_e	Elastic Mean Free Path
λ_i	Inelastic Mean Free Path
λ_t	Total Mean Free Path
ν	Atomic Displacement
ξ	Number of Bound Electrons in a Particular Sub-Shell
ξ_g	Extinction Distance
ξ_i	$\xi_i = \int_0^\infty \frac{df(w)}{dw} dw$
μ_p	Phonon Absorption Coefficient
σ	Cross Section
σ_c	Counting Cross Section
σ_e	Elastic Cross Section
σ_{exc}	Overall Electronic Excitation Cross Section
σ_f	Cross Section for Inelastic Collision to Final State f.
σ_i	Total Ionization Cross Section (TICS)
σ_z	Partial cross section for ionizing z electrons in a single collision
σ_{nl}	Cross Section measured for the ejection of an electron from the subshel n,l
σ_t	Total Cross Section
Φ	Quantum Efficiency
ψ	Quantum Wave Function
ψ_0	Initial State of Wave Function
ψ_f	Final State of Wave Function
$\lvert\psi\rangle$	Ket

Ω	Solid Angle

List of Abbreviations

ALCHEMI	Atom Location by Channeling Enhanced Microanalysis
BSE	Back Scattered Electron
BE	Binary Encounter
BE	Bose-Einstein
BEA	Binary Encounter Approximation
BEB	Binary Encounter Born Approximation
BED	Binary Encounter Dipole
CCC	Convergent Close-Coupling
CD	Critical Dimension
CFE	Cold Field Emission
CL	Cathodoluminescence
CMA	Cylindrical Mirror Analyser
CTC	Charge Transfer to Continuum
CTMC	Classical Trajectory Monte Carlo
DI	Direct Ionization
DM	Different Mixing/Deutsch-Mark
DCS	Differential Cross Section
DDCS	Doubly Differential Cross Section
DWEBL	Direct Writing Electron Beam Lithography
EBES	Electron Beam Exposure System
EBIC	Electron Beam Induced Conductivity
EBID	Electron Beam Induced Deposition
EBL	Electron Beam Lithography
ECC	Electron Capture to Continuum
EID	Exposure Intensity Distribution
ELC	Electron Loss to Continuum
ELNES	Energy Loss Near Edge Structure
ERDA	Elastic Recoil Detection Analysis
eSE	Secondary Electrons Generated by an Incident Electron Beam
iSE	Secondary Electrons Generated by an Incident Ion Beam
EXELFS	Extended Energy Loss Fine Structure
FD	Fermi-Dirac
FIB	Focus Ion Beam
FSE	Fast Secondary Electron
GOS	Generalized Oscillator Strength
IPA	Isopropanol
LNS	Linhard Nielsen Scharff
LWR	Line Width Roughness
MC	Monte Carlo
MED	Maximum Energy Deposition

MIBK	Methyl Isobutyl Ketone
PEB	Post Exposure Bake
PIXE	Particle Induced X-ray Emission
PMMA	Poly Methyl Methacrylate
QM	Quantum Mechanics
RBS	Rutherford Back Scattering
RCF	Resist Contrast Function
SAM	Scanning Auger Microscopy
SE	Secondary Electron
SFE	Schottky Field Emission
SEM	Scanning Electron Microscopy
SIM	Scanning Ion Microscopy
TEM	Transmission Electron Microscopy
TICS	Total Ionization Cross Sections
VI	Visual Instrument
VLSI	Very-Large Scale Integration
ULSI	Ultra-Large Scale Integration
WPH	Wafers Per Hour

Chapter 1

1. Introduction

1.1. Motivation

In 1959, Richard Feynman[1, 2] gave his famous address to the American Physical Society entitled "There's Plenty of Room at the Bottom". In this talk, he proposed a number of challenges to the scientific community in the area of miniaturization. These propositions proved to be visionary, and made remarkably accurate predictions regarding many aspects of nanotechnology. Among these was the use of "scanning cathode rays" for the deposition of materials

Why can not we write the entire 24 volumes of the Encyclopedia Britannica on the head of a pin? ... How do we write small? ... We can reverse the lenses of the electron microscope in order to demagnify as well as magnify. ... We could write with that spot like we write in a TV cathode ray oscilloscope ... and having an adjustment which determines the amount of material which is going to be deposited.

Feynman already realized that the direct modification of metal by scanning beams would be inefficient so he proposed a yet undiscovered electron beam resist:

If it doesn't work for a metal surface, it must be possible to find some material with which to coat the original pin so that, where the electrons bombard, a change is made which could be recognized later.

These ideas were prophetic, considering that they were made during the early, formative years of the scanning electron microscope.

In the past 100 years, for the first time a majority of nations were putting substantial effort into the goal of miniaturizing devices and structures. Until recently, the goal of kings and rulers was to have the biggest of everything; the biggest ships and palaces or the tallest towers. In this new era the ability to build smaller is more powerful. The essential means to achieving such a minute size in structures is the understanding of the interaction mechanisms between an energetic charged particle and a solid material, which stems from the roots of modern physics and is part of the ongoing need to understand the basic nature of matter.

Miniaturization and integration started as a trend in electronics manufacturing in the seventies and is still a continuing at this moment, at this moment, extending rapidly to other fields like molecular biology, analytical chemistry and mechanical

engineering. Almost thirty years ago the resolution requirement for integrated circuits was 10μm while today it is under 100nm. The challenge of large scale manufacturing is to find the right methods to fabricate sub-100 nm features. Electron beam lithography has been a useful technique for nano-scale patterning since its discovery in the latter half of the previous century. While speed limitations will prevent its widespread use for commercial applications, it remains a useful tool for the rapid prototyping of future generations of electronics. It has long been known that an electron beam can write extremely small line-widths. The latest generations make this easy to achieve over large areas, and with nanometer-scale placement accuracy.

In 1981 Lord A.N. Broers[3] suggested that the ultimate spatial limit of direct writing electron beam lithography (DWEBL) would be limited by the laterally scattered fast secondary electrons even in an atomically thin resist. As the feature size of the next generation devices is approaching the range of secondary electrons, this resolution limit becomes more important. Fast secondary electrons are generated when the incoming electrons have knock-on collisions with the electron in the matter. Their energy is in the range of 50eV to $E_0/2$, where E_0 is the primary incident energy of the electrons[4]. Experiments and simulations have been carried out to quantify the contribution of fast secondary electrons to the energy deposition that results in exposure of the resist at high electron beam energies (E_0>50keV). Broers noted that the size of the smallest feature that could be written decreased as the resist layer was made thinner, because of the reduced scattering of the electron beam. When the resist became sufficiently thin this improvement ceased. The resolution was then pinned at a level of 8-10 nanometers, a figure which he noted approximately corresponded to the lateral spatial range of fast secondary electrons-- the secondary electrons generated in the resist by knock-on. Broers therefore deduced that electron beam lithography, even under the most optimum conditions, would be unable to fabricate structures of a size less than a few nanometers. This thesis is designed to test whether or not Broers' hypothesis is correct, and to identify what other problems and new techniques might modify these conclusions.

The charge to the mass ratio, which determines the physical response of a particle, of the electron is the largest of all elementary particles. The typical electron wavelength is much shorter than that of the photons used in photolithography. Electron gun sources with high stability and life time, fine beam probe, and small energy spread are widely available in the market. These are the least reasons for doing electron beam lithography as a fabrication tool. The results achieved in this effort are extremely important for the semiconductor industry as it evolves towards smaller and smaller critical dimensions in its chips. In research, low voltage electron beam lithography has played a major role in making nano- and micro- devices. These devices have been used in numerous fields from bio devices to quantum devices. To achieve low proximity and less damage to the substrate, low voltage electron beam lithography has been preferable to high voltage lithography.

1.2. Objective

As noted above, the objective of this thesis is to examine whether or not fast secondary electrons do exist and are responsible for a limit to electron beam lithography. Are there any other resolution limits to electron beam lithography? Is there any alternative technology that might perform better than using electron beams? This will be done by studying lithography performed at low energies and on thin resists so that the fast secondary electron effect, if it exists, would be the dominant contribution to the minimum feature size.

The scope of this thesis includes both theoretical and experimental research of electron scattering in solids. The understanding of a physical process requires the development of a model that embodies the conceptual understanding of the system. In turn, this model must be reduced to a mathematical and then to an algorithmic model in order to yield predictions to compare with an experiment. Thus, a set of models have been devised to describe most of the interactions of an electron scattering in a solid medium. Once the theoretical framework was put in place, a Monte Carlo simulation code and experiments using electron beam lithography were devised to compare theory with practice.

Theoretically, electron interactions in solids under non-relativistic situations, such as those encountered in electron beam lithography specifically in low energy electron beams were studied. The emphasis was made on the important role of fast secondary electrons in the resolution of the mentioned lithography processes. I have developed an improved model that describes electron energy losses and a parameterized point spread function of the electron energy distribution process in a solid material. Using the dose distribution of a source spread function, the patterning ability and ultimate resolution can be predicted correctly. Experimentally, with the aid of scanning electron and atomic force microscopy, I have characterized material property changes due to exposure by low energy electrons. I have therefore been able to detect the effect that electrons have on a solid material in a direct manner.

The framework developed here can also be extended to electron microscopy, metrology, and polymer chemistry. These accomplishments have not been achieved before and are my contribution to the knowledge of how electrons interact with solid materials.

1.3. Outline

After the Introduction, the thesis begins with a brief introduction to electron beam lithography. The electron beam lithography methods used in this effort and their advantages and disadvantages are explained.

Since in lithography the electron-matter interactions are used to generate interactions in the solid, in chapter 3, a review of these interactions is presented. Elastic and inelastic interactions are explained and a number of classical, quantum mechanical, and hybrid models are presented.

In Chapter 4 the physics and chemistry of resists with the emphasis on PMMA are given. The essential parameter, which determines the properties of the resist / developer, is explained. At the end, different development models for electron beam resists are reviewed. In this manner, chapters 1 through 4 set the basis for the rest of the chapters.

The emphasis in chapter 5 is on the low energy ion beam interactions with matter, and its application to the recent development of microscopes equipped with advanced ion sources, ion optics, imaging, and microanalysis and a possible solution to ion beam lithography.

In chapter 6, the experimental set up and processes are covered. The Monte Carlo simulation developed for the thesis is proposed. The experimental and simulation data and results are explained in detail. Also the data obtained at low voltage e-beam is compared with Broers' hypothesis. The exposure characteristics and sensitivity of the system at these energies have been investigated using Monte Carlo simulation methods. Saturation doses were calculated at low energies, which would give a useful condition to target for routine exposure because it ensures the critical dimensions will not be affected by any random changes in beam intensity.

The dissertation concludes with chapter 7, which gives a brief conclusion about the research work.

The Appendices contain most of the technical aspects of the research undertaken for this thesis. Several of the sections contain original contributions, while a few are shown for completeness on a subject.

Chapter 2

2. Electron Beam Lithography

2.1. Introduction

Electron beam lithography (EBL) is the writing of patterns on films of electron sensitive material using a finely focused electron beam. In the mid fifties, the basic relationships governing electron beam current, diameter, lens aberration and source brightness were described by K.C.A. Smith[5]. Scanning electron beam lithography is an advanced and mature technology that in the early 1960s evolved from the scanning electron microscope (SEM) [6-24]. This technology was established after Richard Feynman gave his famous talk entitled "There's Plenty of Room at the bottom" in 1959 [1]. In 1960, the first scanning EBL system was presented [25] by Mollenstedt and Speidel. They demonstrated patterning with a resolution of about 20 nm on a thin substrate. In 1964 the first electron beam lithography instrument to record digital information [26] was presented by R. Thornley at IBM. This would become the first vector scan electron beam lithography system that used the electron beam optics to steer the electron beam to create a pattern.

Until 1967 photographic emulsions, such as Kodak photo resist [27] were used as e-beam resists because by then dedicated e-beam resists for EBL had not yet been developed [28, 29]. By 1966 many organic materials and dielectrics had been electron beam (e-beam) deposited. In the following years the first resists developed explicitly for electron beam lithography were presented. Surprisingly enough, one of those resists, polymethyl-methacrylate [30, 31] (PMMA) is still today one of the highest resolution resists available. Previous to this time, most semiconductor fabrication had been performed by wet etching or ion milling, i.e. subtractive processing.

In 1975, the first commercial electron beam lithography system for semiconductor applications, Electron Beam Exposure System (EBES), was developed by AT&T Bell Labs [10] and is employed today as the MEBES mask making machines. This machine grew out of the television technology and the electron microscopy technology. By the 1980's the technology had progressed from the research laboratories, and commercial systems were available for direct-write and mask-making. These instruments were significantly different from the modified SEM type systems that had been used for research. While these early lithography systems sacrificed ultra-high resolution in order to maintain uniformity over millimeter-sized fields, by 1985 JEOL integrated the functions of the microlithography systems:

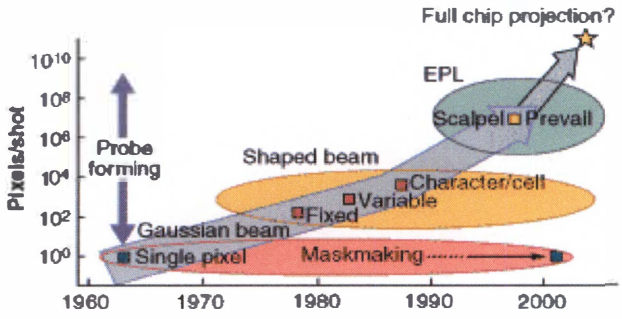


Figure 2-1: Evolution of EBL.

pattern generation, stage motion, and registration; with the high performance of the nanolithography research instruments. Figure 2-1, showing the evolution of EBL.

For commercial applications, EBL is usually performed using dedicated beam writing systems that are very expensive (>$2M USD), but for research applications, it is still common to perform electron beam lithography using an electron microscope with a home-made or relatively low cost lithography accessory.

At a moment the major drawback of EBL is its low throughput and high capital cost. E-beam direct-write technology clearly has not kept pace with the pixel growth in the semiconductor industry and with Moore's observation (for details see Appendix A). However, progress in the field of EBL continues at a rapid pace, which would solve the current problems.

In section 2, the four major subsystems in any EBL system are explained. Emphasis is given to those subsystems that were manipulated in this research and to scanning modes.

In section 4, an introduction to e-beam resists is presented. The last section, section 5, illustrates a number of EBL applications in industry and science.

2.2. Electron Beam Lithography Systems

E-beam systems can be conveniently subdivided into two broad categories: those using scanned focused electron beams that expose the resist-coated substrate in serial fashion, and those projecting the entire pattern simultaneously onto the substrate. The latter, parallel-exposure techniques offer the advantage of higher

exposure rates compared with the serial exposure approach, in which only small features or portions of a feature are written at a time. As the main experiments in this project were done in an SEM environment, the attention would be given to raster and

vector scanning (These scanning methods will be explained in section 2.2.2.). Figure 2-2 illustrates the variety of electron-beam strategies that have been investigated over the past 40 years, where the present writing done in this project is characterized in red.

2.2.1. Scanning Electron Beam Systems

The scanning e-beam approach offers the highest resolution of all e-beam patterning techniques. The e-beam, focused to a fine spot, is controlled [deflected and turned on and off (blanked)] by a computer as it is scanned across the surface of the resist. Two beam-forming approaches have been used. The first utilizes a Gaussian round beam in the same manner as a conventional scanning electron microscope. The beam diameter defines the pixel size, and pixels are exposed serially (Figure 2-3(a)). The second approach utilizes a shaped beam that is imaged to a square or rectangular spot on the writing surface, thereby allowing several pixels (pixels if exposed by Gaussian round beam) to be printed in parallel (Figure 2-3 (b)).

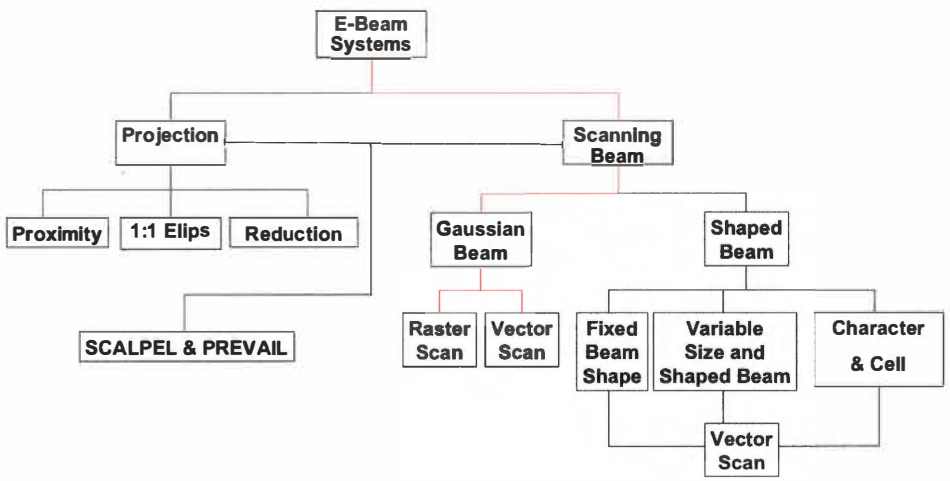
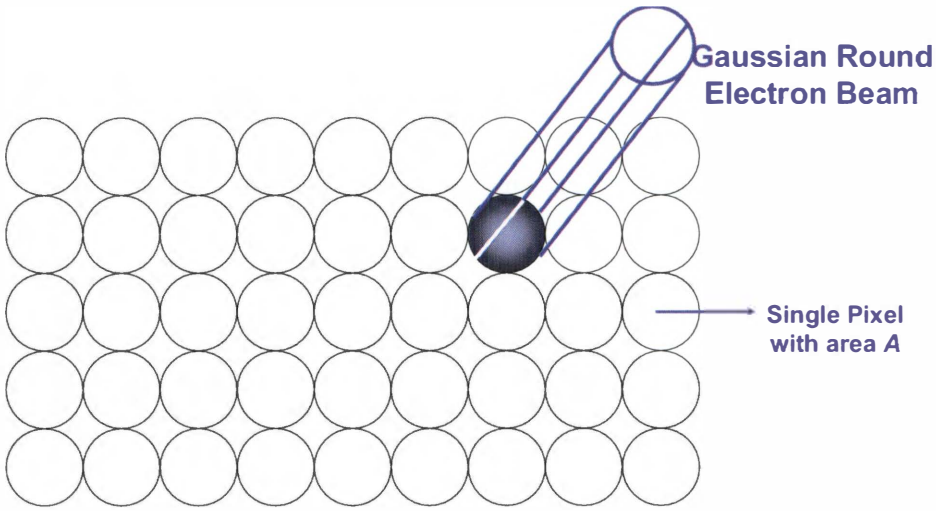
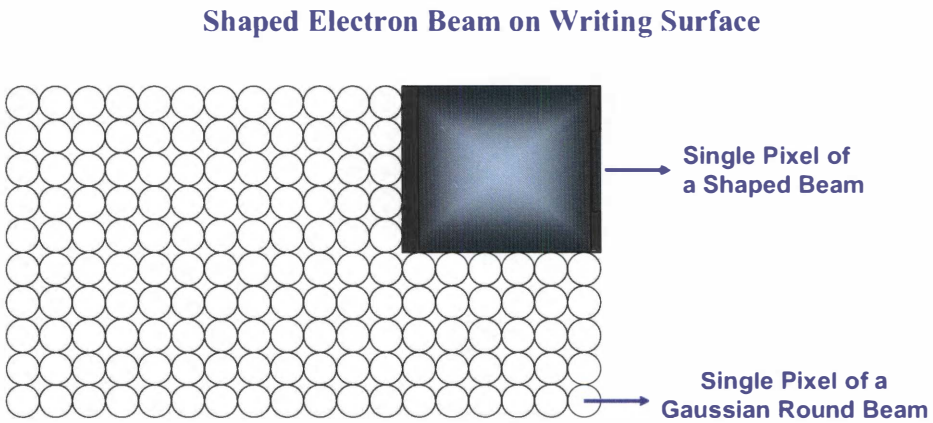


Figure 2-2: Electron beam lithography strategies. The red branches are the writing strategies used in this thesis.



(a)



(b)

Figure 2-3: Schematic of pixel exposure (a) Gaussian round beam (b) shaped beam.

In all e-beam systems the incident exposure area of a single pixel is equal to the area A of the beam. The maximum current, i_{max} that can be delivered to this area is limited by the brightness of the source and the design of the column. The computer and electronics that control the electron beam limit the frequency (i.e., writing rate) at which the beam can be scanned and modulated and thus define the minimum "dwell" time, t_{min} of the beam. These parameters define the maximum dose (maximum areal dose), D_{max} per unit dwell time in coulombs per square centimeter, which is given by

$$D_{max} = \frac{i_{max}\ t_{min}}{A}. \qquad (2,1)$$

The maximum available areal dose per unit dwell time defines the resist sensitivity needed to maximize throughput.

All scanning-beam systems have certain hardware similarities, disregard of their particular writing mode. Figure 2-4 shows a simplified schematic diagram of an electron-beam exposure system, which consists of four main subsystems: (1) electron source (gun), (2) electron optical, column (beam-forming system), (3) mechanical stage, and (4) electronics including the computer used to control the various machine subsystems and transfer pattern information to the beam deflection coils. The performance capability of each of these subsystems determines the limitations imposed by the hardware on resolution. In the following, these main systems are explained.

(1) Electron gun sources applicable to electron beam-lithography are the same as those used in conventional electron microscopes. These guns vary in the amount of current density and brightness they can produce, the size of the source, the stability of the emitted current, and the life time of the filament (Table 2-1). The details about different kind of filaments are explained in Appendix B.

The current density, J of an electron beam at any point in the column is the beam current passing through the beam cross section at that point (The beam cross section is defined to be perpendicular to the optical axis, unless otherwise stated); i.e.

$$J = \frac{\text{beam current}}{\text{beam cross section}}. \qquad (2,2)$$

Brightness incorporates the current density and the angular spread of the electron beam and is defined as the current density per solid angle (Ω). To have a better understanding, assume we have a converging e-beam with a convergence angle α, and a circular cross section with a beam current I_b (Figure 2-5). The beam current density J_b at the cross section with diameter d is:

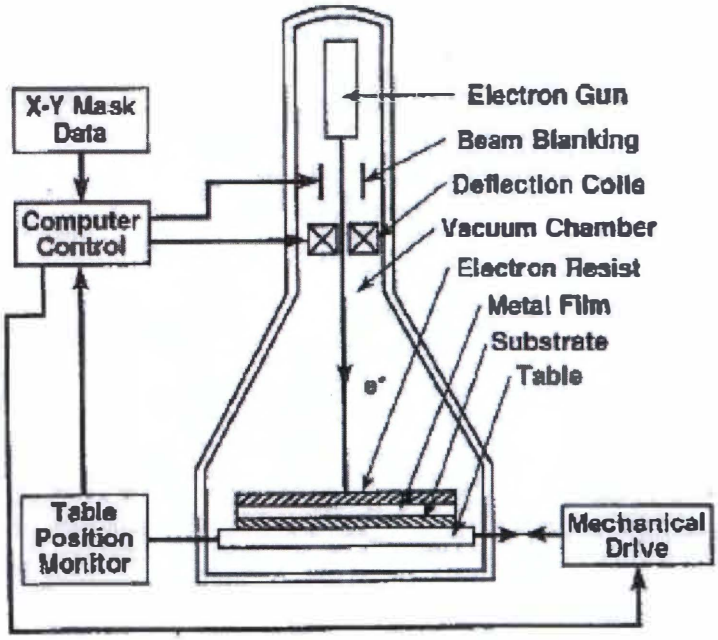


Figure 2-4: A simplified diagram of an e-beam exposure system.

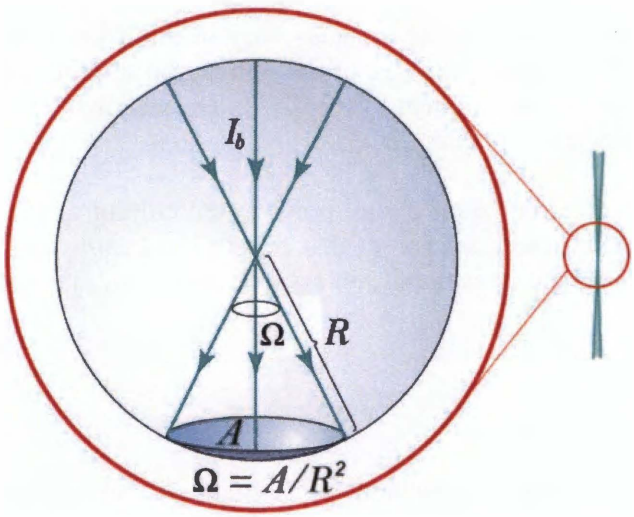


Figure 2-5: A schematic of the electron optics' geometry. The electron beam at the intersection point is magnified to show the parameters used.

Table 2-1: A list of electron gun filaments and their physical properties.

	Units	Tungsten Filament	LaB_6 Filament	CeB_6 Filament	Cold Field Emission Filament	Schottky Field Emission Filament
Reference		32	33, 34	35	36, 32, 37, 38, 39	36, 32, 40, 41, 37, 42, 38, 43
Angular Current Intensity	mA/str	n/a	n/a	n/a	<0.1	0.1 - 1.0
Source Brightness		10^6	10^7	10^7	10^9	10^8 - 10^9
Emitting Surface Area	μm^2	>>1	>1	>1	0.02	0.2
Crossover or Virtual Source Diameter	nm	$>10^4$	$>10^3$	$>10^3$	3.1 - 5	15 - 25
Energy Spread	eV	1 - 3	1 - 1.5	1 - 1.5	0.2 - 0.3	0.3 - 1.0
Source Temperature	K	25 - 2900	1800	1800	300	1800
Work Function	eV	4.5	2.6	2.4	4.5	2.8
Operating Vacuum	Pa	10^{-4}	10^{-6}	10^{-6}	10^{-9} - 10^{-11}	10^{-8} - 10^{-9}
Short Term Beam Current Stability	% RMS	<1	<1	<1	4.1 - 6	<1
Typical Service Life	h	40 - 100	1,000	>1,500	>>2,000	>2,000

$$J_b = \frac{4I_b}{\pi d^2}. \tag{2,3}$$

The solid angle for this beam is:

$$\Omega = \frac{A}{R^2} = \frac{\int_0^{2\pi} d\varphi \int_0^{\alpha} R^2 \sin\theta d\theta}{R^2} = 4\pi \sin^2(\frac{\alpha}{2}). \tag{2,4}$$

α is a small angle, so Ω and B become:

$$\Omega = \pi\alpha^2$$
$$B = \frac{J_b}{\Omega} = \frac{J_b}{\pi\alpha^2} = \frac{4I_b}{\pi^2 d^2 \alpha^2} \tag{2,5}$$

(2) The electron optical column consists of a source (described earlier), one or more lenses (used to focus and define the spot), a method of modulating the beam (beam blanker), beam-limiting apertures, and a beam-deflection unit to position the beam precisely and accurately over the scan field. All of these elements can be configured in a variety of ways, depending on the purpose and design of the particular column and system (for a more detailed discussion, see references [7, 44, 45]. In sum, the column is designed with a minimum of aberrations so that a spot or an edge profile (for shaped-beam systems) equivalent to the desired address structure can be achieved. The edge profile depends on the intended use of the machine, for example, whether it is to be used for mask making or direct-write applications.

(3) To expose a wafer sized substrate, it is necessary to deflect the beam over the entire area. However, there are limits to how far the electromagnetic or electrostatic scan coils can deflect the beam without introducing intolerable errors. The attainment of good pattern quality requires the edge gradient of the electron-beam profile, the distortion of the exposed pattern, and the positional stability of the beam to be held below a fraction (tenth) of the minimum feature size. These considerations limit the size of the scan field to several millimeters at most and necessitate mechanical stages to move the substrate through the deflection field of the electron-beam column. Stages can be operated in a step-and-repeat mode in which a field containing a circuit, or portion of a circuit, is exposed by deflecting the electron beam over the field while the table is stationary. The table is then stepped to the adjacent field, and the next circuit or portion is exposed. This operation is continued until the exposure of the entire substrate has been completed. The correct positioning of the stage is critical for registration or stitching of adjacent patterns and is controlled either by laser interferometers or by locating registration marks on the substrate within each pattern area by using the electron beam as a probe in a manner similar to that of a scanning electron microscope. Alternatively, stages can be operated in a continuous mode in which the pattern is written on the substrate in one

direction while the stage is slowly moving in an orthogonal direction. This strategy was perfected at Bell Laboratories in the 1970s [46].

(4) These subsystems are controlled by a computer, which, in real time, monitors the various operating parameters of the column and stage position and, in addition, transfers primary pattern data directly to the electron deflection system. The rate at which the data can be transmitted to the electron optical column ultimately governs the modulation rate of the electron-beam machine, that is, the writing rate (and hence the dwell time). Commercial e-beam tools process data at rates approaching 1GHz.

2.2.2. Scanning Strategies

Raster and vector scanning are the two basic scanning methods applied in EBL. In raster scanning mode, Figure 2-6(a), the deflector scans an overall field. The e-beam is blanked off in the non-patterned regions and in un-blanked in the pattern regions only. In vector scanning mode, Figure 2-6(b), the deflector scans only the pattern region. This approach, compared to raster scanning, requires complex beam deflection systems to compensate for hysteresis effects and large angle deflections.

There are relative advantages and disadvantages to either raster or vector scanning modes. Firstly, if the exposed area is much less than the field size, generally less than 20%, vector scan will have a time advantage, as it does not waste time scanning areas that are not to be exposed. Secondly, the above advantage for vector scan holds if the time taken by the beam to be deflected from one feature to another and to settle to the required accuracy is insignificant. Because of eddy currents

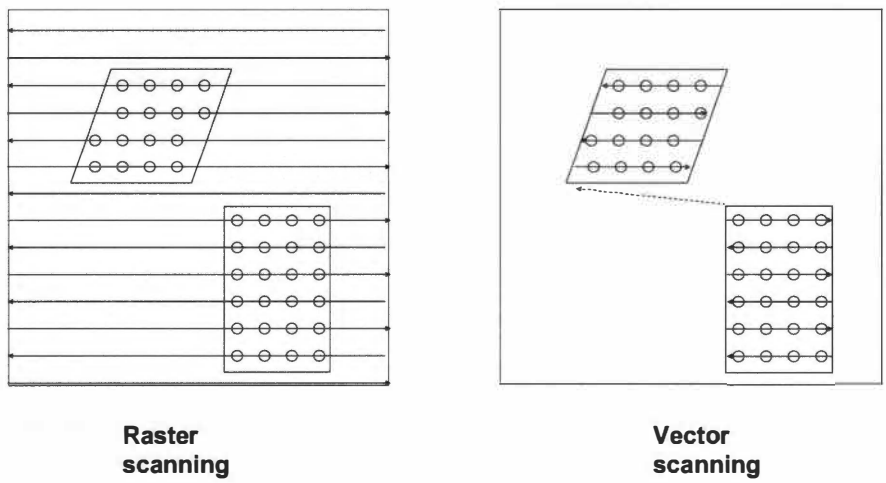


Figure 2-6: A schematic of raster and vector scanning.

induced by the rapid deflection signals in conducting material within the deflecting field, this is an essential problem to overcome. Thirdly, raster scanning does not require both positive and negative resists to be available, because tone reversal can be achieved simply by reversing the polarity of the blanking signal. With vector scanning, tone reversal can be managed by recording the pattern, which is possible in simple patterns, but becomes a data processing challenge with VLSI and ULSI patterns.

Both modes could be combined with writing on a continuously moving stage or varied exposure dose. By arranging the features to be exposed in a suitable order, and by continuously adjusting the stage speed or exposure dose, the throughput of EBL could be increased substantially.

2.3. Advantages and Disadvantages of EBL

The major advantages of EBL are:

1) Small feature size,
2) Ability to register accurately over small areas of a wafer,
3) Low defect densities,
4) Fast turn around, permitting the rapid modification of a pattern on a work-piece,
5) Direct generation of patterns from circuit design data.

The limitations of EBL are set by:

1) Minimum electron beam size,
2) Scattering of electrons in the work-piece and the resolution of the resist,
3) The size of the field of view that can be patterned without loss of resolution or image placement accuracy,
4) The accuracy of beam placement on the work-piece,
5) The speed of beam placement on the work-piece,
6) The current and current density of the beam,
7) The sensitivity of the resist.

Items 1-4 limit the quality of the lithography patterns and items 5 through 7 limit the throughput of the system.

As mentioned, finely focused electron beams are used in lithographic processes to expose polymer resist layers. Very complex device patterns with high resolution nanometer size can be created. Such resolution is in general superior to presently available optical lithography techniques because the electron probe size

may be much smaller than the corresponding diffraction limited image in optical lithography.

2.4. Resists in Electron Beam Lithography

Electron beam resists are the recording and transfer media for EBL. There are a variety of electron sensitive resists, but attention is usually concentrated on polymer resists and in particular PMMA. There are two types of electron beam (e-beam) resists: positive tone and negative tone. The incident electrons have energies far greater than the bond energies in the resist molecules, and so all these energies are effective. However, because scattering cross section of the incident beam is inversely proportional to the incident beam's energy, low energy electrons will be most effective. Both, bond scission and bond formation occur simultaneously. Which predominates determines whether the resist is positive or negative. In a negative resist, electron - beam - induced crosslinks between molecules increase the molecular weight of the polymer and reduces its solubility in the developer solution. One crosslink per molecule is sufficient to make the polymer insoluble. The opposite holds for positive resists where the resists are developed away at exposed areas where there was chain scission (Figure 2-7). Table 2-2, has a list of a few common e-beam resists[47]. Values for sensitivity and resolution are approximate. Because faster electrons penetrate more deeply, more current is required at higher voltages, thus a resist is about one half as sensitive for 20 keV electrons as it is for 10 keV electrons. In chapter 4, characteristics such as sensitivity, contrast, and resolution will be explained.

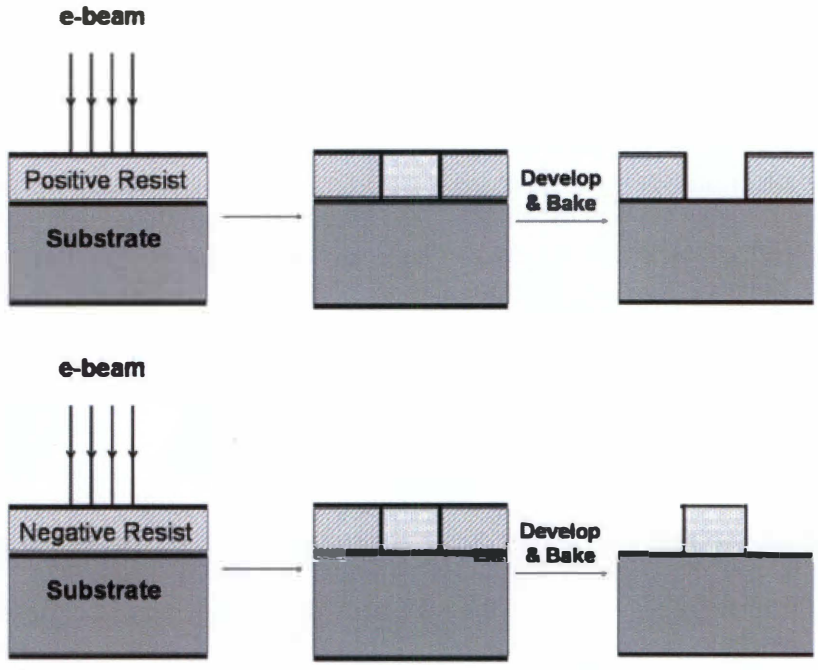


Figure 2-7: Schematics of positive and negative resists reaction to e-beam and resist development.

Table 2-2: A few common e-beam resists and some of their characteristic parameters at 20keV incident.

Resist	Polarity	Sensitivity (μC/cm²)	Resolution (μm)	Contrast γ
PBS	+	1.8	0.5	1.7
PMMA	+	100	< 0.1	2
EBR - 9	+	1.2	0.5	3
FBM - 110	+	1.5	1.5	5
AZ 2400	+	200	0.5	2
COP	-	0.5	1.5	0.8
OEBR-100	-	0.5	1.5	0.8
SEL - N	-	1	1	0.6
GMCIA	-	7	0.5	1.7
CMS	-	2	0.7	1.5

2.5. Applications of Electron Beam Lithography

The most important use of EBL is in the production of photolithography masks. EBL remains the major tool for manufacturing lithography masks. Simple masks are made by coating a chrome clad glass plate with e-beam resist layer which is subsequently exposed and developed to generate the required pattern on the mask. This is the preferred technique for masks production, because of its flexibility in providing rapid turnaround of a finished part described by a CAD file. The ability to meet rigorous line width control and pattern placement specifications, on the order of 50nm or less each, is a remarkable achievement.

There is considerable interest today in exploring device physics in the nanometer regime, that is, devices and structures with line widths less than or equal to 100 nm. Quantum transport and single-electron effects become important here, providing new tools for studying the behavior of electrons in metals and semiconductors. In addition, conventional devices and circuits reach fundamental limits at these dimensions, and completely different approaches to electronics can be explored. This has made the advanced prototyping of integrated circuits and manufacturing of small volume specialty products, such as gallium arsenide ICs and optical wave-guides, possible. This mean of lithography has been used in mask repairs [18, 20, 48, 49], curing techniques to improve etch and CD-SEM [50], Electron Beam Induced Conductivity (EBIC), Electron Beam Induced Deposition (EBID), and etc. EBL has been used when the throughput is not an important factor. This is usually the case for research laboratories, where achieving the best and most novel devices and experiments are the main goal. Mainly electron-beam lithography techniques produce higher resolution than corresponding ion or X-ray methods because the resolution of electron-beam writing systems is higher.

Chapter 3

3. Interaction of electron with matter

3.1. Introduction

Electrons interact strongly with matter. Even in a transmission electron microscope specimen, where the target is only 100nm thick, the high energy electrons are scattered many times. Interaction of a charged particle with a complex system of charged particles in a dynamic state of equilibrium such as an atom, molecule or solid is usually divided into two main sets of channels of physical importance. The first is the interaction of the charged projectile with the unperturbed field of the target, which does not lead to a change of its internal energy (elastic collision):

$$e^- + AB \rightarrow e^- + AB \tag{3,1}$$

where e^- is the primary electron and AB denotes target composed of A and B. Generally, A and B would have internal structures but in the case of elastic scattering the system AB (the target) and the projectile could be assumed particles. In this case the interaction is a two-body interaction, which make it simple to analyze. The interaction of an incoming primary charged particle with the nucleus is also an elastic scattering leading mainly to the backscattering of the projectile.

The second and the most important set of channels is the interaction of the primary charged particle with the individual elements of the system (electrons), which is characterized as an inelastic collision where the internal state of the target and/or projectile changes. For example,

$$e^- + AB \rightarrow \begin{cases} e^- + AB^* & \textit{excitation} \\ e^- + AB^{+z} + ze^- & \textit{(multiple)ionization} \\ e^- + A^+ + B + e^- & \textit{dissociative ionization} \\ e^- + A^+ + B^- & \textit{ion pair formation} \\ \quad . & \textit{more} \\ \quad . & \\ \quad . & \end{cases} \tag{3,2}$$

Here, electrons are the primary projectile with no structure. In the case of excitation and simple break up channels, there will be no secondary electrons created.

However, there are many effects that cause secondary electron production in a solid. Nonetheless, the interaction is not a two-body interaction and for the simplest case of an electron interacting with atomic hydrogen, it is a three-body interaction. This makes the problem of inelastic scattering a hard one to analyze and subject of many simplifications. In this chapter, the interaction of electrons with matter will be summarized with emphasis on secondary electron production. There are similarities between the interaction of electrons with matter in the gaseous form and the solid form, but the interaction is more complex for solids and involves many effects associate with the interaction of electron with atoms and/or molecules that are not well understood. The excitation, the ionization of individual atoms or molecules, inner shell ionization and the Auger electron emission from atoms are common features of the interaction of electrons with the matter in gaseous form and solid form. While moving through the solid targets, the primary electron takes part in a large number of different inelastic excitation channels that include excitation of surface and bulk plasmons, inter- and intraband electron transitions (from core to empty levels), and electron hole pair generation as well. However, the fundamental effects of electron scattering from atoms or molecules are essential in understanding its interference in solids. Thus, in this chapter, the interactions of electrons with atoms and molecules are discussed in the early sections and the effects unique to solids are covered in the later sections. In Figure 3-1 a schematic diagram of the processes involved in the interaction of electrons with matter is presented. The probability of these processes to happen and the effect they might have on the sample depends on the energy of the primary, the type of sample and the thickness of the sample.

3.2. General Kinematics of the Collision

The general kinematics of the interaction of electrons where the interaction could involve the target's electron is presented in Figure 3-2. The momenta $\hbar\mathbf{k}_0$, $\hbar\mathbf{k}_s$, $\hbar\mathbf{k}_{se}$, and $\hbar\mathbf{q}$ are the primary electron momentum, the scattered electron momentum, the secondary electron momentum (if any) and the "recoil" momentum, respectively. According to the type of collision, the "recoil" momentum should be appropriately defined. The conservation of momentum reads as:

$$\hbar\mathbf{k}_0 = \hbar\mathbf{k}_s + \hbar\mathbf{k}_{se} + \hbar\mathbf{q}\,. \tag{3,3}$$

The energies E_0, E_s, E_{se} and E_r are the primary electron kinetic energy, the scattered electron kinetic energy, the secondary electron kinetic energy and the energy associated with the "recoil", respectively. The energy conservation reads as:

$$E_0 = E_s + E_{se} + E_r\,. \tag{3,4}$$

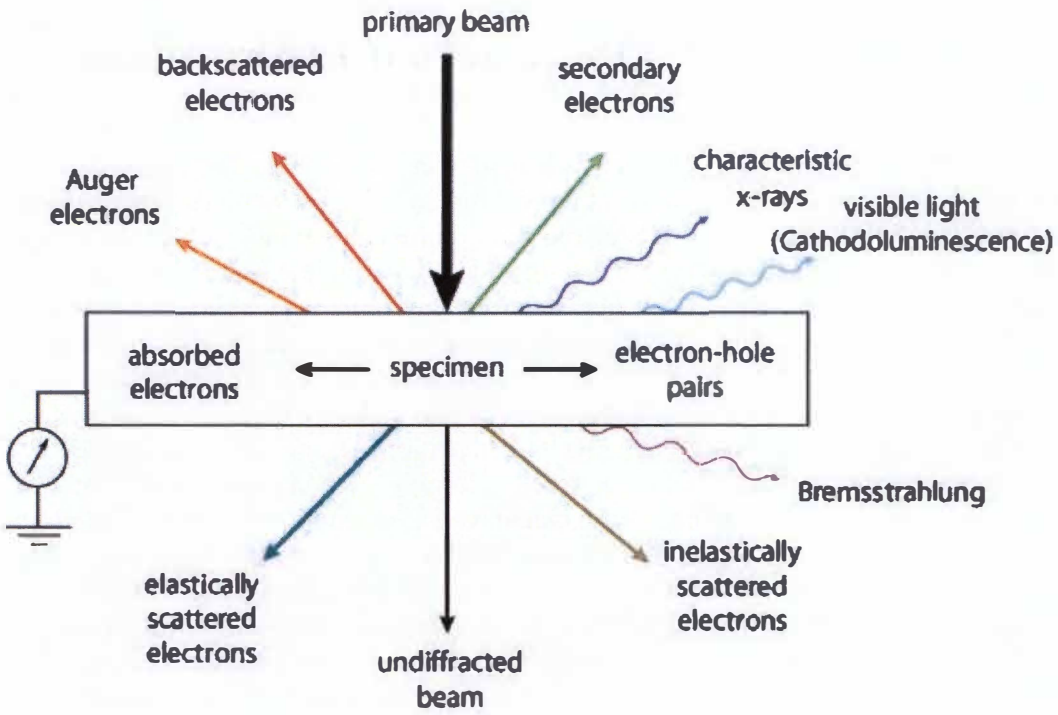


Figure 3-1: A schematic diagram of the processes involved in the electron with matter interaction.

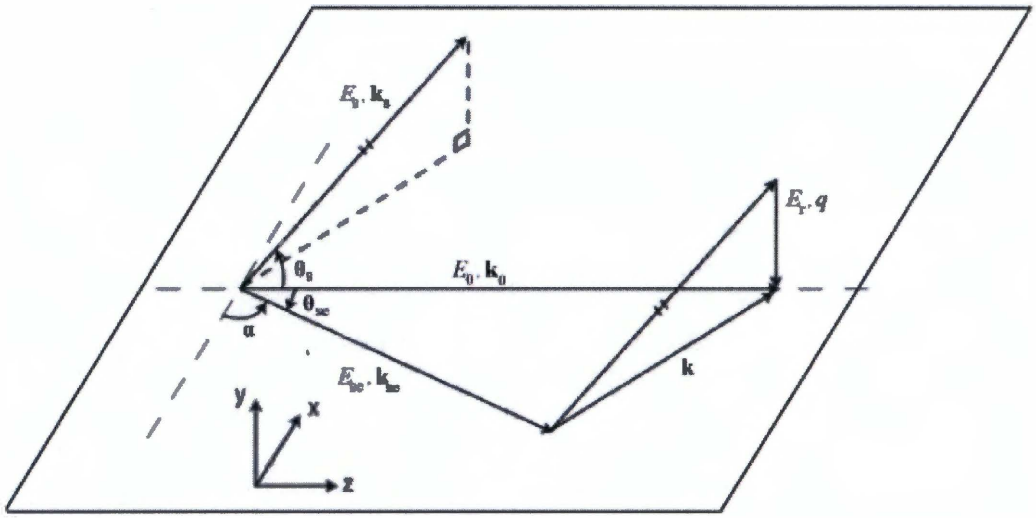


Figure 3-2: The general kinematics of an electron colliding with the target's electron. The kinematic representation here is applicable to the bound electrons as well as free electrons from the target. $\mathbf{k}_0$ and $\mathbf{k}_{se}$ are in the plane shown, and all the vectors are drawn in polar coordinates $\left(\hat{r},\hat{\theta},\hat{\varphi}\right)$. $\mathbf{k}=\mathbf{k}_0-\mathbf{k}_{se}$. θ_{se} & θ_s, are the polar angles between $\mathbf{k}_0$ & $\mathbf{k}_{se}$ and $\mathbf{k}_0$ & $\mathbf{k}_s$ respectively.

Note is added that the general kinematics shown in Figure 3-2, represents an inelastic collision as a secondary electron is ejected from the target. For an elastic collision one expects no ejected electrons. The energy which is not in the form of kinetic energy in equation (3,4) is considered as the energy lost in the collision, ΔE. Therefore, in an elastic collision quantities E_{se} and ΔE should be zero. In this case, the energy E_r is the "recoil" energy of the target. In the case of ionization, the "recoil" energy is equal to the energy of the target electron prior to ejection which could also be called ΔE. This will be discussed later.

3.3. Definitions

3.3.1. Secondary, Fast Secondary, and Back Scattered Electrons

Electrons in the conduction or valence band do not need much energy (low work function) to be promoted into vacuum. The interaction of primary electrons, as

discussed before, with the electrons in the outer shells, the valence band or the conduction band is considered as a sudden interaction. Thus, the majority of the secondary electrons (SE) produced have energies below 50eV. Electron microscopists define SE to have energies less than 50 eV and back scattered electrons (BSE) to have energies larger that 50 eV. However, many of the SEs will acquire energies up to $E_0/2$. These electrons in the range of 50eV to $E_0/2$ are usually referred to as the fast secondary electrons (FSE). The electrons with energies larger than $E_0/2$ will be denoted as scattered and treated as a new primary electron making further collisions. These later electrons are observed in the forward and backward angles. The energy distribution of the cross sections for secondary electron, shown in Figure 3-3, it is evident that there is smaller probability of FSE production. This probability should be added to the probability of inner-shell ionization and Auger electron production giving the total yield of FSE. Even though the cross sections for the production of FSEs are small, their total number is high enough to affect the pattern production in the sample. Note that in quantum mechanics, identical particles (in this case, electrons) are indistinguishable, and the above definitions based on the energy and distribution of the electrons are only made to understand and describe the interactions in a more detailed manner.

In the work described here, the sample is composed of a thin layer of PMMA at the top with a thick Si substrate. The secondary electrons, fast or slow, produced in the top layer will increase the rate of exposure in PMMA. The angular distribution of the FSE shows that they are usually produced at large angles with respect to the initial primary electron velocity. An example is presented for the electron impact with water in as there are no experimental cross sections for PMMA.

Excitation of Outer-Shell Electrons

Most of the inelastic collisions of a fast electron arise from interaction with electrons in outer atomic shells and result in an energy loss of less than 100 eV. In a solid, the major contribution comes from valence electrons (referred to as conduction electrons in a metal), although in some materials (e.g., transition metals and their compounds) underlying shells of low binding energy contribute appreciable intensity in the 0-100 eV range.

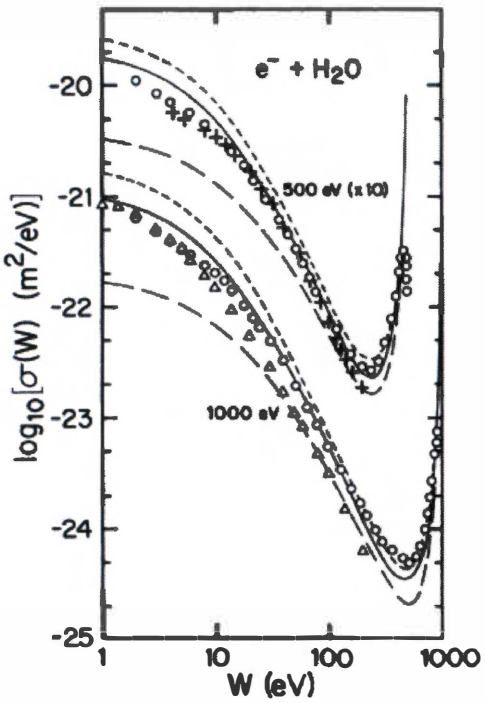


Figure 3-3: The energy variation of the secondary electron cross section for the electron-water collision[51] (W is the secondary electron's kinetic energy).

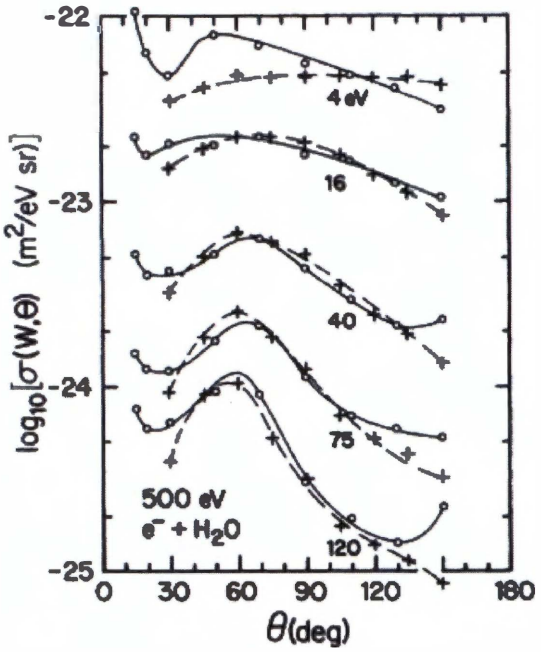


Figure 3-4: The angular distribution of the secondary electrons as a function of scattering angle θ ($\theta = \pi/2 - \alpha$) is plotted for different ejection energy for the primary electrons of 500eV, in the electron-water collision. +, Ref[51].; ○, Ref[52]

3.3.2. Bosons and Fermions

In quantum mechanics (QM), when a system includes a number of identical problems, only certain kets (wave functions) of its space can describe its physical states. For identical particles, the kets of the system are either completely symmetric or completely antisymmetric with respect to permutation of these particles. Those particles for which the physical kets are symmetric are called *bosons*, and those for which they are antisymmetric, are called *fermions*. The above QM postulate is the most general definition of the two main classes of particles, bosons and fermions. The other definition of bosons and fermions that is known as spin statistics theorem, provable in quantum field theory, asserts that in three dimensions, particles with magnitude of total angular momentum equal to an even multiple of $\hbar/2$ are bosons, and those with magnitude of total angular momentum equal to an odd multiple of $\hbar/2$ are fermions. However this proven in three dimensions, does not apply to other dimensions, where it is not possible to define spin or any form of angular momentum

(as is clear classically) and the only way to find if a particle(s) in one dimension is a boson or fermion is to determine the symmetry of the kets as described above.

A fundamental result from the above postulate (*exchange symmetry principle*) is known as "*Pauli's exclusion principle*". It has numerous important physical consequences which will be mentioned. This principle can be stated as follows

Two identical fermions cannot be in the same individual quantum mechanical state.

All particles are either bosons or fermions. A photon, which is massless, is a boson. So depending on whether the particle is a boson or fermion, its QM properties varies. This would be clear in the next statements.

A QM state of a system of particles (ket or wave function), $|\psi\rangle$, can be written as a tensor product of a spin $|s\rangle$ (in general total angular momentum) state and a spatial wave function $|r\rangle$ (Operators **S** and **R** commute), $|\psi\rangle = |s\rangle \otimes |r\rangle$.

A system with identical bosons has symmetric wave functions. As the spin states of such a system are always symmetric, the spatial wave functions for this system will always be symmetric. Therefore for an ideal bosonic beam with energy E, all bosons can be placed in the same QM state (and position $\mathbf{r}$). For fermions the problem gets more complicated. The spin state of a system of fermions can be either symmetric or antisymmetric. Such a system has antisymmetric wave functions, so depending on the polarity of the spin states, the spatial states of the system can be symmetric and antisymmetric. In QM we deal with probabilities, so always a system consisting of bosons has a higher chance of achieving a fine particle beam, and a higher beam current than fermions under the same conditions. There is theoretically no limit to how many bosons can occupy the same quantum state and specific position. Fermions have a tendency to avoid each other and this is described by Fermi-Dirac statistics. In contradiction, bosons have the tendency to conglomerate, in the manner described by Bose-Einstein statistics.

The exchange symmetry principle plays an essential rule in the optics of particles Symmetry effects in the elastic scattering cross section of identical particles are presented in the Mott Formulas section.

3.4. Elastically scattered electrons*

Elastic scattering of electrons from a target is due to the (screened) coulomb field of the nucleus. This process can be treated classically either in accordance with a particle based Rutherford scattering or the Huygens principle as a wave packet. It is assumed that electrons are elastically scattered when there is no change in the state of the target; i.e. $\Delta E = 0$, and therefore there will be no change in the wave function of the target. The only energy transferred to the target in an elastic process is the "recoil" energy as kinetic energy and therefore there is no secondary electrons; i.e. $E_{se} = 0$ and $\mathbf{k}_{se}=0$ in equation (3,3) as well. This process is coherent in principle and the scattered electrons are mostly observed at small scattering angles, which include the undiffracted electrons where the target recoil energy is zero. This is an important issue in TEM. For gaseous as well as thin solid targets, elastically scattered electrons contribute the most in the total cross section, where single scattering conditions are present (Figure 3-5)[53]. The scattering angle depends strongly on how close the projectiles get to the nucleus thereby decreasing the shielding effect of the electron cloud in the target[54, 55]. This process is schematically shown in Figure 3-6. The Rutherford (forward) and backward scattering are examples where the primaries (electron or any ion) scatter off the target elastically.

For dense gaseous targets as well as thick solids, multiple scattering conditions hold and therefore, several collisions may take inelastic channel as well. In this case elastically scattered electrons are not an important issue and they are only responsible for interactions that happen deeper in the solid. As shown in Figure 3-6, high energy electrons scattered off the nucleus elastically may result in Bremsstrahlung radiation.

Because a nucleus is some thousands of times more massive than an electron, the energy transfer involved in elastic collisions is usually negligible. However, for the small fraction of electrons which are scattered through large angles (including head-on collisions for which $\theta \rightarrow \pi$), the transfer can amount to some tens of eV, as evidenced by the occurrence of displacement damage at high incident energies[56].

Although inelastic scattering and the secondary electron production are essential in nanolithography, elastic scattering is of relevance for the following reasons:

1. Because primary electrons are involved both in elastic and inelastic channels

* It is convenient to divide the scattering of fast electrons into elastic and inelastic components. An experimentalist can distinguish between the two on an empirical basis, the term "elastic" being taken to mean that the energy loss to the sample is less than some experimental resolution limit. Such a criterion results in electron scattering by phonon excitation being classified as elastic (or quasi-elastic) if measurements have been made using an electron microscope, where the energy resolution is usually not better than 1 eV.

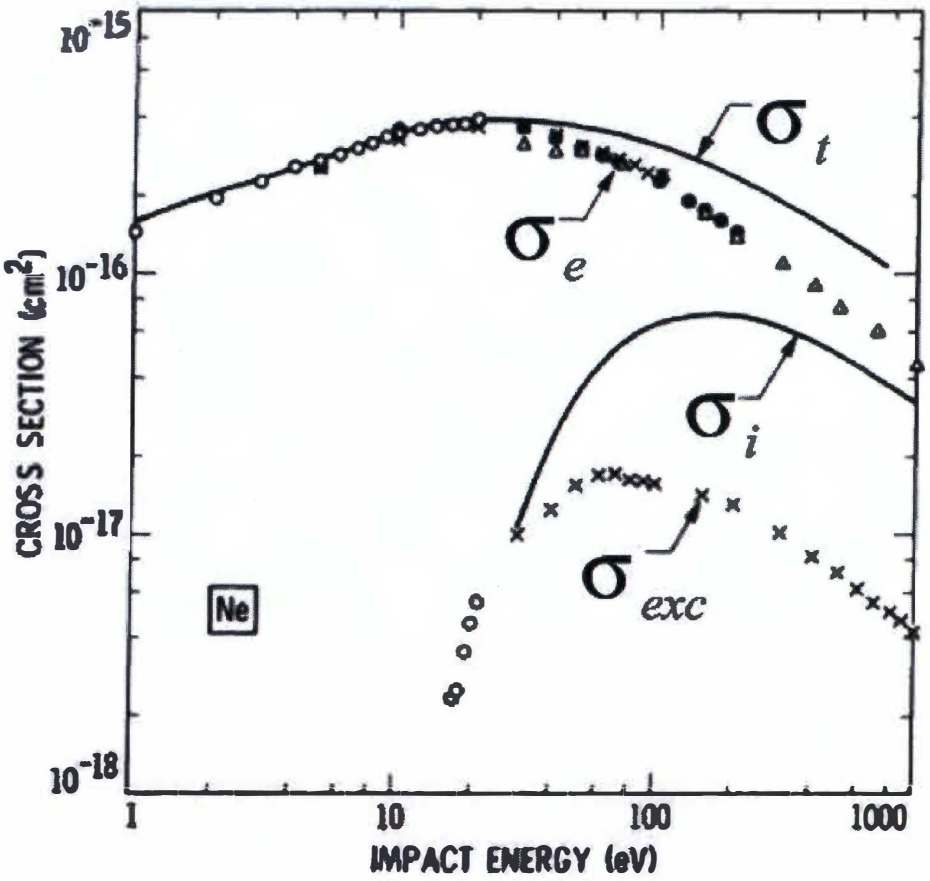


Figure 3-5: An overview of the total electron scattering data for Ne. σ_t : solid line was drawn on the basis of the average data presented in references[53, 57-59]. σ_e : ○, Ref.[53]; Δ, Ref.[60]; ●, Ref.[61]; ×, Ref.[53]; σ_{exc} : ○, Ref.[62]; ×, Ref[60].

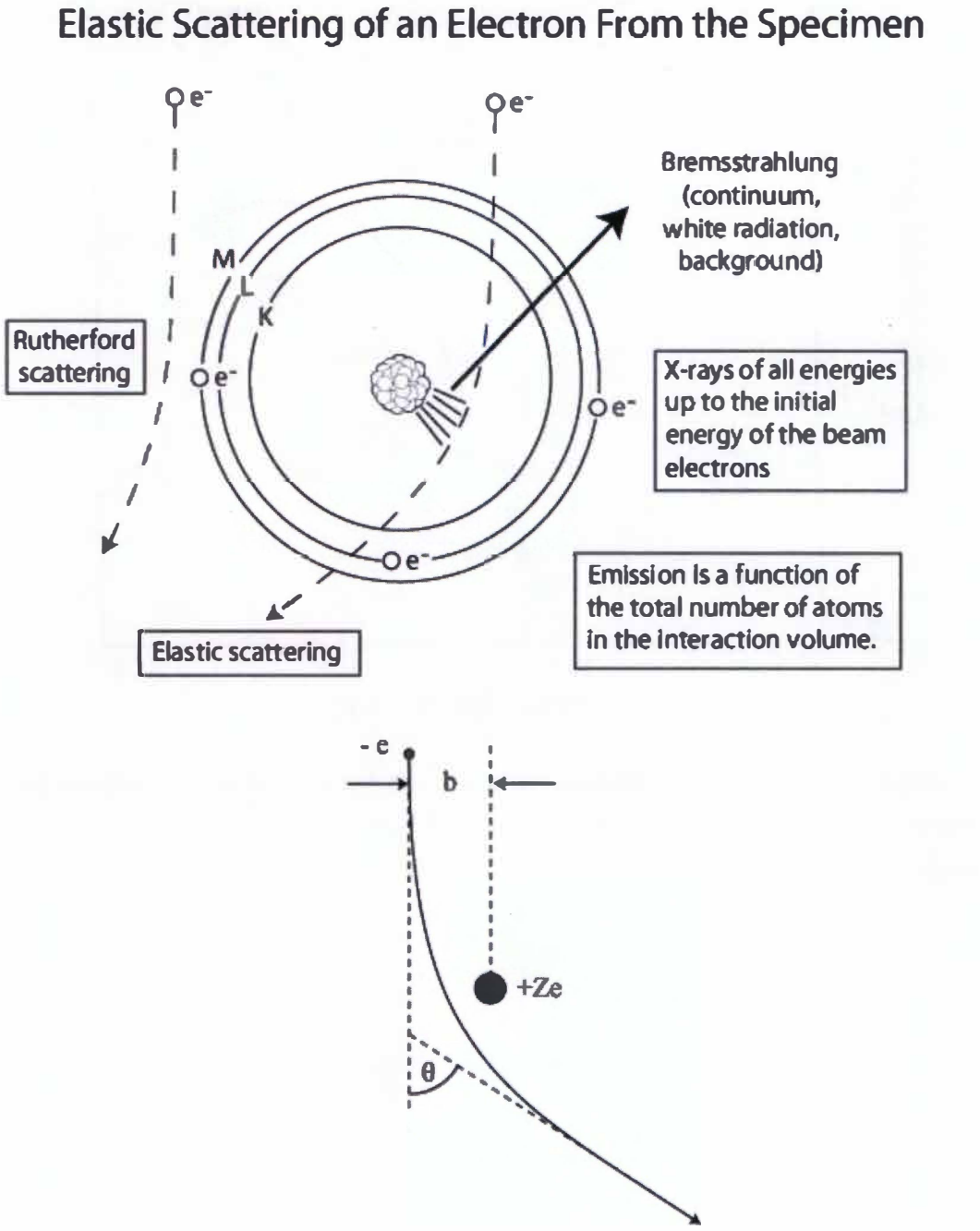


Figure 3-6: Schematics of the processes involved in the elastic scattering of an electron from an atom or molecule. The atom or molecule may be a part of a gaseous target or solid sample. The impact parameter, *b*, and the scattered angle, θ, are also shown.

within the sample, elastic scattering greatly affect the angular and energy distribution of the inelastically scattered electrons;

2. In a crystalline material, elastic scattering may redistribute the electron flux (current density) within each unit cell and thereby alter the probability of inelastic channels;

3. The intensity of elastic scattering (as a ratio of the inelastically scattered intensity) can provide an estimate of the local atomic number or chemical composition of a specimen.

3.4.1. General Formulas

A quantity of basic importance in scattering theory is the differential cross section (DC) $d\sigma/d\Omega$, which represents the probability of an incident electron being scattered (per unit solid angle Ω) by a given atom. For elastic scattering, one can write

$$\frac{d\sigma}{d\Omega} = |f(\theta)|^2 \tag{3,5}$$

, where $f(\theta)$ is the (complex) scattering amplitude or scattering factor, which is a function of the scattering angle θ or the recoil momentum $\hbar\mathbf{q}$ ($q = 2k_0 \sin(\theta/2)$), $f(\mathbf{q})$, as shown in Figure 3-2 ($\theta = \theta_{se}$). In the case where the mass of the projectile is comparable with that of the target, the target would gain quite a large kinetic energy and therefore the value of $\mathbf{k}_s$ is smaller than that of the initial momentum of the projectile, $\mathbf{k}_0$. This will affect the relation between the momentum transfer and the scattering angle. The phase component of $f(\theta)$ is important in high-resolution phase-contrast microscopy[63], but for the calculation of scattered intensity only the amplitude is required, as implied in equation (3,5). The scattering amplitude for the elastic collision of a particle with a target having an interaction potential $V(r)$ is defined as:

$$f(\mathbf{q}) = -\frac{m}{2\pi\hbar^2}\int V(r)\psi^*\psi \exp(i\mathbf{q}\cdot\mathbf{r})d^3\mathbf{r} \tag{3,6}$$

where ψ is the wavefunction of the target before and after the collision and m is the reduced mass of the electron. Within the first Born approximation (equivalent to assuming only single scattering within each atom), $f(\mathbf{q})$ is proportional to the three-dimensional Fourier transform of the atomic potential $V(r)$; i.e.:

$$f(q) = -\frac{2m}{\hbar^2}\int_0^\infty \frac{\sin(qr)}{qr}V(r)r^2 dr$$
$$= -\frac{2m}{\hbar^2 q^3}\int_0^\infty \frac{\sin(\rho)}{\rho}V(\rho/q)\rho^2 d\rho \qquad (3,7)$$

Note that the scattering amplitude depends on the values of **q** only. One can simplify the formula (3,7) as:

$$f(q) = -\frac{1}{a_0 q^2}F(q) \qquad (3,8)$$

, where $F(q)$ is called the elastic form factor and defined as:

$$F(q) = q^{-1}\int_0^\infty \frac{\sin(\rho)}{\rho}U_{\text{int}}(\rho/q)\rho^2 d\rho \qquad (3,9)$$

and $U_{\text{int}}(r) = 2mV(r)/\hbar^2$ is called the reduced potential for the interaction. Here a_0 is the Born radius. Introduction of the reduced potential facilitates the change of units from SI to atomic units, which is easier in computer programming.

If one assumes a simple Coulomb interaction[†]:

$$U_{\text{int}}(r) = -\frac{Z}{a_0 r} \qquad (3,10)$$

, between the electron and the target nucleus of charge Z, then the form factor would be equal to the total charge of the nucleus. Generally, when the electron traverses a sample, the potential between the electron and the target will include the interaction between the target's electrons as well, and therefore the interaction would be:

$$U_{\text{int}}(r) = -\frac{Z}{a_0 r} + \frac{1}{a_0}\sum_{i=1}^{z}\frac{1}{|\mathbf{r} - \mathbf{r}_i|} \qquad (3,11)$$

, where $\mathbf{r}_i$ is the position vector of the i^{th} electron in the target. The first term in equation (3,11) represents Coulomb attraction by the nucleus while the second term is a sum of the repulsive effects of each atomic electron. Thus the quantity,

---

[†] The forms for reduced potential in equations (3,10), (3,11) and (3,13) is chosen so that inserting 1 for a_0 will convert the formulas to atomic units.

$d\sigma/d\Omega$ can be expressed in terms of an "atomic" *form factor* $F_a(q)$[64]:

$$\frac{d\sigma}{d\Omega} = \frac{4\gamma^2}{a_0^2 q^4} |Z - F_a(q)|^2 \tag{3,12}$$

where γ is the relativistic factor for the relativistic projectile and introduced into this equation outside the present derivation[65]. In this equation, $\hbar\mathbf{k}_0 = \gamma m\mathbf{v}$, where **v** is the speed of the projectile. Electrons with energy of the order of 100 keV should be treated as the relativistic projectile. The equation (3,12) is a general relation for the elastic scattering of electron, ion and photons from targets. Note that both F and F_a are unitless.

3.4.2. Atomic Models

The earliest and simplest model for elastic scattering of charged particles is based on the unscreened electrostatic field of a nucleus and was first used by Rutherford in the context of classical mechanics to account for the scattering of α-particles seen by Geiger and Marsden. Whereas an α-particle is repelled by the nucleus, an incident electron is attracted; by applying classical mechanics, the trajectories can be shown to be hyperbolic. For light elements, equation (3,12) is a reasonable approximation at large scattering angles[66] and can be useful for estimating rates of backscattering ($\theta > \pi/2$) in solids[32]. Because no allowance has been made for screening of the nuclear field by the atomic electrons, the Rutherford model greatly overestimates the elastic scattering at small θ (corresponding to large impact parameter b) and gives an infinite cross section if integrated over all angles. For the case of electrons as the projectile and assuming the simple interaction by equation (3,10), $F_a(q)$ is equal to zero and therefore the quantum mechanical treatment leading to equation (3,12) leads to a formula similar to the classical Rutherford model.

A simpler way of incorporating screening, the second term in equation (3,11), is to assume a charge density for the target (atom in general or unit cell for solids) in which the reduced potential will take the form of a Yukawa expression in which the nuclear potential is attenuated exponentially as a function of distance r from the nucleus:

$$U_{\text{int}}(r) = \frac{Ze^{(-r/r_0)}}{a_0 r} \tag{3,13}$$

where r_0 is the screening radius. The angular distribution of the elastic scattering is:

$$\frac{d\sigma}{d\Omega} = \frac{4\gamma^2}{a_0^2 q^4}\left(\frac{Z}{1+(qr_0)^{-2}}\right)^2 . \qquad (3,14)$$

The equation (3,14) solves the problem associated with the Rutherford's model which is overestimating the cross section at the small angles. However, it depends on the choice of r_0. In Figure 3-7, the "scaled" angular distribution, $(a_0/2\gamma Z)^2 (d\sigma/d\Omega)$, of the elastically scattered electrons is plotted against the relative momentum transfer, $2q/\hbar k_0$, for different values of r_0. The figure shows a strong effect of r_0 on the cross sections, especially at low momentum transfer or small scattering angle. One choice of r_0 is on the basis of a Thomas-Fermi statistical model that gives a value equal to $a_0 A^{-1/3}$, which is similar to the radius of a proton in the shell model.

More accurate cross sections are achieved by calculating the atomic potential from an iterative solution of the Schrodinger equation, as in the

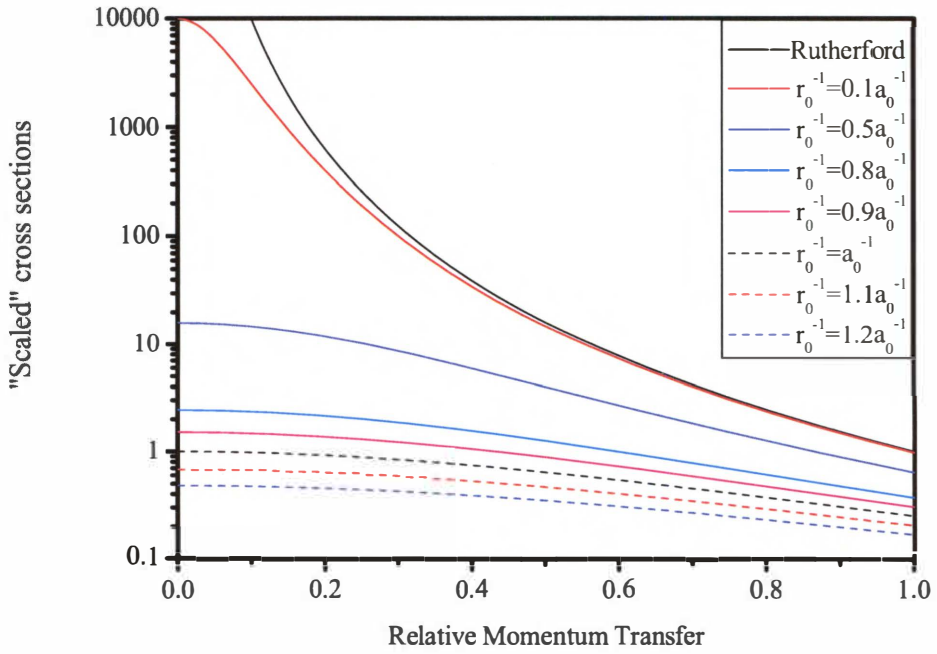


Figure 3-7: The "scaled" angular distribution, $(a_0/2\gamma Z)^2 (d\sigma/d\Omega)$, of the elastically scattered electrons with atoms assuming different r_0, is plotted against the relative momentum transfer, $2q/\hbar k_0$.

Hartree-Fock and Hartree-Slater methods[67, 68]. Alternatively, electron spin and relativistic effects within the atom can be included by using the Dirac equation[69], leading to so-called Mott cross sections. Partial-wave methods may be used to go beyond the Born approximation[70], which fails if Z approaches or exceeds $137(v/c)$ (137 is equal to the inverse of the fine structure constant), in other words for heavy elements or low incident energies.

The scattering calculations which have been mentioned are all based on properties of a single isolated atom. In a molecule, the cross section per atom is reduced at low scattering angles, typically by 10%-20%, as a result of chemical bonding[71]. In a crystalline solid, the angular dependence of elastic scattering is altered dramatically by Bragg diffraction. In *amorphous* solids, Bragg diffraction is relatively weak and an atomic model can be used as a guide to the magnitude and angular distribution of elastic scattering.

As an alternative to describing the amount of scattering in terms of an elastic cross section (σ_e per atom), one can use an inverse measure: $\lambda_e = (\sigma_e n_a)^{-1}$, where n_a is the number of atoms per unit volume of the sample. The *mean free path* λ_e represents the mean distance between elastic collisions in the amorphous material. In the same way, the *mean free path* λ_i represents the mean distance between inelastic collisions.

3.4.3. Diffraction Effects

In crystalline materials, the regularity of the atomic arrangement requires that the phase difference between waves scattered from each atom be taken into account by introducing a *structure factor* $f_s(\theta)$ defined by

$$f_s(\theta) = \sum_j f_j(\theta) \exp(-i\mathbf{q}\cdot\mathbf{r}_j) \tag{3,15}$$

, where $\mathbf{r}_j$ and f_j are the coordinate and scattering amplitude of atom j; $\mathbf{q}\cdot\mathbf{r}_j$ is the associated phase factor and the integration is carried out over all atom (j=1,2, etc.) in the unit cell. Note that θ and q can be easily interchanged due to the definition given before. The above equation can also be expressed in the form:

$$f_s(\theta) = \frac{1}{4\pi} \int U_{\text{int}}(r) \exp(-i\mathbf{q}\cdot\mathbf{r}) d^3\mathbf{r} \tag{3,16}$$

where the integration is carried out over all volume elements within a unit cell. Similar to the elastic form factor, equation (3,16) indicates that the structure factor is related to the Fourier transform of the lattice potential. The angular distribution

of the cross section in a direction θ relative to the incident beam is $|f_s(\theta)|^2$, and peaks at values of θ for which the scattered waves are in phase with one another.

Each diffraction maximum (Bragg beam) can also be regarded as arising by "reflection" from atomic planes, whose spacing d depends on the unit-cell dimensions and on the Miller indices. Bragg reflection occurs when the angle between the incident beam and the diffracting planes coincides with a Bragg angle θ_B defined by

$$\lambda = 2d \sin(\theta_B) \qquad (3,17)$$

, where $\lambda = 2\pi/k_0$ is the incident-electron wavelength and the scattering angle θ is twice θ_B. For a 10keV incident electron, $\lambda = 0.0117\ nm$ and the scattering angles corresponding to Bragg reflection for a typical crystalline target is usually around 30 mrad. Larger scattering angles are due to the planes of smaller separation or to higher-order reflections whose phase difference is a multiple of 2π.

The Bragg-reflected beams can be recorded by a two-dimensional detector such as a photographic plate. For a single-crystal specimen, the diffraction pattern consists of an array of sharp spots whose symmetry and spacing are closely related to the crystal symmetry and lattice constants. In the case of a polycrystalline sample whose crystallite size is much less than the incident-beam diameter, random rotational averaging produces a diffraction pattern that consists of a series of concentric rings rather than a spot pattern.

In a crystalline solid, it is difficult to apply the concept of a mean free path for elastic scattering; the intensity of each Bragg spot depends on the crystal orientation relative to the incident beam and is not proportional to crystal thickness. Instead, each reflection is characterized by an *extinction distance* ξ_g, which is typically in the range *25-100* nm for 100-keV electrons and low-order (small θ_B) reflections. In the "ideal two-beam" case, where equation (3,17) is approximately satisfied for only one set of reflecting planes and where effects of *inelastic* scattering are negligible, *50%* of the incident intensity is diffracted at a crystal thickness of ξ_g */4* and 100% at ξ_g */2*. For thickness larger than ξ_g */2*, the diffracted intensity decreases with increasing thickness and would go to zero at thickness equal to multiples of ξ_g if inelastic scattering could be neglected. This oscillation of intensity gives rise to the "thickness" or Pendellosung fringes, which are seen in transmission-microscope images.

3.4.4. Electron Channeling

A solution of the Schrodinger equation for an electron moving in a periodic potential results in wave functions known as Bloch waves, which are plane waves whose amplitude is modulated by the periodic lattice potential. Inside the crystal, an incident electron is represented by the sum of a number of Bloch waves, each having the same total energy. Because each Bloch wave propagates independently without change of form, this representation is generally preferable to describing electron propagation in terms of direct and diffracted beams whose relative amplitudes vary with the depth of penetration. In the ideal two-beam situation, there are only two Bloch waves, whose flux-density distributions (as a function of atomic coordinate) are illustrated in Figure 3-8. The type-2 wave has its intensity maximum located halfway between the planes of Bragg-reflecting atoms and propagates parallel to these planes. The type-1 wave propagates in the same direction but has its current density peaked exactly *on* the atomic planes. Because of the attractive force of the atomic nuclei, the type-1 wave has a more negative potential energy and therefore a higher kinetic energy and larger wave vector than the type-2 wave. This difference in wave vectors between the Bloch waves their combined intensity leads to a "beating" effect, which provides an alternative but equivalent explanation for the occurrence of thickness fringes in the TEM image.

The relative amplitudes of the Bloch waves depend on the crystal orientation. For the two-beam case, both amplitudes are equal at the Bragg condition (Figure 3-8), but if the crystal is tilted towards the "zone-axis" orientation (such that the angle between the incident beam and the atomic planes is less than the Bragg angle) more intensity is added to Bloch wave 1. Conversely, if the crystal is tilted in the opposite direction, Bloch wave 2 becomes more prominent. Moreover, away from the Bragg orientation the current-density distributions within the Bloch waves become more uniform, such that they more nearly resemble plane waves. Besides having a larger wave vector, the type-1 Bloch wave has a greater probability of being scattered by *inelastic* events occurring close to the center of an atom, such as inner-shell and thermal-diffuse (phonon) excitation. Electron microscopists refer to this inelastic scattering as *absorption,* meaning that the scattered electron is absorbed by an angle-limiting "objective" aperture introduced to enhance image contrast or limit lens aberrations. The effect is incorporated into diffraction-contrast theory by adding to the lattice potential an imaginary component $V_0^i = 2\lambda_i/\hbar v$, where λ_i is an appropriate inelastic mean free path. The variation of this "absorption" with crystal orientation is called anomalous absorption and is characterized by an imaginary potential V_0^i. In certain directions the crystal appears more "transparent" in a bright-field transmission microscope image; in other directions it is more opaque owing to increased inelastic scattering outside the objective aperture. This behavior is analogous to the Borrmann effect in x-ray penetration and is similar in many respects to the

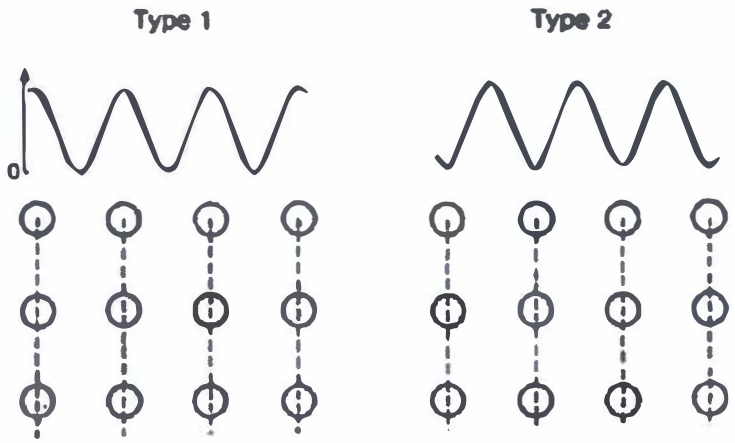


Figure 3-8: Schematic diagrams of the two types of Bloch wave present in a simple cubic crystal at the exact Bragg-reflecting orientation, assuming two-beam conditions. The Bloch wave intensities are shown at the top of the diagram, in relation to the planes of reflecting atoms. (After Hirsch *el al.*, 1977, but following a more recent numbering scheme)

channeling of nuclear particles through solids. Anomalous absorption is also responsible for the Kikuchi bands which appear in the background to an electron diffraction pattern[72, 73].

The orientation dependence of the Bloch-wave amplitudes also affects the intensity of inner-shell edges visible in the energy-loss spectrum. As the crystal is tilted through a Bragg orientation, an ionization edge will become either more or less prominent, depending upon the location (with the unit cell) of the atoms being ionized, relative to those which lie on the Bragg reflecting planes[74]. Inner-shell ionization is followed by deexcitation of the atom (involving the emission of Auger electrons or characteristic x-ray photons), so as a further result of the orientation dependence of absorption, the amount of x-ray emission varies with the crystal orientation, provided the incident beam is sufficiently parallel[75, 76]. This variation in x-ray signal is utilized in the Atom Location by Channeling Enhanced Microanalysis method (ALCHEMI) of determining the site of an emitting atom[77].

In the more typical situation in which a number of Bragg beams are excited simultaneously, there are an equally large number of Bloch waves whose current-density distribution may be more complicated than in the two-beam case[78]. The current density associated with each Bloch wave has a two-dimensional distribution when viewed in the direction of propagation[79].

3.4.5. Phonon Scattering

Due to their thermal (and zero-point) energy, atoms in a crystal vibrate about their lattice sites and this vibration acts as a source of electron scattering. An equivalent statement is that the transmitted electrons generate (and absorb) phonons while passing through the crystal. Since phonon energies are of the order of $k_B T$ (k_B = Boltzmann's constant, T = absolute temperature) and do not exceed $k_B T_D$ (T_D = Debye temperature), the corresponding energy losses (and gains) are below 0.1 eV and are not resolved by the usual electron-microscope spectrometer system. There is, however, a wealth of structure in the vibrational-loss spectrum, which can be observed using reflected low-energy electrons[80, 81].

Except near the melting point, the amplitude of atomic vibration is small compared to the interatomic spacing and (as a consequence of the uncertainty principle) the resulting scattering has a wide angular distribution. Particularly in the case of heavier elements, phonon scattering provides a major contribution to the diffuse background of an electron-diffraction pattern. This extra scattering occurs at the expense of the purely elastic scattering; the intensity of each elastic (Bragg-scattered) beam is reduced by the Debye-Waller factor: $\exp(-4\pi\sin(\theta_B)/\lambda)\overline{v^2}$, where λ is the electron wavelength, and $\overline{v^2}$ is the component of mean-square atomic displacement in a direction perpendicular to the corresponding Bragg-reflecting planes.

The *total* phonon-scattered intensity (integrated over the entire diffraction plane) is specified by an absorption coefficient $\mu_p = 2V_0^p/\hbar v$, where V_0^p is the phonon contribution to the imaginary potential and v is the electron velocity. An inverse measure is the parameter $\lambda_p = 1/\mu_p$, which is roughly equivalent to a mean free path for phonon scattering with a typical values of the order of 100nm depending on the mass of the target element and the temperature. Unlike other scattering processes, phonon scattering is appreciably temperature dependent, increasing by a factor of 2-4 between 10 K and room temperature. Like elastic scattering, it increases with the atomic number Z of the scattering, roughly as $Z^{3/2}$ [82].

3.5. Inelastic Collision (Inelastically Rearranged Electrons)

The primary electrons interacting with matter, as stated before, may take any of the several inelastic channel available where $\Delta E \neq 0$. In contrast with the elastic scattering of electrons by matter, electron-electron interactions are responsible for the inelastic process. Again there are different phenomena involved with respect to the gaseous or thin solid targets and the thick solid target. Common to both thin and thick

targets are the secondary electron production or the ionization process which includes the Auger process as well. In Figure 3-9, schematics of the inelastic processes involved with the scattering of electrons from matter are shown.

In this work, the phenomenon of interest in the inelastic scattering of electrons from a target is the formation of secondary electrons. This includes simple ionization or the Auger electron production, which requires ionization from inner shells. In either of the two cases, the quantity E_r in equation (3,6) is equal to the energy of the target electron prior to the collision. However, two ionized electron are detected in the case of the Auger process. For solids one should add the energy of the vacant state in the conduction band to the energy loss. Usually the recoil energy and momentum of the target are negligible and especially for solid targets it is zero. In this case, the "recoil" momentum is:

$$\mathbf{q} = -\mathbf{p} \tag{3,18}$$

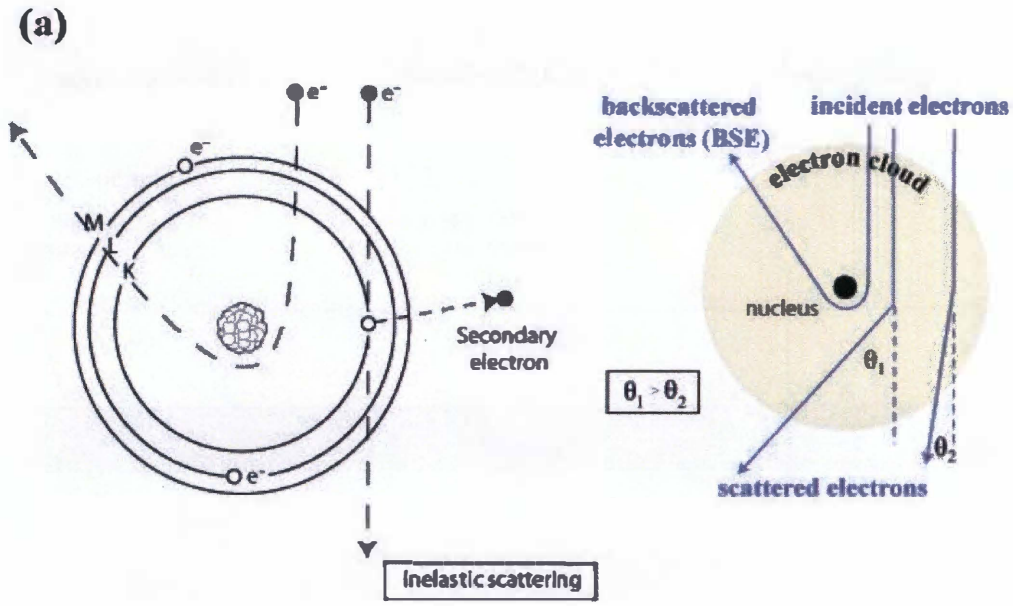
, where $\mathbf{p}$ is the momentum of the bound electron.

For the bound electron, there is a dispersion relation between its energy and momentum as:

$$E_r = E_r(\mathbf{p}) \tag{3,19}$$

In principle, this equation is the dispersion relation representing the Hamiltonian of the target in the energy-momentum phase space which is not generally known and one can measure it in an (e,2e) experiment[83] or angle resolved photoelectron spectroscopy[84]. Equation (3,19) could be a known equation added to equations (3,3) to (3,18) to solve for the kinematical parameters of the collision. This is a "luxury' which is not usually available. However, neglecting only the "recoil" momentum (momentum of the bound electron) in equation (3,3), one can solve for the scattering angles from equations (3,3) and (3,4) as:

$$\sin(\alpha) \cong (k_{se}^2 + m|E_r|/\hbar^2)/k_0 k_{se} \tag{3,20}$$



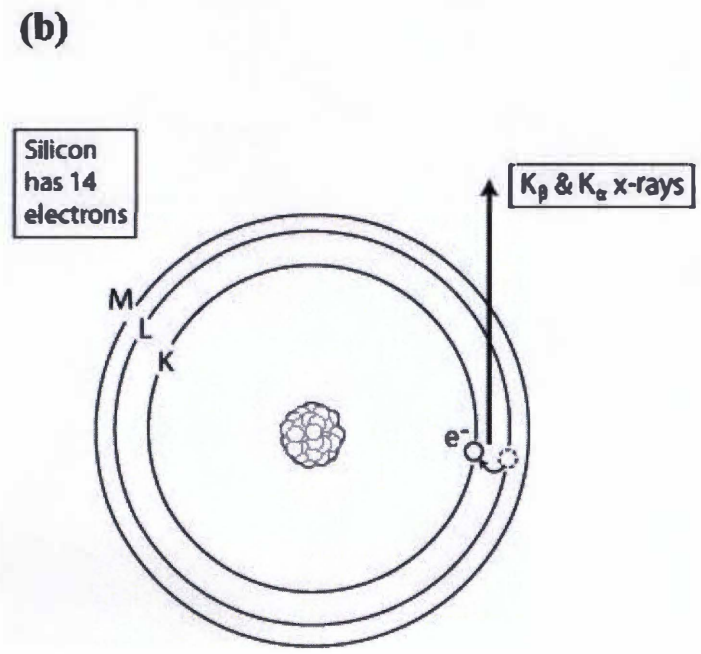


Figure 3-9: Schematics of the processes involved in the inelastic scattering of an electron from (a) an atom/molecule including BSE, (b) X-rays from Silicon, and (c) a solid. Again, the atom or molecule may be a part of a gaseous target or solid sample.

(c)

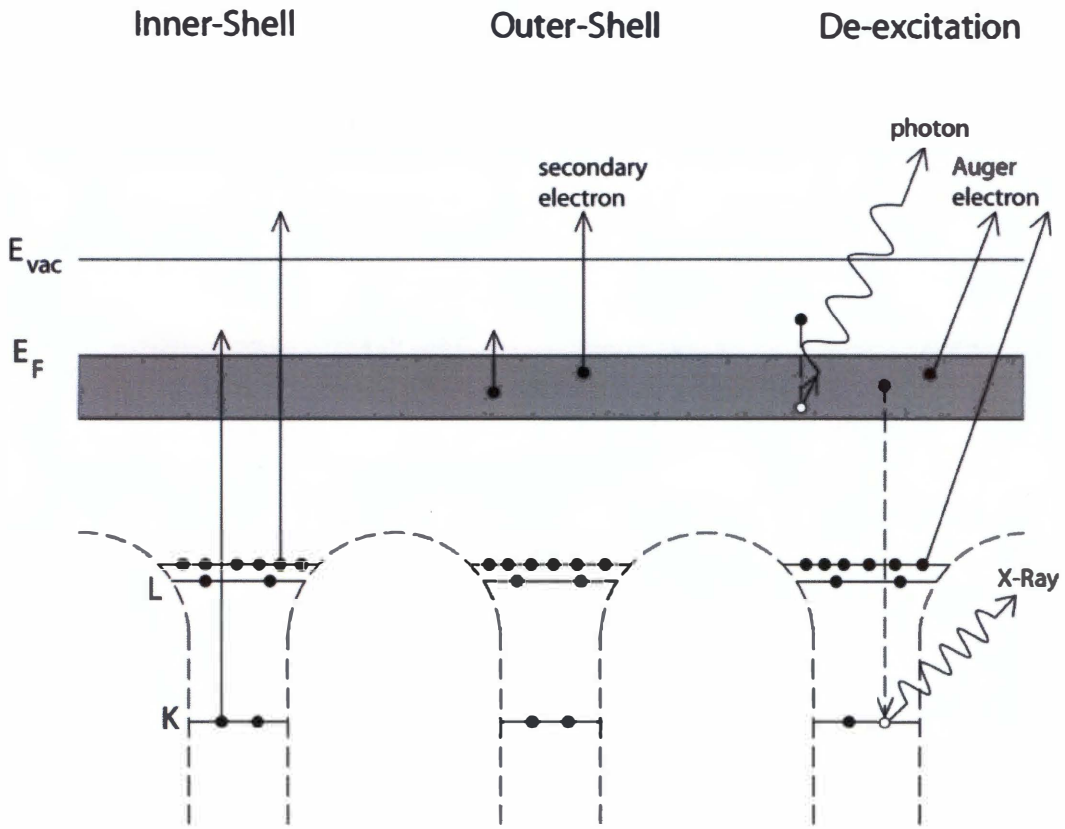


Figure 3-9: Continued.

, where m is the electron mass. This shows that the secondary electrons would leave the target at an angle close to 90^{o} with respect to the primary electrons. Nonetheless, this is a very simplified classical picture and one should consider the experimental results from the literature into account. In Figure 3-4, the angular distribution of ejected electrons are plotted as a function of scattering angle $\theta = \pi/2 - \alpha$ .The ejected electron energies from 4eV up to 120 eV are considered when the primary electron energy is 500eV[51, 52]. There is a maximum at about 45^{o} to 70^{o} in the scattering angle.

The high-energy electrons of the incident beam can transfer a critical amount of energy to an inner-shell electron of an atom, whose ground-state energy lies at least several 100 eV below the Fermi level of the solid, leading to the ejection of this electron. Unoccupied states exist only above the Fermi level and, therefore, the incoming electron loses energy due to a loss of electron from the inner shell. Subsequently, the hole in the inner energy levels involves other processes, generally called de-excitation, such as production of Auger electrons, low energy photons or X-ray emission. The energy for the inner-shell ionization is provided by the incident electron, reducing its energy. For some material where the energy loss due to inner-shell vacancies is small, radiationless transitions are also possible which the lost energy appears as heat.

Outer shell electrons can also undergo single-electron excitation. In any insulator or semiconductor, a valence electron makes an inter-band transition across the energy gap; where in the case of a metal, a conduction electron makes a transition to a higher state, possibly within the same energy band. If the final state of these transitions lies above the vacuum level of the solid and if the excited atomic electron has enough energy to reach the surface, it may be emitted as a secondary electron. As before, the incoming electron supplies the necessary energy of about few eV and scatters off loosing little energy. The incoming electron scatters at a small angle, but the secondary electron moves at an angle close to 90^{o} with respect to the incoming electron as suggested by equation(3,20).

As an alternative to the single-electron mode excitation, outer-shell inelastic scattering may involve many atoms in the solid. This collective effect is known as a plasma resonance (an oscillation of the valence-electron density) and takes the form of a longitudinal traveling wave. This is a similar effect as a sound wave, but rather with the electrostatic forces as the restoring force. In a quantum mechanical picture, this is referred to as a (pseudo) particle creation, being known as the plasmon and having a characteristic energy. The plasmon energy is proportional to the square root of the valence-electron density, which is of the order of 5 to 30eV. In addition to the bulk plasmons, the incoming electron may create surface plasmons, which are very important for thin samples.

Plasmon excitations and single-electron excitations represent alternative modes of inelastic scattering. In materials in which the valence electrons are "quasi-

free" electrons (alkali metals), the collective form of response is predominant. In rare gas solids plasmon effects are weak. Most materials fall between these two extremes.

3.5.1. Atomic Models for Ionization

Firstly, it is needed to clarify the difference between two terms with regards to the ionization cross section. Two terms have been used: counting cross section σ_c and the gross (or total) ionization cross section σ_i[85]. Depending on the method used to measure the ionization cross section, one may measure any of the above cross sections. Assume the partial cross section for the production of z-times ionized residual ion by a single collision to be σ_z, then the counting cross section is defined as:

$$\sigma_c = \sum \sigma_z \tag{3,21}$$

while the total cross section is:

$$\sigma_i = \sum z\sigma_z \,. \tag{3,22}$$

Also note that sometimes the word total cross section is meant to imply the partial cross section when the cross section has been found by integrating over angle and/or energy.

An inelastic collision is generally due to the collision of a primary electron with the individual electrons in the atom, where classically a collision is called binary (one on one) collision.

Ionizing collisions of an electron with an atom or molecule can be classified either as fast or slow, or hard or soft, collisions. When the speed of the electron as compared with the mean speed of the (sub-) shell electron under study is high, it is considered a fast collision and when is it smaller it is characterized as a slow collision. The soft (distant) collision is regarded as a collision with large impact parameter, while a hard (close) collision is due to small impact parameter. In the case of a fast collision, the interaction of the primary electron with the target is treated as sudden and therefore an approximation due to an external interaction such as Born approximation is carried out[86-89]. Bethe derived the first Born cross sections assuming the dipole interaction of a fast electron with the atom and is therefore appropriate for the soft collision[86]. However, the slow incoming electron forms a combined system with the target with a positive energy is assume which is usually more difficult to

vigorously being studied. Under this regime, only classical models have been applied based on the "so called" binary encounter approximation[90]. The simplest theoretical model to describe this type of collision is the Rutherford scattering between two electrons taking into account that the target electron is bound and need some energy to escape the target[91]. Mott took into account the electron exchange effects best describing the hard collisions[92] where the two electrons are assumed free.

The theoretical descriptions of ionization cross section are characterized as (a) the classical method, (b) the quantum mechanical method and (c) the method that is referred to as "hybrid methods" here.

3.5.1.1. The classical methods

As opposed to other phenomena in the collision of electron with matter, it is possible to treat the ionization classically since the final atomic state of the ionized electron lies in the continuum and its final quantum number is not uniquely defined. The latter allows one to assume or include the sum over all possible angular momenta. Three basic assumptions are essential in utilizing a classical approach to the ionization process by electron impact.

(1) A classical description must be found for the initial state of the bound state of the target electron. It is a usual practice to assume the bound electron at rest, having a fixed velocity, or having a well defined velocity distribution. Usually the distribution over angle is averaged.
(2) A method is developed to describe the many-body problem of ionization as a two-body one.
(3) The classical laws of motion shall be used where no quantum-interference effects is being taken into account.

Different classical methods to describe the ionization have been developed, depending on how they have incorporated the conditions (1) and (2). Semi-classical treatments have also been developed by partially applying the condition (3).

The Method developed by Thomson

The earliest classical treatment of ionization was developed by Thomson[90] prior to the advent of quantum mechanics. Thomson defines the cross section between the incoming electron and the target electron in the collision course of impact parameter, b, as:

$$\sigma = 2\pi \int_0^{b_{max}} b db \tag{3,23}$$

, where b_{max} is the maximum impact parameter attainable in the collision. Thomson measures the energy loss by the projectile as a function of impact parameter by the following relation:

$$\Delta E = \frac{E_0}{1 + b^2 E_0^2}, \tag{3,24}$$

, and defines the maximum impact parameter by setting the energy loss equal to the ionization potential, I, of the target electron and arrives at the total ionization cross section and stopping power as:

$$\sigma_i = 4\pi a_0^2 \left(\frac{R_y}{I}\right)^2 \left(\frac{1}{u} - \frac{1}{u^2}\right) \tag{3,25}$$

$$S = 4\pi a_0^2 \left(\frac{R_y}{I}\right)^2 \frac{\ln u}{u} \tag{3,26}$$

, where $u = E_0/I$. If one sets $\Delta E = I + k_{se}^2/2$ and find the integration in equation (3,25) the Born expression for ionization is deduced, while the Rutherford cross section is evaluated by change of variable from b to $\theta/2$ in equation (3,25) where θ is the scattering angle. Thomson's method was improved by Williams[93] and Thomas[94].

Method developed by Gryzinski

Another classical theory of inelastic atomic collision has been evolved on the basis of a binary collision incorporating the Coulomb interaction by Gryzinski[95]. The binary collision is referred to the independent pair interaction of the individual elements of the colliding system; i.e. the incoming electron and the target electron. As it is originally stated by Gryzinski, the "diffraction" of elementary particles on atomic system is explained on the basis of classical mechanics, where the discrete energy state of the target was included. It was also shown that the anisotropy of the space orientation of their velocity in the case of crystals is responsible for the main features of the diffraction pattern.

In 1959, Gryzinski[96] developed a method to describe the ionization cross section of electrons by assigning an initial velocity of zero to the atomic electron and

then assumed that the primary electron loses an amount of energy greater than or equal to the ionization potential of the target's electron. This did not improve the Thomson's formula and similar energy dependence was predicted. Gryzinski[95, 97] assumed an empirical velocity distribution for the target electron in a subshell defined by principal number n and angular quantum number l, whose form was:

$$f_{nl}(\mathrm{v}) = (\bar{\mathrm{v}}/\mathrm{v})^3 \exp(-\bar{\mathrm{v}}/\mathrm{v}) \tag{3,27}$$

where v and $\bar{\mathrm{v}}$ are the speed and the average speed of the electron bounded by the target before the collision, respectively. Gryzinski defined the total ionization cross section and the stopping power of the sample as:

$$\sigma_i = \sum_{n,l} N_{nl} \int f_{nl}(\mathrm{v}) \sigma_{nl}(\mathrm{v}) d\mathrm{v} \tag{3,28}$$

and

$$S = \sum_{n,l} N_{nl} \int f_{nl}(\mathrm{v}) S_{nl}(\mathrm{v}) d\mathrm{v} \tag{3,29}$$

where N_{nl} is the number of electrons in the subshell n,l, and $\sigma_{nl}(\mathrm{v})$ is the cross section measured for the ejection of an electron from the subshell. To arrive at the latest definitions, Gryzinski neglected the effect of the field of the nucleus on the motion of the primary electron and the final results are:

$$\sigma_i = \sum_{n,l} 4\pi (a_0)^2 N_n (R_y / E_{nl})^2 h_{nl}(\mathrm{u}) \tag{3,30}$$

$$\begin{aligned} h_{nl}(\mathrm{u}) = {} & d(1/U)[(U-1)/(U+1)]^a \times \\ & \{b + c[1-(1/2U)] \ln[2.7 + (U-1)^{0.5}]\} \end{aligned} \tag{3,31}$$

where $a = 3/2$, $b = 1$, $c = 2/3$, $d = 1$ and $N_n = \sum_l N_{nl}$. Also U is the reduced energy defined as $U = E_0/E_{nl}$ for a subshell energy of E_{nl}. Due to this latest assumption, one expects that the Gryzinski's method to be applicable at high energy and for soft collisions.

In these works, an empirical distribution was assumed for the electron by Gryzinski to arrive at the proper energy distribution of the cross sections at high energies. Later, Gryzinski reconsidered[98] the issue of velocity distribution for the atomic electron and argued that the best distribution is the one with isotropic angular distribution and took the following:

$$f_{nl}(\mathrm{v}) = \frac{4(|2E_{nl}|)^{3/2}/\pi}{\left(\mathrm{v}^2 + 2|E_{nl}|\right)^2} \tag{3,32}$$

where E_{nl} is the energy of electron in the subshell (n,l).

3.5.1.2. Quantum Mechanical Methods

There are many theoretical calculations based on Born approximation of which the examples are the Born-Oppenheimer, the Born-Exchange, the Born-Exchange, and the Distorted-Wave Born-Oppenheimer and many more as reviewed by Rudge[99].

3.5.1.2.1. Bethe-Born Approximation

In order to describe more precisely the inelastic scattering of electrons by an atom (including the dependence of scattered intensity on energy loss), the behavior of each atomic electron must be specified in terms of transition from an initial state described by a wave function ψ_0 to a final state described by a wave function ψ_f. Using the first Born approximation, the angular distribution of the cross section for the transition from initial state (0) to a final state (f), $d\sigma_f/d\Omega$, is[88]:

$$\frac{d\sigma_f}{d\Omega} = \left(\tfrac{1}{4\pi}\right)^2 \frac{k_s}{k_0}\left|\int U_{\mathrm{int}}(r)\psi_f^*\psi_0 \exp(i\mathbf{q}\cdot\mathbf{r})d^3\mathbf{r}\right|^2. \tag{3,33}$$

It is assumed that the interaction potential is primarily electrostatic and the interaction potential is of the form given in equation (3,11), as the inelastic

scattering involves only interaction with the atomic electrons, and there are appreciable energy transfer in the collision due to this channel. Combining equations (3,33) and (3,11), the differential cross section can be written in the form:

$$\frac{d\sigma_f}{d\Omega} = \left(\frac{2}{a_0 q^2}\right)^2 \frac{k_s}{k_0} \left|F_f(\mathbf{q})\right|^2 \tag{3,34}$$

where $F_f(\mathbf{q})$ is the inelastic form factor related to the final state *f*, and $F_f(\mathbf{q})$ is defined similar to a transition-matrix element as:

$$F_f(\mathbf{q}) = \left\langle \psi_f \left| \sum_j \exp(i\mathbf{q}\cdot\mathbf{r}_j) \right| \psi_0 \right\rangle. \tag{3,35}$$

Like the *elastic* form factor of equation (3,9), it is a dimensionless factor which modifies the Rutherford scattering that would have taken place if the atomic electrons were free; it is a property of the target atom and is independent of the incident-electron velocity.

A closely related quantity is the generalized oscillator strength (GOS), $f_{GOS}(\mathbf{q})$, defined[88] as:

$$f_{GOS}(\mathbf{q}) = \frac{\Delta E}{R_y} \frac{|F_f(\mathbf{q})|^2}{(qa_0)^2} \tag{3,36}$$

where R_y is the Rydberg energy.

For the case of not "distinguishable" electrons, the general quantum mechanical formula for the cross sections in momentum space and integrated over angular distribution takes the form:

$$\sigma_i = (4\pi^2 k_0)^{-1} \int_0^{(E_0 - I)} k_s k_{se} \left(\int |f(\mathbf{k}_s, \mathbf{k}_{se})|^2 \, d\hat{\mathbf{k}}_0 d\hat{\mathbf{k}}_s d\hat{\mathbf{k}}_{se} \right) dE_{se} \tag{3,37}$$

where $f(\mathbf{k}_s, \mathbf{k}_{se})$ is the scattering amplitude. The Born approximation (equation (3,37)) is based on the choosing the separable wave functions ($\langle \mathbf{r}, \mathbf{R} | s \rangle = \phi_s(\mathbf{r}) e^{i\mathbf{K}_s \cdot \mathbf{R}}$ and $\langle \mathbf{k}, \mathbf{K} | s \rangle = (2\pi)^{9/2} \tilde{\phi}_s(\mathbf{k}) \delta(\mathbf{K} - \mathbf{K}_s)$), which are appropriately chosen for the Coulomb interaction. When the coulomb interaction is assumed, the separable wave functions

should be used. Usually the exchange is neglected in a Born approximation. Therefore, the following equation is commonly used for ionization:

$$\sigma_i(Born) = (\pi k_0)^{-1} \int_0^{(E_0 - I)} k_s k_{se} \left(\int | f_B(\mathbf{k}_s, \mathbf{k}_{se}) |^2 \, d\hat{\mathbf{k}}_s d\hat{\mathbf{k}}_{se} \right) dE_{se} \tag{3,38}$$

This approximation is usually referred to as the Coulomb-Born approximation in contrast with the ordinary Born approximation which employs the plane wave. Integrating this equation, one concludes the Bethe approximation for ionization cross section as:

$$\sigma_i(Bethe) = \frac{4\pi R_y a_0^2}{E_0} \left[A_{nl} \ln(4 c_B E_0 / I) + b_B \right] \tag{3,39}$$

where the quantity A_{nl} is defined as follows:

$$A_{nl} = 4 \left[\tfrac{1}{3} \left\langle r_{nl}^2 \right\rangle - \sum_{n'l'} \frac{\overline{f}_{n'l'nl}}{2 | E_{nl} - E_{n'l'} |} \right]. \tag{3,40}$$

In equation (3,39), c_B and b_B are constants known as Bethe parameters. The parameter c_B is a form of cut-off parameter and the quantities $\left\langle r_{nl}^2 \right\rangle$ and $\overline{f}_{n'l'nl}$ are the mean square radius of the (n,l) subshell and the average oscillator strength. The Bethe theory can be applied to complex atoms with the definition of A_{nl} in the new form:

$$A_{nl} = 4 \left[\tfrac{1}{3} \left\langle \left(\sum_i r_i \right)^2 \right\rangle_{nl} - \sum_{n'l'} \frac{\overline{f}_{n'l'nl}}{2 | E_{nl} - E_{n'l'} |} \right]. \tag{3,41}$$

The total K-shell cross sections under the Bethe formula is plotted in Figure 3-10 as a function of incident energy for different elements[100]. Note that Bethe derived the cross section formula for the dipole interaction involving fast incident electrons and thus accounting well for soft collisions. Conversely the Mott cross section formalism, which is a generalized Rutherford cross section, takes into account

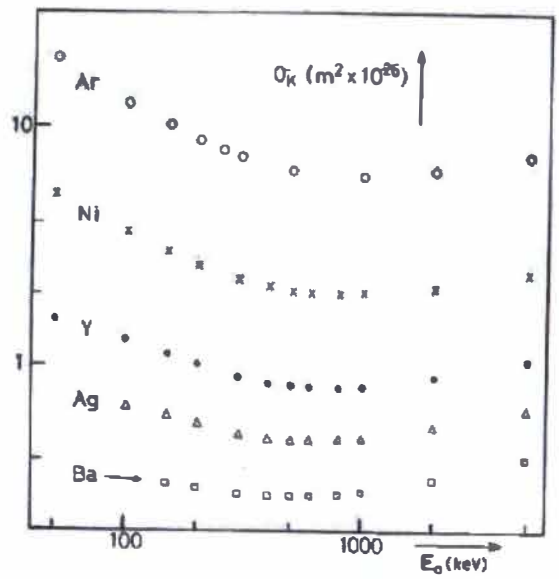


Figure 3-10: The total K-shell cross sections under the Bethe formula is plotted against the incident energy for Ar, Ni, Y, Ag, and Ba.

electron exchange effects, and describes the collision of two free electrons, thus accounting well for hard collisions. The Mott formula will be explained in the following section.

3.5.1.2.2. Mott Formula

In the case of electrons interacting with the target's electron, the symmetry effects should be considered. The reason is that the colliding particles are identical and it is experimentally impossible to distinguish between identical projectile and target particles. Therefore the wave function describing the system must satisfy certain symmetry properties with respect to the interchange of the two particles coordinates.

The interchange of the position of the interacting particles is equivalent to a reversal of the direction of the radial vector joining them. In this reversal, r remains unchanged while θ changes to (π- θ). Therefore, the scattering amplitude should be replaced by $f(\theta) \pm f(\pi - \theta)$ when the symmetry of wavefunction is taken into account[64]. Thus, if the total spin of the particles is even, then the differential cross section (DC) is:

$$\left(\frac{d\sigma}{d\Omega}\right)_{sym} = \left|f(\theta) + f(\pi - \theta)\right|^2 \qquad (3,42)$$

, and for odd total spin

$$\left(\frac{d\sigma}{d\Omega}\right)_{anti} = \left|f(\theta) - f(\pi-\theta)\right|^2 \tag{3,43}$$

The interference term $[f(\theta)f^*(\pi-\theta) \pm f^*(\theta)f(\pi-\theta)]$ is characteristic of quantum mechanics, and does not appear in the classical solution, which is

$$\left(\frac{d\sigma}{d\Omega}\right)_{class} = \left|f(\theta)\right|^2 + \left|f(\pi-\theta)\right|^2 \tag{3,44}$$

So far it was assumed that the total spin of the particles had a definite value, but in practice all the spin states need to be included. To determine σ, we assume that all the spin states are equally probable. The total number of spin states for two particles of spin s is $(2s + 1)^2$. For the two cases, integer and half integer s, the differential cross sections are

$$\left(\frac{d\sigma}{d\Omega}\right)_{FD} = \frac{s}{2s+1}\left(\frac{d\sigma}{d\Omega}\right)_{sym} + \frac{s+1}{2s+1}\left(\frac{d\sigma}{d\Omega}\right)_{anti} \tag{3,45}$$

for half integer s, and

$$\left(\frac{d\sigma}{d\Omega}\right)_{BE} = \frac{s}{2s+1}\left(\frac{d\sigma}{d\Omega}\right)_{anti} + \frac{s+1}{2s+1}\left(\frac{d\sigma}{d\Omega}\right)_{sym} \tag{3,46}$$

for integer s. Subscripts FD and BE are abbreviations for Fermi-Dirac and Bose-Einstein.

For distinguishable particles the differential cross section (DCS) is:

$$\left(\frac{d\sigma}{d\Omega}\right)_{dist} = \frac{1}{4k^2}\left|\sum_{l=0}^{\infty}(2l+1)(e^{i2\delta_l}-1)P_l(\cos\theta)\right|^2 \tag{3,47}$$

For identical particles we need to multiply equation (3,47) by 2, since we cannot distinguish between the scattered waves representing the two particles. Because $P_l(\cos\theta)$ is odd for all odd l and even for all even l, assuming that the total spin has a definite value, the DCS for even total spin is:

$$\left(\frac{d\sigma}{d\Omega}\right)_{sym} = \frac{1}{2k^2}\left|\sum_{even\ l}(2l+1)(e^{i2\delta_l}-1)P_l(\cos\theta)\right|^2 \tag{3,48}$$

And for odd total spin is

$$\left(\frac{d\sigma}{d\Omega}\right)_{anti} = \frac{1}{2k^2}\left|\sum_{odd\ l}(2l+1)(e^{i2\delta_l}-1)P_l(\cos\theta)\right|^2 \tag{3,49}$$

Up to this point the fundamentals for calculating the Mott Formula has been explained. Substituting $f(\theta)\pm f(\pi-\theta)$ for $f(\theta)$ in equation (3,5) and following the procedure leading to equation (3,12), and assuming the interaction potential of equation (3,10), one arrives at the formula known as Mott formula:

$$\frac{d\sigma}{d\Omega} = \frac{4\gamma^2 Z^2}{a_0^2 q^4}\left[1+\frac{q^4}{(4k_0^2-q^2)^2}+\frac{2q^2}{(4k_0^2-q^2)}\cos\left(\frac{Z}{2k_0}\log\left(\frac{q^2}{(4k_0^2-q^2)}\right)\right)\right] \tag{3,50}$$

It is assumed that the charged particles are spinless. Figure 3-11 presents the angular distribution of the inelastic cross sections of the Mott formula of Silicon for 20, 75, and 100 eV normal incident electrons.

To study the proximity effect, it is necessary to know both $\frac{d\sigma}{d\Omega}$ and the differential cross section with respect to the incident electron's energy $\frac{d\sigma}{d\varepsilon}$, which it is:

$$\left(\frac{d\sigma}{d\varepsilon}\right)_{Mott} = \frac{2\pi e^4}{m_e \upsilon^2}\frac{1}{E}\left[\frac{1}{\varepsilon^2}+\frac{1}{(1-\varepsilon)^2}+\left(\frac{\tau}{\tau+1}\right)^2-\frac{2\tau+1}{(\tau+1)^2}\frac{1}{\varepsilon(1-\varepsilon)}\right] \tag{3,51}$$

, where ε is the energy transfer ΔE normalized to E and τ is the kinetic energy normalized to the rest mass energy of an electron.

For non-relativistic electrons (small values of τ), equation (3,51) reduces to:

$$\left(\frac{d\sigma}{d\varepsilon}\right)_{Mott} = \frac{2\pi e^4}{m_e \upsilon^2}\frac{1}{E}\left[\frac{1}{\varepsilon^2}+\frac{1}{(1-\varepsilon)^2}-\frac{1}{\varepsilon(1-\varepsilon)}\right] \tag{3,52}$$

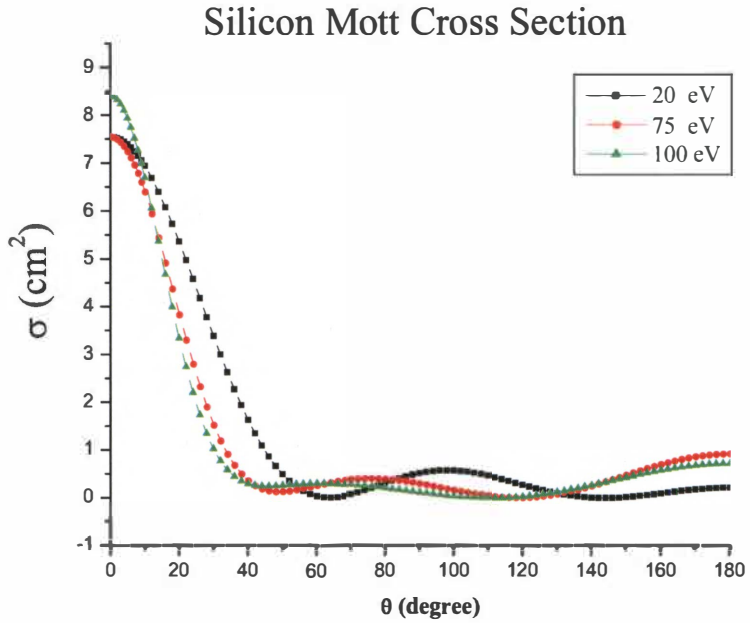


Figure 3-11: The angular distribution of the Mott inelastic cross sections of Silicon for 20, 75, and 100 eV normal incident electrons.

As expected, the Mott cross section is symmetric in terms of the kinetic energies of the outgoing electrons, i.e. in terms of εE and $E(1-\varepsilon)$ for the secondary (or ejected) electron and the "scattered" electron, respectively. As mentioned in the previous sections, the Mott cross section is more suitable for lower energies, but not appropriate for energy transfer near to or below the ionization potential of an atom. This is the main reason that it has been used it this thesis. The value of the minimum transferred energy $\varepsilon_c E$ (cut off energy) should be much larger than the binding energy of the atomic electrons.

Note: In the Mott cross section, in contrary to the Gryzinsky's, the binding energy of atomic electrons is not taken into consideration.

3.5.1.2.3. (Convergent) Close Coupling

Convergent Close-Coupling (CCC) is a quantum mechanical method for the ionization of atoms and molecules that is applicable at low energy and has been developed quite successfully. In this method the total wavefunction is expanded in a set of square-integrable states obtained by diagonalizing the target Hamiltonian in an explicitly antisymmetric two-electron Laguerre basis for the radial part of the wavefunction. Increasing the basis size gives a better description of both the discrete and continuum subspaces. In the former case simply more discrete states are obtained which are good approximations to the true corresponding eigenstates. In the latter case a more dense representation of the continuum is obtained using square-integrable (L^2) positive-energy states. The method explained is applied to any atom under the frozen-core model. In a frozen-core model, it is assumed that the atom has only one active electron, and all other electrons are frozen. The nucleus of the atom and the frozen core forms the initial target where the incoming electron joins in with the active electron and forms a Helium-like anion. The active electron is assumed to be in the 1s orbital of the helium anion, while the other electron occupies a continuum level. This approximation leads to good excited-state wave functions and a satisfactory ground state. In addition, the total ionization cross section is obtained by summing the cross sections corresponding to excitation of positive-energy states. Detailed ionization information is deduced directly from the T-matrix elements corresponding to excitation of positive-energy states arising in the CCC calculations.

In CCC type calculations, it is assumed that ionization is essentially the same as inelastic scattering, where the ionization processes is described by excitation of the positive-energy states. For example, if for total energy E we write the T-matrix elements resulting from a CCC calculation using N states as $\left\langle \mathbf{k}_f \Phi_f^N \middle| T \middle| \Phi_i^N \mathbf{k}_i \right\rangle$, where the initial and final Φ^N and $\mathbf{k}$ are, respectively, the target states and plane waves whose corresponding energies satisfy $\varepsilon^N + k^2/2 = E$, then the total ionization cross section σ_i is simply

$$\sigma_i = \sum_{f,0<\varepsilon_f^N<E} \left| \left\langle \mathbf{k}_f \Phi_f^N \middle| T \middle| \Phi_i^N \mathbf{k}_i \right\rangle \right| \qquad (3,53)$$

The convergent close-coupling (CCC) method for the calculation of electron-impact excitation and ionization of atoms has proved to be extremely successful. It was developed initially for the e-H system by Bray and Stelbovics[101], whom

demonstrated that the discrete excitation and total ionization transitions could be accurately obtained at any projectile energy by expanding the total wave function with a sufficiently large number N of square-integrable states obtained from an orthogonal Laguerre basis.

A critical test of the method is provided by the application to the Temkin-Poet model[102] of e-H scattering[101]. This model retains the complexity of a true three-body problem, but is simpler than the full problem in that it treats only states with zero orbital angular momentum. The ability to obtain accurate total ionization cross sections (TICS) has attracted a great deal of interest in the CCC method, and there is now almost complete agreement between various numerical approaches. The successful application to the Temkin-Poet model has also led to the application of the method to real scattering problems. The CCC theory yields good agreement with very detailed electron-impact discrete excitation data in the case of sodium and helium as well as to the electron-impact total ionization cross sections of different atoms even near the threshold.

3.5.1.3. "Hybrid" methods

Method of Khare and co workers

There have been many efforts to combine these two ideas to arrive at a correct formula for the counting or the total cross sections which are applicable in both the soft and hard collision cases. The first attempt is due to Khare and co workers[103] which have introduced a semi-empirical formula for the calculation of the energy loss cross section $d\sigma(E_0,\Delta E)/d(\Delta E)$ in the collision of primary electron with ionizing energy E_0. They were also calculating the single differential cross section $d\sigma(E_0,E_{se})/dE_{se}$ where ε is the ionization energy of the target electron. The total cross section, therefore, is calculated by integrating over the secondary electron energies from 0 eV to $(E_0-\varepsilon_1)/2$ where ε_1 is the first ionization potential. Nonetheless, Khare and co workers have extended their work to calculate the partial ionization cross sections of molecules[104, 105] where a specific parent or fragment ion is produced. They used a mixing method to calculate the ionization cross sections differential in energy. Their mixing was based on the Bethe surface, where the hard and soft collision regimes could be assigned to the extremes on this surface. Let's assign $d\sigma(E_0,E_{se})/dE_{se}|_M$ [88] and $d\sigma(E_0,E_{se})/dE_{se}|_B$ [106] to the hard collision (Mott differential cross section) and to the soft collision (Bethe differential cross section), respectively, where they have assigned two arbitrary factors f_1 and f_2 to these two terms as:

$$d\sigma(E_0,E_{se})/dE_{se} = f_1\, d\sigma(E_0,E_{se})/dE_{se}|_B + f_2\, d\sigma(E_0,E_{se})/dE_{se}|_M \qquad (3,54)$$

$$f_1(E_0, E_{se}) = \frac{1}{1+\varepsilon_i/E_0}\left[1 - \frac{E_{se}\ln(1-C(E_0-\varepsilon_i))}{(E_0-\varepsilon_i)\ln(CE_0)}\right] \tag{3,55}$$

$$f_1(E_0, E_{se}) = \frac{E_{se}^3(1-\varepsilon_i/E_0)}{(E_{se}^3+\varepsilon_0^3)} \tag{3,56}$$

where C and ε_0 are the collisional parameter and a mixing parameter, respectively[106]. C is generally defined as a function of energy loss. Khare and co workers have assumed the collisional parameter to be independent of energy loss and assumed to be calculated using an experimentally known cross section at high energy.

Method of Rudd and Kim

In 1994, Kim and Rudd[107] extended the approach of Khare and co workers in several ways. The symmetric form of the binary encounter approximation (BEA)[108], where a velocity or momentum distribution, was attributed to the target electron was chosen to replace the Mott cross section. This resulted to a new form of the Mott cross section by an extra term incorporating the average kinetic energy $\overline{E_0}$. Then they combined the new form of Mott cross section with the Bethe cross section by requiring the ionization cross section to follow the high energy behavior of the Bethe theory. After some further approximation, they arrived at the following formula:

$$\frac{d\sigma(E_0, E_{se})}{dE_{se}} = 4\pi a_0^2\left(\frac{R_y}{B_E}\right)^2 \xi \frac{1}{B_E(1+u+t)}\left\{\frac{\left(\frac{\xi_i}{\xi}\right)-2}{(1+t)}\left(\frac{1}{(1+w)}+\frac{1}{(t-w)}\right)\right.$$
$$\left.+\left(2-\left(\frac{\xi_i}{\xi}\right)\right)\left(\frac{1}{(1+w)^2}+\frac{1}{(t-w)^2}\right)+\frac{\ln t}{\xi(1+w)}\frac{df(w)}{dw}\right\} \tag{3,57}$$

where t, w, u, and ξ_i are defined as:

$$t=\frac{E_0}{B_E} \quad w=\frac{E_{se}}{B_E} \quad u=\frac{\overline{E_0}}{B_E}$$
$$\xi_i=\int_0^{\infty}\frac{df(w)}{dw}dw \tag{3,58}$$

for the single differential cross section for a particular subshell. $f(w)$, ξ , and B_E are the oscillator strength, number of bound electrons in a particular sub-shell, and the binding energy of the ejected electron respectively. They refer to this approach as the Binary Encounter-Dipole (BED) model. The total ionization cross section is then:

$$\sigma_i(t)=\sum_{\substack{\text{all subshells that}\\ \text{contributes to ionization}}} 4\pi a_0^2\left(\frac{R_y}{B_E}\right)^2 \xi\frac{1}{(1+u+t)}\left\{D(t)\ln t + \left(2-\left(\frac{\xi_i}{\xi}\right)\right)\left(\frac{(t-1)}{t}-\frac{\ln t}{(1+t)}\right)\right\} \tag{3,59}$$

where

$$D(t)=\xi^{-1}\int_0^{(t-1)/2}\frac{1}{w+1}\frac{dg(w)}{dw}dw \tag{3,60}$$

The subshell cross sections are added appropriately to find the total (gross) cross sections or the counting cross sections for comparison with the proper measurements. In reality, only the valence shell and a few subshells below it will make significant contribution to σ_i.

DM formalism:

A different mixing of the classical and the quantum methods is introduced by Deutsch and Märk[109] which had a different origin from the formalism of Khare and co-workers and Kim and Rudd. This method which has been modified many times[110, 111] was reviewed[112] and is found to be applicable to the single ionization of ground-state[109, 113], excited-state (metastable) atoms, the removal of a specific single outershell and innershell electron of atoms as well as to the single ionization of molecules, radicals, C_{60} and atomic ions as well as to the multiple ionization of atoms[114]. Deutsch and Märk[109] suggested replacing the Bohr radius a_0 in the Gryzinski formula by the radius $\langle r_{nl}\rangle$ of the corresponding electronic subshell (labeled by the quantum numbers n and l), on the basis of a comparison between the

classical binary encounter formula and the quantum mechanical Born–Bethe formula. The Bethe formalism for the ionization cross section of an atomic electron with quantum numbers (n, l) results in the cross sections approximately proportional to the mean square radius $\langle r^2 \rangle$ of the (n,l) subshell[65, 115] and also the experimental observations suggest that there exists a correlation between the maximum of the atomic ionization cross section and the sum of the mean square radii of all outer electrons[116].

$$\sigma_i = \sum_{n,l} \pi g_{nl} \langle r_{nl} \rangle^2 N_{nl} h_{nl} (\mathrm{u}) \tag{3,61}$$

where $\langle r_{nl} \rangle$ is the mean radius of the (n,l) subshell and g_{nl} are weighting factors that were originally introduced by Bethe[86]. Bethe calculated these weighting factors as a function of the quantum numbers n and l using hydrogenic wave functions. In contrast, the generalized weighting factors g_{nl} introduced by Margreiter et al.[110] were obtained from a either by fitting procedure using reliable experimental ionization cross section data or by keeping the product $E_{nl} \times g_{nl}$ independent of the nuclear charge Z for completely filled subshells[110]. A comparison of the three "hybrid" formalism with the available experimental data for water vapor is presented in Figure 3-12.

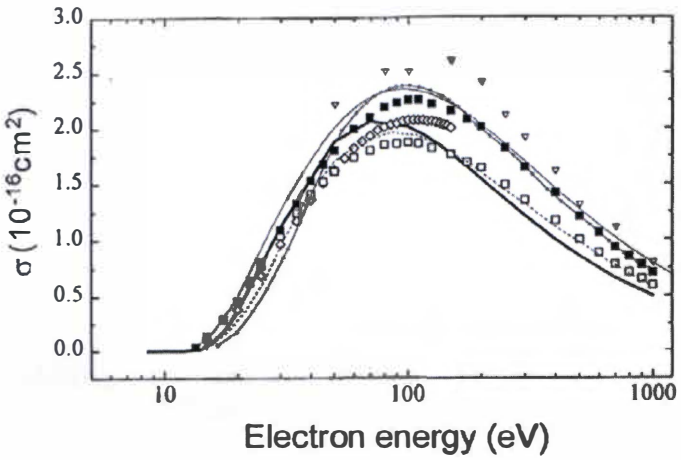


Figure 3-12: Electron impact ionization cross section of H_2O as a function of electron energy. The experimental data points are from[117] (filled squares),[118] (open diamonds), [51] (open inverted triangles), and [119] (open squares). The thick solid line represents the present DM calculation, the thin solid line denotes the BEB calculation[120], the dashed line refers to the calculation of Khare and co-workers[103], and the open circles connected by a solid line denote the calculation of Saksena et al.[121, 122].

3.5.2. Solid State Effects

Three different modes of the inelastic interaction are commonly distinguished for thick targets due to intrinsic and/or extrinsic losses. The bulk (volume) excitations occur inside an infinite medium when the polarization field is set up as a response to the interacting electrons. Surface excitations occur as a consequence of the boundary conditions of Maxwell's equations at either side of an interface of two media with different electrical susceptibility. In the case that the above processes are experienced by an electron (i.e. an Auger or photoelectron) that was generated in the course of an ionization process these loss mechanisms are referred to as extrinsic losses, to distinguish them from an energy loss inherent to the ionization. The latter process is referred to as an intrinsic loss. These intrinsic excitations are only experienced by electrons generated in the course of an ionization event that feel the response of the solid to the sudden appearance of the core hole they leave behind. The different types of inelastic process are schematically illustrated in Figure 3-9.

In a solid state sample, the incident electrons lose their energy through many collisions, adding to the complexity of the problem. The stopping power is defined to summarize in one value all possible energy losses through inelastic interactions of an energetic electron with its surrounding medium.

Usually, the electron stopping power, S, is defined by[88]:

$$S = \frac{dE}{ds} = n_a \overline{\Delta E} \sigma_i \qquad (3,62)$$

where $\overline{\Delta E}$, n_a, σ_i, and s are the average energy loss, the number of atoms per unit volume, the inelastic cross section, and the path along the trajectory respectively. The stopping power is defined as the total energy loss per unit path length of the electron, and is a function of the kinetic energy of the electron. The energy dependence of the stopping power depends on the response of the medium to the incident electron. $S(E)$ has the dimension of force. It is the "braking" force of the medium acting on the incoming charged particle. Typical values are of the order of 10 eV/Å or 10^{-8} N. At high electron energies this braking force leads to Bremsstrahlung radiation, but at low electron energies this effect can be neglected.

Bethe Equation Stopping Power

Bethe's stopping power is usually written in the following form[123].

$$\frac{dE}{ds} = -785\frac{\rho Z}{AE}\ln\left[\frac{1.166E}{I}\right](eV/A^{\circ}) \tag{3,63}$$

, where E is the instantaneous energy of the electron in eV, s is the path along the trajectory, ρ is the density in g/cm^3, Z is the atomic number, A is the atomic mass of the target, and I is the mean ionization energy of the target in eV. The value of I can be found from tabulated values[124], or approximated from an analytical fit such as that of Berger and Selzer[125] giving:

$$I(eV) = \begin{cases} 11.5\,Z & \text{for } Z \le 12 \\ \left[9.76\,Z + \frac{58.5}{Z^{0.19}}\right] & \text{for } Z \ge 13 \end{cases} \tag{3,64}$$

From equation (3,63) and the Bethe cross section, it should be clear that I is rather energy dependent. Therefore the Bethe stopping power can be modified:

$$\frac{dE}{ds} = -785\frac{\rho Z}{AE}\ln\left[\frac{1.166E}{I'}\right](eV/A^{\circ}) \tag{3,65}$$

, where

$$I' = \frac{I}{1 + k\frac{I}{E}} \tag{3,66}$$

, and the variables have the same form as in equation(3,63). k is a constant, which depends on the material. k is always close to, but less than one (Table 3-1). This modified version was proposed by Joy and Luo in 1989[126].

This modified Bethe equation is used in the Monte Carlo program used in this thesis. The details of the Monte Carlo program are explained in the simulation section.

In order to fully finish this chapter, the followings important processes, which exist in most solids and which exhibits several features not predicted by the atomic models, will be briefly explained.

Table 3-1: k values for a few elements.

Element	C	Al	Si	Cu	Ni	Ag	Au
k value	0.77	0.815	0.822	0.83	0.83	0.852	0.851

Phonons

Phonons are lattice vibrations, which are the result of energy thermalized in the specimen. This effect may lead to a damage of the sample.

Plasmons

Plasmons are longitudinal oscillations of free electrons, which decay either in photons or phonons.

Surface Plasmons

Volume Plasmons

The valence electrons in a solid can be thought of as a set of coupled oscillators that interact with each other and with an incident electron via electrostatic forces. In the simplest situation, the valence electrons behave essentially as free particles (although constrained by Fermi-Dirac statistics) and constitute a "free-electron gas". Interaction with the ion-core lattice is assumed to be a minor perturbation which can he incorporated phenomenologically by using an

effective mass for the electrons, which differs from their rest mass m_o, and by introducing a damping constant in the Drude theory of electrical conduction in metals. The behavior of the electron gas is described in terms of a dielectric function, just as in Drude theory. In response to an external electric field, such as that produced by an incident electron, a collective oscillation of the electron density occurs at a characteristic angular frequency ω_p and this resonant motion would be self-sustaining if there were no lattice damping.

Cathodoluminescence

In semiconductors hit by high-energy electrons, electron-hole pairs are formed. Filling this hole with an electron from the conduction band leads to the emission of light with a frequency that corresponds to the band gap.

Bragg diffraction

If a crystalline specimen is struck by electrons, then Bragg diffractions happen as well. Each atom in such a regular arrangement acts as a scattering center. The scattered electron waves may interact with each other in a constructive or destructive way, which gives rise to a diffraction pattern.

Chapter 4

4. Electron Beam Resist

4.1. Introduction

In this chapter a brief discuusion will be made about poly methylmethacrylate (PMMA). The basic properties of PMMA are as follows:

Density: ρ=1.88 g/cm^3
Molar weight: 100.01 g/mol
Avogardo's number = 6.022 x 10^{23}
Mass of one molecule: M_{molec} = 1.661 x 10^{-22} g/molec
Density of molecules: $\eta = \rho / M_{molec}$
η = 7.153 molec/nm^3
$1/\eta$ = 0.14 nm^3 / molec
Average distance between molecules = 0.52 nm
Energy to have a scission event in PMMA = 4.9 eV

Figure 4-1 is a PMMA monomer drawn in PCMODEL. Figure 4-2 illustrates the geometry of PMMA at minimum total energy.

Bond scission and bond formation occur simultaneously. Which predominates determines whether the resist is positive or negative. In a positive resist such as PMMA, electron beam induces both scission and cross link between molecules. As shown in Figure 4-3, the scission process dominates the cross link process (This is shown with a thicker arrow), which decreases the molecular weight of the polymer and increases its solubility in the developer solution.

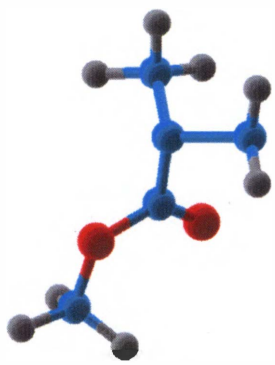


Figure 4-1: PMMA monomer. Carbon, Oxygen, and Hydrogen atoms are shown with Blue, red, and grey balls respectively. (This sketch was drawn using PCMODEL)

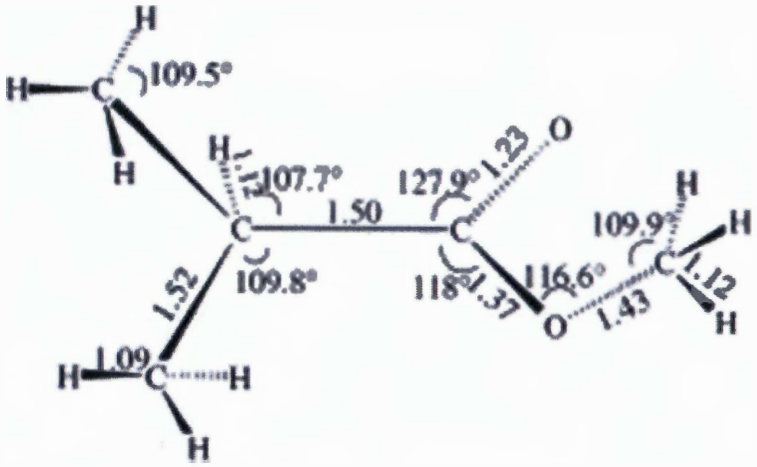


Figure 4-2: Geometry of methyl methacrylate after optimization of the total energy of the molecule.

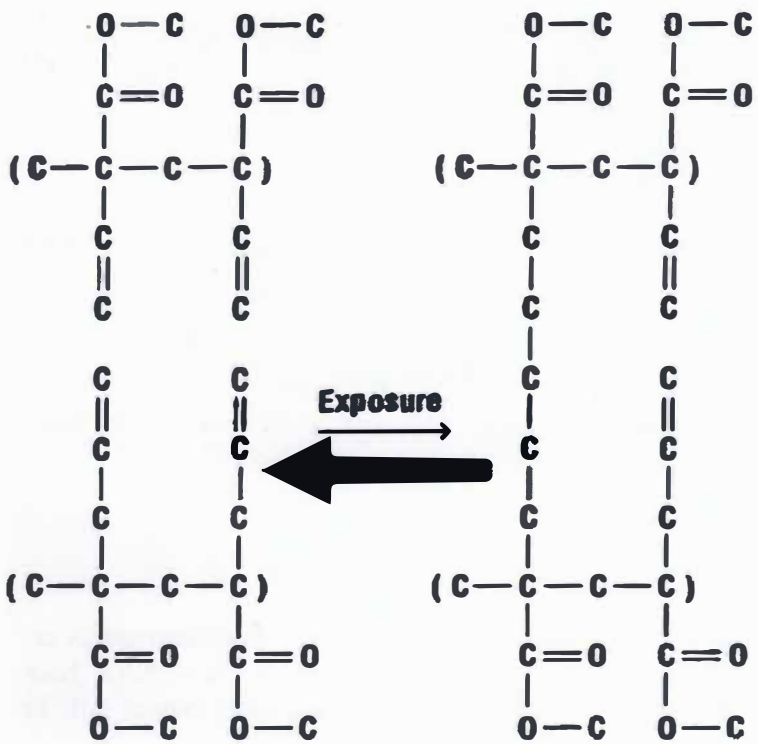


Figure 4-3: In PMMA the scission process dominates the cross link process (The scission and cross link processes are shown with thick and narrow arrows respectively).

Other subjects of interest and relevance (but beyond the scope of this thesis) on PMMA include:

Spectroscopy: electron energy loss[127], chain transfered fluorescence[128, 129], absorption coefficient[130], and ion mass spectrometry[131].The chain transfered fluorescence experiments study the transfer of external excitations along the chain backbone. Chain transfered excitations would affect the locality of the energy transfered by the electron to the polymer chain.

Thermal degradation[132, 133]. These experiments probe the thermal stability of PMMA at high temperatures and study thermal degradation mechanisms.

Thermo-mechanical properties[134, 135]. These are studies of stress and elasticity of PMMA at high temperatures.

Thin film properties[136-140].

4.2. Contrast

In defining the resolution of a resist, the most common attribute is the *contrast* γ , which is defined as:

$$\gamma = \left|\ln(D_f / D_i)\right|^{-1} \tag{4,1}$$

Here, for a positive (negative) resist, D_i is the maximum (minimum) dose for which the developed resist thickness is unchanged and D_f is the minimum (maximum) dose for, which the developer can completely remove the resist. The absolute magnitude sign arises since for negative resists $D_f < D_i$, while for positive resists $D_f > D_i$. That is, in a negative resist, the unexposed regions are removed, while in a positive resist the exposed regions are removed by the developer.

4.3. Profile Modeling

In order to predict resist profile, both development and exposure models are required. This chapter will summarize development models that have been constructed. In chapter 6, the results of the Monte Carlo exposure model will be presented.

4.4. Development Model

In a positive electron resist, exposed areas are removed by development and in a negative resist unexposed areas are removed. With polymeric resists, positive behavior is usually the result of the predominance of chain scission of the molecules during exposure whereas negative behavior is the result of cross-linking. In general, both processes occur simultaneously. Most of the published studies related to profile modeling have used poly-methyl-methacrylate (PMMA) because it is a relatively simple, well understood system and because it has high contrast and does not significantly swell or alter its dimensions during development. Negative resists tend to be more difficult to model, largely because they do swell and deform during development. A great deal of research is currently underway aimed at producing new types of resists, both positive and negative, with high contrast, resolution, and sensitivity. Since most of the work on profile modeling has concentrated on positive resists and in particular PMMA, this chapter will focus on this area.

The exposure of PMMA can be characterized in terms of energy dissipation per unit volume resulting in a change in the local solubility rate during development. The results for PMMA can be applied to other organic resists that can also be characterized by an exposure which depends upon the energy dissipation and by a development model.

4.5. Molecular Weight of PMMA

The average molecular weight after exposure, M_a for a positive polymeric resist is less than the original molecular weight before the exposure M_b. The final molecular weight can be expressed in terms of the absorbed energy density, D_E (eV/cm^3) by

$$\frac{1}{M_a} = \frac{1}{M_b} + \frac{gD_E}{\rho N_A} \tag{4,2}$$

, where ρ is the resist density, N_A is Avogadro's number, and g is the number of scission events per eV of absorbed energy. This relationship only applies to exposures such that the resist remains positive. The solvent in which the resist is developed selectively removes the material of decreased molecular weight. The solubility rate as a function of dissipated energy, $R(D)$ depends on the solvent, as shown in Figure 4-4.

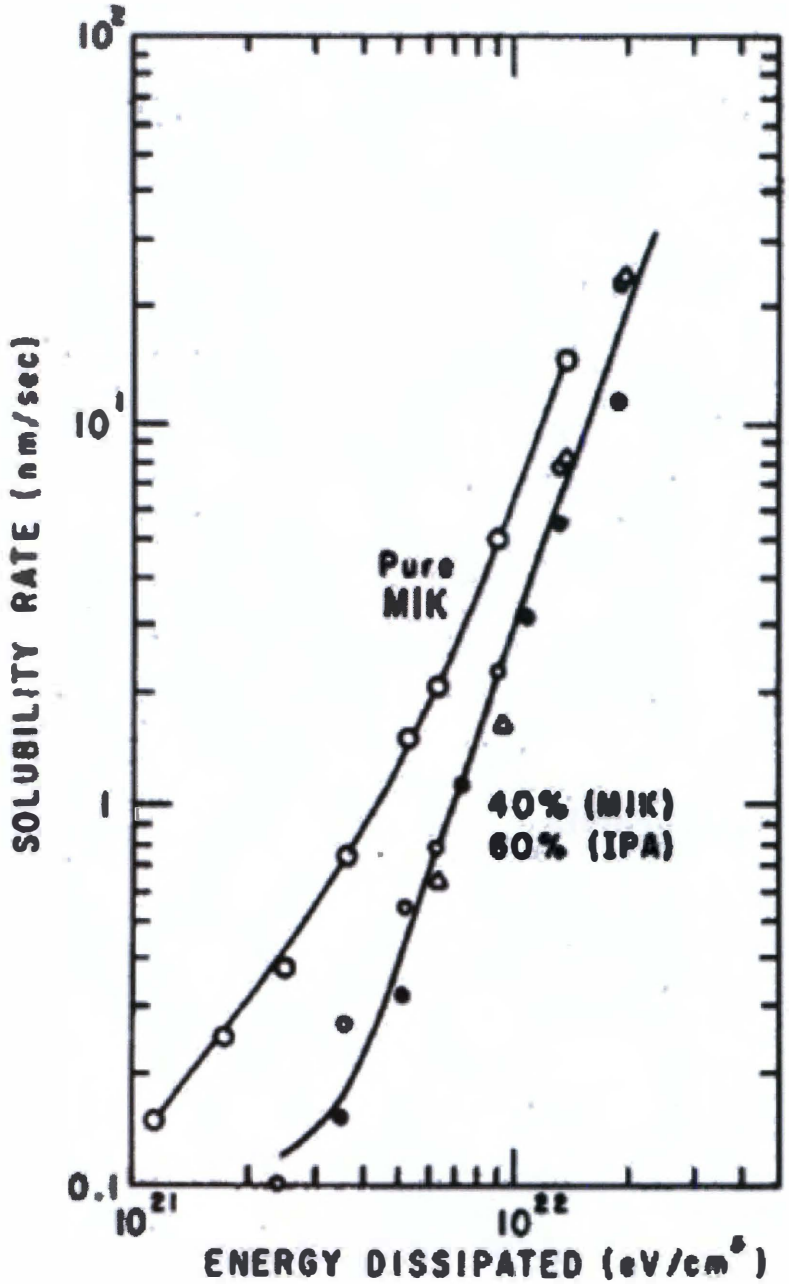


Figure 4-4: Solubility rate of PMMA as a function of energy dissipation in the polymer for two different solvents: 40% MIK / 60% IPA and pure MIK. The open circles and triangles denote exposure by a 20 keV electron beam, and the closed circles exposure by a 10 keV electron beam[141]

The data can be fitted using several different approaches. The fitting procedure used by Greeneich[142] is:

$$R = R_0 + \frac{\beta}{(M_a)^{\alpha}} \tag{4,3}$$

, where R_0, β, and α are empirical constants that depend upon the solvent. The solubility rate also depends upon the temperature[142], which must be controlled to achieve reproducibility.

This hypothesis that the solubility rate is a function of dissipated energy was originally tested by Ting[143]. He plotted the removed thickness of the resist as a function of time for various incident electron densities D (C/cm^2), for large area exposures. The energy density dissipated in the resist is given by:

$$D_E(z) = \frac{D \cdot E(z)}{e} \left(\frac{eV}{cm^3}\right) \tag{4,4}$$

, where e is the electron charge and $E(z)$ is the energy dissipated per electron. $E(z)$ can be obtained from Monte Carlo simulation[4]. From the measurements of the film thickness removed and the calculations of the energy dissipated as a function of depth, the solubility rate as a function of energy can be obtained at a given depth. For PMMA, which was used by Ting[143], the predicted curves of film thickness removed agreed well with the measured removal rate as shown inFigure 4-5, thus verifying the hypothesis that the solubility rate varies with dissipated energy.

The development contours can be identified as contours of equi-energy density or equi-molecular fragmentation. This is called the threshold energy density model and is used extensively in algorithms used to correct the exposure for the proximity effect. Typical values of the threshold energy density, $D_{E,threshold}$, required to develop a profile in PMMA range from 6.8×10^{21} (eV/cm^3) — 2.4×10^{22} (eV/cm^3)[141, 144-147].

Since the solubility rate is a function of dissipated energy, the developed profile for any exposed pattern, in principal can be evaluated provided the spatial distribution of energy dissipation is known. Three different approaches for simulating the development process for infinitely long lines have been compared by Jewett et al.[148]: cell removal, ray tracing, and the string model.

In the cell removal model, the polymer is subdivided into stacks of cells[141, 148-150]. The solubility rate of each cell is determined by the energy dissipated in that cell. The solvent dissolves only those cells with which it is in contact at a rate determined by the local solubility rate. If a cell is dissolved, then the solvent attacks the surrounding cells (Figure 4-6).

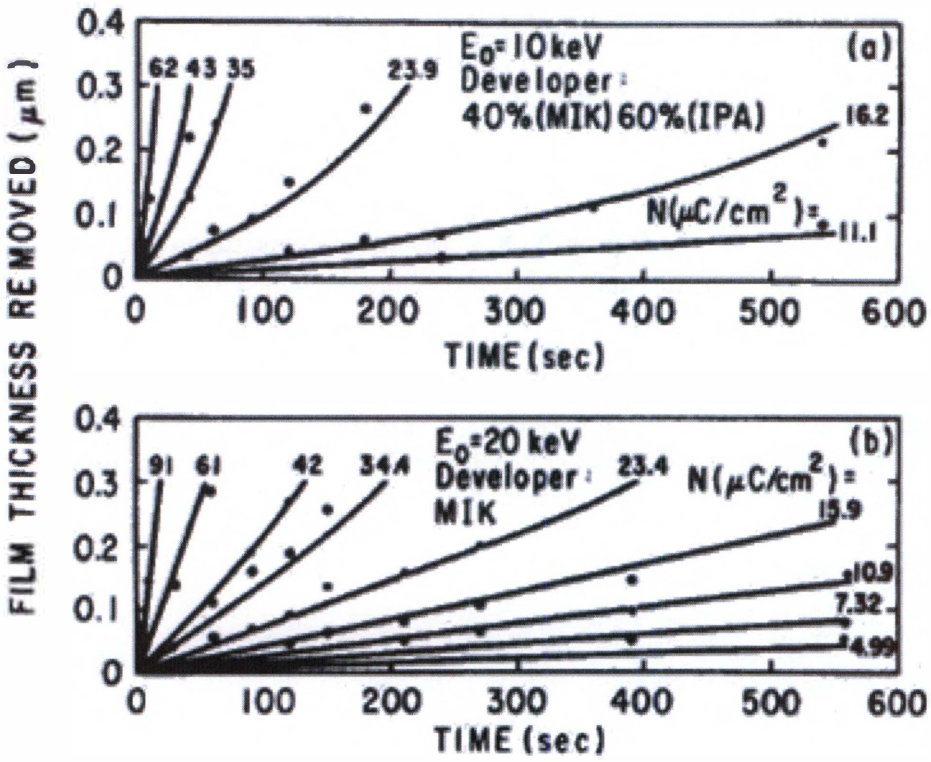


Figure 4-5: Film thickness removed as a function of the develoment time for the several values of the incident electron density N for a 0.3 μm thick film of PMMA. (a) is for exposure by 10 keV electrons and development in 40% MIK, 60% IPA, and (b) is for exposure by 20 keV electrons and development is pure MIK. The circles and dots are experimental results and the solid curves are theoretical calculations based upon the solubility rate of Figure 4-4.

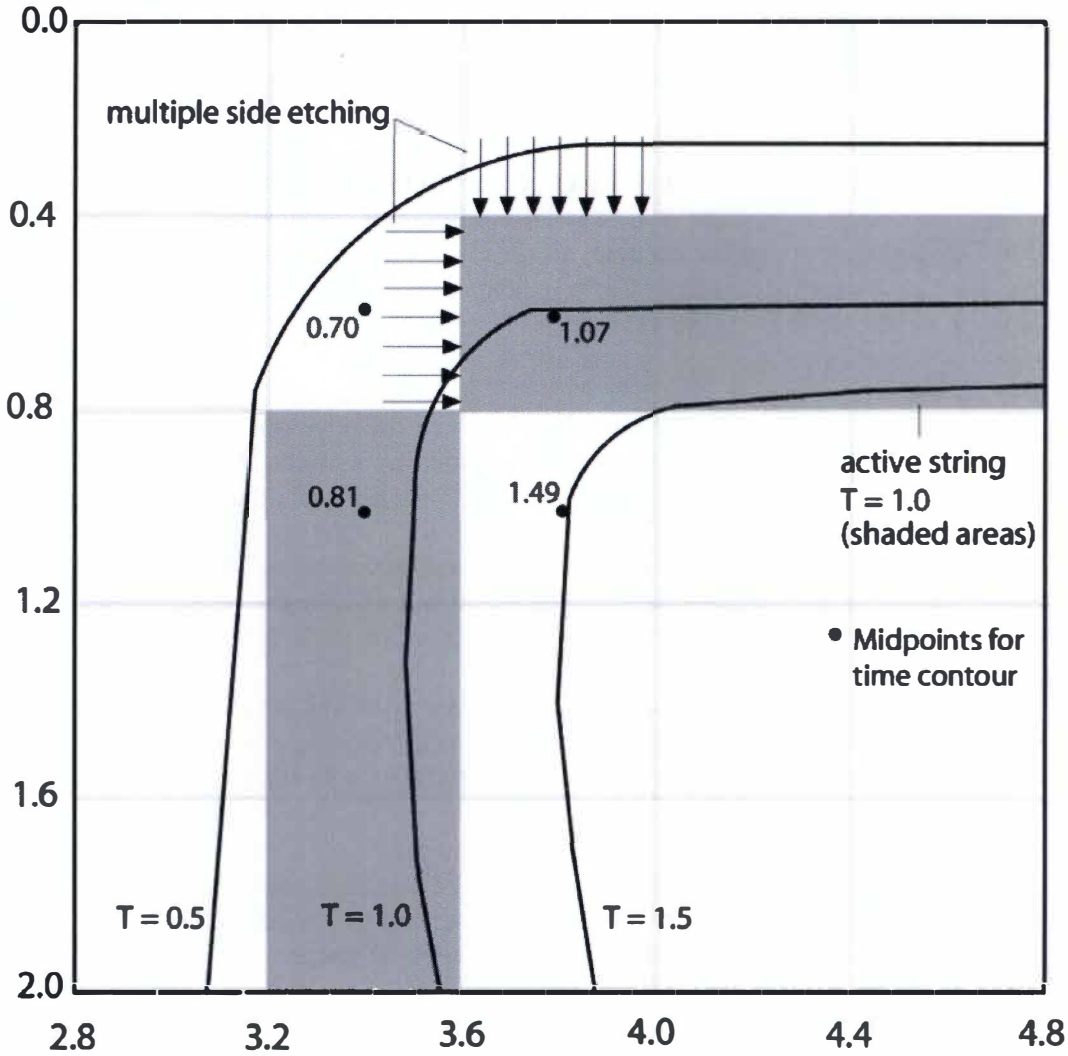


Figure 4-6: Cell-removal model. The contours shown are ones calculated for a simulated electron beam exposure. The numbers shown at the centers of the cells are the times (T) of dissolution of the cells. The contours are interpolated from these numbers. The time and distances shown have been normalized by use of a rate function

$$R(x,y) = \text{Larger of}\left[\left(10 - x^2(1+\frac{y}{8})^{-1} \text{ or } 0.5\right)\right] \text{(units/time step)}$$

In the ray tracing model, an etch ray is a vector perpendicular to the boundary between a developed and undeveloped region[148]. The etch ray is refracted or bent at boundaries between regions of different etch rates. The trajectories of a series of rays are followed as a function of time starting at the top surface of the resist. At the end of each time step, the end points of the rays are joined together and define a developed contour. The ray tracing model is a very elegant approach to calculate the developing contours. However, it does depend upon placing a sufficient number of rays at the right place to form a well-defined contour. Also, not only must the local etch rate be known but so must the spatial gradients of the etch rate. This imposes additional requirements on the accuracy of the energy dissipation calculations. This is especially important for Monte Carlo calculations where statistical accuracy is attained at computational expense (Figure 4-7).

In the string model[148], the boundary between the developed and undeveloped regions is approximated by a series of points joined by straight line segments. Each point advances along a line (the angle bisector), which bisects the angle formed by the adjoining points, according to the local etch rate. Points are added or deleted to improve the accuracy of the calculations and minimize the computation time. In comparison to the cell removal model, both the string and the ray tracing models are shown to be somewhat faster and more accurate for infinitely long lines (Figure 4-8).

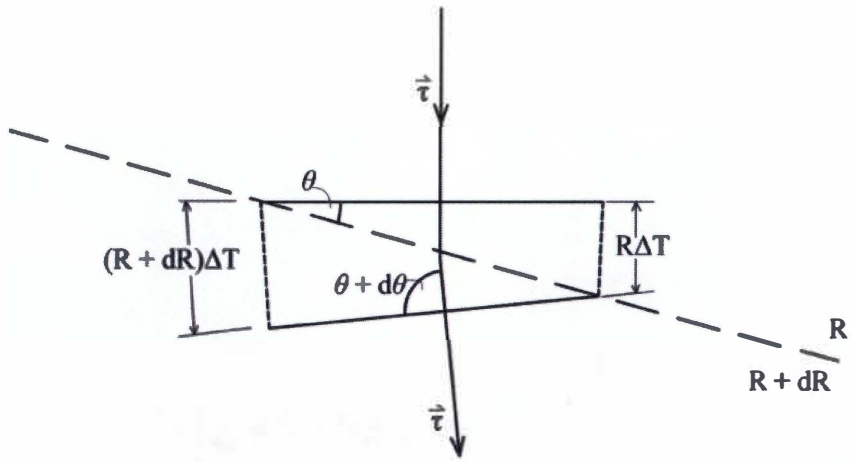
One implication of the threshold energy density model is that the resist should act like a linear recording medium in the sense that the exposure is additive. This has been verified by comparing the exposure of isolated dots with lines over a wide range of exposures in a high contrast resist[141].

The sensitivity of the profile shape to resist contrast, which is determined by the combination of resist and solvent, has been analyzed by several authors[151-153]. Three general conclusions have emerged for low contrast resists.

First, the resolution of the profile is degraded. Second, the profiles are more sensitive to variations in dose and development conditions. Third, the resist thickness in the unexposed area decreases and thus the profile cannot be simply approximated by equi-energy density contours. The implication of these studies is that proximity effect algorithms that do not take into account profile development may be less accurate for low contrast resists.

In experiments with both ion and electron beams, Hall et al.[154] have shown that the fluence required to expose different resists correctly is not simply a function of the energy dissipated but also is a function of the ion/electron mass and of whether the resist is positive or negative. This effect is attributed to the production of secondary electrons by the ion beam. These electrons in turn cause either cross-linking or scission of polymer bonds.

a)



$$\frac{d}{ds}\left(n_R \vec{\tau}\right) = \overrightarrow{\text{grad}}\ n_R \qquad \frac{R + dR}{R} = \frac{\sin(\theta + d\theta)}{\sin\theta}$$

b)

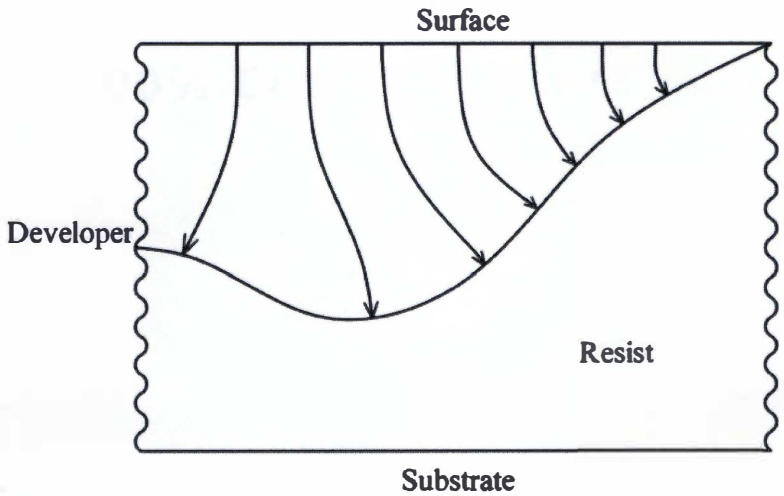


Figure 4-7: Ray tracing algorithms. (a)Etch ray is referred at a boundary between regions having etch rates R and R+dR according to Snell's law. The effective refractive index for the resist is $n_R = \frac{\text{Maximum Etch Rate}}{\text{Local Etch Rate}} = \frac{R_{max}}{R}$. (b) Rays are started at the surface and the contour joining their endpoints after a given time (etch front).

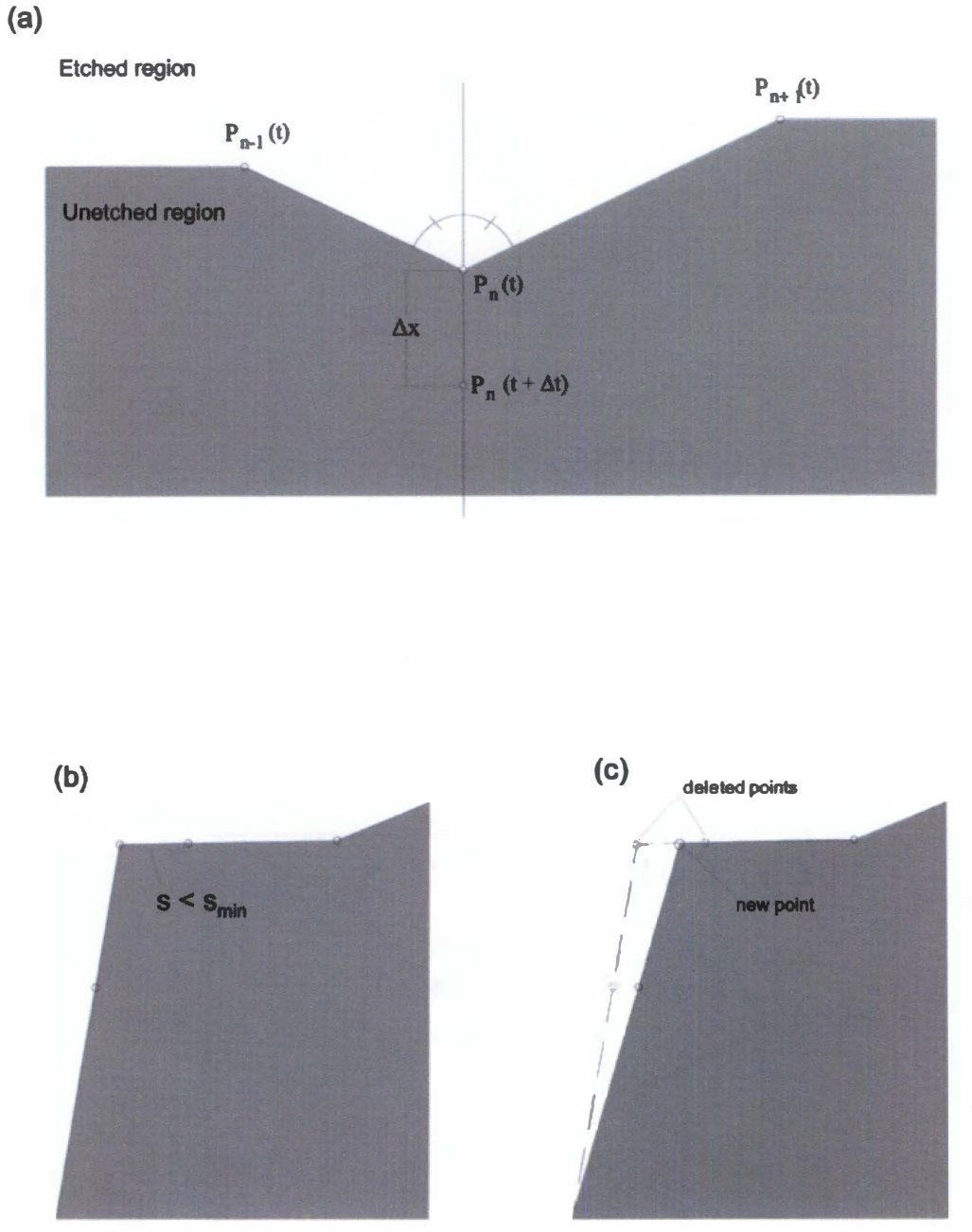


Figure 4-8: Algorithm for the string model. (a) The advancement of a point by a distance Δx in a time Δt is along the bisector of the angle between the segments of the line at point $P_n(t)$. The distance $\Delta x = \Delta t.R(P_n(t))$, where R is the rate. All points along the string are advanced in this manner. (b) The string where a point is about to be eliminated. The segment length is S and the minimum allowed value is S_{min}. (c) The string after change that eliminated one point.

Depending upon the type of resist, one bond or two bonds must be activated and this alters the fluence requirements. The fluence requirements also depend upon the range of the secondary electrons produced by the ion beam. In practice, PMMA can be modeled adequately only as function of dissipated energy. Therefore in electron beam lithography, the solubility rate is a function of both energy dissipation and beam voltage.

Chapter 5

5. Interaction of Ions with Matter

5.1. Introduction

The study of the interaction of charged ions with solids and surfaces is of great importance in atomic/molecular physics and condensed matter physics. With the recent development of microscopes equipped with advanced ion sources and ion optics, there is now new interest in imaging and microanalysis in this mode [ALIS SIM]. The analysis of the ion-solid interactions enables us to extract information about the electronic structure of the solid under investigation. This information is obtained using fast and slow ions, partially ionized or fully stripped ions and observing the electron emissions (Auger emission and kinetic emission), sputtering yields, x-ray emission and many other phenomena involved in the process. There has been extensive theoretical and experimental work in the area of ion-solid interactions.[155-163]

Before proceeding further some terminology should be clarified. Gryzinski[95] named the projectile and the target as the test particle and the field particle, respectively. In spectroscopic applications Gryzinski's terminology is a better description of the process while in scattering problems the terms projectile and target are widely used. In reality, the target and the projectile are the issue of observer. If the collision is observed by one having zero speed with respect to the field particle, then the field particle is the target and the test particle is the projectile. If one has zero speed with respect to the test particle, then the test particle is the target and the field particle is the projectile. It should be added that the interaction potential (field) is a characteristic of both particles not just the field particle. This is most important when the projectile is not an electron and will have an internal energy structure before or after the collision. This is the phenomenological difference between the interaction of matter with electrons or ions.

Different channels in electron matter interactions are summarized in chapter 3, equation (3.2), however, the interaction of ions with matter can proceed into more channels. The ions used in an ion-matter interaction could be fully or partially stripped and one could even use neutrals as well as anions. Fully stripped ions would not have any structure, while partially stripped ones, neutrals and anions contain electrons and therefore possess a structure. The structure of projectiles will add to the complexity of the observed "spectra". In this section (chapter) the term I^{+z} denotes a general ion where z could be any positive/negative or zero integer. However, the term P^{+z} is solely used for fully stripped ions, where z is equal to the total number of electrons in the original atom. As is expected there is always an elastic channel:

$$I^{+z} + AB \rightarrow I^{+z} + AB \tag{5,1}$$

where AB stands for any molecule as a part of the matter being tested. There are also inelastic channels in the ion-matter interactions as:

$$I^{+z} + AB \rightarrow \begin{cases} I^{+z} + AB^{*} & \textit{excitation} \\ I^{+z} + AB^{+z'} + z'e^{-} & \textit{(multiple) ionization} \\ I^{+z'} + AB^{+z''} + (z' + z'' - z)e^{-} & \textit{(transfer) ionization} \\ I^{+z_1} + A^{+z_2} + B^{+z_3};\ z = z_1 + z_2 + z_3 & \textit{ion pair formation} \\ I^{+z} + AB^{+z'} + z'e^{-} + h\nu & \textit{radiative ionization} \\ \cdot & \\ \cdot & \end{cases} \tag{5,2}$$

The channel that is named "*(transfer) ionization*" is by itself a set of channels depending on the charge values. In the case that $z' = z \pm 1$ and $z'' = \mp 1$, the process is called charge transfer, or charge exchange when no secondary electron is observed. In other cases this channel is termed transfer ionization under the condition that $z' + z'' - z > 0$. Most of the channels happening in an ion-matter collision emit a secondary electron that originated from the target or the projectiles. In the case of high energy ion interaction with matter in the MeV/amu range, nuclear reactions would have high enough probabilities to be important. In Figure 5-1, the processes in the ion-matter interaction are shown schematically.

5.2. Kinematics of Ion-Matter Interactions

It is conventional to use energy regimes for the classification of ion-matter interaction. This interaction category has been studied in the high energy regime where the ion's kinetic energy is comparably higher as compared with the bound electrons in the target. Because of the speed of the ions in the high energy regime, the relativistic nature of the collisions needs to be considered.

Another terminology that should be used is the speed expression, which can be discussed under the Bohr Criterion[164]. Simply, ions with a speed less than or equal to the bound electron in the target will be considered as slow ions. Fast ions have speeds higher than the bounded electrons of interest. We will define "**equivalent electron to projectile**" to be an electron having the same speed as the projectile. The typical scale of the electron orbital velocity with an ionization potential I_{nl} is

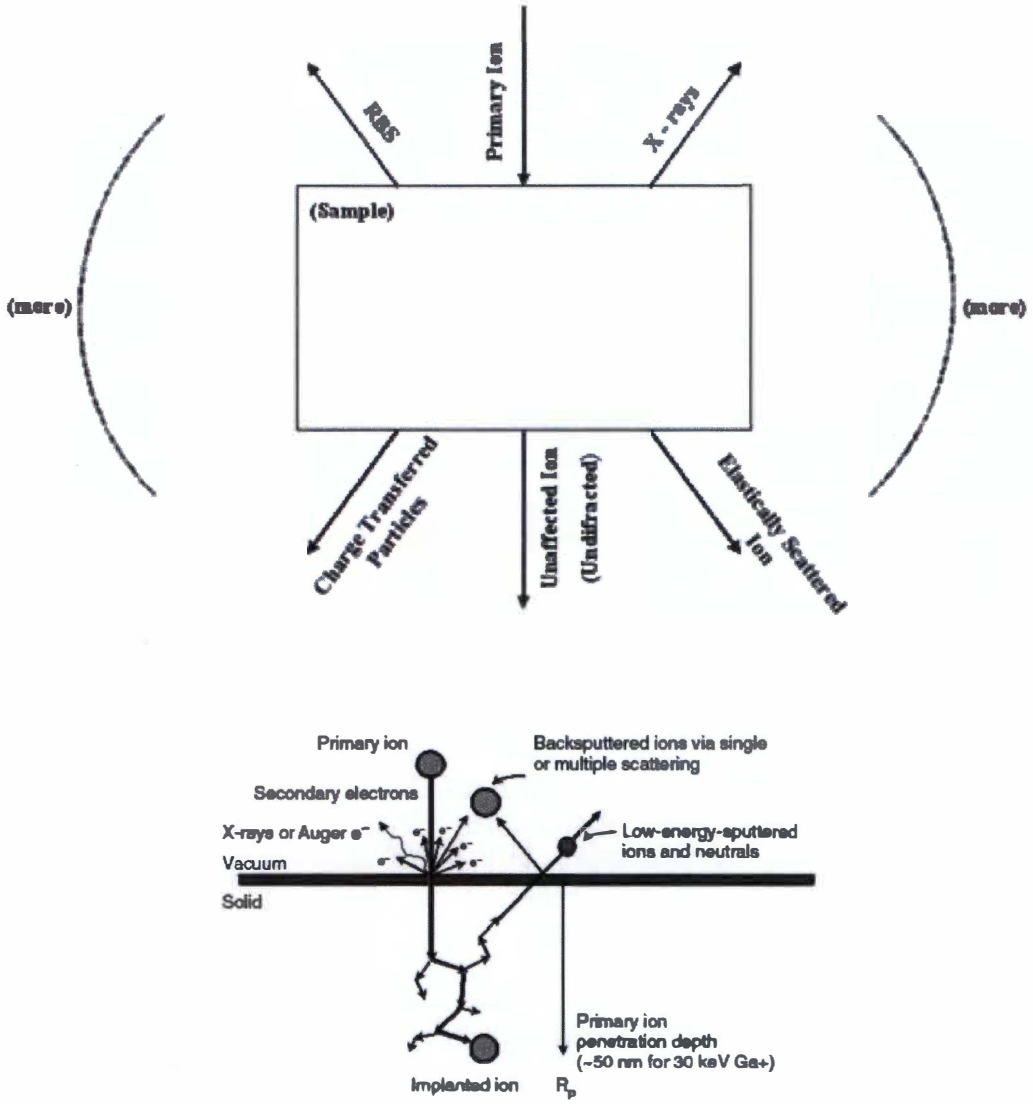


Figure 5-1: A schematic diagram of the processes involved in the interaction of primary ions with matter. (The nuclear reactions are not shown and are not of concern, especially for low energy ions.)

$$\upsilon_{nl} = \upsilon_0 \sqrt{I_{nl}/R_y} \qquad (5,3)$$

Here, n, l is the standard notation for the principal quantum number and the orbital angular momentum quantum number, υ_0 (= 2.19×10^8 cm/s) and R_y (= 13.6 eV) are the speed and the energy of the first Bohr's electron, respectively. The collision dynamics depends strongly on whether projectile particle velocity υ is smaller or larger than υ_{nl}.

The kinematics of the interaction of ions with matter depends on the type of collision. Kinematics of interaction is different when the collision involves electrons or the nucleus. If the ion is interacting with the electron in matter, the kinematics would be similar to Figure 3-2 and equations (3,3) and (3,4) hold.

5.3. Elastic Scattering of Ions from Matter

Partially or fully stripped ions interact with solids through interactions with nuclei and electrons of the matter atoms. At projectile velocities exceeding the electron orbital velocity, υ_{nl}, the dominant process is inelastic interaction, i.e. excitation and ionization of bound electrons, which dominates over elastic interaction by at least an order of magnitude[165]. Elastic interaction is the result of electrostatic repulsion between the impinging ion nucleus and the nucleus of the target atom screened by electrons. Elastic collisions of ions with lattice nuclei prevail in the region of ion velocities less than the orbital electron velocity. Although generally elastic scattering has a lower cross-section for interaction with ions in matter, this is an important process affecting the penetration depth as well as spectroscopic tools such as Rutherford back scattering and elastic recoil detection analysis, (ERDA).

In the quantum-mechanical picture, elastic ion scattering is described by the transition from an initial state to a final state for the target and a plane wave for the incident and outgoing ion. The first Born approximation usually results in a differential cross section similar to the classical Rutherford formula. The discussion made on electron scattering in sections 3.3.1 and 3.3.2, holds.

5.3.1. Rutherford Back Scattering (RBS)

Rutherford Back Scattering is a spectroscopic tool based on the elastic scattering of ions colliding with solid targets. As is illustrated in Figure 5-2, the incoming ion, usually of small mass M_1, hits the target and traverses it. The projectile interacts with the nuclei of atoms elastically, having mass M_2, and bounces off in the

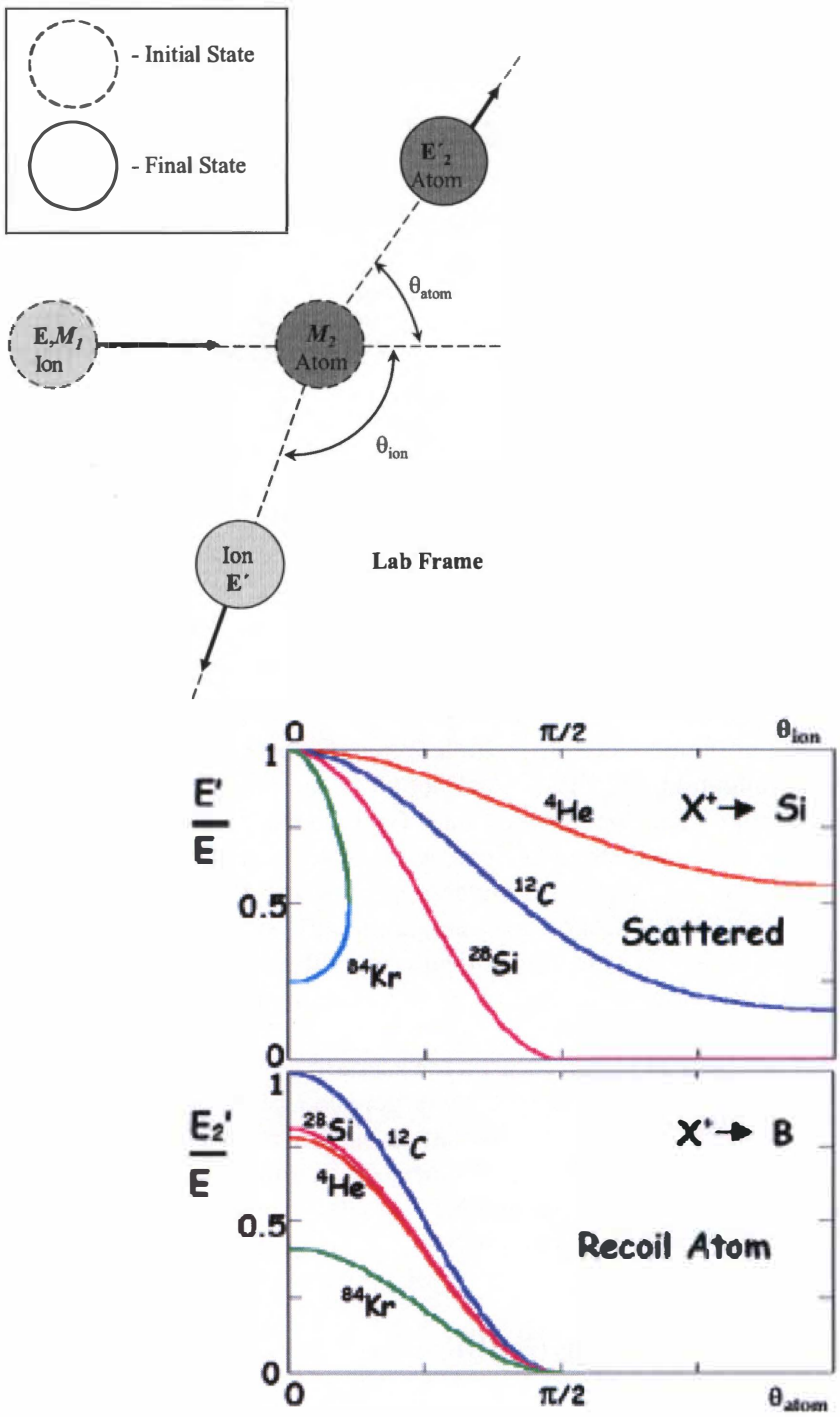


Figure 5-2: The general kinematics of the interaction of ions that involves the target's nucleus, excluding nuclear reactions, is quite simple and it could be discussed in the context of elastic scattering and Rutherford Back Scattering (RBS).

backward direction, since the target mass is considerably higher than projectile mass. The scattering cross section is found classically as:

$$\frac{d\sigma_{RBS}}{d\Omega}=\left(\frac{Z_1 Z_2 e}{2E_0}\right)^2 \times \frac{1}{\sin^4\theta} \times \frac{\left(\sqrt{1-\left(\frac{M_1 \sin\theta}{M_2}\right)^2}+\cos\theta\right)}{\sqrt{1-\left(\frac{M_1 \sin\theta}{M_2}\right)^2}}, \tag{5,4}$$

where Z_1, Z_2, E_0 and θ are the atomic number of incident ion, atomic number of target atom, energy of incident ion, mass of incident ion, mass of target atom and the angle of incidence, respectively.

If the atomic nucleus is lighter than the incident ion, the atomic nucleus recoils in the forward direction since the term under the radical, $\sqrt{1-(M_1 \sin\theta/M_2)^2}$, should be positive. Another spectroscopic method has been developed on this basis called ERDA. The recoil element can, therefore, be detected if the sample is tilted. This way the beam enters the sample at a grazing angle and the recoiled nucleus can escape the target. The spectrum detected by RBS and ERDA reflects the mass of their atomic nuclei.

5.4. Secondary Electron Production

The production of secondary electrons by the interaction of electrons with matter was discussed in chapter 3. There are similarities and differences in the interaction of ion/atom and electron with matter and it is intended not to repeat them here. The two interactions are similar when the projectile and the target is assumed particles or at least the target's electron to be in a binary interaction with the projectile. The differences between them are enhanced when the structure of the target and/or projectile become important. Here, the word ion is used in a general sense that includes the fully stripped ones as well as those that retain some of their electrons. When a projectile ion carries electrons, the interaction has similarities with neutral atoms or anion projectiles.

5.4.1. Atomic Models

In 1912 Thompson[90] calculated the ionization cross section in the limit $\upsilon \gg \upsilon_{nl}$. His treatment neglected the orbital motion of the target electrons and assumed a straight-line trajectory of the projectile, which gives

$$\sigma_{Bohr}(\upsilon, I_{nl}, Z_P) = 4\pi Z_P^2 a_0^2 \frac{\upsilon_0^2 R_y}{\upsilon^2 I_{nl}} \tag{5,5}$$

, where a_0 (= 0.529 Å) is the Bohr radius.

In 1966 Gerjuoy[166] calculated the cross section by averaging the Rutherford electron-ion scattering cross section over the phase space of the atomic electrons, leading to an ionization cross-section

$$\sigma_{GGV}(\upsilon, I_{nl}, Z_P) = 4\pi Z_P^2 a_0^2 \left(\frac{R_y}{I_{nl}}\right)^2 G_{GGV}(\frac{\upsilon}{\upsilon_{nl}}) \tag{5,6}$$

, where G_{GGV} is the scaling function.

Bethe made use of the Born approximation to calculate cross sections. The Born approximation is valid for $\upsilon/\upsilon_0 > 2Z_p$ and $\upsilon \gg \upsilon_{nl}$. This yields the relation

$$\sigma_{Beth}(\upsilon, I_{nl}, Z_P) = \sigma_{Bohr} \times \left[0.566 \ln(\frac{\upsilon}{\upsilon_{nl}}) + 1.26\right]. \tag{5,7}$$

The logarithmic term in the bracket is a result of the quantum mechanical calculations done. The Bethe formula describes well the cross sections for $\upsilon \gg \upsilon_{nl}$. At large energies, the GGV formula underestimates the cross section, whereas Gryzinsky's formula gives results close to the Bethe formula and the experimental data. Both the GGV and Gryzinsky formulas disagree with the experimental data at small energies because they assume free electrons, neglecting the influence of the target atom potential on the electron motion during the collision.

In order to match the asymptotic behavior of the Bethe formula in equation (5,7) at large projectile velocities, Gryzinsky assumed an empirical electron velocity distribution function. After a number of additional simplifications and assumptions, Gryzinsky suggested an approximation for the cross section in the form given by equation (5,6) with another function $G^{Gryz}(x)$. The Gryzinsky formula can be viewed as an empirical fit to the Bethe formula at large velocities $\upsilon \gg \upsilon_{nl}$, with some rather arbitrary continuation to small velocities $\upsilon < \upsilon_{nl}$.

For $\upsilon \approx \upsilon_{nl}$, a universal curve is expected if both the cross sections and the square of the impact velocity are divided by Z_P (Bohr's model). This scaling was established for the total electron loss cross section σ_{el}, which includes both the charge exchange cross section σ_{ce} and the ionization cross section, based on the results of classical

trajectory Monte Carlo (CTMC) calculations by Olson[167]. The Olson scaling can be written in the universal from similar to equation (5,6),

$$\sigma_{el}(\upsilon, I_{nl}, Z_P) = 4\pi Z_P^2 a_0^2 \left(\frac{R_y}{I_{nl}}\right)^2 G_{Olson}\left(\frac{\upsilon}{\upsilon_{nl}}\right) \tag{5,8}$$

where

$$G_{Olson}(x) = \frac{5}{3x^2}\left[1 - \exp(-4x^2/5)\right]. \tag{5,9}$$

5.4.1.1. Binary Encounter Peak

The simplest mechanism for the interaction of an ion with an atom/molecule is the direct collision of the ion with the atomic/molecular electron, which is signaled by a peak, called binary encounter (BE) peak, at a specific electron momentum and energy in the energy and angular distribution of electrons ejected. As the electron is initially bound, the BE peak is broadened by the Compton profile of the initial state. However, the BE peak is not a signature of the target dynamic. Classically, the electron should be ejected at energy E given by:

$$E \cong 4\frac{m}{M} E_0 \cos^2\theta \tag{5,10}$$

, where M, m, E_0 and θ are the mass of ion, mass of electron, initial ion energy and the scattering angle of the ejected electron, respectively. This process is relevant in the electron-atom interaction but equation (5,10) would take the form of equation (3, 20) in the case of electrons.

In Figure 5-3, the typical energy and angular distribution of ejected electrons are presented for the collision of 500 keV H^+ on H_2 molecule[168]. This should yield a "broad" binary encounter peak around 900eV at 20°, and moves toward smaller energies for higher scattering angles up to 90°. These electrons are not observed at 90° scattering angles and are mostly scattered at forward angles.

5.4.1.2. Direct Ionization, DI

Another mechanism for electron ejection in the ion-atom/molecule interaction is the direct ejection of slow electrons, where the field of the fast charged particle at large impact parameters perturbs the atom so that it is excited or ionized in the final

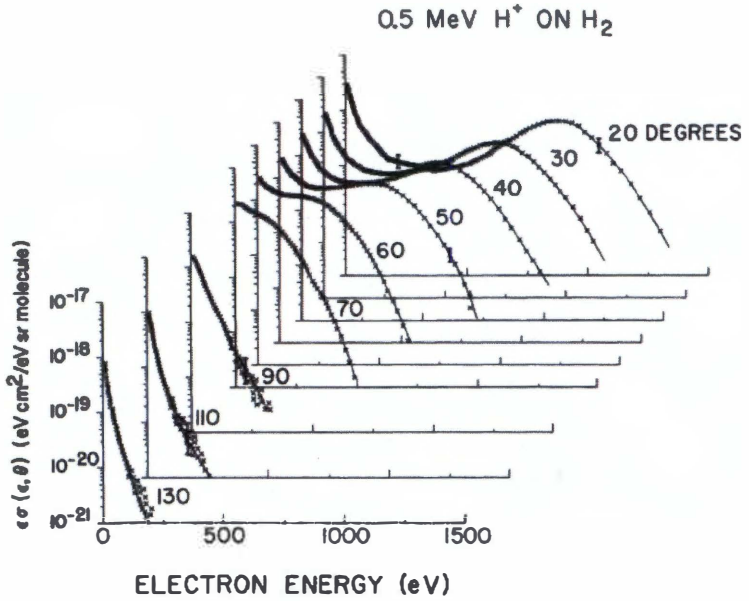


Figure 5-3: The angular and energy distribution (DDCS) of the ionization cross section are plotted as a function of secondary electron energy for 0.5 MeV H+ on H2.

state. This will show a rise towards low energy secondary electron's energy distribution. The corresponding zero-energy peak is well understood in terms of the first Born theory for direct ionization[65, 88]. This peak is observed at zero energy in Figure 5-3. This mechanism is common to the electron-atom and ion-atom interaction and is detected at all angles, but still has a predominant tendency towards the forward angles.

5.4.1.3. Electron Capture to Continuum, ECC

Another mechanism was later identified[169-171] having a peak in the ejected electron energy spectrum showing that the ejected electron has the same speed as the projectile. The speed dependence of the third process implicates it as a rearrangement process, making this process, similar to a charge transfer reaction, except that the transfer is into the continuum of the projectile. This yields a secondary electron ejection with speed about equal to that of the electron and the projectile ion. This mechanism is sometimes called the charge transfer to continuum, CTC, and is not familiar in the electron-atom interaction since two electrons do not form a bound state. This type of process has been observed when a channel is allowed for a projectile to have a structure in the final state. Therefore, this process is strongly enhanced in the positron-atom interaction[172]. In Figure 5-4, the ECC process is evident at secondary electron energies of about 80eV, which is called "equivalent

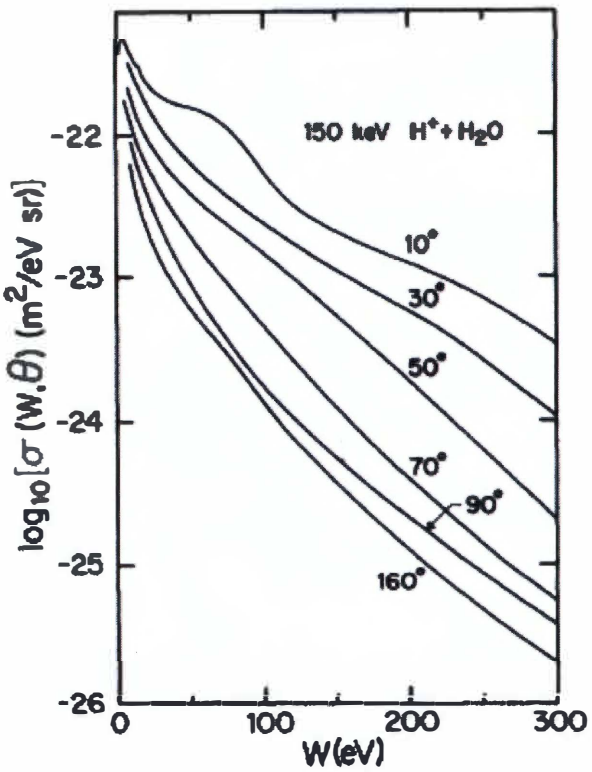


Figure 5-4: The energy and angular distribution of electrons ejected in the collision of 150 keV H^+ on H_2O.[173]

electron" to the projectile here. This mechanism is not pronounced in Figure 5-3, which may be due to the interference of the broad binary peak. However, this process is more likely to happen at higher impact energies and again it is mostly favored at forward angles.

5.4.1.4. Electron Loss to Continuum, ELC

An important difference between the collision of an electron or an ion with atoms or molecules is due to the electrons in the projectile for the partially stripped ion or neutral atom projectiles. If the projectile ion has electrons and therefore has an electronic structure, a portion of secondary electrons are the result of a process called "Electron Loss to Continuum, ELC". During the collision, the electrons that are carried by the projectile, test particle, will gain enough energy to excite to a continuum state of the ion and eventually scatter off. Usually, these secondary electrons would have the same speed as the projectile. This process is observed by many[174-176] and an example is shown in Figure 5-5. In Figure 5-5, the energy

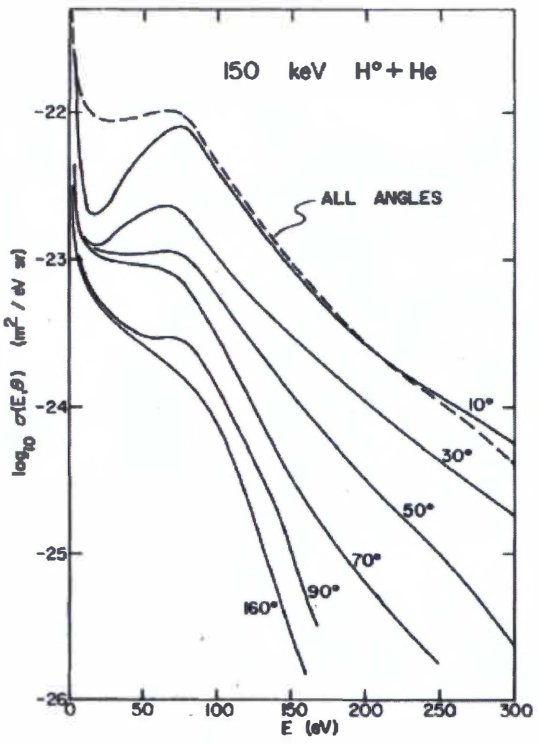


Figure 5-5: Double differential cross section; i.e. the cross sections differential in the scattering angle and the energy of the secondary electrons, is plotted against the ejected electron energy for the impact of 150 keV H^0 on He. Dotted line shows the singly differential cross sections, integrated over all angles, in m^2/eV on the same numerical scale.

dependence of ejected electrons is plotted for the measured doubly differential ionization cross sections at various forward and backward angles. This process has a prominent peak at the same energies as ECC, and could be observed at any angle (even at 90°), but it is more pronounced at the forward angle. Doubly differential cross sections are integrated over angle and are plotted as a dashed line in Figure 5-5. In Figure 5-6, ejected electron energy dependence of the singly differential cross sections is plotted. Also note that the ELC peak moves to smaller secondary electrons energies as the primary energy decreases.

A comparison between the ionization of Helium atoms by electron, proton, and atomic hydrogen as projectiles is possible from the experiment performed by Rudd et al[176], which is presented in Figure 5-7. The comparison is provided in this figure for primary electrons of 100eV and H^0 and H^+ primaries of 150 keV, where the angle of ejection are nearly the same. It is expected that the cross section be close at large ejection energies which correspond to small impact parameter. This is expected since for close encounters between the projectile and Helium atom, electrons carried by the H^0 have little effect. The "equivalent electron" to this projectile has an energy

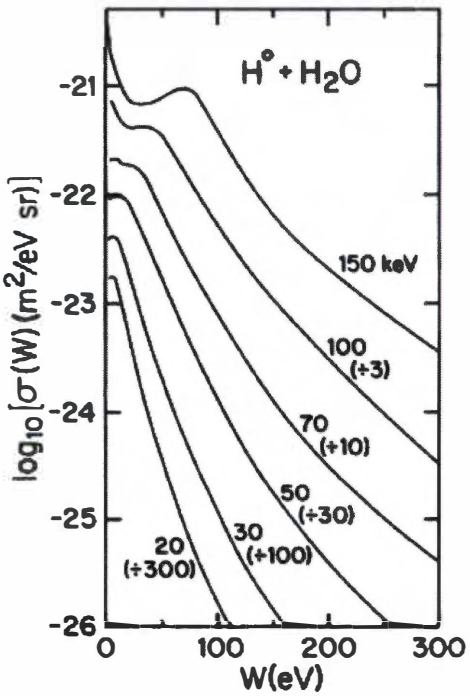


Figure 5-6: Differential cross sections in energy is plotted against the energy of ejected electron for the collision of 20-150 keV H^0 on H_2O.[175]

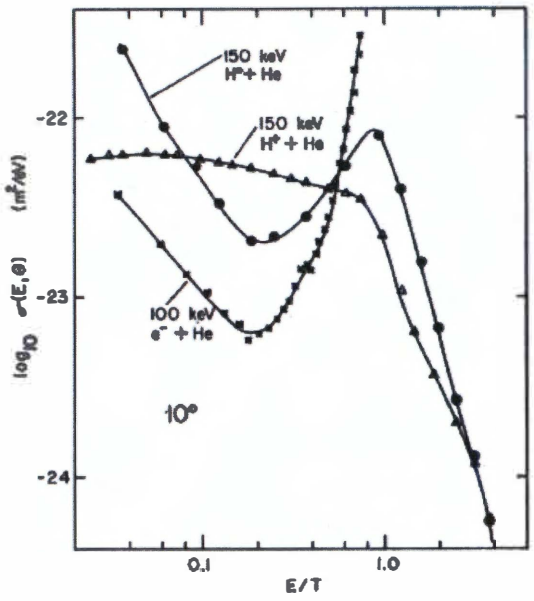


Figure 5-7: The doubly differential ionization cross sections for the collision of 150-keV H^0 and H^+ impact and 100-eV electron impact on Helium. Electron ejected at 10° relative to the beam[169]. T is the energy of the "equivalent electron" to the projectile. The annotation in the figure is wrong about the energy of primary electron.

of about 80 eV. At lower energies, the cross section for electron ejection by e^- and H^0 is higher than those for H^+ projectiles. This is due to the ELC process, where the electron in the projectile transferred to the continuum and interacted with the target in the same way as an electron interacts. At still lower energies, where the DI mechanism is important, the cross section for H^0 impact on He is smaller than those of H^+ due to the shielding effect of the electron. However, at very low energies the cross section for H^0 impact is similar to the electron impact in shape and higher than both H^+ and electron impact.

The ejected electron energy dependence of the doubly differential cross sections for the atomic hydrogen as the projectile is divided by the similar cross sections for the protons as projectile and the results are plotted in Figure 5-8 for the primaries of 150 keV. It is evident that the ELC peak is prominent at all angles. The ejected electron energies of the singly differential cross sections, determined by integrating over angles, for different primary energies, are plotted in Figure 5-9. As it is shown, this phenomenon is observed at higher energies and it is less probable at smaller impact energies.

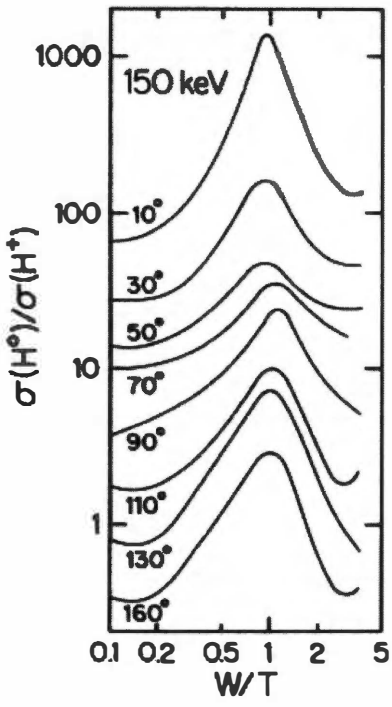


Figure 5-8: Doubly differential cross sections for the ejecting electrons in the collision of 150 keV primaries are plotted against the ejected electron energies scaled by the equivalent electron energies. The ordinate is the cross sections for neutral divided by similar cross sections for ions. Here, W is the energy of the ejected electron and T is the "equivalent electron" energy.

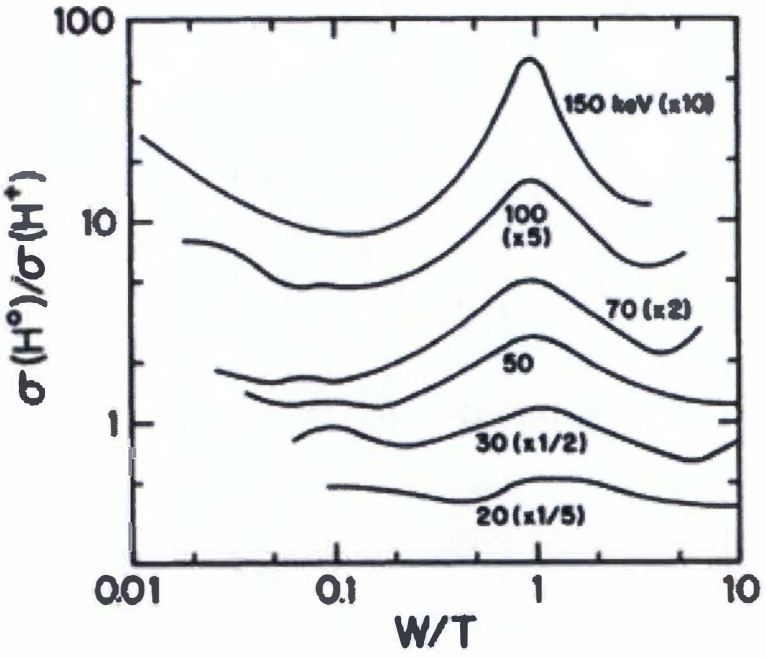


Figure 5-9: Doubly differential cross sections for the ejected electrons in the collision of 150 keV primaries are plotted against the ejected electron energies scaled by the equivalent electron energies. The ordinate is the cross sections for neutral divided by similar cross sections for ions. Here, W is the energy of the ejected electron and T is the "equivalent electron" energy.

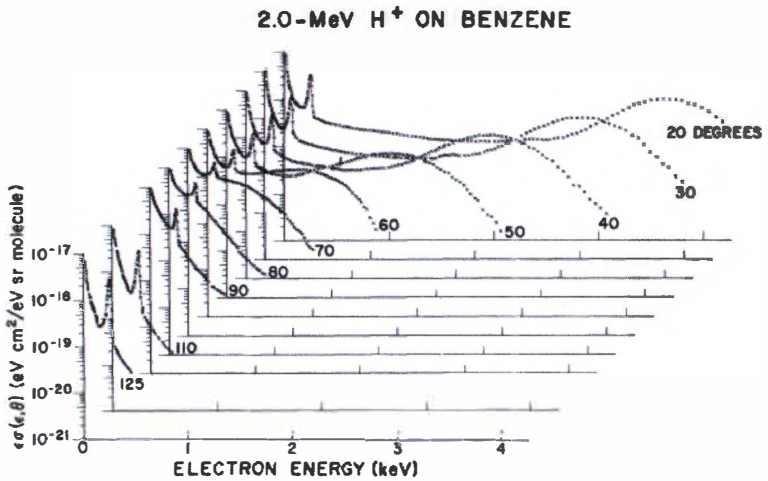


Figure 5-10: The doubly differential cross sections for the ionization of Benzene plotted against the ejected electron energies for the 2.0 MeV H^+ projectiles[177].

5.4.1.5. Inner-shell Vacancies

When ions collide with an atom, innershell vacancies are possibly generated, which could result in an Auger electron ejection or x-ray fluorescence emission. As shown in Figure 5-10, the inner shell vacancies are present as a relatively sharp peak which having a $\cos^2\theta$ dependence.

5.4.2. Low Energy Ions

For slow ions, a similar assumption to the CCC is applicable. This is discussed as an example by Macek[178]. In CCC, which considers the electron scattering at low energies, it is assumed that the incoming electron forms a system with the target. The new system has a positive total energy. Thus, it should be in a continuum state. Therefore, the state of this new system is calculated and the cross sections for ionization or excitation or any other allowed channel is deduced.

For slow ions colliding with a target, where the target is T and the projectile is P, it is assumed that a compound molecule is formed for a short time. The compound system, PT, would have a positive energy in the center of mass frame. Then the probability or the cross section for any channel is calculated by calculating the continuum states of the combined system. One possibility is the ejection of an inner shell electron of any two components of the molecule AB. The inner shell vacancies

are subject to be filled up by electrons from the higher shell and therefore a characteristic X-ray or an Auger electron is emitted. ***I believe this makes SIM a useful tool, if stripped ions are used. Because otherwise the secondary electrons are being emitted by the projectile and therefore reduce the quality of information deduced from the target.***

This method is elaborate and cannot easily be used in applications. A more straightforward treatment of the scattering is possible on the basis of the so-called transport cross section in the low energy region of the projectile. Lindhard and Scharff[179] arrived at:

$$S_e = \frac{4e^2 a_0}{\varepsilon_0} \frac{Z_1^{7/6} Z_2}{\left(Z_1^{2/3} + Z_2^{2/3}\right)^{3/2}} \frac{E_0}{R_y}, \qquad (5,11)$$

for the stopping power, where interaction of ion with the electrons of the target is taken into account.

A general remark is needed in the context of the angular distribution of the secondary electrons generated in ion-atom collisions. In contrast with the electron-atom interaction where secondary electrons were favored close to perpendicular to the primary electron incidence, this is not the case for the ion-atom interaction. As shown in Figure 5-11 and Figure 5-12, the secondary electrons generated in the forward and backward direction have higher probability or cross section as compared with the normal to the incoming beam. As the energy of primary ion increase, the tendency for secondary electron production increases as compared with other directions[173].

5.5. Ion-Solid Interaction

As discussed earlier, the interaction of fast ions with a solid may occur via collisions with the screened nucleus, and collisions with the bound electrons or the interstitial electrons of a solid. The former is described in the context of a potential scattering specifically designed for the problem to include the screening, whereas the interaction with individual electrons is governed by the Coulomb potential. Classically, the trajectory method developed by Gryzinski[97] has been assumed. The validity of the classical scattering problem is limited by the principle of uncertainty, which is formalized under the Bohr Criterion. In the quantum-mechanical picture, the incident particle is represented by a plane wave and therefore it is similar to the diffraction of waves.

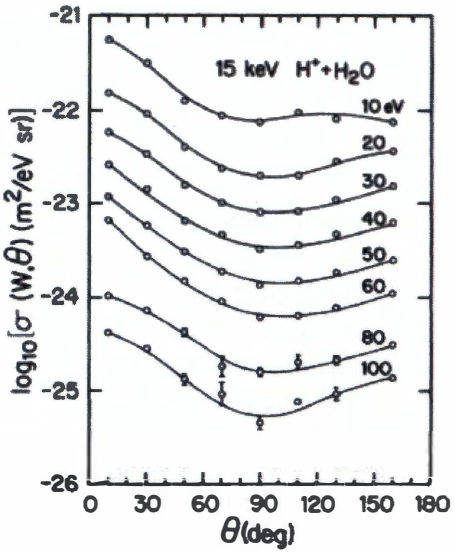


Figure 5-11: Doubly differential cross sections for secondary electrons by 15-keV protons from water vapor as a function of angle of ejection for various ejection energies. Error bars on some data points show the error due to statistical fluctuations in the count.

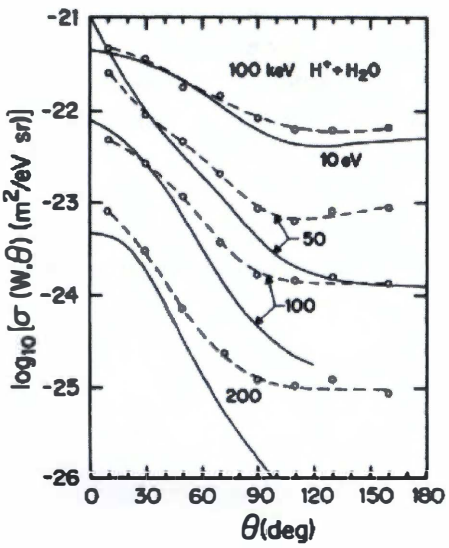


Figure 5-12: Doubly differential cross sections for secondary electrons by 150 keV protons from water vapor as a function of ejection energy for various angles of ejection.

5.5.1. Stopping of Ions

When travelling along a path x through matter, an ion will continuously lose energy due to the interaction with electrons and screened nuclei. The energy loss per unit path length is denoted as "stopping power", $(-dE/dx)$. Often, the stopping is normalised to the atomic density n (or mass density ρ) of the substance, resulting in the "stopping cross section", $(-dE/ndx)$. Although a correlation is expected between the collisions with screened nuclei and the collisions with the electrons, it is assumed that the stoping power due to the "nuclear" or "elastic" interaction, S_n, is independent of the stopping power due to the "electronic" or "inelastic" interaction, S_e, for simplicity. Therefore, the total stopping, S_{tot} is expressed linearly in terms of the nuclear and electronic stopping power as

$$S_{tot} = S_n + S_e . \tag{5,12}$$

In addition to the change in energy, the electronic interaction of an ion passing through matter results in charge changing as a result of collisions and therefore, the actual charge state of a impinging ion continually fluctuates as determined by a balance between electron loss and charge transfer. The average charge of the ion depends on its velocity and one can define an "effective" charge, Z_1^{eff}. The effective charge of the ion is quickly established (typically within some nm) when an ion of arbitrary charge state impinges onto a solid surface. The very low energy ion becomes neutral and therefore, the atomic electrons interact only with the electrons of the solid as the electron loss mechanism has low cross section. At higher velocities, electron loss dominates, so that the ions become fully stripped with $Z_1^{eff} = Z_1$ at sufficiently high energy.

The stopping power could be determined under the first Born approximation described in chapter 3, for high energy ions incident on atoms as:

$$S_e = \frac{2\pi e^2}{(4\pi\varepsilon_0)^2}\frac{Z_1^2 Z_2}{E_0}\log\left(4E_0/\langle I\rangle\right) \tag{5,13}$$

, where $\langle I\rangle$ is the average ionization energy of the target. This average ionization energy is hard to calculate, but roughly can be shown to be proportional to the charge of the atomic nucleus, Z_2. This will add to the Z_1 and Z_2 dependence of the electronic stopping power of ion.

As seen above, the electronic stopping can be reasonably well described in the limits of high and low energies. For the intermediate regime, where nether of these approximations are valid the calculations are very complex, in particular due to electron loss and charge transfer. As discussed for the electron-matter interaction, a "hybrid" formalism can be obtained by assuming the relation:

$$\frac{1}{S_e} = \frac{1}{S_e^{low}} + \frac{1}{S_e^{high}} \tag{5,14}$$

to be valid, where S_e^{low} and S_e^{high} are the low and high energy limit for the electronic stopping power. In Figure 5-13 and Figure 5-14 the stopping power is plotted against the primary ion energy for a light ion on a heavy target and an ion on a target of comparable mass, respectively, showing the validity of the models discussed.

The nuclear stopping power, S_n, is treated with an elastic model. The most important point is how to include the screened charge of the nucleus. The effect of charge screening was discussed in section 3.4 in the context of elastic scattering of electrons from atoms. The same idea is valid here and care should be taken in the type of charge distribution assumed. Assuming the Thomas-Fermi screening function with a range of r_0, based on an approximation by Lindhard, Nielsen and Scharff (LNS)[180-182] derived an analytical approximation to the nuclear stopping power which is simplified as:

$$S_n = 4\pi r_0^2 \mu \frac{3.44 E_0^{1/2} \log(E_0 + 2.718)}{1 + 6.35 E_0^{1/2} + E_0 (6.882 E_0^{1/2} - 1.708)} \tag{5,15}$$

, where μ is the reduced mass of the target atom and the projectile, and E_0 is the primary projectile energy. Equation (5,15) shows that nuclear stopping, like electronic stopping, is proportional to the ion velocity in the limit of low velocity. At very high energy, it is proportional to $E_0^{-1} \log E_0$, which is just the energy scaling of electronic stopping. Figure 5-15 shows the universal nuclear stopping together with these limits.

Figure 5-16 and Figure 5-17 show the total stopping cross section defined by equation (5,12). For heavier ions, nuclear stopping dominates at low energy and becomes negligible in the limit of high energy. This is a further justification of the independent treatment of electronic and nuclear interaction. For very light ions, nuclear stopping can be neglected in a broad range of energies.

The stopping power of ions rises with energy and reaches a maximum depending on the charge of the ion and the target. A comparative picture is shown in Figure 5-18 for the lower energy region and usually they are an order of magnitude higher than comparable energy. The stopping power of ions rises with energy because it depends on ion velocity and is at least an order of magnitude higher than for comparable electron impacts.

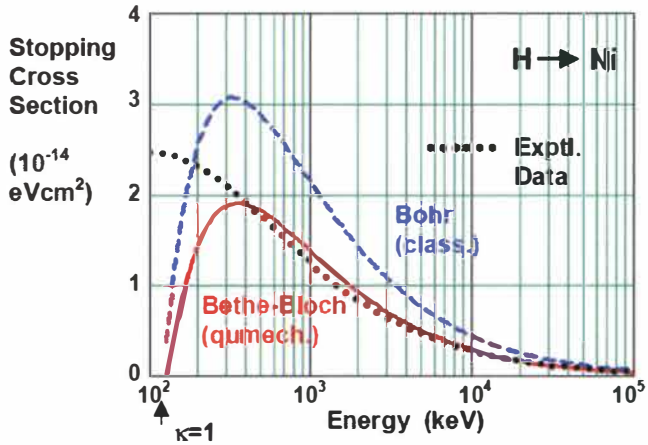


Figure 5-13: High-energy electronic stopping of a proton in Ni from quantum mechanical (Bathe-Bloch) and classical (Bohr) calculations. The predictions are compared to semi-empirical data from the SRIM-2000 package . The energy of the Bohr Criterion is indicated at the lower left.

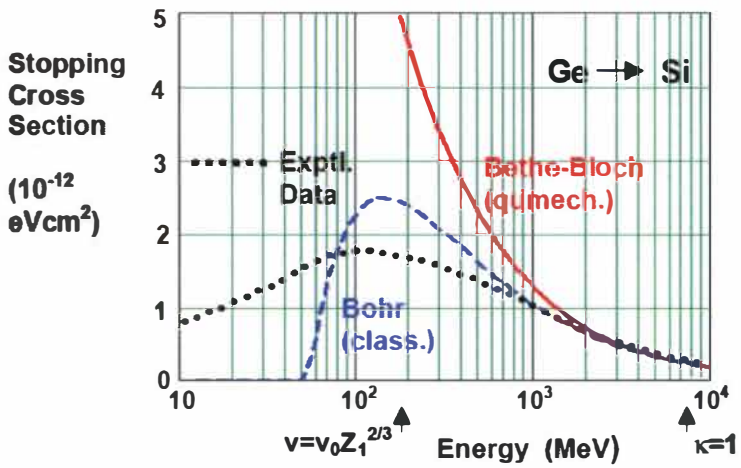


Figure 5-14: As in Figure 5-13, but for Ge ions colliding with Si. Note the different scales used. The energy of the Bohr Criterion is indicated at the lower left.

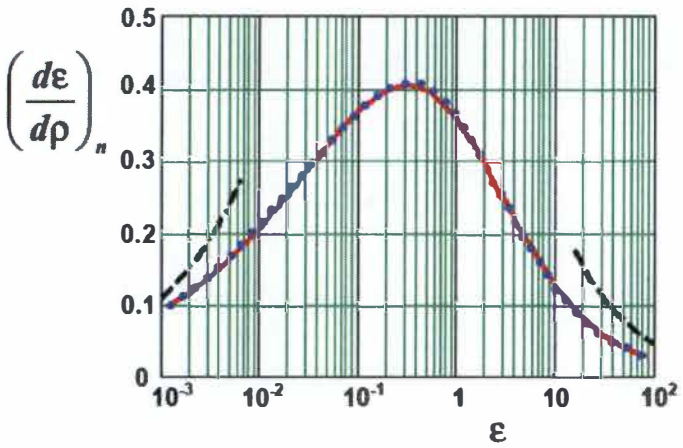


Figure 5-15: Nuclear stopping power as function of the reduced energy for Thomas-Fermi screening according to an exact calculation based on Fermi-Dirac screening function (solid line) and the Matsunami approximation (dotted line), with high- and low-energy limits (dashed-dotted and dashed line, respectively). The x- and y- axis are represented in a relative scale.

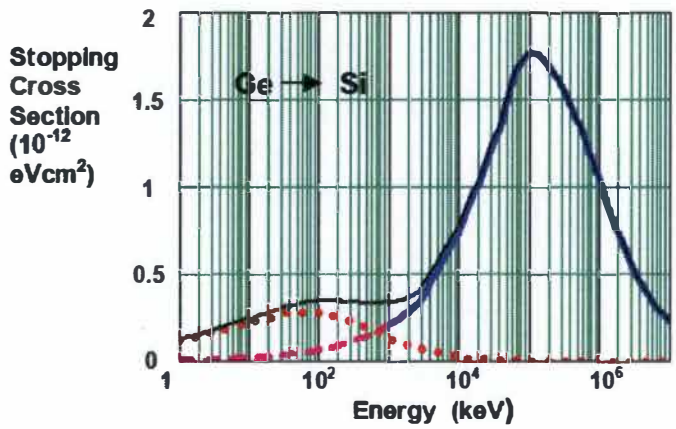


Figure 5-16: Nuclear (dotted line), electronic (SRIM package, solid line, and equation (5,11), corrected by fitting factor of 1.2, dashed line) and total stopping (thin solid line) cross section versus ion energy, for germanium in silicon.

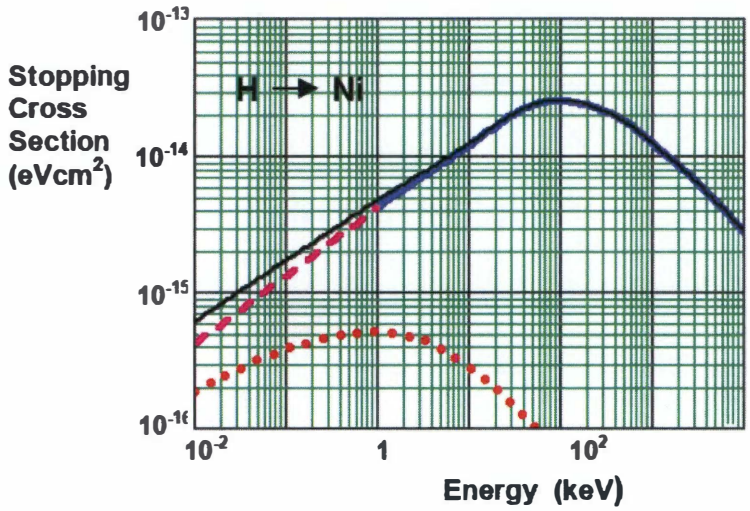


Figure 5-17: As Figure 5-16, but for hydrogen in nickel. The Lindhard-Scharff electronic stopping has been corrected by a fitting factor of 1.3. Note the different scales.

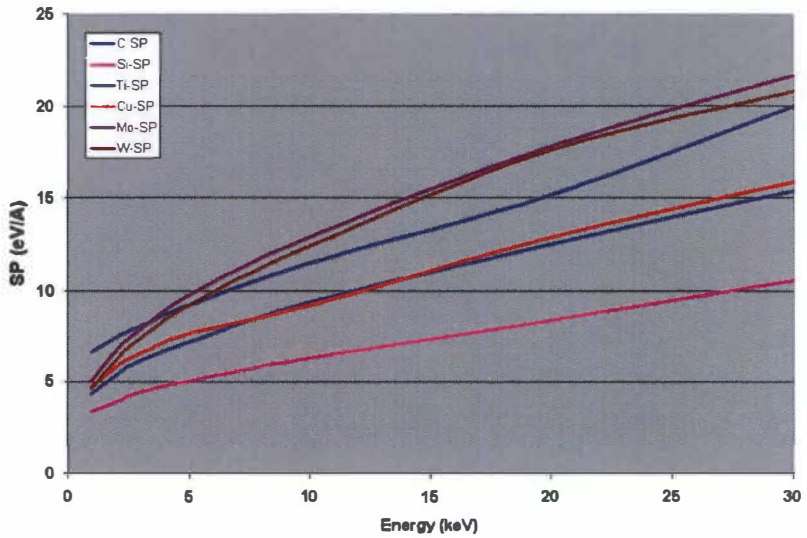


Figure 5-18: The stopping power of He^+ ions on different solids as a function of ion energy which is calculated by SRIM-2000 package.

5.5.2. Key Data to Compare Between Secondary Electrons Generated by an Electron Bean and an Ion Beam

In this section secondary electrons generated in ion-target collisions will be referred as iSE. In contrast secondary electrons generated in the electron-target interactions will be referred as eSE. Z_1 and Z_2 are defined as the atomic number of the incident ion (projectile ion) and the target respectively.

5.5.2.1. Topographic Secondary ElectronYield Behavior

Figure 5-19 presents a topographical yield curve for both eSE and iSE in terms of the incident angle. Although the shape of the curves for each SE is different, the magnitude of variation is similar. As expected the eSE at higher incident angles saturates as the iSE does not. The iSE yield increases as the incident angle rises. iSE signals are less noisy (cleaner) than the eSE ones for the same amount of beam current. That is because the amount of SE induced by the ion beam is significantly higher than the SE ones induced by the electron beam (Figure 5-18). More details on this will be covered in the following section.

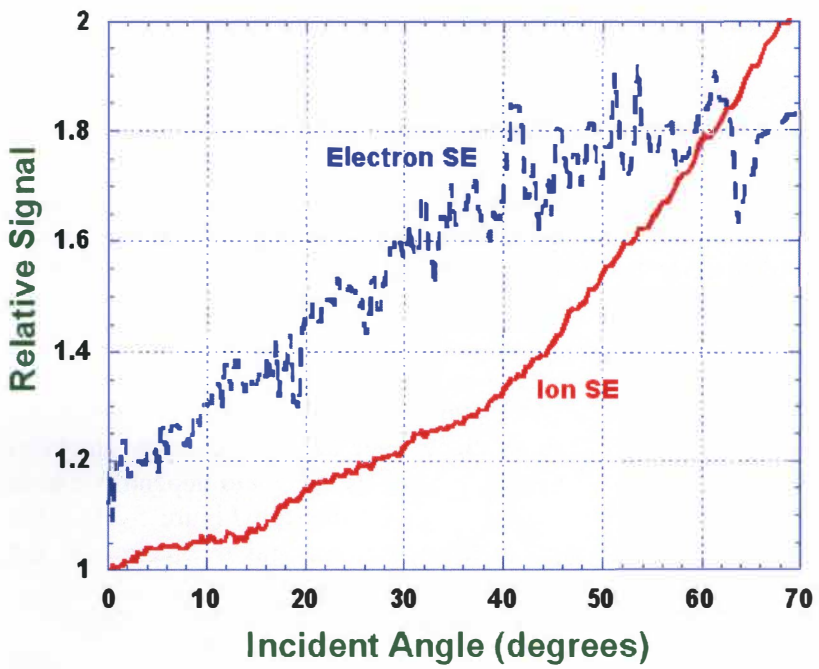


Figure 5-19: Topographic secondary electron (SE) yield data for 3 keV Ar+ ions and electrons. In both cases the beam current was the same.

5.5.2.2. iSE Versus eSE Yield for Different Samples and Beam Energies

There are two laws for the SE production. The first one is that the SE generation is proportional to the stopping power of the incident beam in the target. The second is that the SE escape is described by the diffusion equation (Salow 1942). These two laws are presented in

$$\text{SE generation rate} \propto \frac{dE}{ds}$$
$$\text{SE escape at } z \propto \exp(-\frac{z}{\lambda}) \qquad (5,16)$$

iSE and eSE generation rates will differ in magnitude and vary with the incident beam energy, target material, and the ion type.

As explained in section 5.5.1, the stopping power of ions rises with energy because it depends on ion velocity and is at least an order of magnitude higher than for comparable electron impacts (Figure 5-18). Figure 5-20 is a result of (5,16) and the stopping power properties of ion beams. The iSE yield does not reach a maximum until energies of the order of 100 keV. Also as the cross section is velocity dependent there should be a kinetic limit in the stopping power (Figure 5-18) and iSE yield curve (Figure 5-20).Typically SE yields are greater than one per ion.

Figure 5-21 shows an ion SE yield vs Z_2 (target) for 30 keV He^+ and Ar^+ incident ion beams. Figure 5-22 adds the stopping power (SP) to Figure 5-21.

There is a general correlation between SP and iSE yield for He^+ generation but the Ar^+ data is anomalous Figure 5-22. But without correcting for the escape probability variation the agreement is very poor. Much more data are needed. Ion SE yield vs Z_1 (projectile) for solid Ag, C, Cr, and Al targets. 30keV ion -beam has been used.

The variation of ion-induced SE (iSE) yield with the atomic number of the target is almost as complicated as the case for electron-generated secondary electrons and the variation is much larger. But the magnitude of the SE yield depends on both Z_1 (the projectile ion) and Z_2 (the target) (Figure 5-20 through Figure 5-23). This variation can be attributed to the change in the ion range and to changes in the stopping power, as a function of Z_1. Therefore the similarities between eSE and iSE images of an object are only visible and not fundamental. Key aspects of SE image formations including topographic behavior, beam penetration, sensitivity to target chemistry, and beam energy are very different in the two ion and electron beam cases

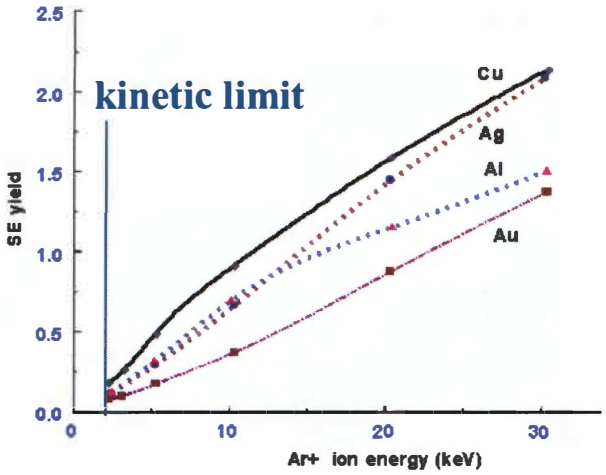


Figure 5-20: iSE Yield Curve of Ar beam at different energies on Cu, Ag, Al, and Au solid targets.

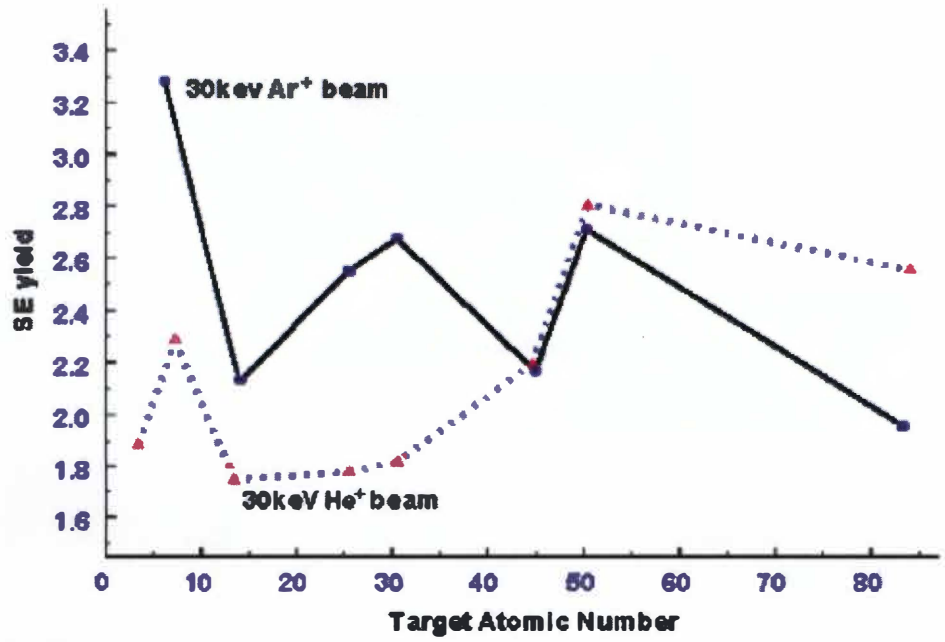


Figure 5-21: Ion SE yield vs Z_2 (target) for 30 keV He^+ and Ar^+ incident ion beams.

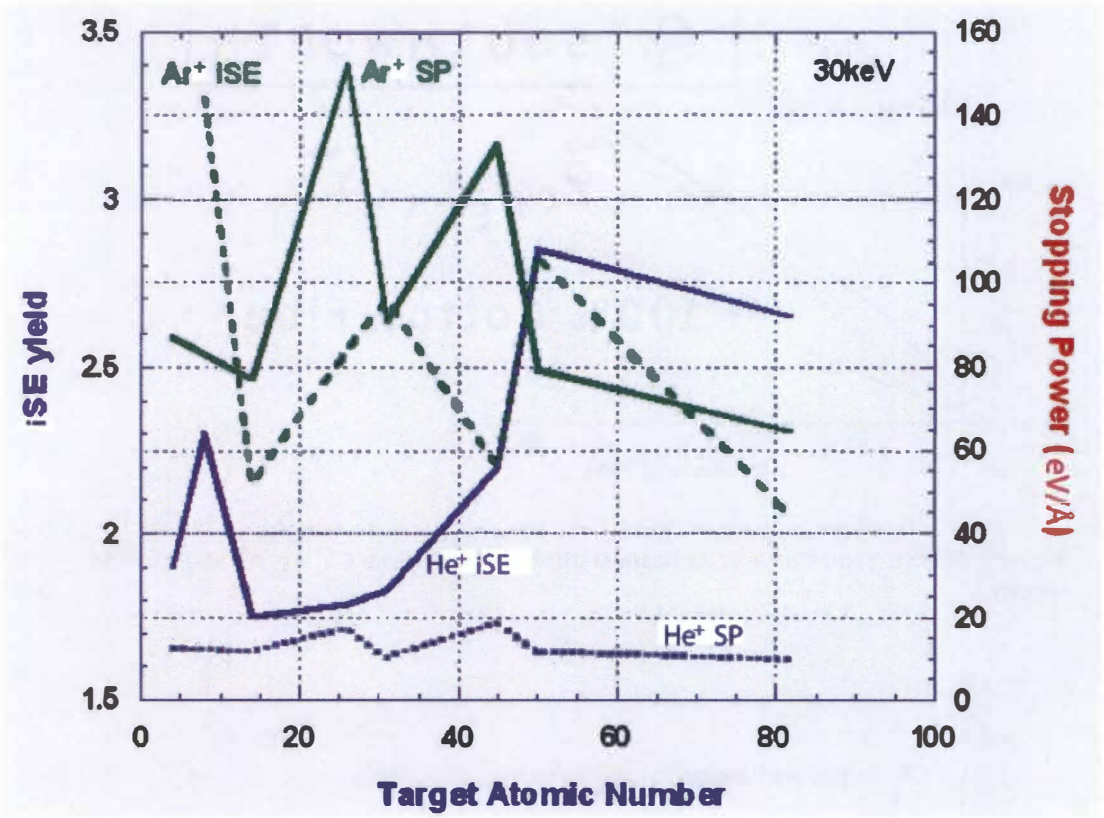


Figure 5-22: Compare iSE and SP as a function of Z1 and Z2.

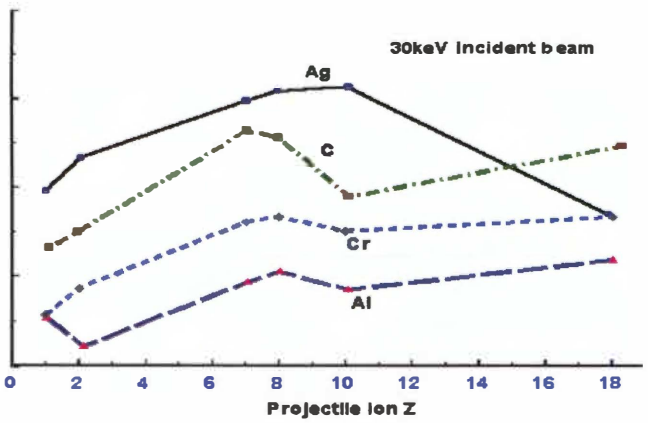


Figure 5-23: Ion SE yield vs Z_1 (projectile) for solid Ag, C, Cr, and Al targets. 30keV ion -beam has been used.

5.5.2.3. Charging by Electrons and Ions

With regards to the target charging, electron beams have E_1 and E_2 crossovers and both positive and negative charging regimes. For all feasible ion energies, samples will charge positive because of the high iSE yield and the injection of positively charged ions. Figure 5-24, shows the total SE yield data for quartz (SiO_2). The black solid line represents the eSE, and the blue dashed lines represents the iSE produced by an He^+ ion beam.

Since iSE yield is strongly dependent on surface potential, it can be expected that this effect will be a dominant one in the CD metrology and ion beam lithography of resists and insulators.

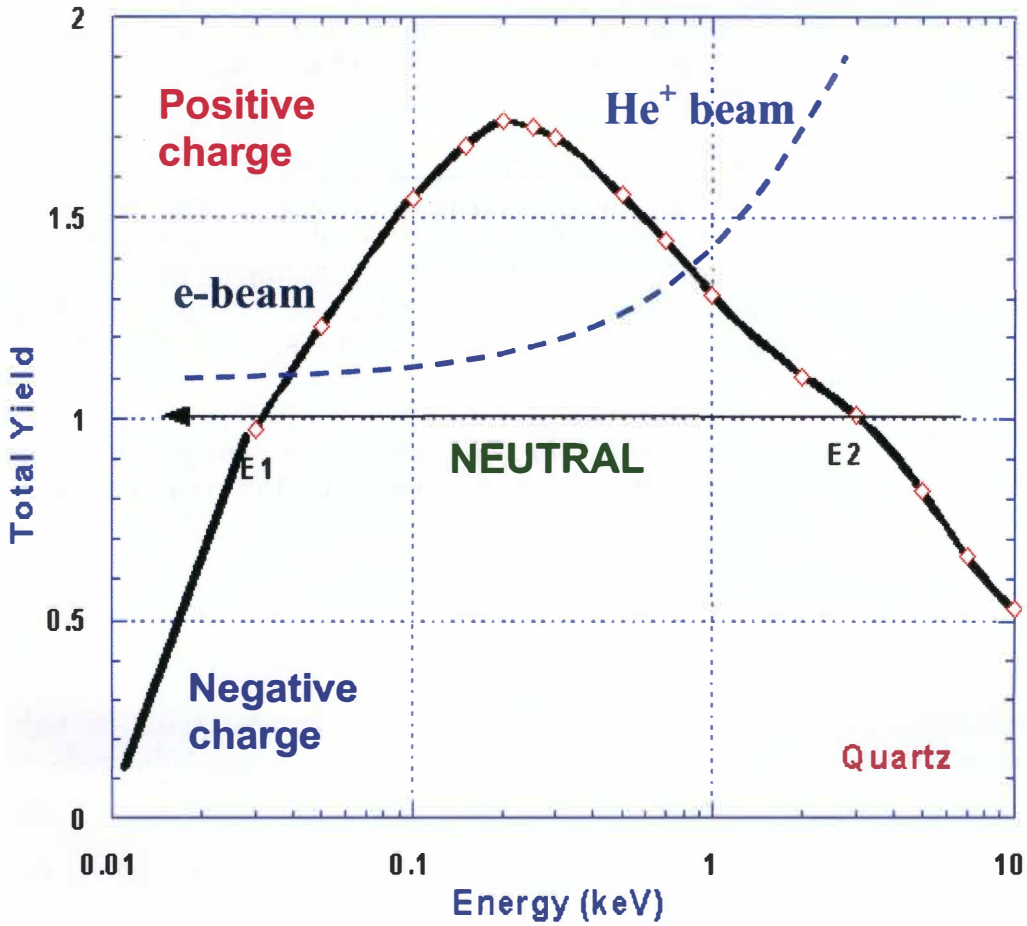


Figure 5-24: Total SE yield data for quartz (SiO_2). The black solid line represents the eSE and the blue dashed lines represents the iSE produced by an He^+ ion beam.

5.5.2.4. The Spectrum of Electron Signals Produced by Electron and Ion Beams[‡]

The objective of this section is the following question. Are the ion SE signals the same as the electron SE signals and why? To answer this quaetion we have used a PHI Model 680 Auger Electron Spectroscopy (AES)/Scanning Auger Microscopy (SAM), which is based upon a field emission electron source and a cylindrical mirror analyzer (CMA). The target was Fe and different electron beam energies were used. Figure 5-25 and Figure 5-26 are the Fe spectrum using a 1 keV e-beam. Figure 5-26 is the magnified SE portion of Figure 5-25 and it shows that the eSE peak is at ~6eV with a FWHN width of 15 eV. The dynamic range of this spectrum from 0 to 50 eV is of the order of 7. It is a diffferent case with Figure 5-27, which presents Fe spectrums with different Ar^+ ion beam energies. In Figure 5-27 the iSE peak energy is vary narrow (a few eV) and the dynamic range from 0 to 50 eV is of the order of 10^5. It does not have the long tail, as the SE energy increases, as it was seen for the e-beam case and the spectrum tail almost plunges to the recording noise level of the system. Therefore the same diffusion model for an ion beam is different than the case using an e-beam.

This could be explained by the following. SE generated by the e-beam is through many mechanisms such as FSE, plasmon decay, and ionization processes. For the same energy, ion velocity compare to electron velocity is slow and ion's interaction cross sections are velocity dependent. Main mechanism for the generation of iSE is proposed to be the formation of a short life-time molecular complexe followed by an Auger-type decay process. Therefore the SE emission does not continue to decrease.

For an electron beam, the backscattered electrons have energies up to the incident electron beam. This is not the case for an ion beam. The maximum energy they can transfer to an electron is:

$$E_{el} \approx 4\left(\frac{M_{ion}}{m_{el}}\right)E_{ion} \qquad (5,17)$$

, which is only a few tens of eV for a He^+ ion with keV energy. As a result, the high energy extension of the emission spectrum is limited and the intensity falls rapidly as E_{el} increases.

Table 5-1 summerizes an optimization between SEM and SIM as the electron/ion beam energy increases.

[‡] The experiments mentioned in this section were not performed by the author. The author was responsible for the physical explanations and interpretations of the experimental results.

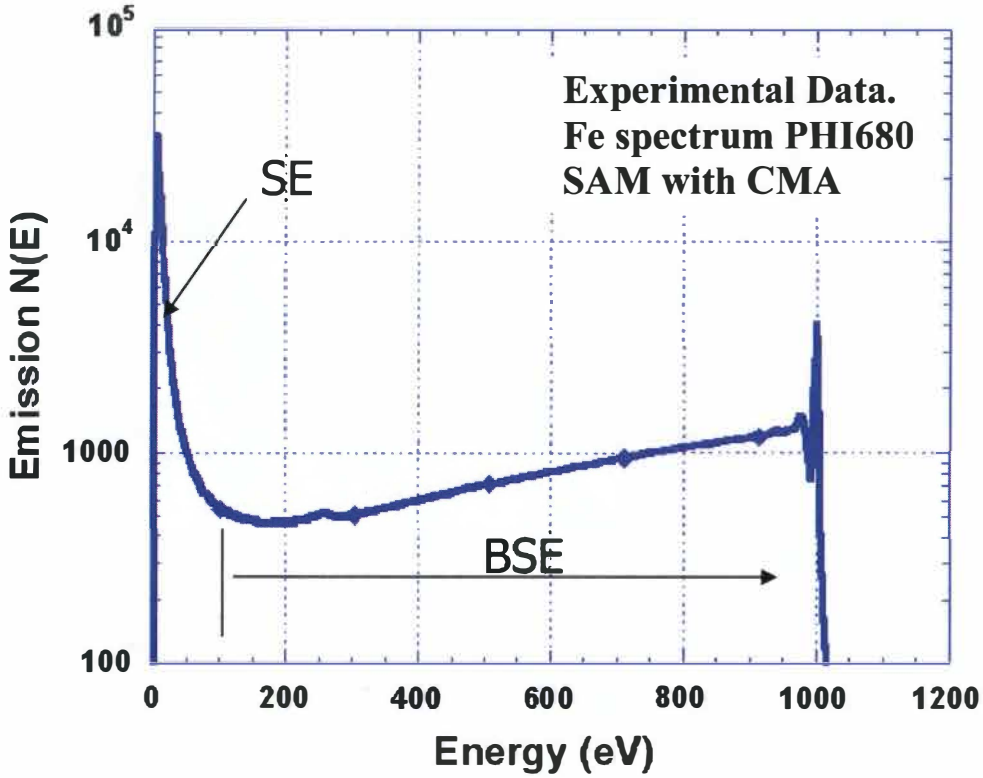


Figure 5-25: N(E) Eletron emission spectrum Fe at 1keV e-beam using a PHI680 SAM with CMA.

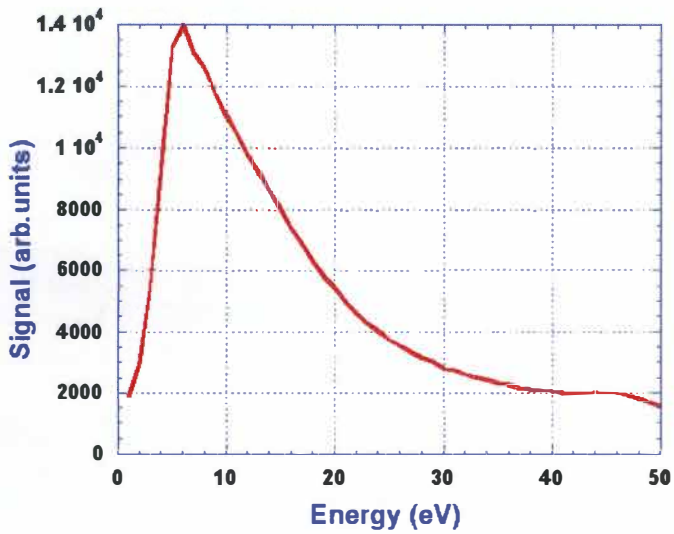


Figure 5-26: eSE spectrum – Fe at 1keV. The peak SE emission energy is ~6eV depending on surface state. The FWHM width of the SE peak is about 15eV. Dynamic range 0-50eV is ~ 7

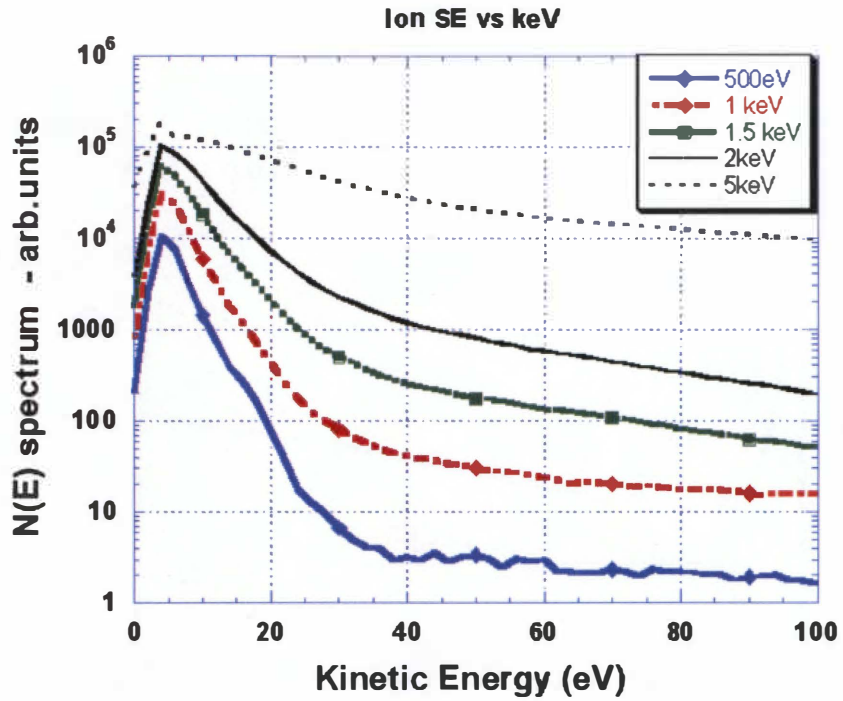


Figure 5-27: iSE spectra from Fe Ar+ vs keV. SE peak energy similar to eSE but peak is very narrow (few eV) Dynamic range from 0 to 50eV is ~ 10^5.

Table 5-1: Comparison between SEM and SIM as the electron/ion beam energy increases.

	SEM	SIM
SE Yield	falls	rises
BSE Yield	constant	BSI yield falls
Gun brightness	rises	rises
Signal	constant or falls	rises
Beam Range	rises	rises slowly
SE2 Yield	rises	disappears
Contrast	degrades	enhanced

5.6. X-ray Fluorescence in an Ion-Atom Interaction

5.6.1. Bremsstrahlung

It is a well known classical phenomenon that an accelerating charged particle emits electromagnetic radiation (photons). If a charged particle of charge q, with velocity $\mathbf{v}$ and the acceleration $\dot{\mathbf{v}}$ radiates, by the relativistic form of the Larmor formula:

$$P = \frac{2q^2\gamma^6}{3c^3}\left[\dot{\mathbf{v}}^2 - \frac{1}{c^2}(\mathbf{v}\times\dot{\mathbf{v}})^2\right] \tag{5,18}$$

, where c is the speed of light and $\gamma = \sqrt{1-\mathbf{v}^2/\mathbf{c}^2}$. The charged particle will be accelerated by a positive or negative value parallel to its speed, where only the first term in the bracket is non-zero. It could also be accelerated by changing its direction, where the second term in the bracket will be important. This later motion in the interaction of charged particles with matter is observed mostly for electron impact and high energy ion impact. The high energy ions will produce x-rays, which is the basis of a spectroscopic method called Particle Induced X-ray Emission, PIXE.
In the case that the ion is accelerated in the same direction as the velocity, the second term in equation (5,18) is simplified as:

$$P = \frac{2q^2\gamma^6}{3c^3}\dot{\mathbf{v}}^2 . \tag{5,19}$$

This later form could easily be written in terms of the stopping power as:

$$P = \frac{2q^2}{3M^2c^3}\left(\frac{dE}{dx}\right)^2 \tag{5,20}$$

, where M is the mass of the projectile and $-dE/dx$ is the stopping power of the target.

5.6.2. Characteristic X-rays

As was discussed earlier, ion-solid interactions result in inner-shell vacancies. The inner-shell vacancies are filled by electrons emitting either Auger electrons or X-

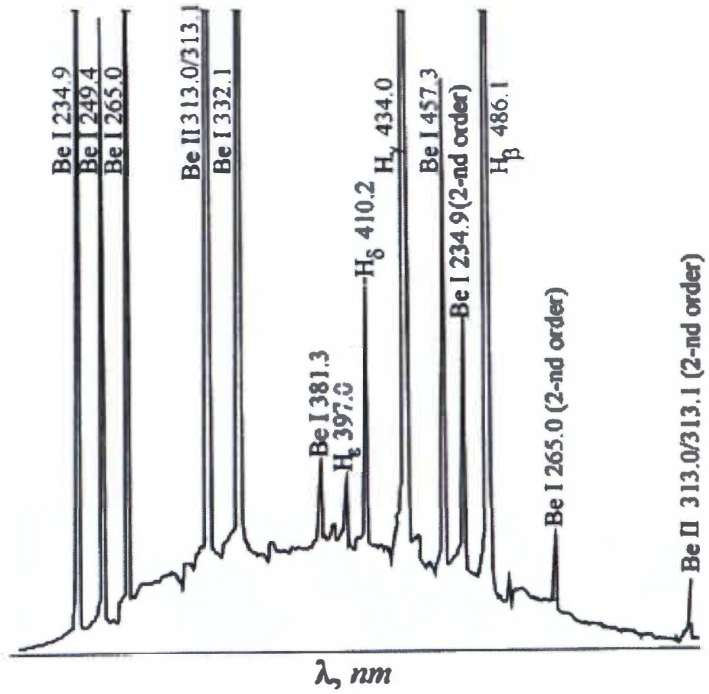


Figure 5-28: X-ray fluorescence emission in the interaction of 15 keV ions with a Be surface. The target was bombarded at an angle of 60° with respect to the normal. (After, Sharodi, Yu.A. Bandurin and Pop)

ray fluorescence. The X-rays emitted could be characterized as an electron-hole recombination process. An example is presented in Figure 5-28, where the Be surface is bombarded by 15 keV H_2^+ ions[183]. The characteristic lines from Be and H_2^+ can be distinguished.

One can also observe a broad background in the X-ray spectrum in Figure 5-29 while it is not expected to have a Bremsstrahlung type continuum in for ions at 15keV. This can be explained through an electron-hole recombination process of the solid, where electrons are in continuum states.

Characteristic x-ray emission may also result from ion/solid interactions and is the basis for the well-known, high-energy analysis technique referred to as particle-induced x-ray emission (PIXE)[184]. X-rays produced from the PIXE technique are typically collected using conventional Si(Li) energy-dispersive spectrometers (EDS). Characteristic x-rays may be emitted from either bombardment by MeV protons or heavy ions of a few keV[185]. As an example, the x-ray yield of the carbon *K* emission has been determined for H^+, He^+, C^+, O^+, Ne^+, Kr^+, and Xe^+ from 20–80 keV[186].

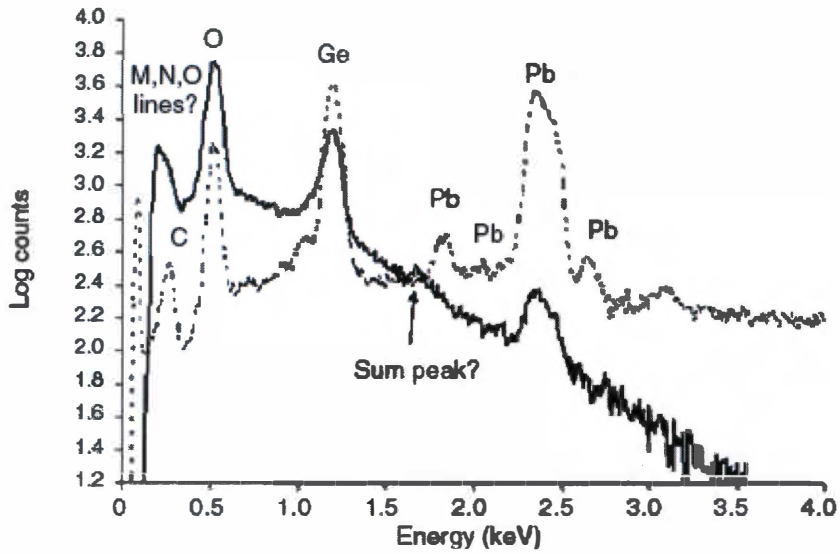


Figure 5-29: X-ray energy-dispersive spectroscopy spectra acquired for 100's from standard K968 using a 30 keV, 20 nA Ga^+ beam with a focused ion beam (solid line) and a 15 keV electron beam with a scanning electron microscope (dashed line) as the primary source[187]

5.7. Secondary Ion Emission

Another phenomenon that is important in ion-solid interactions is secondary ion emission in the collision of ions with solids. This, in principal, is a solid state analogue to the break up channel presented in equation (5,2), and also known as sputtering in solids. Low energy secondary ions are emitted during a collision of ions with solids. This is investigated thoroughly and is the basis for a spectroscopic analysis method called SIMS. Sputtering is a very important issue for low energy ion-solid interactions.

Chapter 6

6. Experimental and Simulation Techniques

6.1. Experiment

Table 6-1 shows the processes that have been performed in this thesis' experiments.

6.1.1. Low Voltage EBL Experiment Setup

To achieve a low voltage e-beam, a SEM was used. The majority of EBL machines function at energies higher than 5 keV. A Hitachi S-4300 SE/N was the main exposure tool in this project. As opposed to a dedicated electron beam writer, which is in general a closed system, this SEM allows easy access for modifications and innovations. This is very important, particularly for a laboratory interested not only in the fabrication and measurement of nanodevices, but also in the development of technologies for innovative devices that involve more complex and precise steps of nanolithography. However the SEM generally has a limited speed of beam deflection, so it is only possible to use it as a lithography tool when writing speed and throughput are not important issues. In addition the scanning microscope is optimized for operation in the center of the field of view because it is principally used for high resolution imaging, which implies that a small scanning field is essential. For this

Table 6-1: Experiment Flowchart.



reason all of the writing was done in the center of the field and the stage was locked during the writing process to minimize vibration and drift. In an industrial apparatus, particular care is put into lowering stage mechanical vibration, and minimizing lens distortion on large areas and temperature control of the stage prevents distortions due to thermal drift of the optics in long exposure works.

For some of the work described here a, Leo 1525 field emission SEM was used, as well. For low energies this SEM, in contrast to S-4300 SE/N, generates the electron beam at a high energy but then decelerates the electrons just before they impact the sample. This procedure results in enhanced electron-optical performance at the lowest energies as compared to the more conventional optics of the S4300 SE/N. Because the Leo 1525 uses a cold field emitter the long term stability of the beam current was worse than that available from the Schottky emitter on the Hitachi SEM. Both instruments displayed some sensitivity to external electro-magnetic interference but the resultant beam deflections were not significant enough to affect the lithography.

The landing energy of the electron beam on the specimen is often different from the value selected by the choice of accelerating voltage because of charge build-up in the sample. The SEM software controls on the market are not fully capable of fixing this problem. In reality, as the sample charges under the electron beam bombardment, this energy difference becomes more complicated. To overcome this issue, before the wafer was inserted into the SEM stage, the stage was connected to a DC voltage supply. This solution was possible through a BNC connector that is connected to the sample stage inside the SEM chamber and voltage (V_{bias}) can be applied to it from outside the chamber. At the same working distance (WD) that the writing is planned, a highly conductive sample was imaged. As the power supply's voltage, V_{bias}, is increased, the landing energy of the incident electron, E_L, decreases until E_L becomes zero (Figure 6-1). At this point the contrast of the SEM image of the sample compare to when the voltage was not applied to the stage has inverted.

The incident current was measured with a Faraday cup mounted on a sample stage so that the beam dose could be precisely controlled. Patterning was controlled by an external pattern generator constructed for this purpose. External electron-magnetic interference with the beam was minimized by using a short working distance (~ 4 mm).

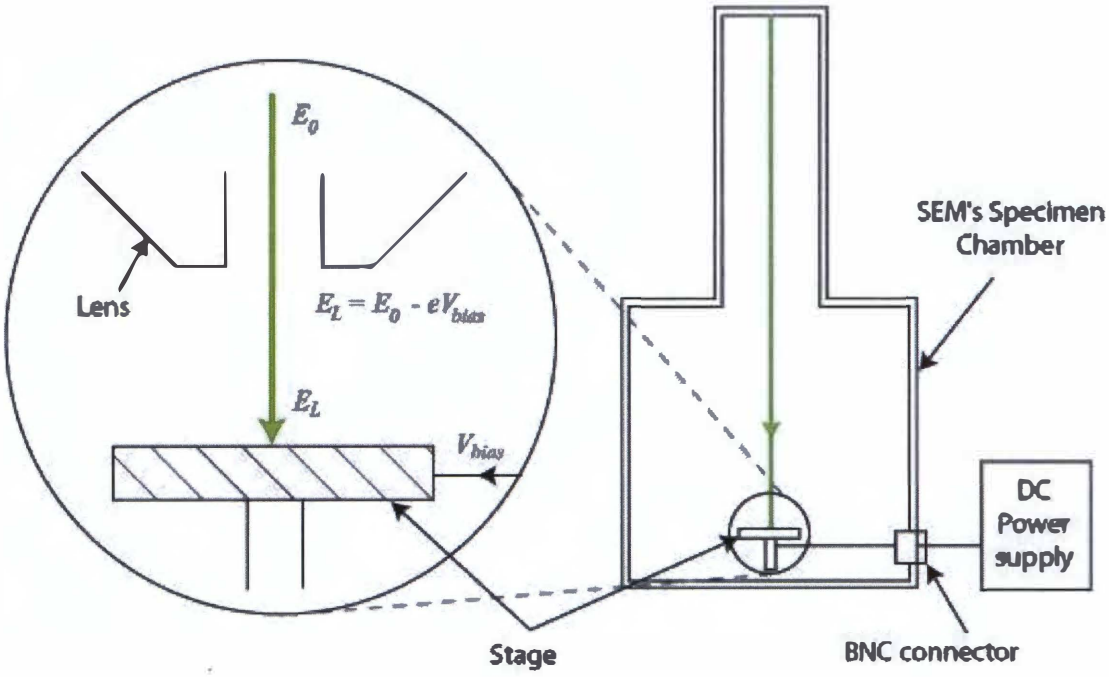


Figure 6-1: Schematics of the experimental set up, known as cathode lens mode, to measure the true landing energy of the electron beam on the specimen.

6.1.1.1. Image Input

The system was designed to accept any size of raster image. Raster, pixel images, or bitmaps are broke down to rectangular pixels in contrast to vector images. A bitmap is characterized by the width and height of the image in pixels and the number of bits per pixel, which determines the number of colors it can represent (Figure 6-2). Files such as ppm, rgb, gif, and jpg are raster images. The quality of a raster image is determined by the total number of pixels (*resolution*), and the amount of information in each pixel (often called *color depth*). Color depth describes the number of bits used to represent the color of a single pixel in a bitmapped image or video frame buffer. This concept is also known as bits per pixel (bpp), particularly when specified along with the number of bits used. Higher color depth gives a broader range of distinct colors.

Commercial EBL machines are equipped with varying dose capabilities during the writing process. This capability makes it possible to draw gray scale images. Darker pixels are assigned higher doses compare to lighter pixels. During the writing process the dose of the SEM's beam could not be changed, therefore we saved the images as black and white pictures. If the original image was a color or

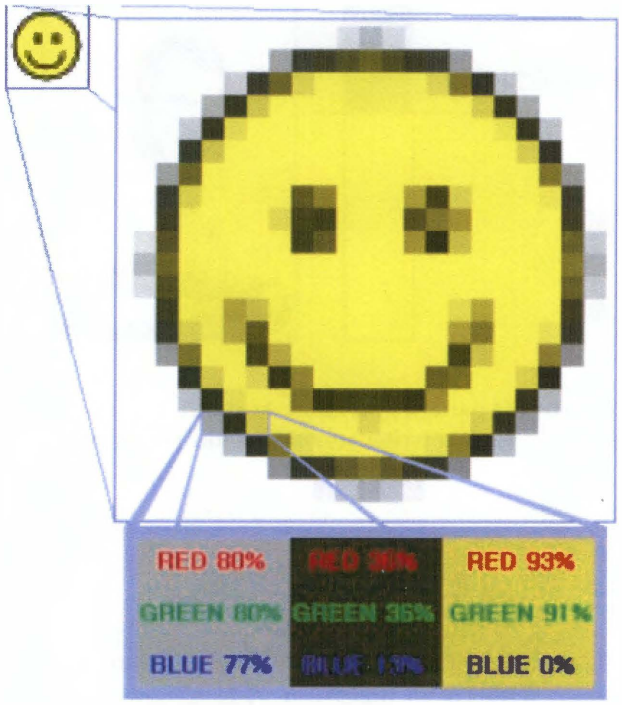


Figure 6-2: Smiley face in the top left corner is an RGB bitmap image. When zoomed in, it might look like the big smiley face to the right. Every square represents a pixel. Three adjacent pixels whose colors are constructed by adding the values for red, green and blue are shown.

gray scale one, depending on the application and how we want the output to be a threshold level is defined. Pixels with color depths equal and above the threshold level are assigned the color black and the rest are assigned the color white Figure 6-3. This sets the exposure threshold in the EBL system and can be done on the majority of design and image software (Photoshop, ImageJ, and…). The raster image is sent to the digitizer.

6.1.1.2. Digitizer

The digitizer was written in Matlab version 6. It reads the black and white raster image and saves the coordinates of the black pixels into a text file. This capability makes the digitizer a versatile program. The text file is read by the pattern generator program that will be explained in the next section.

Depending on the computer's processing speed and the geometry of the pattern, the digitizer can be integrated to the pattern generator program as a subroutine. This will save time and memory space as the coordinates of the black pixels will be simultaneously sent to the Digital Beam Control (DBC).

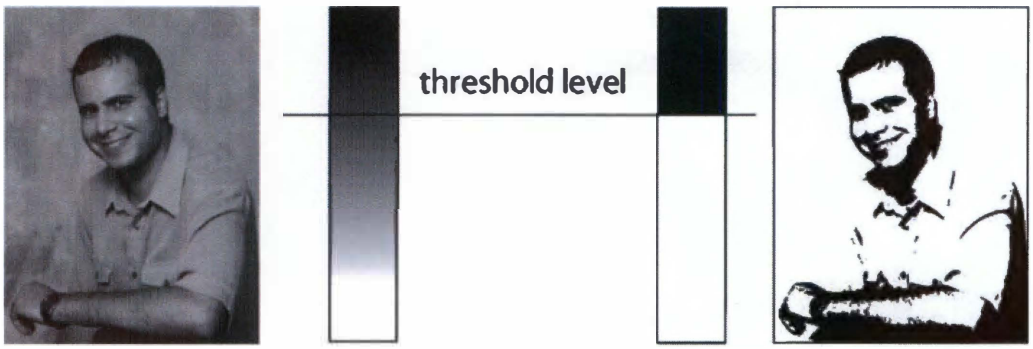


Figure 6-3: The raster image in the left is read by the pattern generator. As shown in this figure, the threshold level is defined and the output of the e-beam writer would look like the right image (only in black and white).

6.1.1.3. Pattern Generator

The pattern generator has been implemented in the LabView environment and uses a commercially available DAC board with 16-bit precision. A LabView program is built of visual instruments (VI), which are platform independent. A major benefit of this generator is that it can perform vector or raster scanning. For example raster writing can be performed on any electron/ion lithography instruments and Focus Ion Beam (FIB) columns. That includes those that do not posses a very high-speed beam blanker (almost all scanning electron microscopes (SEM)). The pattern is fabricated by selectively exposing pixels in the field of view and moving the beam at high speed across pixels that are not to be exposed.

The pattern generator is the intermediate between the digitizer and the DBC on the SEM. Following are read by the pattern generator:

1) Output of the digitizer, that is the coordinates of the black pixels of the raster image.
2) Dwell time.
3) Pixel dimensions of the raster image, Nx and Ny.
4) Pattern dimensions, Lx and Ly.
5) Maximum voltages of the analog output (AO) to the DBC, Vx and Vy.

Numbers 3-5 defines the magnification of the scan generator. Figure 6-4 shows a schematic of the parameters used in both pixel and voltage spaces.

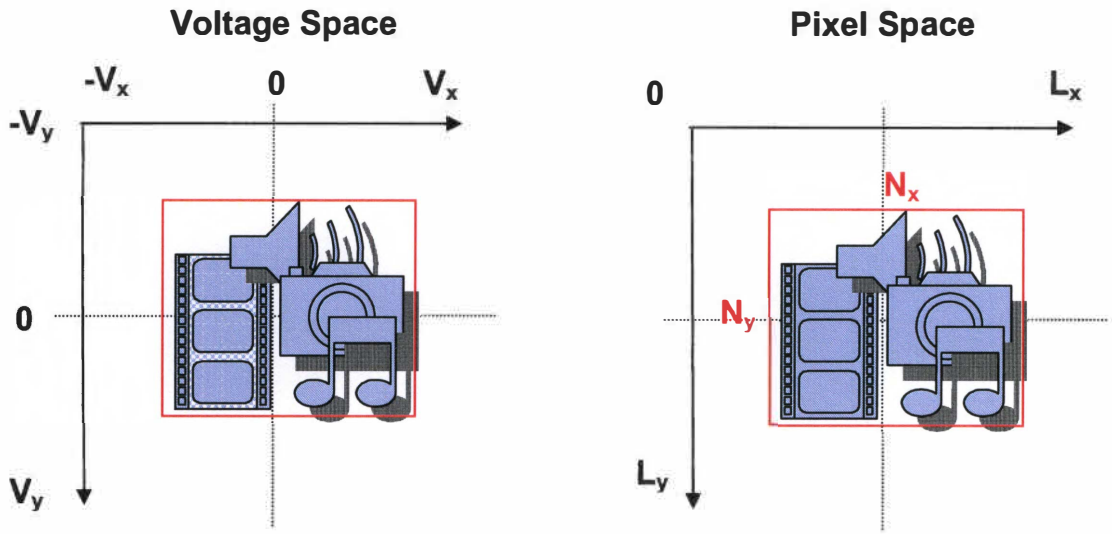


Figure 6-4: Magnification is defined by these parameters: Lx & Ly, dimensions in pixels; $0 < V_x$ & $V_y < 10$, dimensions in volts.

The maximum voltage input to the DBC of the SEM was 10 volts. Figure 6-5(a) shows the AO voltage of the pattern generator to the DBC in the case when the e-beam of the SEM is scanning the field that consists of four parallel scan lines pointing in the positive x direction Figure 6-5(b).

The voltages Vx and Vy take control over the orthogonal X and Y direction through a double deflector arrangement. The deflector allows a normal beam incident over the whole exposed area, telecentric beam path, by fixing a favorable pivot point in the backfocal plane of the upper pole piece of the objective lens.

The maximum deflection of SEM based systems was minimal. Also, the systems were not automatic and usually required a great deal of tweaking by the user in order to achieve the stated resolution. Adjustments such as focusing and stigmation were performed manually by the operator. Any fluctuations of the height of the sample could not be corrected automatically, leading to focus errors.

The maximum scanning rate is limited by the response time of the magnetic deflector coils (100 kHz).

Following is a list of the advantages and properties of our home made pattern generator:

1) It is novel as it has been implemented in the LabView environment (Virtual Instruments (VI's) are platform independent).

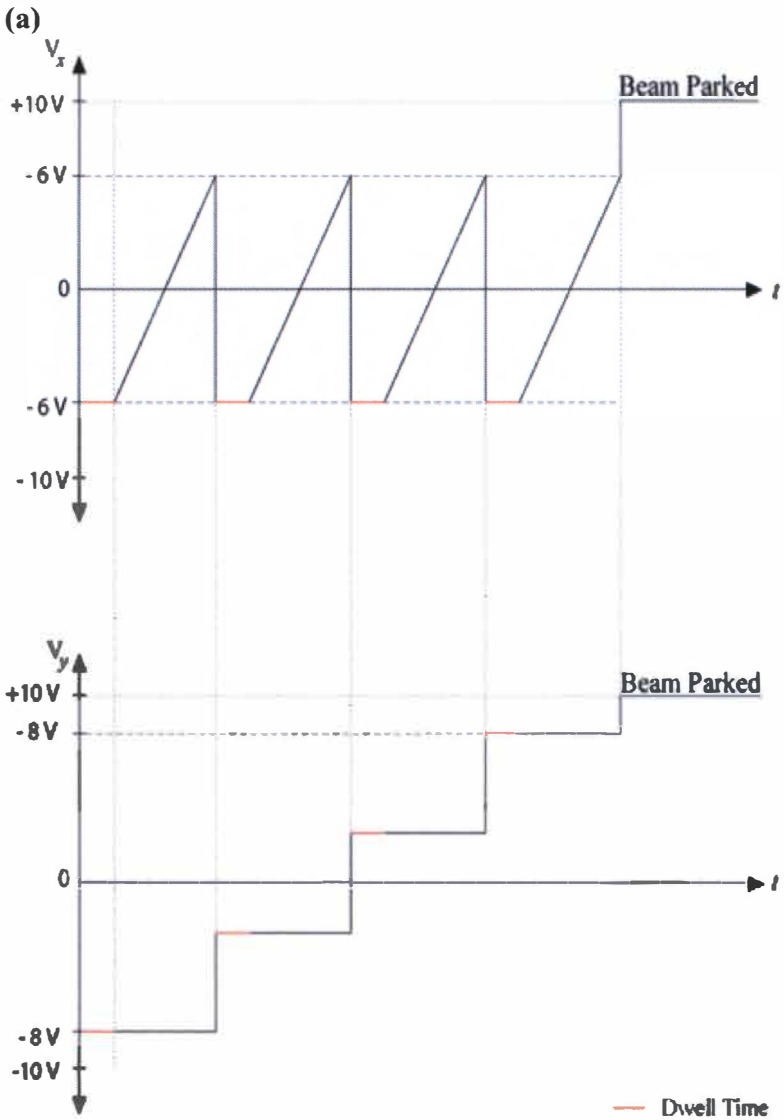


Figure 6-5: (a) Shows the AO voltage of the pattern generator to the DBC in the case when the e-beam of the SEM is scanning the largest field that consists of four parallel scan lines pointing in the positive x direction as shown in part b.

(b)

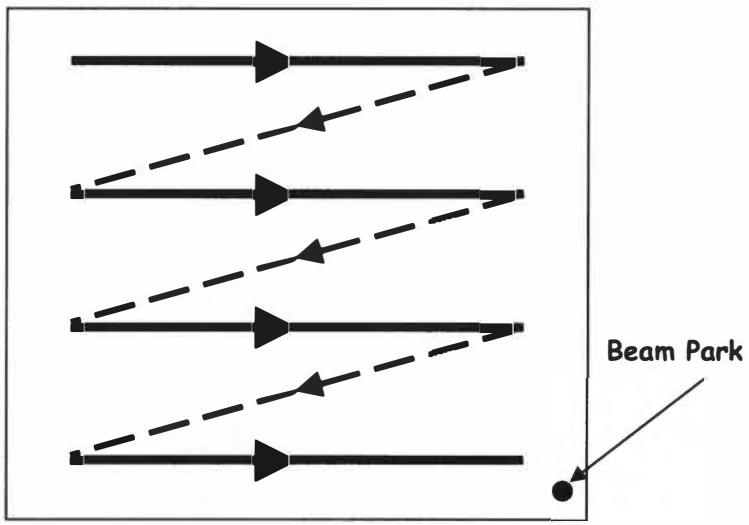


Figure 6-5: Continued

2) Uses a commercially available DAC board with 16-bit precision.

3) It is versatile, being programmable for either Raster or Vector scanning. It can be performed on any electron/ion lithography instruments and Focus Ion Beam (FIB) columns.The Matlab program that sets the exposure threshold outputs both a field of X, Y coordinates and appropriate dose values to the scan amplifier and the scanning electron microscope coils.

4) This generator is compatible with columns that do not posses a high-speed beam blanker (almost all scanning electron microscopes (SEM)). The pattern is fabricated by selectively exposing pixels in the field of view and moving the beam at high speed across pixels that are not to be exposed.

5) Images can be stored at a high pixel density (5k × 5k).

6) Low magnification, patterns may be written over a large area (1.3x1.3 mm^2).

6.1.2. Sample Preparation

6.1.2.1. Substrate Cleaning

Silicon wafers where used as the substrate. Wafers were used straight from the container, opened under the hood, and spin coated with the resist. All the work done, was not in the clean room, so we were not compromising the quality of the process by using the wafers in this manner.

6.1.2.2. Resist

For the purposes of this analysis, PMMA has been chosen as the resist. Although more advanced materials are certainly available, PMMA is a convenient generic system whose properties are well characterized and whose performance is generally compatible with that of any proprietary resist. PMMA used was diluted with Aerosal. The mixture was spun into the Si wafer. A CEE® Model 100CB was used to achieve this (Figure 6-6). This model is equipped with both a spinner and a baking plate. Depending on the thickness of the resist, different speeds and PMMA densities were used.

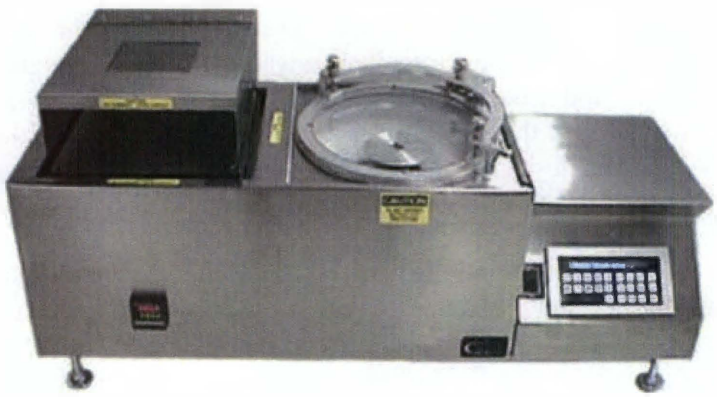


Figure 6-6: CEE® Model 100CB, which consists of a programmable spinner and a hotplate.

6.1.2.3. Spin Coating Process Theory

Spin coating has been used for several decades for the preparing thin films on substrate. A typical process involves depositing a small puddle of a fluid resist onto the center of a substrate and then spinning the substrate at high speed (typically around 3000rpm). Centripetal acceleration will cause the resist to spread to, and eventually off, the edge of the substrate leaving a thin film of resist on the surface. Final film thickness and other properties will depend on the nature of the resist (viscosity, drying rate, percent solids, surface tension, etc.) and the parameters chosen for the spin process. Factors such as final rotational speed, acceleration, and fume exhaust contribute to how the properties of coated films are defined.

One of the most important factors in spin coating is repeatability. Subtle variations in the parameters that define the spin process can result in drastic variations in the coated film.

The following is an explanation of some of the effects of these variations.

6.1.2.3.1. Spin Coating Process Description

A typical spin process consists of a dispense step in which the resist fluid is deposited onto the substrate surface, a high speed spin step to thin the fluid, and a drying step to eliminate excess solvents from the resulting film. Two common methods of dispense are Static dispense, and Dynamic dispense.

Static dispense is simply depositing a small puddle of fluid on or near the center of the substrate. This can range from 1 to 10 cc depending on the viscosity of the fluid and the size of the substrate to be coated. Higher viscosity and or larger substrates typically require a larger puddle to ensure full coverage of the substrate during the high speed spin step.

Dynamic dispense is the process of dispensing while the substrate is turning at low speed. A speed of about 500 rpm is commonly used during this step of the process. This serves to spread the fluid over the substrate and can result in less waste of resist material since it is usually not necessary to deposit as much to wet the entire surface of the substrate. This is a particularly advantageous method when the fluid or substrate itself has poor wetting abilities and can eliminate voids that may otherwise form. This is the type of dispense that was used in this thesis.

After the dispense step, it is common to accelerate to a relatively high speed to thin the fluid to near its final desired thickness. Typical spin speeds for this step range is1500-6000 rpm, depending on the properties of the fluid and the substrate. This step can take from 10 seconds to several minutes. The combination of spin speed and time selected for this step will generally define the final film thickness.

In general, higher spin speeds and longer spin times create thinner films. The spin coating process involves a large number of variables that tend to cancel and average out during the spin process and it is best to allow sufficient time for this to occur.

A separate drying step is sometimes added after the high speed spin step to further dry the film without substantially thinning it. This can be advantageous for thick films since long drying times may be necessary to increase the physical stability of the film before handling. Without the drying step problems can occur during handling, such as pouring off the side of the substrate when removing it from the spin bowl. In this case a moderate spin speed of about 25% of the high speed spin will generally suffice to aid in drying the film without significantly changing the film thickness.

6.1.2.3.2. Spin Speed

Spin speed is one of the most important factors in spin coating. The speed of the substrate (rpm) affects the degree of radial (centrifugal) force applied to the liquid resist as well as the velocity and characteristic turbulence of the air immediately above it. In particular, the high speed spin step generally defines the final film thickness. Relatively minor variations of ±50 rpm at this stage can cause a resulting thickness change of 10%. Film thickness is largely a balance between the force applied to shear the fluid resist towards the edge of the substrate and the drying rate which affects the viscosity of the resist. As the resist dries, the viscosity increases until the radial force of the spin process can no longer appreciably move the resist over the surface. At this point, the film thickness will not decrease significantly with increased spin time.

6.1.2.3.3. Acceleration (Ramp Rate)

The acceleration, angular acceleration, of the substrate towards the final spin speed can also affect the coated film properties (Figure 6-7). Since the resist begins to dry during the first part of the spin cycle, it is important to accurately control acceleration. In some processes, 50% of the solvents in the resist will be lost to evaporation in the first few seconds of the process.

Acceleration also plays a large role in the coat properties of patterned substrates. In many cases the substrate will retain topographical features from previous processes; it is therefore important to uniformly coat the resist over and through these features. While the spin process in general provides a radial (outward) force to the resist, it is the acceleration that provides a twisting force to the resist. This twisting aids in the dispersal of the resist around topography that might otherwise

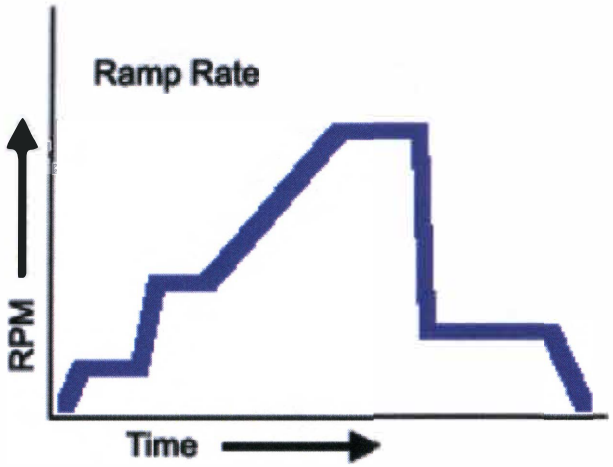


Figure 6-7: A schematic of ramp rate.

shadow portions of the substrate from the fluid.

6.1.2.3.4. Fume Exhaust

The drying rate of the resist fluid during the spin process is defined by the nature of the fluid itself (volatility of the solvent systems used) as well as by the air surrounding the substrate during the spin process. It is well known that such factors as air temperature and humidity play a large role in determining coated film properties. It is also very important that the air flow and associated turbulence above the substrate itself be minimized, or at least held *constant*, during the spin process.

The closed bowl (Figure 6-8) of the spin coater offers three distinct advantages: slowed drying of the fluid resist, minimized susceptibility to ambient humidity variations, and reduced susceptibility to variations in air flow around the spinning substrate.

The slower rate of drying offers the advantage of increased film thickness uniformity across the substrates. The fluid dries out as it moves toward the edge of the substrate during the spin process. This can lead to radial thickness nonuniformities since the fluid viscosity changes with distance from the center of the substrate. By slowing the rate of drying, it is possible for the viscosity to remain more constant across the substrate.

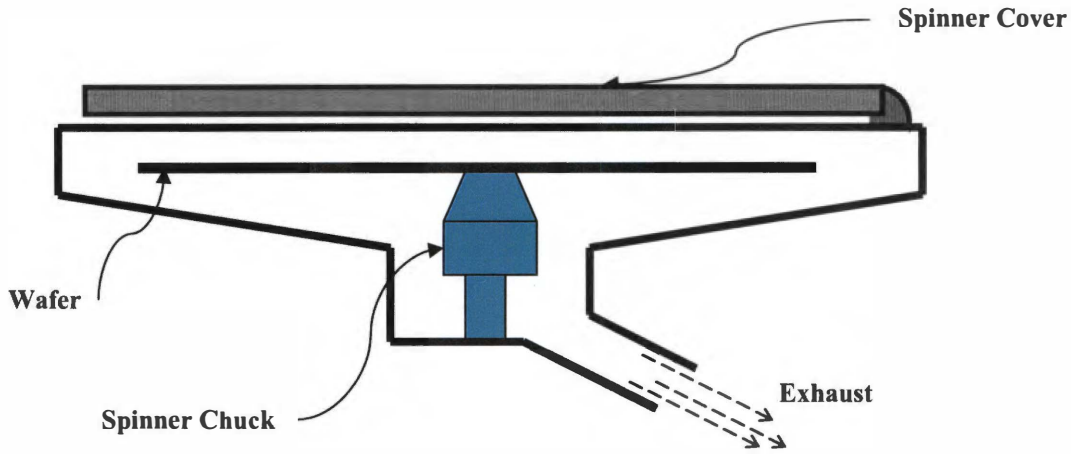


Figure 6-8: A schematic of the closed bowl of the spinner.

Drying rate and hence final film thickness is also affected by ambient humidity. Variations of only a few percent relative humidity can result in large changes in film thickness. By spinning in a closed bowl the vapors of the solvents in the resist itself are retained in the bowl environment and tend to overshadow the affects of minor humidity variations. At the end of the spin process, when the lid is lifted to remove the substrate, full exhaust is maintained to contain and remove solvent vapors.

Finally another advantage to this "closed bowl" design is the reduced susceptibility to variations in air flow around the spinning substrate. In a typical clean room, for instance, there is a constant downward flow of air at about 100 feet per minute (30m/min). Various factors affect the local properties of this air flow. Turbulence and eddy currents are common results of this high degree of air flow. Minor changes in the nature of the environment can create drastic alteration in the downward flow of air. By closing the bowl with a smooth lid surface, variations and turbulence caused by the presence of operators and other equipment are eliminated from the spin process.

6.1.2.3.5. Process Speed Charts

These charts represent general trends for the various process parameters. For most resist materials the final film thickness will be inversely proportional to the spin speed (
Figure 6-9) and spin time (Figure 6-10). Final thickness will be also be somewhat proportional to the exhaust volume although uniformity will suffer if the exhaust flow is too high since turbulence will cause non uniform drying of the film during the spin process.

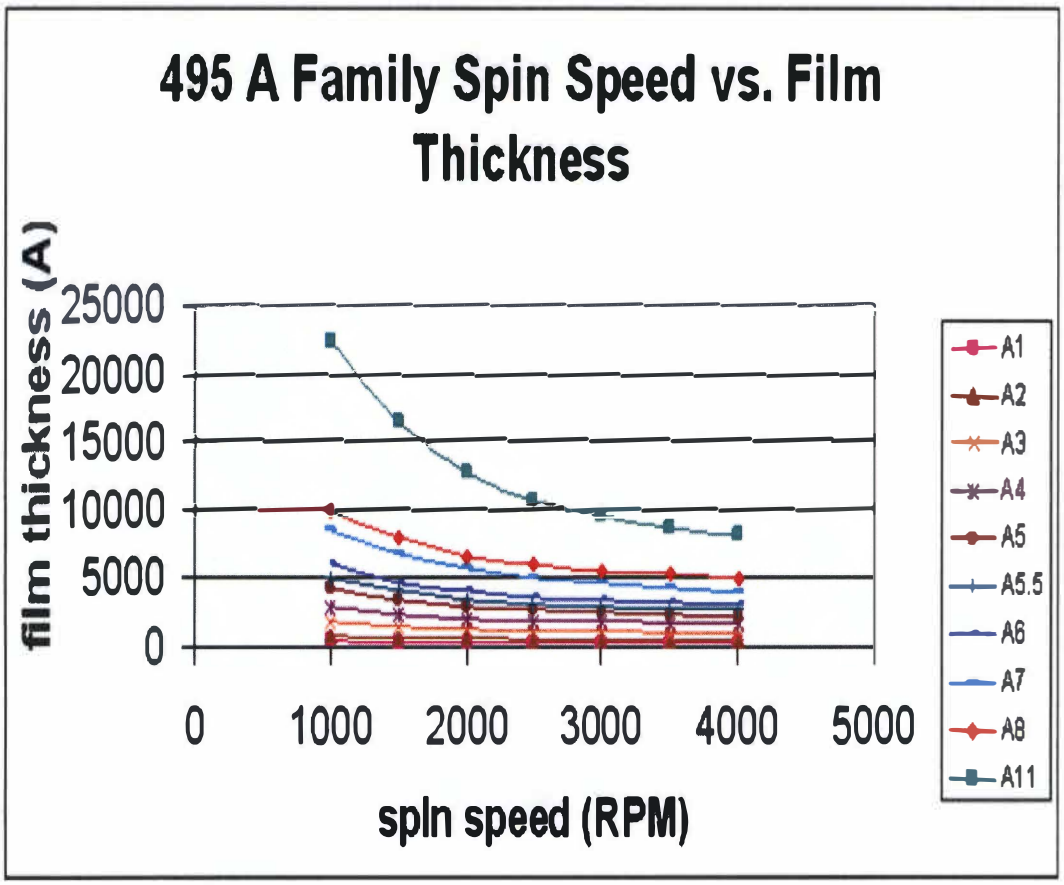


Figure 6-9: Spin speed vs. film thickness for different solutions of PMMA in Aerosal. The number following the letter "A" is the percentage of PMMA in the Aerosal + PMMA solution.

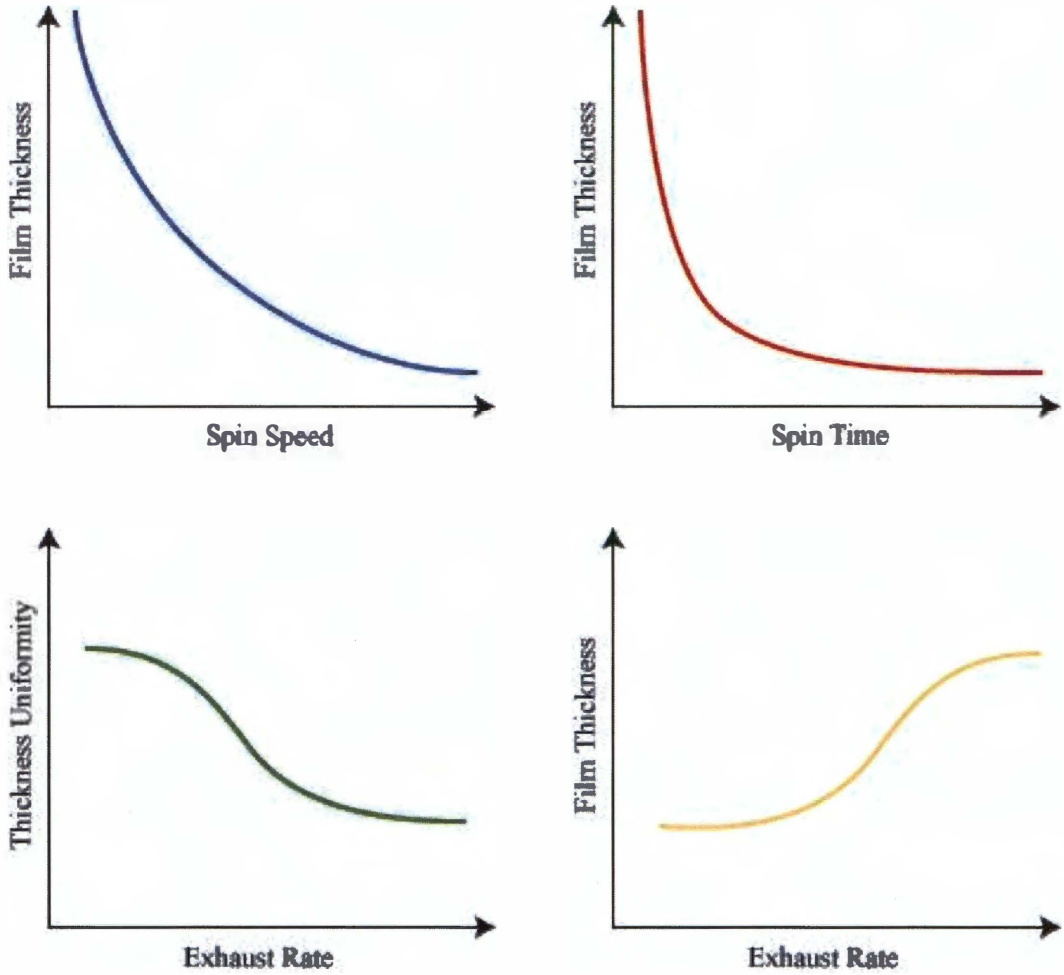


Figure 6-10: The above charts show the film thickness dependence on spin speed, spin time, and exhaust rate.

summarizes the film thickness relationship with the spin speed, spinning time, and the exhaust rate. Process parameters vary greatly for different resist materials and substrates so there are no fixed rules for spin coat processing, only general guidelines The wafer was hard baked for 90 sec at 180°C. In hard bake, through a vacuum
After the bake,

6.1.2.4. Hotplate Bake Process Theory

No matter if baking is needed before or after the EBL (pre- and post-bake), the same principles and guidelines are used. This section explains the main points in the baking process and the reasons to use hotplate baking instead of conventional oven baking.

Hotplate bake processing has increased in popularity since the early 1980s. Previously the most common technique for film drying and curing was the convection oven. Stratification, the formation of different temperature zones in the oven, is a problem associated with convection ovens and can severely affect film quality and reproducibility (Figure 6-11). Hotplates offer several advantages in the form of increased throughput, increased uniformity and reproducibility and decreased particle contamination. In a typical bake process the substrate is placed into contact with a heated surface of known temperature. The substrate quickly rises to a peak temperature slightly lower than the hotplate surface temperature. Drying and curing steps generally take about 1 minute. This is in contrast to traditional oven processes taking 30 minutes or more. Particle generation also occurs within a standard oven. In a forced-air, convection oven, substrates are commonly exposed to a flow of particle laden air. In convention ovens, the substrates stays in the oven for a long time (compare to hotplate), so during resist film cure, the substrates will be exposed to considerable particulate contamination.

6.1.2.4.1. Hotplate Bake Variables and Methods

A typical bake process consists of preheating the surface to a known temperature, loading the substrate onto the surface for a specific length of time and removing it promptly at the end of the cycle. Including the bake method employed, all affect the overall performance of the process.

Bake Temperature

The bake temperature used is dependent on several factors. The material and substrate being baked as well as the results desired are key factors to be considered in developing a bake process.

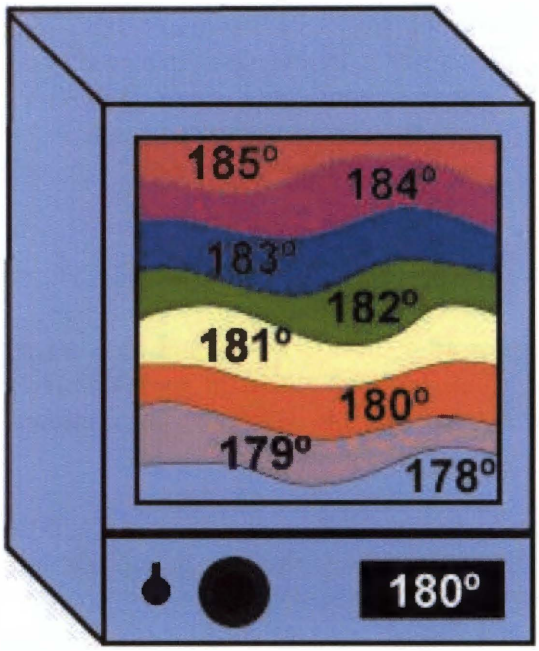


Figure 6-11: Non uniform temperature zones in a convection oven.

In general hotplate baking will be performed at temperatures slightly higher than those used in oven bake processes. The film being baked will reach a temperature somewhere between the temperature of the hotplate and the ambient air above the film.

Thicker substrates and /or substrates with lower coefficients of thermal conductivity will require even higher temperatures to compensate for this phenomenon. Another reason for using higher temperatures is to increase process throughput. In oven processes there is a problem commonly known as the "skin effect". This is a result of the outer exposed layer of the film drying and forming a skin before all of the solvents in lower layers have evaporated. Most oven processes are adjusted to use lower temperatures and bake times measured in minutes and hours to prevent this. During a hotplate bake process the film is baked from the bottom up, thus preventing the formation of a skin over the surface. Because of this it is possible to increase temperatures and adjust bake times to be measured in seconds without danger of blistering or cracking in the film.

Bake Methods

Another important factor is the method of bake. There are three distinct bake methods; Proximity, Soft, and Hard contact (Figure 6-12).

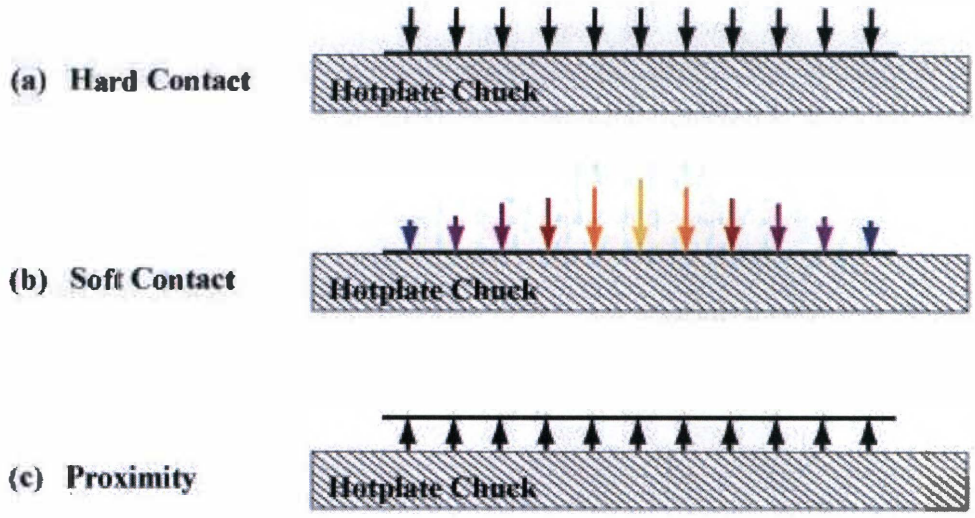


Figure 6-12: (a) Hard Contact Hotplate Chuck (b) Soft Contact Hotplate Chuck (c) Proximity Hotplate Chuck. The arrows are representative of the forces applied to the wafer.

In a hard contact bake the substrate is clamped onto the hotplate surface by the application of vacuum to the underside of the substrate. Small holes are machined into the hotplate surface in a pattern which optimizes vacuum distribution without the formation of cold spots or warping of the substrate. This method is usually preferred for silicon and other flat substrates where back side contact is not a problem.

Soft contact baking uses gravity alone to hold the substrate onto the hotplate. This method generally offers less uniformity since the substrate-hotplate thermal interface is not as efficient as in hard contact baking and can be somewhat random in variation. As shown in the figure there would be a larger pressure in the center of mass compare to the edges.

Proximity baking is accomplished by forcing heated gas (usually nitrogen) through the same ports in the hotplate surface that are used for vacuum in the hard contact method. This forces the substrate to float at a distance of one to four mils (25-100 μm) above the hotplate surface. Proximity baking allows a slower warm-up than contact bake methods and can be advantageous when baking thick films where blistering would otherwise be a problem. Another advantage of proximity baking in this manner is that in many cases cambered or warped substrates can be baked with a high degree of uniformity. This is usually not possible with the contact methods since it is not possible to achieve a vacuum under a substrate that is not flat to start with.

Processing cambered substrates with the soft contact method creates hot spots where the substrate touches the hotplate and cold spots where it does not. It should be noted as well that this type of proximity process is "self-leveling" in that the substrate will tend to form a uniform gap to the hotplate surface. This is a significant advantage not found in "pin lift" type systems. Proximity baking also offers the unique advantage of allowing hotplate processing without touching the bottom side of the substrate. An example of this application is photomask processing. In processing these relatively thick glass plates it is important that the back side of the glass not directly touch the hotplate since this causes microfractures in the glass itself from rapid heating. By performing the entire bake process in the proximity mode the integrity of the substrate is not endangered and the uniformity is excellent.

Bake Time

The selection of the bake time parameter plays an important role in the reproducibility of the bake process. Substrate thermal properties and the choice of bake method greatly affect the amount of time necessary for the substrate and therefore film temperature to stabilize during the bake. Thicker substrates and the use of proximity bake methods will increase the time necessary for the film to reach its final temperature. It is important that most of the baking action in the film takes place after this temperature is reached. A silicon wafer will reach a stable temperature within a few seconds and so it is traditional to adjust an e-beam resist bake processes to be completed in 60-90 seconds with an appropriate bake temperature. For thicker substrates such as photomasks and ceramic modules the increased time necessary to heat the larger mass of the substrate results in bakes times approaching five minutes. It should be noted that these substrates can be processed with higher temperature and much shorter bake times but reproducibility may suffer. If the bake time is too short then a significant amount of the actual bake process will take place during the loading and unloading steps as well as the substrate cooling after removal from the hotplate. This is an unstable condition since it is very difficult to exactly reproduce conditions during these steps.

In general the temperature-time relationship in a bake process can be taken as the bake temperature being inversely proportional to the bake time. Increasing the bake temperature results in a need for decreasing bake time. The limits for both of these parameters can be considered to be reached when the process is no longer reproducible or when the physical temperature limitations of the resist or substrate have been reached.

Exhaust

In addition to the three factors explained, the exhaust system of the hotplate is essential in the quality and reproducibility of the resist films. The design of the Cee® exhaust cover promotes the dissipation of vapors removed from a substrate placed on the chuck, without actually drawing air across the chuck surface (Figure 6-13).

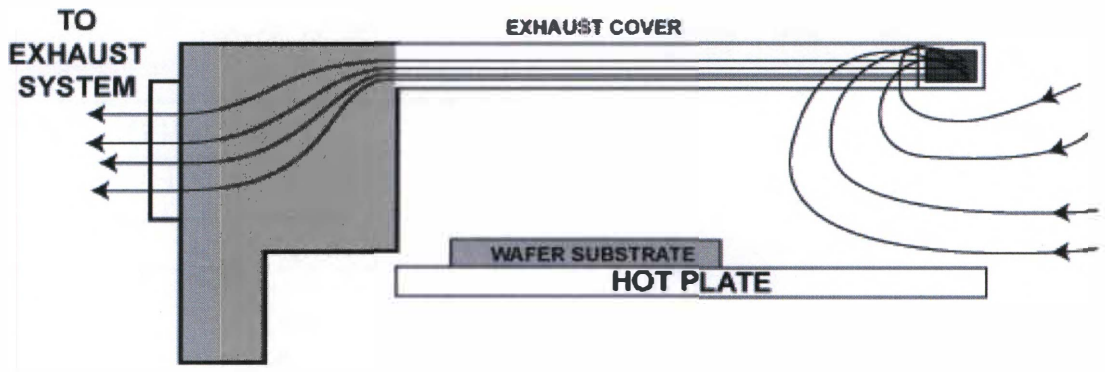


Figure 6-13: Cee® exhaust cover above the hotplate. The wafer was placed at the end of the hotplate to be at a fare distance for the air turbulence.

6.1.2.4.2. General Guidelines in the Bake Process

As with the spin coating process there are no absolute rules for hotplate baking, only general guidelines. Following is a list of issues to consider for specific hotplate process problems (Table 6-2).

6.1.2.5. Post-Exposure Treatment

After the polymeric resist film has been exposed and the latent image generated, chemical reactions may continue to occur after exposure. As a consequence, it is often necessary or advantageous to control the environment of the exposed polymer film to allow the desired reactions to continue to completion or induce new reactions that aid in developing subsequent relief images in the resist film.

For PMMA, thermal curing was done. The wafer was hard baked for 30 seconds on a hotplate at 100°C. As mentioned in Table 6-1, this treatment was not done in every process.

Table 6-2: Hotplate process problems.

Issue	Reason	Solution(s)
Film Underbaked	• Bake Temperature Too Low. • Bake Time Too Short.	• Select Higher Temperature. • Increase Bake Time.
Film Blistering or Cracking	• Unstable Balance in Temp. / Time Parameters. • Warm-up Time Too Fast.	• Decrease Temp. / Increase Time. • Use Proximity Bake to Preheat Substrate.
Non-Uniform Bake	• Unstable Balance in Temp./ Time Parameters. • Operating with Exhaust Lid Raised. • Unstable Ambient Conditions. • Bake Time Too Short.	• Decrease Temp./ Increase Time. • Lower the Exhaust Lid. • Protect Against Major Fluctuation. • Increase Bake Time.
Film is Thicker on One Side, Wedge	• Hotplate Surface is Contaminated.	• Clean Surface of Hotplate.
Film Overbaked	• Bake Temperature Too High. • Bake Time Too Long.	• Select Lower Temperature. Decrease Bake Time.

6.1.3. Developing Process and Liftoff

After exposure the resist was developed in a 1:3 solution of methyl-iso-butyl-ketone: isopropyl alcohol (MIBK:IPA) for 1 min. Then Cr was evaporated onto the wafer using an electron-beam evaporation system (base pressure ~ 10-7 Torr), and finally lifted off in acetone under ultrasonic agitation. The metal structures were able to survive ultrasonic agitation during lift-off. Cr, Ti, Ni, and NiCr have good adhesion with Si. As Cr makes good adhesion with Si (Survives the lift-off process), has a high SE yield contrast with Si, and it is fairly cheap, it was used to metalize the structures made in this research. In contradiction to sputtering, evaporation provides a directional beam. This plays an important role in the development process. In sputtering, because the sputtered metal beam is non-directional, the sputtered metal on the resist edges and the adjacent developed area have a high chance of joining (depending on the thickness of the resist the possibility of this process varies). This causes the whole sputtered area to be removed during the development process (Figure 6-14). Using an e-beam evaporation system instead of a thermal evaporation

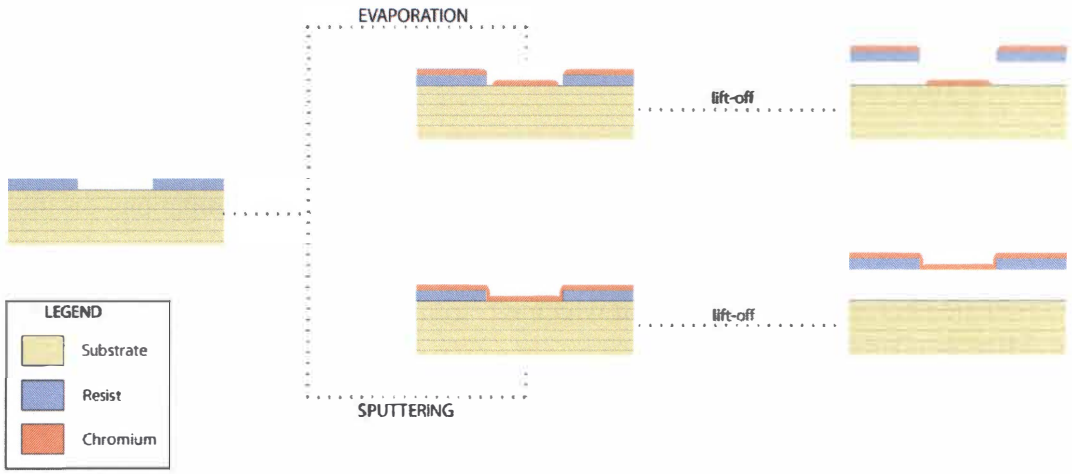


Figure 6-14: A schematic of evaporation and sputtering in the lift-off process.

system allows us to achieve finer metal structures. Note that when making features on this size scale, the grain size of the metal using during liftoff becomes extremely important. For example, if the line width is smaller than the grain size of the metal, it will be impossible to produce a smooth line.

6.1.4. Different Resist Thicknesses

To make writing and finding the pattern easier, a gold alignment frame was made (7 mm × 7mm) and the patterns were written inside the frame. To achieve this, a four inch aluminum mask, which a number of these registering marks were cut into it, was made. This mask was lined up on top of the Si wafer and sputtered Au/Pd using a plasma sputtering machine. Because of the high secondary electron yield of Au and Pd, and the fact that gold does not adhere to Si but adheres to Pd, Au/Pd was sputtered. After that the wafer was broken at the marks so a number of samples was made from a single 4" wafer. All beam electron-optical alignments were made on gold that was electron-beam evaporated onto the silicon with the same thickness as the resist. Having a high Z material for height reference made the beam alignment at low energies easier and more reliable. The electron beam spot size was measured by taking an image of the height reference material and then analyzing the image using the SMART[188] macro in conjunction with SCION[86] image or NIH[146] image software.

The resist thickness was determined by a Filmetrics F20 reflectometer[189] and by step height measurements using an MFP-3DTM atomic force microscope (AFM).

In this thesis each reported thickness is an average of at least five measurements over each deposited sample.

6.1.5. Probe Sizes

This section will cover a brief description of the minimum probe sizes achieved in this research. To have a better understanding of the limitations on this process, chromatic and spherical aberrations are explained.

Chromatic aberration is the effect in which electrons of different energy are focused to different planes.

$$\Delta z = C_c \alpha \frac{\Delta E}{E} \tag{5,21}$$

, where C_c is the Chromatic aberration constant, α is the convergence angle, and ΔE is the energy spread. Every electron source has a natural energy spread and the source of choice -the Schottky field emitter -has a spread of ~ 0.6 eV, which is a high fraction of the beam energy when the lithography is done at low energy.

Spherical aberration is the difference in focus between paraxial and peripheral rays as

$$\Delta z = \frac{1}{2} C_s \alpha^3 \tag{5,22}$$

, where C_s is the Spherical aberration constant All electron-optical lenses have positive-definite spherical and chromatic aberration (Scherzer), so these contributions always add.

As shown by Scherzer (1936), each is inevitable and optimizing the balance between these aberrations leads to undesirable restrictions on performance. In using the Hitachi S-4300 SE/N (a Schottky emitter scanning electron microscope, ΔE = 0.6 eV) with a working distance of 5 mm (the WD used in the lithography process) and an aperture of 20 μm, the minimum probe size achievable is shown in Table 6-3. Figure 6-15 clearly shows the difficulty of achieving fine probes at beam energies less than 1 kV.

Table 6-3: Minimum probe size achievable at a working distance of 5 mm using the Hitachi S-4300 SE/N with an aperture of 20 μm.

Energy (kV)	0.5	1	2	5	15
Minimum Probe Size (nm)	37.5	19.0	9.8	4.4	2.7

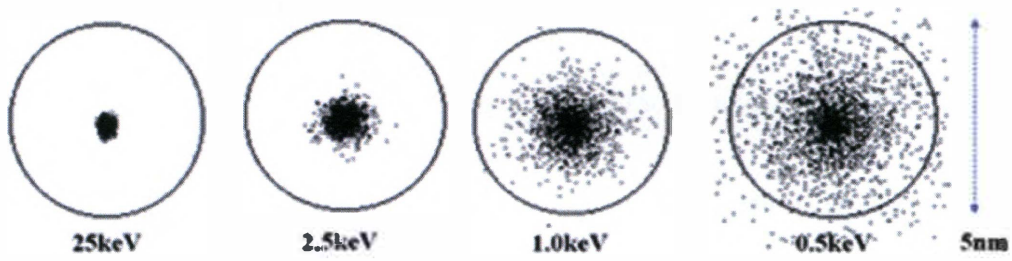


Figure 6-15: Using Kenway-Cliff numerical ray-tracing simulations of electron arrivals with a lens Cs=3mm,Cc=3mm, α =7 m.rads, the aberration effects are shown for different energies.

6.1.6. Critical dose and resolution test

An array of dots with a 170nm pitch was patterned onto 45 nm and 85 nm thick layers of PMMA, at beam energies ranging from 1 keV to 25 keV. The development process was kept fixed and the dose for each voltage was adjusted to minimize the dot size. The SEM images of a few patterns of 10 nm Cr after liftoff are shown in Table 6-4. The resolution increases with increasing voltage. For the 85 nm PMMA thickness at 1 keV the metal did not lift off, and there were continuous films instead of separate dots. This decrease in resolution is due to increased scattering and decreased penetration depth of low voltage electrons in the resist. Monte Carlo simulations show that 1 keV electrons are scattered laterally up to 25 nm, much more than the higher energy electrons. In addition, the electron range is only about 55 nm at 1 keV, so the resist did not develop completely. The penetration depth at 2 keV is increased to 120 nm, thus clearing the resist. This test shows that it is possible to achieve sub-200 nm resolution for 2 kV in 85 nm of PMMA, but thinner resists are needed for higher resolution or lower voltage.

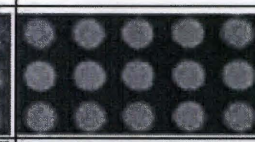
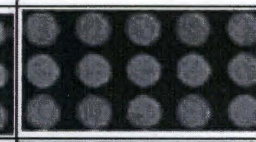
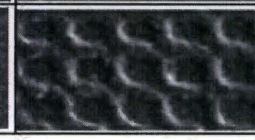
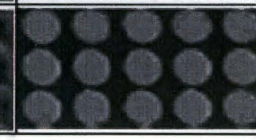
6.1.7. Charging effects

Charging is expected to be more severe at low voltages due to more efficient electron stopping in the resist. Nevertheless, any obvious charging effects, which would show up in bending of the single pass lines near a square — a large charged area, were not observed. This suggests that the increased sensitivity to charging is offset by the reduced resist thickness, which does not support a large surface voltage. Electron diffusion in thin films should further eliminate charging[190]. Depending on details of their geometry, patterns were exposed in an order chosen so as to reduce the error due to geometrical distortions of the exposure field[191]. During the writing, our sample was well grounded.

6.1.8. Resist Thickness Effects

An array of dots was patterned on 85 and 45 nm thicknesses of PMMA with 0.5keV, 1 keV, 2 keV and 25 keV electrons maintaining the same exposure dose for each voltage. There is almost no difference among the patterns at high voltage (Table 6-4). This is not surprising because the 25 keV electron's penetration depth is several microns and 45 nm and 85 nm resist exposures should look essentially the same. For 2 keV, however, there is some difference as the pattern was not well developed for the 85 nm but was for the 45 nm thick resist. This test shows that the resist thickness is critical at low voltages, and that an optimized resist thickness should be used for reliable patterning.

Table 6-4: An array of dots with a 170nm pitch was patterned on a 45 nm and an 85 nm thick layer of PMMA, with beam energies 1, 2, and 25 keV.

Energy (kV) / Resist Thickness (nm)	1	2	25
45			
85			

6.1.9. Dot Arrays

In this section a few examples of the dot arrays fabricated are shown. To show some of the EBL challenges both successful and non-successful patterns are presented.

As shown in Figure 6-16, for each beam dose, a 51 × 51 square dot arrays is drawn. As explained in section 6.1.1, the SEM is optimized for operation in the center of the field, and that is where the lithography was done. After each square of dot arrays was written, manually the stage was moved to the new position, and the arrays where written again, but with a different dose. In Figure 6-16, seven set of dot arrays are written. From left to right the beam dose was increased. The line of larger spots on the button of the figure is where the beam was parked after each set of dots were plotted. As seen in Figure 6-16, the last set of dots is not properly developed. This is mainly because the resist is not uniform over the wafer. This has been observed because of the low beam dose. The same problem exists for Figure 6-17.

Figure 6-18 and Figure 6-19 are written at 2 kV and 1 kV respectively. From images like these, the line edge roughness of the patterns and the shot noise effects were studied. Shot noise will be covered in more details at section 6.1.10. Figure 6-20 is an example of an underdeveloped process. The dot arrays where written at 0.5 kV, but beam dose, was not sufficient to have a successful writing.



Figure 6-16: Seven 51 × 51 square dot arrays are drawn. From left to right the beam dose is decreased. At the end of each lithography, the beam is parked.

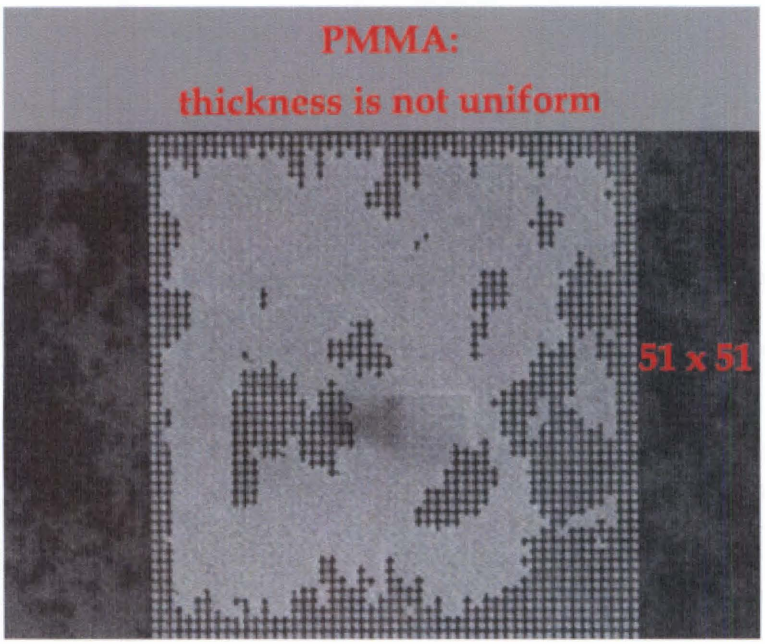


Figure 6-17: The dots are not properly developed. This is mainly because the resist is not uniform over the wafer.

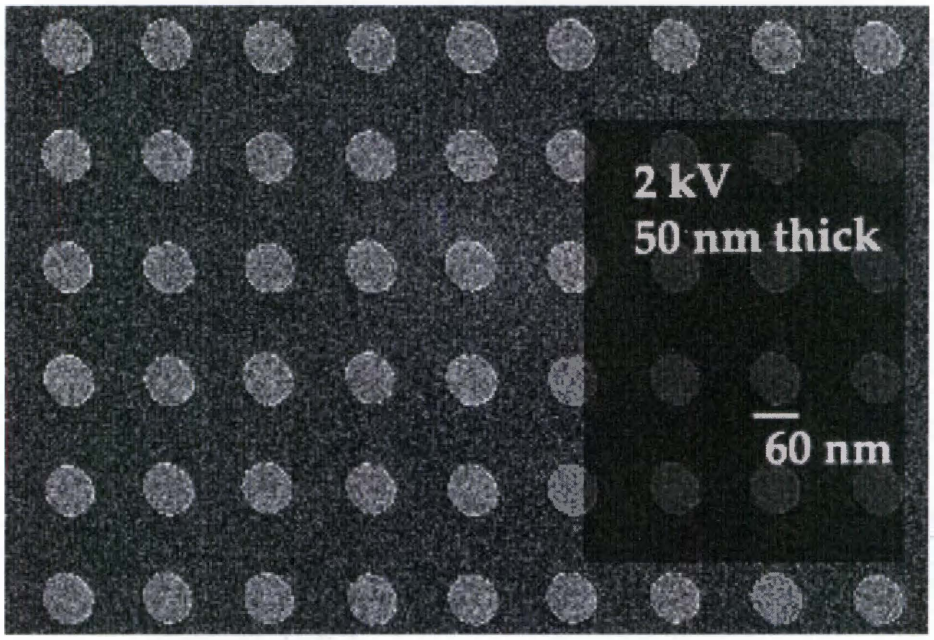


Figure 6-18: The EBL is done on a 50 nm thick PMMA on Silicon at 2 kV. The white bar represents the scale.

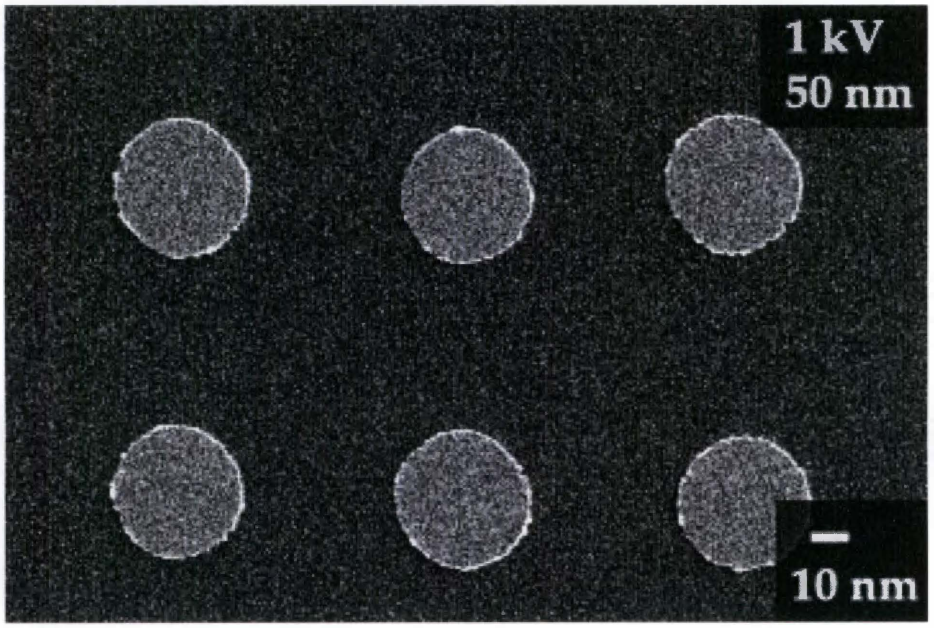


Figure 6-19: The EBL is done on a 50 nm thick PMMA on Silicon at 1 kV. The white bar represents the scale.

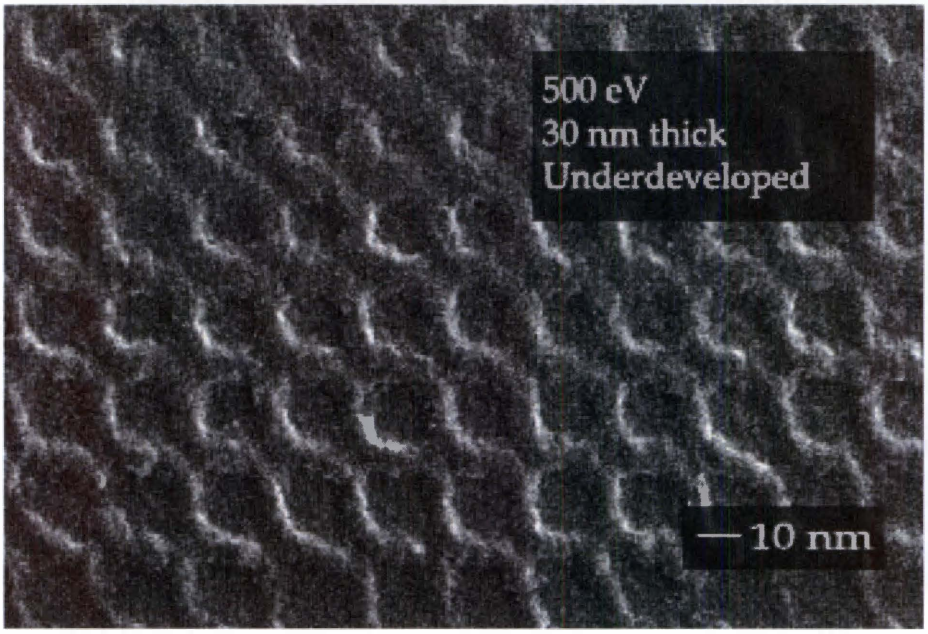


Figure 6-20: An example of an underdeveloped process. The white bar represents the scale.

6.1.10. Shot Noise

As feature size gets smaller the required electron beam dose (D) gets lower so error (noise) decrease. The noise in this case has a Poisson distribution and is called shot noise. Therefore if N electrons pass a point in a given time t on the average, the mean dose and the dose fluctuations (σ_D which is the dose's standard deviation) should be:

$$D\ (\text{Dose}) = \frac{eN}{At}$$
$$\sigma_D = \frac{e\sqrt{N}}{At} \qquad (5,23)$$
$$\frac{\sigma_D}{D} = \frac{1}{\sqrt{N}}$$

The correlation of the mean and standard deviation in counting independent, discrete occurrences is useful scientifically. By monitoring how the fluctuations vary with the mean signal, one can estimate the contribution of a single occurrence, *even if that contribution is too small to be detected directly.*

Line width roughness (LWR) is highly influenced by the shot noise. To measure LWR for the fabricated dot arrays the deviation of the spot's edge from the red circle is measured (Figure 6-21). Figure 6-22 and Figure 6-23 are the LWR plots versus the linewidth for 1 and 2 kV respectively.

6.2. Simulation

6.2.1. Monte Carlo Simulation

In order to utilize EBL successfully in nanometer range, the interaction and scattering of electrons within the resist layer and the underlying substrate must be well understood. For example, the effects of beam energy, type of resist, resist thickness, substrate type, and several other variables are critical in producing an optimal pattern in the resist. The resolution obtainable with electron beams is not ONLY limited by probe characteristics, but rather is presently limited by electron scattering. It is important to understand these limits imposed by electron scattering as well as methods of minimizing scattering effects and thereby improving resolution.

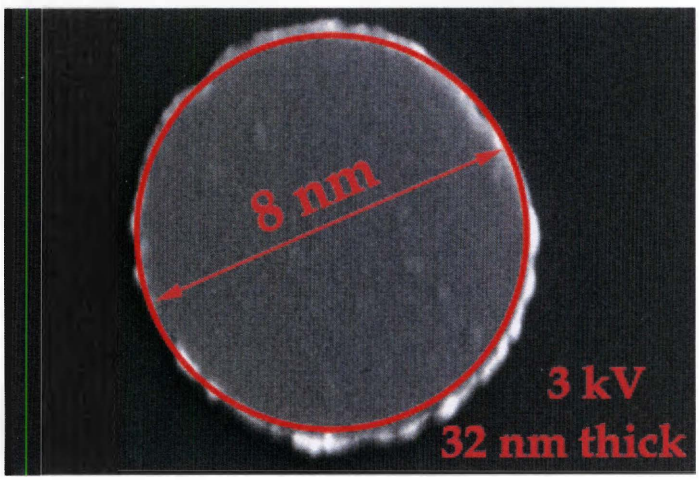


Figure 6-21: The pattern was written on a 32 nm thick PMMA with a 3 kV e-beam. ~10 nm Cr was evaporated and lift-off at the end. The LWR was measured with regards to the red circle of 8 nm diameter.

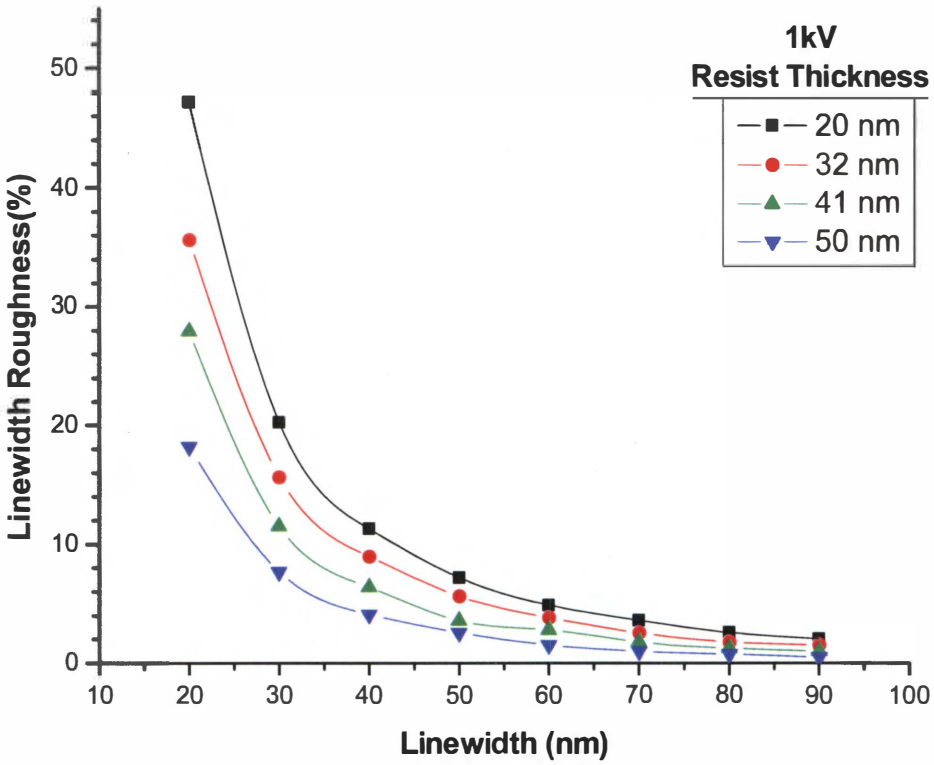


Figure 6-22: LWR versus the linewidth for different PMMA thicknesses. The pattern s were drawn using a 1 kV e-beam.

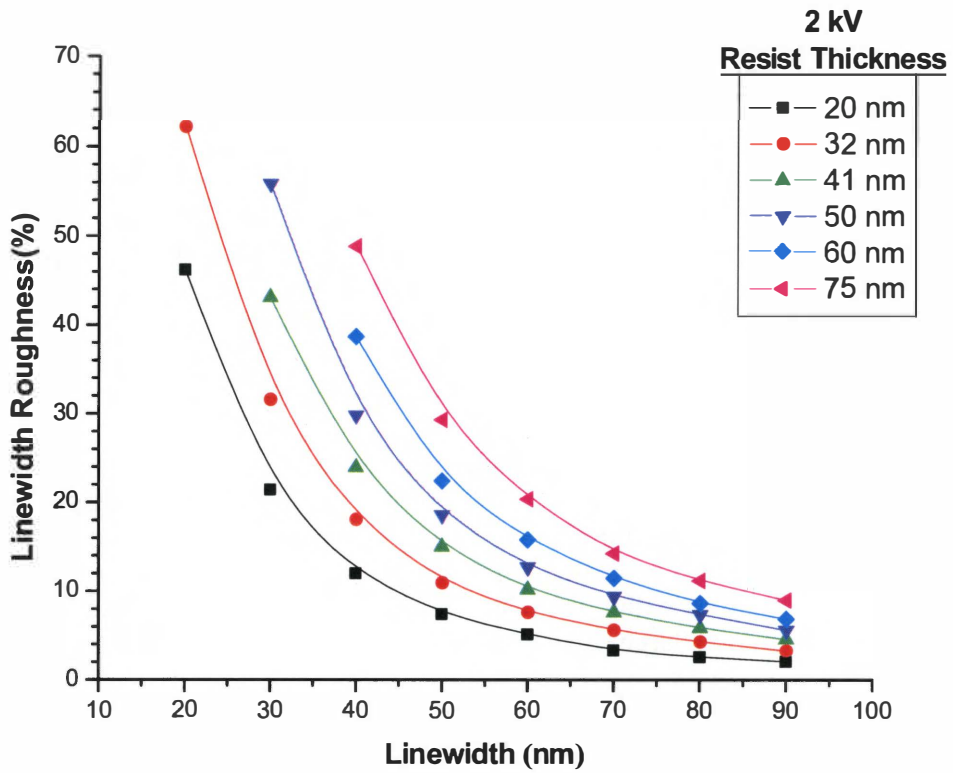


Figure 6-23: LWR versus the linewidth for different PMMA thicknesses. Pattern s were drawn using a 2 kV e-beam.

For optimal high resolution lithography, the beam must only just penetrate the resist in order to minimize the effect of backscattering and the consequent broadening arising from interactions within the substrate. The key factor in determining penetration is the stopping power i.e. the rate (eV/Å) at which the electron deposits its energy into the medium through which it is passing. Because there is no measured stopping power data for PMMA[192], values were estimated using the Joy and Luo[126] low energy modification of the Bethe formalism[86]. Finally, it is assumed that the resist will be chemically processed in the standard way to develop the latent image for subsequent patterning of the substrate. In this case the data of Adesida et al.[146] shows that the lower limit of energy deposition in PMMA is required to produce solubility is 10^{22} eV/cm^3. For any region lying above this dose, the profile of the developed resist can then be derived from the string theory of Greeneich and van Duzer[145].

Under these assumptions, the required resist thicknesses were found to be 10nm at 1keV, 4nm at 500 eV, and about 1.5 nm at 100 eV. Note, however, that the estimated thickness range at 100 eV may be impractical because the fast secondary and backscattered electrons generated within the resist may have a longer travel path than the incident electrons within the resist. In addition it is impracticable to deposit such a thin layer over a large area because as the resist thickness decreases, the number of defects increases.

6.2.1.1. Modeling the electron-solid interaction

The spatial distribution of energy deposition in the resist was computed using a Monte Carlo simulation. Conventional Monte Carlo models of electron-solid interactions assume that the spatial distribution of the electrons is determined solely by elastic scattering, and that the energy deposition is determined from the continuous slowing down approximation (i.e. the Bethe stopping power equation[86]). If this model were totally correct, then for the simplest case of an unsupported thin film of resist a feature of arbitrarily small dimension could be fabricated. This is because the lateral scattering of the beam falls to zero as the thickness of the resist decreases. In fact, as first demonstrated by Broers[3], the thickness of a line dose not fall steadily but instead reaches a limiting lower value as the resist thickness is decreased. This is because of the production of fast secondary electrons (FSE) in the resist. Their initial trajectories lie almost normal to the direction of the incident electron, and as a result it is these electrons that are responsible for most of the energy deposition in the near entry surface region of the resist.

For the purposes of this study, a Monte Carlo model incorporating FSE production was employed (Murata et al.[193], Joy[147]). The program uses a parametrically modified Rutherford scattering cross-section to describe elastic interactions at low beam energies, and the Evans cross-section for FSE production. The Joy and Luo[126] modification of the Bethe[86] stopping power equation was used to

determine the instantaneous energy deposition. The program operates as a double Monte Carlo. The incident electron is tracked in the usual way as it travels through the resist, but at each interaction a random number is used to determine whether the interaction is elastic or inelastic (i.e. producing a FSE). If the interaction is inelastic, then the energy of the FSE generated is determined, and this electron is then tracked until it either comes to rest or leaves the specimen. Tracking the incident electron is then resumed after accounting for the energy transferred from the incident to the emitted electron in the inelastic collision.

In order to achieve statistically valid results, between 30,000 and 100,000 trajectories were modeled for each set of conditions. Figure 6-24, shows a trajectory plot from this program for the case of a 5 keV beam entering a PMMA layer 45 nm in thickness. As a result of the elastic scattering that they suffer, the incident electron trajectories (shown in light dashed lines) can be seen to fan out as the beam penetrates into the resist. The FSE trajectories shown in dark solid lines typically leave the incident trajectory at an angle close to 90 degrees, thus traveling approximately parallel to the sample surface. Because these electrons are of lower energy than the incident electrons, they have a higher stopping power. Consequently, energy deposition around the beam impact point and close to the surface is dominated by the FSE contribution.

6.2.1.2. Results for a Point Source

Figure 6-25 (a), shows the radial distribution of the deposited energy within a resist layer 100 nm thick from a 5 keV point source beam. Note that the length scales in the horizontal and vertical directions are different. The plot has been color coded to produce contours of equal energy deposition. The color code is defined as follow: areas that have received 30% and above of the maximum energy deposition (MED) are colored in magenta, 10% – 30%, 10% – 3%, 1% – 3%, 1% – 0.6%, and 0.6% – 0 of the MED are colored in cyan, red, green, blue, and yellow respectively. The scale shown above the figures is calibrated in units representing the relevant percentage of the maximum energy deposition. It can be seen that under these conditions the energy profile fans out as the beam broadens during its passage through the resist. The first contour (corresponding to 30% of the peak energy deposited in any voxel) occupies a cylindrical region about 10 nm wide about the beam axis and delineates the area where the effect of the energy deposited by the FSE is the dominant term. Outside of this there is a second contour (at 10% of maximum dose) that is conical in shape and broadens from 10 nm at the beam entrance surface out to about 50 nm at the exit surface. This is the region where the energy comes mostly from the scattered incident electrons. Each subsequent contour, representing a further half order of magnitude (three times) reduction in energy deposition, has a similar conical form leading to a further, but modest, increase in the maximum lateral wide of the profile which ultimately extends for a total wide of 250 nm.

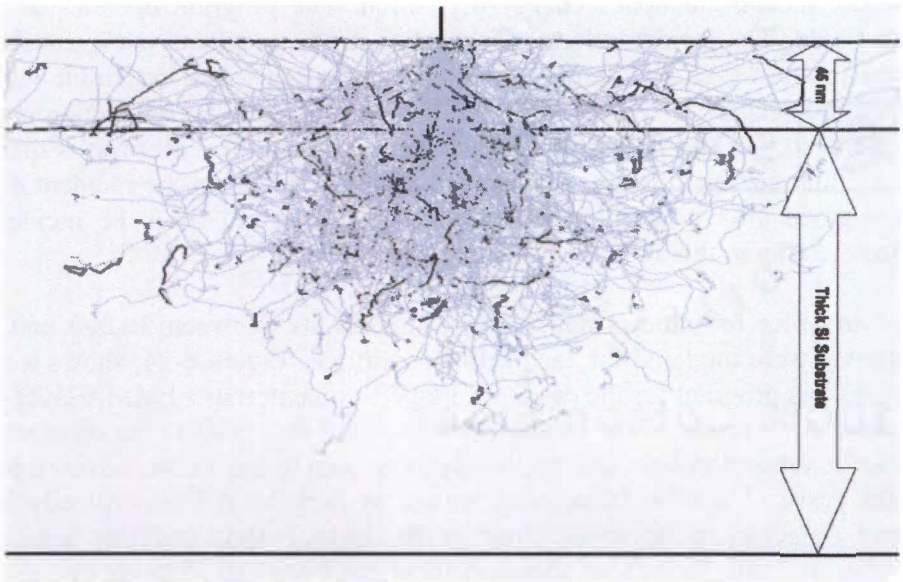


Figure 6-24: Trajectory plot of 5 keV electron beam entering a PMMA layer 45 nm in thickness. Primary trajectories are shown in light dashed lines and the fast secondaries are shown in dark solid lines.

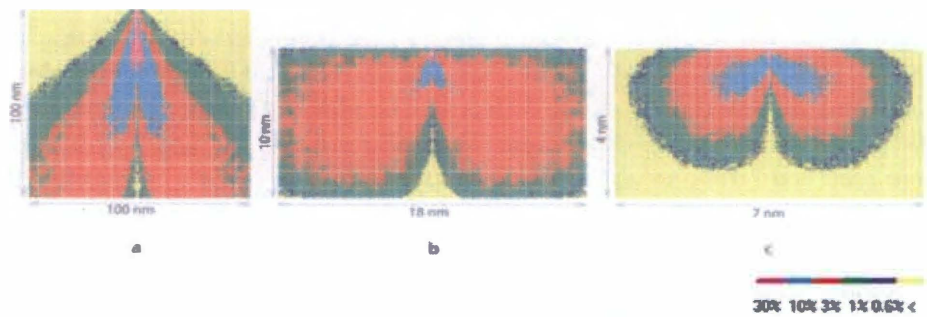


Figure 6-25: Radial energy distributions of a point source beam in a PMMA resist layer. (a) 5 keV incident beam, 100 nm thickness. (b) 1 keV incident beam, 10 nm thickness. (c) 0.5 keV incident beam, 4 nm thickness.

Figure 6-25 (b), shows the corresponding plot for 10 nm of PMMA exposed at 1 keV. The beam is now only just penetrating the resist and consequently the energy profile is significantly different to that shown in the first example. Note that the appearance of these energy deposition profiles varies from that displayed by a more familiar presentation. This is because it is conventional to present such data by projecting the three dimensional distribution onto the plane that includes the incident beam axis, a procedure that masks the true form and symmetry of the profile. The contour representing the 30% level (magenta) has now shrunk to an approximately spherical region only 1 nm or so in diameter and positioned 1 nm below the entry surface. The contour for the 10% of the peak level (cyan) has an open umbrella shape that can be seen to extend about 3 nm to 5nm out from the beam axis and to penetrate though about one third to one half of the thickness of the resist layer. This shape arises because the electrons have, on average, been sufficiently scattered by this depth to be diverging from the axis. The 3% and subsequent lower level contours have the more familiar apple-shape as the electron distribution continues to diffuse away from the axis.

Figure 6-25 (c), shows the corresponding situation for a 500 eV point source incident on a 4 nm resist layer. The shape of the energy deposition profile is very similar to that for the 1 keV case because the angular scattering of the electrons is not strongly sensitive to the actual incident energy. Consequently, under the condition in which the resist thickness is chosen so as to be equal to the beam range, then the form of the energy deposition profile can be assumed to remain constant. However the total width will vary as about $E^{1.66}$.

Figure 6-26 plots the peak energy deposited in the PMMA as a function of the incident beam energy. As the energy is reduced from 3 keV to below 500 eV, the deposited energy density rises by five orders of magnitude from 10^{17} eV/cm^3/el., and the dose required to expose the resist therefore falls very rapidly as the energy is reduced, thus permitting a speeding up of the lithography. For a given electron emitter, however, the maximum current available at the focused probe falls approximately linearly with the beam energy, thus lowering the incident beam energy from a few keV to a few hundred eV can be expected to improve writing speed by a factor of about 10,000 times.

6.2.1.2.1. Modeling of Fast Secondary Electrons

In our model we have used the single scattering[4] method. The single scattering Monte Carlo simulation calculates the passage of the electron through the olid by tracking it from one scattering site to the next. Each scattering event is considered until the electron has less energy than the cut-off energy. This is in contrast to the plural scattering where each electron travels exactly the same total path length within the specimen until it's energy is less than the cut-off energy. For the

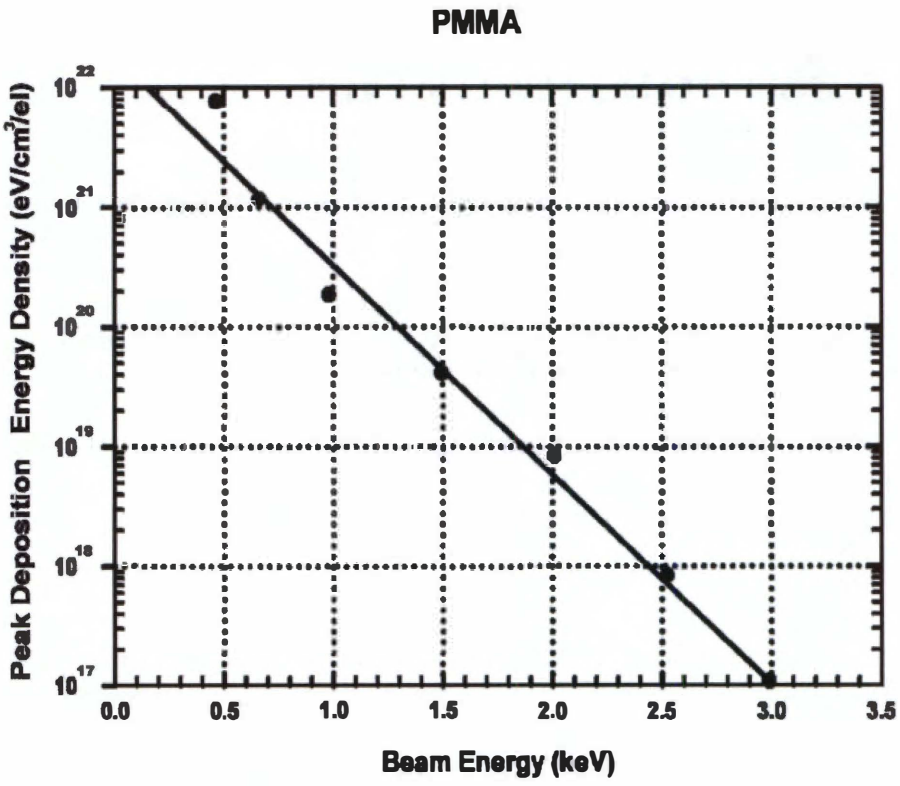


Figure 6-26: Peak energy density deposited in PMMA as a function of the incident beam energy (The data are from 10^5 trajectories with relative error < 1%).

elastic collisions, Screened Rutherford cross section, which has been parametrically corrected at low energies, is used. For inelastic collisions, the stopping power is determined from the modified Beth relation, which is valid at low energies. From the Mott knock on cross section the fast secondary electron production is derived. For statistical validity 10^5—10^6 trajectories were used.

To understand the importance of secondary and fast secondary electrons in EBL, in this section two models have been compared. Model 1, which does not include SE and FSE and our model, Model 2, which includes those types of electrons. Figure 6-27 through Figure 6-29 are the radial energy deposited per volume plots for a point source beam in a free standing PMMA resist slab (resist with no substrate). They compare both Model 1 and 2 for different energies. Both plots are drawn for the same thickness (the number in nm written beside the incident energy) and slab width (the number in nm written under the resist slab). It can be seen that as the incident energy decreases, the plots from Model 1 and 2 varies more and the broadening increases as a result of SE and FSEs. Model 2 has given a more realistic (similar to the experimental results) energy deposition than Model 1 and the point spread function derived from Model 2 agrees with the fabricated EBL patterns.

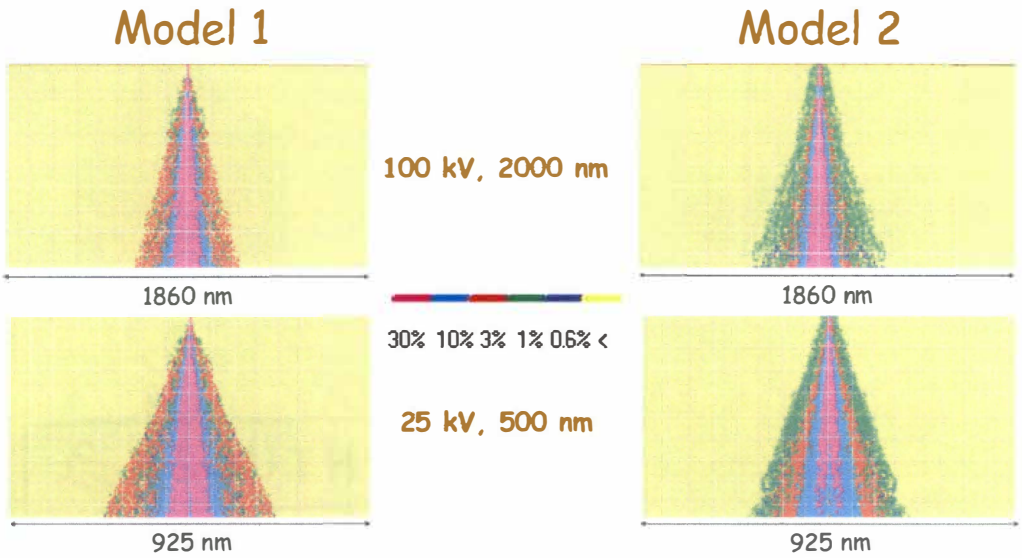


Figure 6-27: The radial energy deposited per volume plots for a point source beam in a free standing PMMA resist slab. Both models 1 and 2 are compared for incident beam energies of 100 and 25 kV on a 2000 and 500 nm thick resist respectively. The energy color bar in the center is explained in section 6.2.1.2.

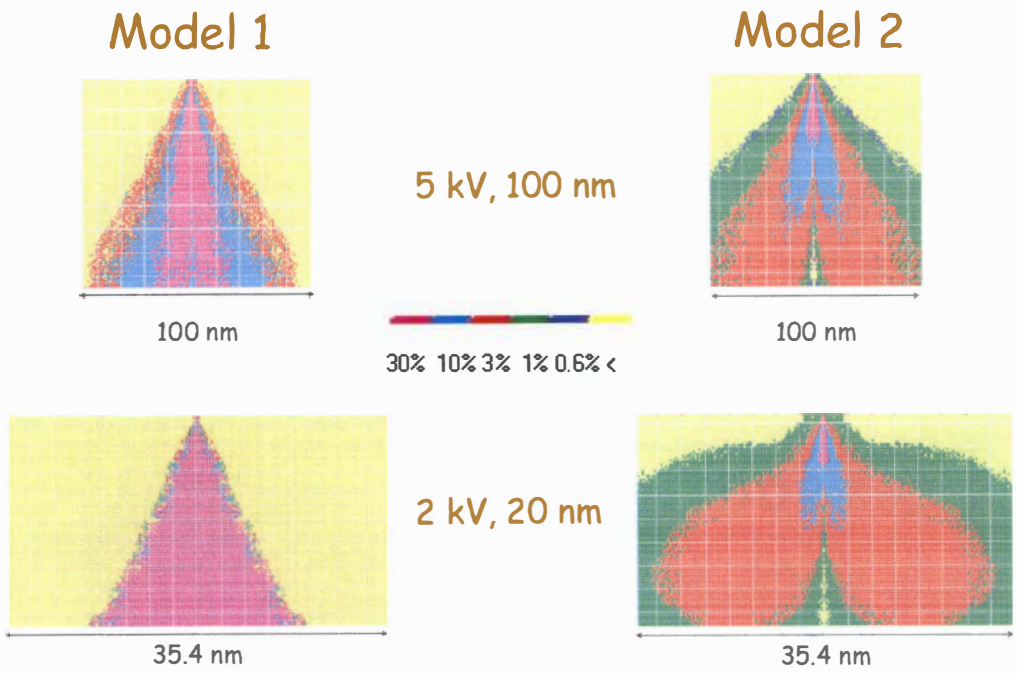


Figure 6-28: The radial energy deposited per volume plots for a point source beam in a free standing PMMA resist slab. Both models 1 and 2 are compared for incident beam energies of 5 and 2 kV on a 100 and 20 nm thick resist respectively. The energy color bar in the center is explained in section 6.2.1.2.

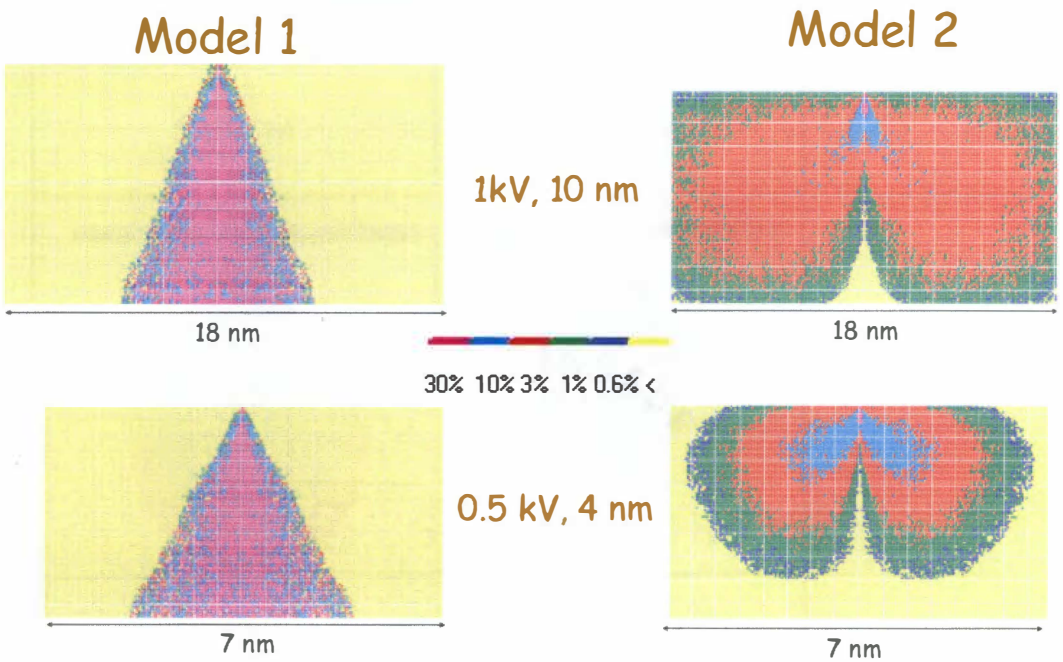


Figure 6-29: The radial energy deposited per volume plots for a point source beam in a free standing PMMA resist slab. Both models 1 and 2 are compared for incident beam energies of 1 and 0.5 kV on a 10 and 4 nm thick resist respectively. The energy color bar in the center is explained in section 6.2.1.2.

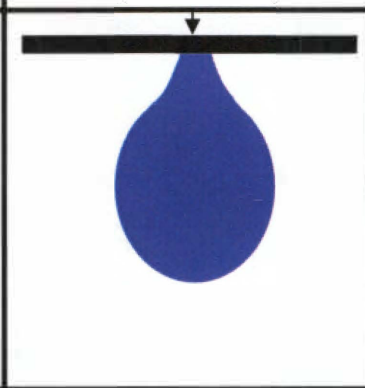
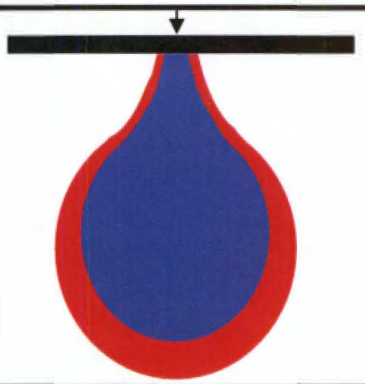
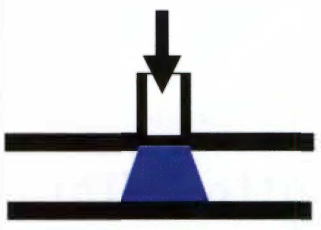
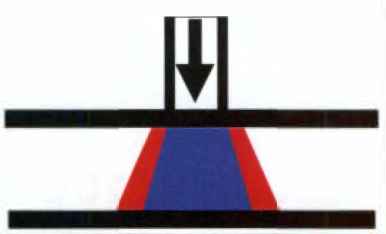
Figure 6-25 and Figure 6-27 through Figure 6-29 are only contour plots. Figure 6-30, includes both the three dimensional and contour energy deposition plots for 20nm PMMA on Si for a 3kV electron beam. The data used in the figure was derived from Model 2, and plotted using Mathematica.

Table 6-5, schematically shows the difference between both Model 1 and 2. Thick resist is defined as the resist having an enough thickness so the cascade of electrons doesn't reach the substrate, and the opposite stands for thin resist.

6.2.1.3. Feature profiles and exposure sensitivity for a point source

Using data such as that shown in Figure 6-25 and Figure 6-27 through Figure 6-26, and the string model, the cross section profile of the feature that will be produced in the resist when the latent image is developed can be predicted together with the dose required to achieve it. The dose required to ensure solubility of the

Table 6-5: Electron Interaction Volume. Model 1 does not include the FSE. Model 2 is equal to Model 1 + FSE. The red volume is caused by secondary and fast secondary electrons.

	Model 1	Model 2
Thick Resist		
Thin Resist		

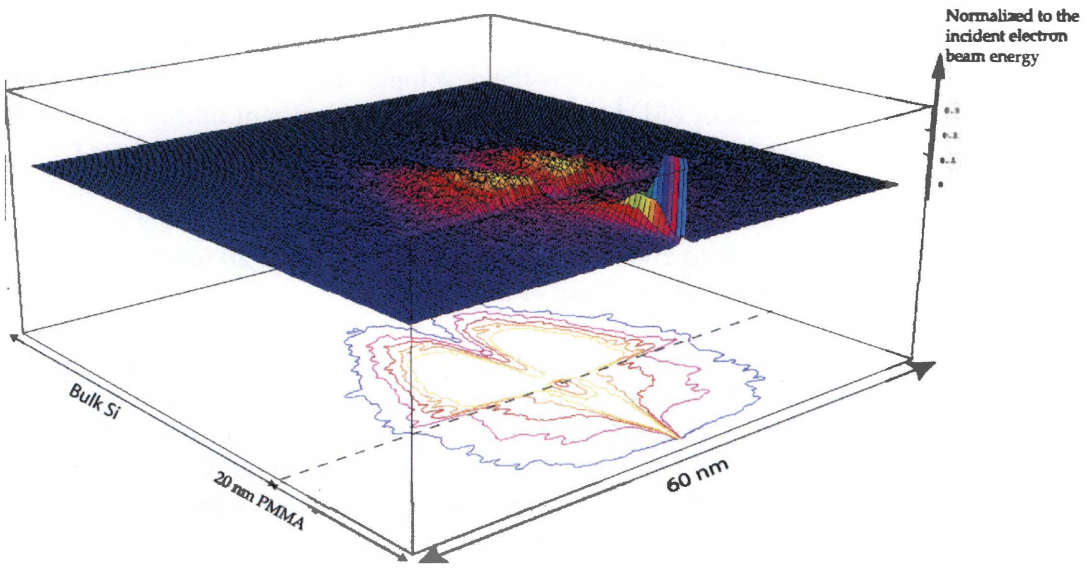


Figure 6-30: It consists of a three dimensional and a contour plot which has been drawn in Mathematica 5.0. The EBL is done on a 20 nm thick PMMA on Silicon at 3 kV.

exposed PMMA during development is 10^{22} eV/cm^3/el. Any region dosed above this value will be assumed to be removed by the developer. The predicted cross-sectional shape and size for 10 nm of PMMA exposed by a 1 keV beam of infinitely small size (i.e. the point source situation illustrated in Figure 6-25(b)) after exposure and development an incident dose of 600 electrons would result in a U-shaped hole with an about 10 nm in diameter width at the surface extending down to about 6 nm in depth, increasing the dose to 20000 electrons would give about 20 nm in total width and extending through the whole depth of the resist.

While these conditions are unrealistic, they do provide basic information on the exposure behavior of the system. For example, in Figure 6-31 it can be seen that as the exposure dose is increased, the feature width initially increases very quickly; then it rises at a reduced rate and eventually reaches a saturation condition where the width remains constant, independent of any further increase in exposure. This would be the correct condition to target for routine exposure because it ensures the critical dimensions will not be affected by any random changes in beam intensity.

For a beam impacting 4 nm thick layer of PMMA at 500 eV (the situation shown in Figure 6-25(c)), the behavior of the system is similar, but as shown in Figure 6-31the saturation dose required has fallen by almost a factor of ten times while the maximum feature width has fallen by only a factor of three times. Thus while writing a pattern would be much faster at 500 eV, even allowing for the decrease in current available from the source at a lower energy, the gain in resolution would be less dramatic. The lateral scattering of the FSE and the consequent energy deposition from the FSE set a lower limit to the size of the exposed region, and this varies only slowly with the incident beam energy.

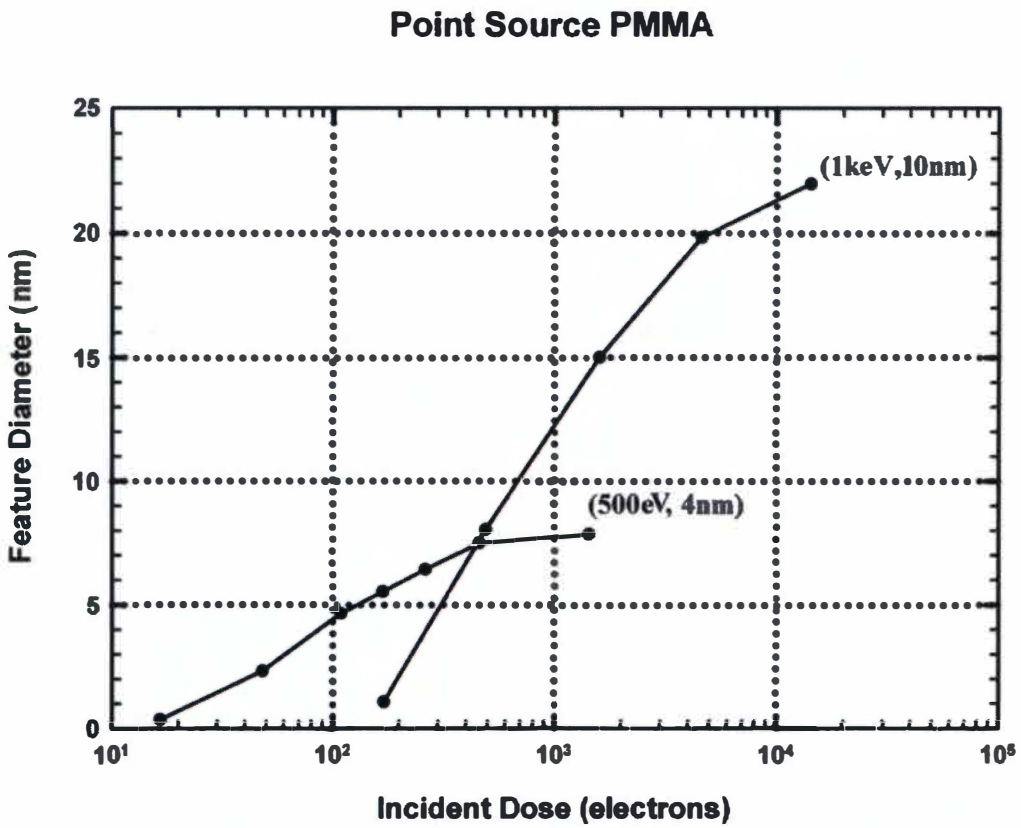


Figure 6-31: Feature diameter in PMMA as a function of incident dose for a point source electron beam with energies of 1 keV onto 10 nm thick PMMA and 0.5 keV onto 4nm thick PMMA respectively. The dose error, which is caused by shot noise is $\frac{1}{\sqrt{N}}$.

Chapter 7

7. Conclusion

The main factors in electron beam lithography (electron beam energy and dose, resist thickness, and charging with the emphasis on low voltage electron beams) were investigated experimentally. An advanced double Monte Carlo model was introduced and simulation was conducted to study electron scattering and energy deposition in low voltage electron beam lithography. Using an approximate representation of the electron matter interactions via the continuous slowing down approximation, the research simulated the spatial distribution of energy losses of the electrons released in electron beam lithography. The presented model showed qualitative agreement with the experimental results. As Broers' hypothesis stated, in a vanishingly thin resist layer, fast secondary electrons are predicted to dominate the energy deposition profile over a substantial volume. These fast electrons will make nanometer lithography difficult even with resist layers no more than a few monolayers in thickness. This study confirms his hypothesis that fast secondary electrons play an essential role in defining the spatial limit of high resolution electron beam lithography.

Calculations show that the dose required to expose the resist falls very rapidly as the energy is reduced, permitting increased speed of the lithography by a factor of about 10,000 times. Saturation doses were calculated at low energies, which would give a useful condition to target for routine exposure because it ensures the critical dimensions will not be affected by any random changes in beam intensity. This property would be valuable for non-industrial electron beam writers. Additionally, it is expected that other organic resists based on scission will suffer from the same limits as PMMA, because, organic bonds have relatively low energy.

Fast secondary electrons are not the only resolution factor in electron beam lithography. As feature size gets smaller, a smaller dose is required, causing the shot noise (Poisson noise) to become more noticeable. To reduce the effect of shot noise, less sensitive resists with high contrast, such as inorganic resists need to be used. Moreover, since polymer resist is not an atomic resist, structure of the resist needs to be considered as a resolution limitation.

New techniques such as ion beam lithography may provide an alternative solution to high resolution lithography. Their small wavelength causes them to have almost no Abbe's aberration limit. Ions don't generate fast secondary electrons (iSE). Their high stopping power offers efficient lithography.

Also from section 5.5.2 it can be concluded that CD Metrology will require the development of new algorithms, and CD-ion SEMs (SIM) will need modified detectors, charge control technology, and very different operating parameters compared to existing CD-eSEMs.

I believe that SIM would be a useful tool, if stripped ions are used. Because otherwise the secondary electrons are being emitted by the ion projectile and therefore reduce the quality of information deduced from the target.

It is still probably not possible to pattern the entire Encyclopedia Britannica on the head of a pin, but this is not far off. Now that the technology has matured, it becomes something to be used as a tool for research, and not merely the object of such research. Advanced lithography systems are available in many labs around the world. SEM-based systems can be found in literally hundreds of university laboratories. The materials scientist, the physical scientist, and the biologist can all benefit from new research directions focused on the nano-scale world. Indeed, as Feynman said, "There is still plenty of room at the bottom."

List of References

1. R. P. Feynman, "There's Plenty of Room at the Bottom: An Invitation to Enter a New Field of Physics", in *Secondary* "There's Plenty of Room at the Bottom: An Invitation to Enter a New Field of Physics". 1960.
2. R. P. Feynman, "There's plenty of room at the bottom [data storage]", Journal of Microelectromechanical Systems 1(1), pp. 60, 1992.
3. A. N. Broers, "Resolution limits of PMMA resist for exposure with 50 kV electrons", Journal of the Electrochemical Society 128(1), pp. 166, 1981.
4. D. C. Joy, "Monte Carlo modeling for electron microscopy and microanalysis", Oxford University Press, 1995.
5. K. C. A. Smith, "Ph.D. Dissertation", 1956.
6. H. C. Pfeiffer, J. Vac. Sci. Technol. 12, pp. 1170, 1975.
7. H. C. Pfeiffer, "Variable spot shaping for electron-beam lithography", Journal of Vacuum Science and Technology 15, pp. 887, 1978.
8. A. N. Broers, "A new high resolution electron probe", Journal of Vacuum Science and Technology 10, pp. 979, 1973.
9. A. N. Broers, "Electron and ion probes", in, Electrochemical Soc., Inc: Houston, TX, USA, 1972.
10. D. R. Herriott, R. J. Collier, D. S. Alles, and J. W. Stafford, "EBES: A practical electron lithographic system", IEEE Transactions on Electron Devices 22(7), pp. 385, 1975.
11. H. C. Pfeiffer, T. R. Groves, and T. H. Newman, "High-throughput, high-resolution electron-beam lithography", IBM Journal of Research and Development 32(4), pp. 494, 1988.
12. J. T. Clemens, "Electron beam lithography: a `gating' item", Solid State Technology 32(3), pp. 69, 1989.
13. A. N. Broers, "Resolution limits for electron-beam lithography", IBM Journal of Research and Development 32(4), pp. 502, 1988.
14. D. R. Herriott, "Electron beam lithography", in 20: Anaheim, CA, USA, 1982.
15. A. Olkhovets and H. G. Craighead, "Low voltage electron beam lithography in PMMA", Journal of Vacuum Science & Technology B (Microelectronics and Nanometer Structures) 17(4), pp. 1366, 1999.
16. D. S. Alles, F. R. Ashley, A. M. Johnson, and R. L. Townsend, "Control system design and alignment methods for electron lithography ", Journal of Vacuum Science & Technology 12, pp. 1252, 1975.
17. T. R. Bedson, P. D. Nellist, R. E. Palmer, and J. P. Wilcoxon, "Direct electron beam writing of nanostructures using passivated gold clusters", in 53, Elsevier: Rome, Italy, 2000.
18. K. Edinger, H. Becht, R. Becker, V. Bert, V. A. Boegli, M. Budach, S. Gohde, J. Guyot, T. Hofmann, O. Hoinkis, A. Kaya, H. W. Koops, P. Spies, B. Weyrauch, and J. Bihr, "A novel electron-beam-based

photomask repair tool", in 5256, SPIE-Int. Soc. Opt. Eng: Monterey, CA, USA, 2003.
19. H. Hatakeyama, T. Omori, K. Hashimoto, and M. Yamayuchi, "Fabrication of SAW devices using SEM-based electron beam lithography and lift-off technique for lab use", in Vol.3, IEEE: Montreal, Que., Canada, 2004.
20. T. Liang, A. R. Stivers, M. Penn, D. Bald, C. Sethi, V. Boegli, M. Budach, K. Edinger, and P. Spies, "Demonstration of damage-free mask repair using electron beam-induced processes", in 5446, SPIE-Int. Soc. Opt. Eng: Yokohama, Japan, 2004.
21. K. Molhave, D. N. Madsen, and P. Boggild, "A simple electron-beam lithography system", Ultramicroscopy 102(3), pp. 215, 2005.
22. S. Myung-Sik, R. Jin-Koo, L. Jun-Ha, and H. Ho-Jung, "Monte Carlo electron beam lithography simulation of sub-0.1- μm T-gate process for millimeter-wave HEMTs considering 50-kV and 100-kV electron beam exposure systems", Journal of the Korean Physical Society 45(2), pp. 540, 2004.
23. T. Nakasugi, A. Ando, R. Inanami, N. Sasaki, T. Ota, O. Nagano, Y. Yamazaki, K. Sugihara, I. Mori, M. Miyoshi, K. Okumura, and A. Miura, "Maskless lithography: a low-energy electron-beam direct writing system with a common CP aperture and the recent progress", in 5037, SPIE-Int. Soc. Opt. Eng: Santa Clara, CA, USA, 2003.
24. K. Yamazaki and H. Namatsu, "5-nm-order electron-beam lithography for nanodevice fabrication", in, Japan Soc. of Appl. Phys: Tokyo, Japan, 2003.
25. G. Mollenstedt and R. Speidel, Physikalische Blatter 16, pp. 192, 1960.
26. R. F. M. Thornley, A. V. Brown, and A. J. Speth, "Electron beam recording of digital information", IEEE Transactions on Electronic Computers 13(1), pp. 36, 1964.
27. R. F. M. Thornley, Journal of the Electrochemical Society 112, pp. 1151, 1965.
28. O. C. Wells, T. E. Everhart, and R. K. Matta, "Automatic positioning of device elctrodes using the scanning electron microscope", IEEE Transactions on Electron Devices ED-12(10), pp. 556, 1965.
29. T. H. P. Chang and W. C. Nixon, "Limits of electron-beam nonthermal interactions", in, San Francisco Press, Inc: Berkeley, CA, 1967.
30. I. Haller, M. Hatzakis, and r. Srinivasan, IBM Journal of Research and Development 12, pp. 251, 1968.
31. M. Hatzakis, "Electron resists for microcircuit and mask production", Journal of the Electrochemical Society 116(7), pp. 1033, 1969.
32. L. Reimer, "Transmission electron microscopy : physics of image formation and microanalysis", New York, Berlin, 1984.
33. C. K. Crawford, Mounting methods and operating characteristics for LaB6, in *SEM/1979/I SEM, Inc.* 1979, AMF: O'Hare, IL p. 19.

34. J. Orloff, "A comparison of lanthanum hexaboride, cold field emission and thermal field emission electron guns for low voltage scanning electron microscopy", in: Ocean City, MD, USA, 1984.
35. L. A. Christman, G. A. Schwind, and L. W. Swanson, "A comparison of CeB6 and LaB6 thermionic cathodes", in *European Conference on Magnetic Sensors and Actuators*, G.W. Bailey and E. Hall, San Francisco Press: 1991.
36. J. Orloff, "Thermal field emission for low voltage scanning electron microscopy", Journal of Microscopy 140, pp. 303, 1985.
37. D. W. Tuggle and S. G. Watson, "A low-voltage field-emission column with a Schottky emitter", in *European Conference on Magnetic Sensors and Actuators*, G.W. Bailey, San Francisco Press: 1984.
38. D. W. Tuggle, J. Z. Li, and L. W. Swanson, "Point cathodes for use in virtual source electron optics", Journal of Microscopy 140, pp. 293, 1985.
39. L. M. Welter, Application of a field emission course to SEM, in *Principles and Techniques of Scanning Electron Microscopy*, M.A. Hayat, Editor. 1975, Van Nostrand Reinhold: New York. p. 195.
40. L. W. Swanson, Field emission source optics, in *Electron Optical Systems.* 1984, SEM Inc.: O'Hare, IL. p. 137.
41. L. W. Swanson, "Comparative study of the zirconiated and built-up W thermal-field cathode", Journal of Vacuum Science & Technology 12(6), pp. 1228, 1975.
42. D. Tuggle, L. W. Swanson, and J. Orloff, "Application of a thermal field emission source for high resolution, high current e-beam microprobes", in 16: Boston, MA, USA, 1979.
43. K. D. van der Mast, "Field emission, developments and possibilities", Journal of Microscopy 130, pp. 309, 1983.
44. M. Born, E. Wolf, and A. B. Bahatia, "Principles of Optics", Cambridge University Press, Cambridge, UK ; New York, 7, 2002.
45. P. Grivet, M. Y. Bernard, and A. L. Septier, "Electron optics ", Pergamon Press, Oxford, New York, 2, 1972.
46. D. S. Alles and M. G. R. Thomson, The evolution of electron-beam pattern generators for integrated circuit masks at AT&T Bell Laboratories, in *VLSI electronics. Microstructure science. Vol.16. Lithography for VLSI.* 1987, Academic Press. p. 57.
47. Resist vendors include: Micro-Chem, OCG Microelectronic Materials Inc., Microlithography Chemical Corp., Mead Chemical Co., Sigma-Aldrich, Toray Ind., Mead Chemical Co., Celanese Corp., Microchemicals Co.
48. K. Edinger, V. A. Boegli, M. Budach, O. Hoinkis, B. Weyrauch, H. W. P. Koops, J. Bihr, and J. Greiser, "Application of electron-beam induced processes to mask repair", in 5130, SPIE-Int. Soc. Opt. Eng: Yokohama, Japan, 2003.
49. W. H. Brunger, "X-ray mask repair by electron beam induced metal deposition", in 9: Vienna, Austria, 1989.

50. M. Padmanaban, E. L. Alemy, R. R. Dammel, K. Woo-Kyu, T. Kudo, L. Sang-Ho, D. S. McKenzie, A. Orsi, D. Rahman, C. Wan-Lin, R. M. Sadjadi, W. R. Livesay, and M. F. Ross, "E-beam curing effects on the etch and CD-SEM stability of 193 nm resists", in 4690, SPIE-Int. Soc. Opt. Eng: Santa Clara, CA, USA, 2002.
51. M. A. Bolorizadeh and M. E. Rudd, "Angular and energy dependence of cross sections for ejection of electrons from water vapor. I. 50-2000-eV electron impact", Physical Review A 33(2), pp. 882, 1986.
52. C. B. Opal, W. K. Peterson, and E. C. Beaty, "Measurements of secondary-electron spectra produced by electron impact ionization of a number of simple gases", Journal of Chemical Physics 55(8), pp. 4100, 1971.
53. D. F. Register and S. Trajmar, "Differential, integral, and momentum-transfer cross sections for elastic electron scattering by neon: 5 to 100 eV", Physical Review A 29(4), pp. 1785, 1984.
54. H. Wyrwich and F. Lenz, "Calculation of the differential cross-section for the scattering of medium-velocity electrons at atoms from Hartree functions", Zeitschrift fur Naturforschung A (Astrophysik, Physik und Physikalische Chemie) 13a(7), pp. 515, 1958.
55. F. Lenz, "On the scattering of electrons of intermediate energy through the smallest angles", Zeitschrift fur Naturforschung A (Astrophysik, Physik und Physikalische Chemie) 9a, pp. 185, 1954.
56. L. T. Chadderton, "Radiation damage in crystals", Methuen; New York, J. Wiley, London, 1965.
57. T. F. O'Malley and R. W. Crompton, "Electron-neon scattering length and S-wave phaseshifts from drift velocities", Journal of Physics B (Atomic and Molecular Physics) 13(17), pp. 3451, 1980.
58. R. W. Wagenaar and F. J. de Heer, "Total cross sections for electron scattering from Ne, Ar, Kr and Xe", Journal of Physics B (Atomic and Molecular Physics) 13(19), pp. 3855, 1980.
59. W. E. Kauppila, T. S. Stein, J. H. Smart, M. S. Dababneh, Y. K. Ho, J. P. Downing, and V. Pol, "Measurements of total scattering cross sections for intermediate-energy positrons and electrons colliding with helium, neon, and argon", Physical Review A 24(2), pp. 725, 1981.
60. F. J. de Heer, R. H. J. Jansen, and W. van der Kaay, "Total cross sections for electron scattering by Ne, Ar, Kr and Xe", Journal of Physics B (Atomic and Molecular Physics) 12(6), pp. 979, 1979.
61. W. C. Fon and K. A. Berrington, "The elastic scattering of electrons from inert gases. II. Neon", Journal of Physics B (Atomic and Molecular Physics) 14(2), pp. 323, 1981.
62. M. Schaper and H. Scheibner, "Absolutbestimmung der Gesamtanregungsquerschnitte der Edelgase durch Elektronenstob", Beitrage aus der Plasmaphysik 9, pp. 45, 1969.
63. J. C. H. Spence, "Experimental high-resolution electron microscopy", New York, Oxford : Clarendon Press, 1980.

64. E. W. McDaniel, "Atomic collisions : electron and photon projectiles", Wiley, 1989.
65. N. F. S. Mott, H. S. W. Massey, Sir, and a. joint, "The theory of atomic collisions", Clarendon Press, Oxford, 3d, 1965.
66. B.-K. Teo and P. A. Lee, "Ab initio calculations of amplitude and phase functions for extended x-ray absorption fine structure spectroscopy", Journal of the American Chemical Society 101(11), pp. 2815, 1979.
67. J. A. Ibers and B. K. Vainschtein, Scattering amplitudes for electrons, in *International tables for x-ray crystallography*, K. Lonsdale, Editor. 1962, Kynoch: Birmingam.
68. H. P. Hanson, F. Herman, J. D. Lea, and S. Skillman, "H.F.S. Atomic scattering factors", Acta Crystallographica 17, pp. 1040, 1964.
69. D. T. Cromer and J. T. Waber, "Scattering factors computed from relativistic Dirac-Slater wave functions", Acta Crystallographica 18, pp. 104, 1965.
70. P. Rez, "Elastic scattering of electrons by atoms", in, Scanning Electron Microscopy: Monterey, CA, USA, 1984.
71. M. Fink and J. Kessler, "Absolute measurements of elastic cross section for small-angle scattering of electrons from N_2 and O_2", Journal of Chemical Physics 47(5), pp. 1780, 1967.
72. Y. Kainuma, "The theory of Kikuchi patterns", Acta Crystallographica 8, pp. 247, 1955.
73. P. B. Hirsch, "Electron microscopy of thin crystals", R.E. Krieger Pub. Co., Huntington, N.Y., 1977.
74. J. Tafto and O. L. Krivanek, "Characteristic energy losses from channeled 100 keV electrons", in 194: Lyons, France, 1982.
75. C. R. Hall, "On the production of characteristic X-rays in thin metal crystals", Proceedings of the Royal Society of London, Series A (Mathematical and Physical Sciences) 295(1441), pp. 140, 1966.
76. D. Cherns and A. Howie, "Characteristic X-ray production in thin crystals", Zeitschrift fur Naturforschung A (Astrophysik, Physik und Physikalische Chemie) 28a(5), pp. 565, 1973.
77. J. C. H. Spence and J. Taft, "ALCHEMI: a new technique for locating atoms in small crystals", in 130: London, UK, 1983.
78. A. Howie, "Diffraction channelling of fast particles in crystals", in, Pergamon Press Inc.: Melbourne, 1966.
79. J. U. Andersen, E. Bonderup, E. Laegsgaard, B. B. Marsh, and A. H. Sorensen, "Axial channeling radiation from MeV electrons", Nuclear Instruments and Methods 194(1-3), pp. 209, 1982.
80. R. F. Willis and B. K. Agrawal, "Vibrational spectroscopy of adsorbates", New York, Berlin, 1980.
81. H. Ibach and D. L. Mills, "Electron energy loss spectroscopy and surface vibrations", Academic Press, New York, 1982.
82. R. F. Egerton, "Electron energy-loss spectroscopy in the electron microscope", Plenum Press, New York, 2nd, 1996.

83. M. A. Coplan, J. H. Moore, and J. P. Doering, "(e, 2e) spectroscopy", Reviews of Modern Physics 66(3), pp. 985, 1994.
84. R. A. Bartynski, R. J. Gaylord, T. Gustafsson, and E. W. Plummer, "Angle-resolved photoemission study of the surface and bulk electronic structure of Mg(0001) and Mg(11 -2 0)", Physical Review B 33(6), pp. 3644, 1986.
85. T. D. Märk and G. H. Dunn, "Electron impact ionization", New York, Wien, 1985.
86. H. Bethe, "Theory of passage of swift corpuscular rays through matter", Annalen der Physik 5(3), pp. 325, 1930.
87. H. Bethe, "Scattering of electrons", Zeitschrift fur Physik 76(5-6), pp. 293, 1932.
88. M. Inokuti, "Inelastic collisions of fast charged particles with atoms and molecules-the Bethe theory revisited", Reviews of Modern Physics 43(3), pp. 297, 1971.
89. M. Inokuti, Y. Itikawa, and J. E. Turner, "Addenda: Inelastic collisions of fast charged particles with atoms and molecules-The Bethe theory revisited [Rev. Mod. Phys. 43, 297 (1971)]", Reviews of Modern Physics 50(1), pp. 23, 1978.
90. J. J. Thomson, "Ionisation by moving particles", Philosophical Magazine 28, pp. 449, 1912.
91. L. D. Landau, L. D. Landau, and a. joint, "Quantum mechanics, non-relativistic theory", Pergamon Press; Reading, Mass., Addison-Wesley Pub. Co., London, 1958.
92. N. F. Mott, "Collision between two electrons", Proceedings of the Royal Society of London 126, pp. 259, 1930.
93. E. J. Williams, "Passage of α-rays and β-rays through matter", Memoirs and Proceedings of the Manchester Literary and Philosophical Society 71, pp. 23, 1926.
94. L. H. Thomas, "Effect of orbital velocity of electrons in heavy atoms on the stopping of α-particles", Proceedings of the Cambridge Philosophical Society 23, pp. 713, 1927.
95. M. Gryzinski, "Two-Particle collisions. I. General relations for collisions in the laboratory system", Physical Review 138(2A), pp. A305, 1965.
96. M. Gryzinski, "Classical theory of electronic and ionic in elastic collisions", Physical Review 115(2), pp. 374, 1959.
97. M. Gryzinski, "Two-particle collisions. II. Coulomb collisions in the laboratory system of coordinates", Physical Review 138(2A), pp. A322, 1965.
98. M. Gryzinski, "Radially oscillating electron - the basis of the classical model of the atom", Physical Review Letters 14(26), pp. 1059, 1965.
99. M. R. H. Rudge, "Theory of the ionization of atoms by electron impact", Reviews of Modern Physics 40(3), pp. 564, 1968.
100. J. H. Scofield, "K- and L-shell ionization of atoms by relativistic electrons", Physical Review A 18(3), pp. 963, 1978.

101. I. Bray and A. T. Stelbovics, "Convergent-close-coupling calculations of electron-hydrogen scattering", Physical Review A 46(11), pp. 6995, 1992.
102. A. Temkin, "Nonadiabatic theory of electron - hydrogen scattering", Physical Review 126(1), pp. 130, 1962.
103. D. K. Jain and S. P. Khare, "Ionizing collisions of electrons with C_2H_4 and C_2H_6", Indian Journal of Pure and Applied Physics 14(3), pp. 201, 1976.
104. S. P. Khare, S. Prakash, and W. J. Meath, "Dissociative ionization of NH_3 and H_2O molecules by electron impact", International Journal of Mass Spectrometry and Ion Processes 88(2-3), pp. 299, 1989.
105. S. Pal, S. Prakash, and S. Kumar, "Differential cross sections for the ionization of the CO molecule by electron impact", International Journal of Mass Spectrometry 184(2-3), pp. 201, 1999.
106. W. F. Miller and R. L. Platzman, "On the theory of the inelastic scattering of electrons by helium atoms", Proceedings of the Physical Society. Section A 70, pp. 299, 1957.
107. K. Yong-Ki and M. E. Rudd, "Binary-encounter-dipole model for electron-impact ionization", Physical Review A 50(5), pp. 3954, 1994.
108. L. Vriens, Binary-encounter and classical collision theories, in *Case studies in atomic collision physics. I.* 1969, North-Holland. p. 337.
109. H. Deutsch and T. D. Mark, "Calculation of absolute electron impact ionization cross-section functions for single ionization of He, Ne, Ar, Kr, Xe, N and F", International Journal of Mass Spectrometry and Ion Processes 79(3), pp. 1, 1987.
110. D. Margreiter, H. Deutsch, and T. D. Mark, "Absolute electron impact cross sections for single ionization of metastable atoms of H, He, Ne, Ar, Kr, Xe and Rn", Contributions to Plasma Physics 30(4), pp. 487, 1990.
111. H. Deutsch, K. Becker, S. Matt, and T. D. Mark, "Calculated cross sections for the electron-impact ionization of metastable atoms", Journal of Physics B (Atomic, Molecular and Optical Physics) 32(17), pp. 4249, 1999.
112. H. Deutsch, K. Becker, S. Matt, and T. D. Mark, "Theoretical determination of absolute electron-impact ionization cross sections of molecules", International Journal of Mass Spectrometry 197, pp. 37, 2000.
113. D. Margreiter, H. Deutsch, and T. D. Mark, "A semiclassical approach to the calculation of electron impact ionization cross-sections of atoms: from hydrogen to uranium", International Journal of Mass Spectrometry and Ion Processes 139, pp. 127, 1994.
114. H. Deutsch, K. Becker, and T. D. Mark, "A semiclassical method for the calculation of cross sections for multiple ionization of atoms by electron impact", Journal of Physics B (Atomic, Molecular and Optical Physics) 29(13), pp. 497, 1996.

115. J. B. Mann, "Ionization cross sections of the elements calculated from mean-square radii of atomic orbitals", Journal of Chemical Physics 46(5), pp. 1646, 1967.
116. P. Tiwari, D. K. Rai, and M. L. Rustgi, "Maximum Ionization Cross Section of Atoms", The Journal of Chemical Physics 50(7), pp. 3040, 1969.
117. H. C. Straub, B. G. Lindsay, K. A. Smith, and R. F. Stebbings, "Absolute partial cross sections for electron-impact ionization of H_2O and D_2O from threshold to 1000 eV", Journal of Chemical Physics 108(1), pp. 109, 1998.
118. N. L. Djuric, I. M. Cadez, and M. V. Kurepa, "H_2O and D_2O total ionization cross-sections by electron impact", International Journal of Mass Spectrometry and Ion Processes 83(3), pp. 7, 1988.
119. J. Schutten, F. J. deHeer, H. R. Moustafa, A. J. H. Boerboom, and J. Kistemaker, "Gross- and partial-ionization cross sections for electrons on water vapor in the energy range 0.1-20 kev", Journal of Chemical Physics 44(10), pp. 3924, 1966.
120. W. Hwang, Y. K. Kim, and M. E. Rudd, "New model for electron-impact ionization cross sections of molecules", Journal of Chemical Physics 104(8), pp. 2956, 1996.
121. V. Saksena, M. S. Kushwaha, and S. P. Khare, "Ionization cross-sections of molecules due to electron impact", Physica B 233(2-3), pp. 201, 1997.
122. V. Saksena, M. S. Kushwaha, and S. P. Khare, "Electron impact ionisation of molecules at high energies", International Journal of Mass Spectrometry and Ion Processes 171(1-3), pp. 1, 1997.
123. H. Bethe and J. Ashkin, "Passage of radiations through matter. " Experimental Nuclear Physics 1, pp. 252, 1953.
124. "Stopping Powers for Electrons and Positrons." International Commission on Radiation Units and Measurements Report No. 37, 1984.
125. M. J. Berger and S. M. Seltzer, "Studies in Penetration of Charged Particles in Matter." Nuclear Science Series Report No. 39, pp. 205, 1964.
126. D. C. Joy and S. Luo, "An empirical stopping power relationship for low-energy electrons", Scanning 11(4), pp. 176, 1989.
127. J. J. Ritsko, L. J. Brillson, R. W. Bigelow, and T. J. Fabish, "Electron energy loss spectroscopy and the optical properties of poly(methyl methacrylate) from 1 to 300 eV", Journal of Chemical Physics 69(9), pp. 3931, 1978.
128. G. Liu and J. E. Guillet, "Application of the "spectroscopic ruler" to studies of the dimensions of flexible macromolecules. 1. Theory", Macromolecules 23(5), pp. 1388, 1990.
129. G. Liu, J. E. Guillet, E. T. B. Al-Takrity, A. D. Jenkins, and D. R. M. Walton, "Application of the "spectroscopic ruler" to studies of the dimensions of flexible macromolecules. 2. Experimental studies of

poly(methyl methacrylate) chains", Macromolecules 23(5), pp. 1393, 1990.

130. B. W. Yates, D. M. Shinozaki, A. Kumar, and W. J. Meath, "The absorption coefficient spectrum of poly(methyl methacrylate) in the soft x-ray region", Journal of Polymer Science, Part B: Polymer Physics 30(2), pp. 185, 1992.
131. P. A. Zimmerman, D. M. Hercules, and A. Benninghoven, "Time-of-flight secondary ion mass spectrometry of poly(alkyl methacrylates)", Analytical Chemistry 65(8), pp. 983, 1993.
132. L. E. Manring, "Thermal degradation of saturated poly(methyl methacrylate)", Macromolecules 21(2), pp. 528, 1988.
133. L. E. Manring, "Thermal degradation of poly(methyl methacrylate). 4. Random side-group scission", Macromolecules 24(11), pp. 3304, 1991.
134. J. Janecek and J. Kolarik, "Secondary relaxations of swollen polymethacrylates and methacrylate copolymers", International Journal of Polymeric Materials 5(1-2), pp. 71, 1976.
135. J. Heijboer, "Secondary loss peaks in glassy amorphous polymers", International Journal of Polymeric Materials 6(1-2), pp. 11, 1977.
136. R. H. G. Brinkhuis and A. J. Schouten, "Thin-film behavior of poly(methyl methacrylates). 1. Monolayers at the air-water interface", Macromolecules 24(7), pp. 1487, 1991.
137. G. Boven, R. H. G. Brinkhuis, E. J. Vorenkamp, and A. J. Schouten, "Interdiffusion of thin polymer layers studied by external reflection infrared spectroscopy", Macromolecules 24(4), pp. 967, 1991.
138. R. H. G. Brinkhuis and A. J. Schouten, "Thin-film behavior of poly(methyl methacrylates). 4. Stereocomplexation of isotactic and syndiotactic poly(methyl methacrylate) at the air-water interface", Macromolecules 25(10), pp. 2725, 1992.
139. R. H. G. Brinkhuis and A. J. Schouten, "Thin-film behavior of poly(methyl methacrylates). 3. Epitaxial crystallization in thin films of isotactic poly(methyl methacrylate) using crystalline Langmuir-Blodgett layers", Macromolecules 25(10), pp. 2717, 1992.
140. R. H. G. Brinkhuis and A. J. Schouten, "Thin-film behavior of poly(methyl methacrylates). 6. Monolayer phase behavior in relation to stereocomplexation in mixed monolayers of i- and s-PMMA", Macromolecules 26(10), pp. 2514, 1993.
141. R. J. Hawryluk, H. I. Smith, A. Soares, and A. M. Hawryluk, "Energy dissipation in a thin polymer film by electron beam scattering: Experiment", Journal of Applied Physics 46, pp. 2526, 1975.
142. J. S. Greeneich, "Developer characteristics of poly-(methyl methacrylate) electron resist", Journal of the Electrochemical Society 122(7), pp. 970, 1975.
143. C. H. Ting, in *Record of the 11th Symposium on Electron, Ion, and Laser Beam Technology*, R.F.M. Thornley, Editor. 1971, San Francisco Press: San Francisco.

144. R. Shimizu, T. Ikuta, T. E. Everhart, and W. J. DeVore, "Experimental and theoretical study of energy dissipation profiles of keV electrons in polymethylmetchacrylate." Journal of Applied Physics 46, pp. 1581, 1975.
145. J. S. Greeneich and T. van Duzer, "An exposure model for electron-sensitive resists", IEEE Transactions on Electron Devices ED-21(5), pp. 286, 1974.
146. I. Adesida, T. E. Everhart, and R. Shimizu, "High resolution electron-beam lithography on thin films", Journal of Vacuum Science & Technology 16(6), pp. 1743, 1979.
147. D. C. Joy, "The spatial resolution limit of electron lithography", Microelectronic Engineering 1(2), pp. 103, 1983.
148. R. E. Jewett, P. I. Hagouel, A. R. Neureuther, and T. Van Duzer, "Line-profile resist development simulation techniques", Polymer Engineering and Science 17(6), pp. 381, 1976.
149. F. H. Dill, A. R. Nuereuther, J. A. Tuttle, and E. J. Walker, "Modeling projection printing of positive photoresists", IEEE Transactions on Electron Devices 22(7), pp. 456, 1975.
150. D. F. Kyser and N. S. Viswanathan, "Monte Carlo simulation of spatially distributed beams in electron-beam lithography", Journal of Vacuum Science and Technology 12(6), pp. 1305, 1975.
151. N. S. Viswanathan, R. Pyle, and D. F. Kyser, "Simulations of lithographic images in electron beam technology", in, Electrochem. Soc: Washington, DC, USA, 1976.
152. A. R. Neureuther, D. F. Kyser, and H. T. Chiu, "Electron-beam resist edge profile simulation", IEEE Transactions on Electron Devices 26(4), pp. 686, 1979.
153. J. S. Greeneich, *8th International Conference on Electron and Ion Beam Technology*, Electrochemical Society: 1980.
154. T. M. Hall, A. Wagner, and L. F. Thompson, "Ion beam exposure characteristics of resists", in 16: Boston, MA, USA, 1979.
155. P. Kurpick, C. O. Reinhold, J. Burgdorfer, and B. Gervais, "Excited-state subshell population of hydrogen atoms after transmission of relativistic H^- ions through thin foils", Physical Review A 58(3), pp. 2183, 1998.
156. L. Hagg, C. O. Reinhold, and J. Burgdorfer, in *Photonic, Electronic, and Atomic Collisions: invited papers of the twentieth International Conference on the Physics of Electronic and Atomic Collisions, Vienna, Austria, 23-29 July 1997 /*, F. Aumayr and H. Winter, Editors. 1998, World Scientific Publishing Co. : Singapore. p. 683.
157. J. Burgdorfer, C. Reinhold, L. Hagg, and F. Meyer, "Interaction of highly charged ions with surfaces", in 49, CSIRO: Canberra, ACT, Australia, 1996.
158. B. Rosner, S. Datz, W. Wu, N. L. Jones, D. R. Schultz, and C. O. Reinhold, "Charge-state dependence of energy loss in random solids", Physical Review A 57(4), pp. 2737, 1998.

159. R. Minniti, S. B. Elston, C. O. Reinhold, J. Y. Lim, and J. BurgdÃ¶rfer, "Measurements of absolute electron-emission spectra from grazing-incidence ion-surface collisions", Physical Review A 57(4), pp. 2731, 1998.
160. M. A. M. J. W. Nastasi and J. K. Hirvonen, "Ion-solid interactions : fundamentals and applications", Cambridge University Press, 1st pbk., 2004.
161. J. Zabloudil, "Electron scattering in solid matter : a theoretical and computational treatise", New York, Berlin, 2005.
162. S. Datz, J. G. del Campo, P. F. Dittner, P. D. Miller, and J. A. Biggerstaff, "Higher-Order Z_1 Effects and Effects of Screening by Bound K Electrons on the Electronic Stopping of Channeled Ions", Physical Review Letters 38(20), pp. 1145, 1977.
163. P. Sigmund, "Stopping of heavy ions : a theoretical approach", Springer, Berlin, 2004.
164. N. Bohr and J. Lindhard, "Electron capture and loss by heavy ions penetrating through matter", Kongelige Danske Videnskabernes Selskab, Matematisk-Fysiske Meddelelser 28(7), pp. 29 pp., 1954.
165. Y. N. Yavlinskii, "Elastic interaction of MeV/amu heavy multicharged ions with solids", in B107, Elsevier: Caen, France, 1996.
166. E. Gerjuoy, "Cross section for energy transfer between two moving particles", Physical Review 148(1), pp. 54, 1966.
167. R. E. Olson, K. H. Berkner, W. G. Graham, R. V. Pyle, A. S. Schlachter, and J. W. Stearns, "Charge-state dependence of electron loss from H by collisions with heavy, highly stripped ions", Physical Review Letters 41(3), pp. 163, 1978.
168. L. H. Toburen and W. E. Wilson, "Distributions in energy and angle of electrons ejected from molecular hydrogen by 0.3-1.5-MeV protons", Physical Review A 5(1), pp. 247, 1972.
169. M. E. Rudd, C. A. Sautter, and C. L. Bailey, "Energy and angular distributions of electrons ejected from hydrogen and helium by 100- to 300-keV protons", Physical Review 151(1), pp. 20, 1966.
170. A. Salin, "Ionization of atomic hydrogen by proton impact", Journal of Physics B (Atomic and Molecular Physics) 2(6), pp. 631, 1969.
171. J. Macek, "Theory of the forward peak in the angular distribution of electrons ejected by fast protons", Physical Review A 1(2), pp. 235, 1970.
172. S. J. Ward and J. H. Macek, "Positronium formation by electron capture from hydrogen-like ions", in 89: Bielefeld, Germany, 1994.
173. M. A. Bolorizadeh and M. E. Rudd, "Angular and energy dependence of cross sections for ejection of electrons from water vapor. II. 15-150-keV proton impact", Physical Review A 33(2), pp. 888, 1986.
174. L. H. Toburen and W. E. Wilson, "Differential cross sections for ionization of argon by 0.3-2-MeV He^{2+} and He^{+} ions", Physical Review A 19(6), pp. 2214, 1979.

175. M. A. Bolorizadeh and M. E. Rudd, "Angular and energy dependence of cross sections for ejection of electrons from water vapor. III. 20-150-keV neutral-hydrogen impact", Physical Review A 33(2), pp. 893, 1986.
176. M. E. Rudd, J. S. Risley, J. Fryar, and R. G. Rolfes, "Angular and energy distribution of electrons from 15- to 150-keV H^0 + He collisions", Physical Review A 21(2), pp. 506, 1980.
177. W. E. Wilson and L. H. Toburen, "Electron emission from proton-hydrocarbon-molecule collisions at 0.3-2.0 MeV", Physical Review A 11(4), pp. 1303, 1975.
178. J. H. Macek and S. Y. Ovchinnikov, "Energy and angular distributions of electrons ejected from atomic hydrogen by low-energy proton impact", Physical Review A 70(5), pp. 052702, 2004.
179. J. Lindhard and M. Scharff, "Stopping power of heavier substances", Physical Review 85, pp. 1058, 1952.
180. J. Lindhard, V. Nielsen, and M. Scharff, "Approximation method in classical scattering by screened coulomb fields (notes on atomic collisions, I)", Kongelige Danske Videnskabernes Selskab, Matematisk-Fysiske Meddelelser 36(10), pp. 32 pp., 1968.
181. N. Matsunami, M. Sataka, and A. Iwase, "Electronic sputtering of oxides by high energy heavy ion impact", in 193, Elsevier: Paris, France, 2002.
182. N. Matsunami, M. Sataka, A. Iwase, and S. Okayasu, "Electronic excitation induced sputtering of insulating and semiconducting oxides by high energy heavy ions", in *Nuclear instruments & methods in physics research. Section B, Beam interactions with materials and atoms* 209, Elsevier: Giardini Naxos, Italy, 2003.
183. I. S. Sharodi, Y. A. Bandurin, and S. S. Pop, "Ion-photon emission during ion bombardment of beryllium surface", in 193, Elsevier: Paris, France, 2002.
184. J. W. Martin, "The local chemical analysis of materials", London, Amsterdam, 2003.
185. P. D. K. J. C. Townsend, N. E. W. joint author. Hartley, and a. joint, "Ion implantation, sputtering and their applications", New York, London, 1976.
186. R. C. Der, T. M. Kavanagh, J. M. Khan, B. P. Curry, and R. J. Fortner, "Production of carbon characteristic X-rays by heavy-ion bombardment", Physical Review Letters 21(26), pp. 1731, 1968.
187. L. A. Giannuzzi, "Particle-induced X-ray analysis using focused ion beams", Scanning 27(4), pp. 165, 2005.
188. D. C. Joy, "SMART-a program to measure SEM resolution and imaging performance", Journal of Microscopy 208(1), pp. 24, 2002.
189. http://www.filmetrics.com.
190. M. A. McCord and T. H. Newman, "Low voltage, high resolution studies of electron beam resist exposure and proximity effect", Journal of Vacuum Science & Technology B 10, pp. 3083, 1992.

191. **K. M. Satyalakshmi, A. Olkhovets, M. G. Metzler, C. K. Harnett, D. M. Tanenbaum, and H. G. Craighead, "Charge induced pattern distortion in low energy electron beam lithography", Journal of Vacuum Science & Technology B 18, pp. 3122, 2000.**

192. **S. L. A tabulated database of measured stopping powers can be found at http://pciserver.bio.utk.edu . For a discussion of this data see D. C. Joy, in *Secondary*.**

193. **K. Murata, D. F. Kyser, and C. H. Ting, "Monte Carlo simulation of fast secondary electron production in electron beam resists", Journal of Applied Physics 52(7), pp. 4396, 1981.**

Appendices

Appendix A

The Continuing Throughput Challenge

Figure A-1 illustrates why maskless lithography today faces a serious throughput challenge. The chart shows the electron lithography EL tool throughput trend in wafer per hour (wph) and in pixels/sec. As previously mentioned, the first EL-1 tool generation had a record throughput of 22wph in 1975. By 1993, after two decades and significant innovation and investment, the throughput of EL-4 had declined to 1wph. The pixel rate of exposure had increased from 2×10^7 to 2×10^9 - two orders-of-magnitude improvement in writing speed. However, the minimum feature size went from 2μm to 0.25μm, and the wafer size went from 57mm to 200mm, increasing the number of pixels to be exposed by three orders-of-magnitude! E-beam direct-write technology clearly had not kept pace with the pixel growth in the semiconductor industry and with Moore's Law.

This trend is continuing. Today, another decade later, the fastest commercially available e-beam direct-write tools require more than 10 hr for the exposure of a single 200mm wafer. The fact that some semiconductor companies still use e-beam direct-write tools [8, 9] under these conditions indicates a very strong demand for maskless lithography. The superior resolution capability of e-beam systems is one additional feature that is exploited during prototyping. For e-beam lithography to become a viable alternative to optical lithography in manufacturing future ICs, however, a quantum leap in exposure efficiency is needed.

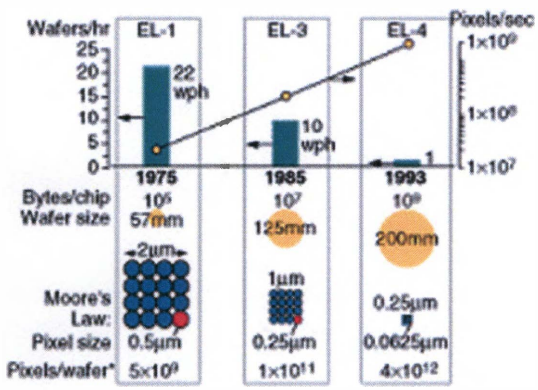


Figure A-1: E-beam throughput trend in wafers/hr and pixels/sec for IBM's EL systems, as contrasted with the trends in wafer and pixel size (*at 50% density).

COST

The progress in the integrated circuit industry over the last 30 years has been driven by dramatic improvements in cost per function in circuits. For the next generation of lithography technology, whether it is based on optical or electron beam, it must be cost effective in order to be consistent with the industry expectations. In estimating the cost of printing a lithographic pattern on a wafer, there are three main elements:

1) The cost of operating the exposure tool, which is proportional to its price divided by its throughput.

2) The mask cost which is the price of the mask divided by the number of wafers to be printed with it.

3) The cost of the resist materials and development of the image. The choice of the next generation lithography technology is likely to be made on this basis rather than on strictly on technical grounds since there are several alternatives that can achieve similar results but at different degrees of difficulty and cost.

Appendix B

There are three various cathode emission mechanisms; thermionic, cold field, and Schottky field emission.

(a) Thermionic emission occurs when enough energy is supplied to the emitter so that electrons can overcome the work function energy, E_W of the material and escape from the material. When the emitter material is heated to a high temperature, a fraction of the electrons at the Fermi level (E_F), acquire enough energy to overcome E_W and escape into the vacuum. The cathode current density, J_C (A/cm^2) obtained from an emitter by thermionic emission is expressed by the Richardson–Dushman equation:

$$J_C = A_C T^2 \exp(-\frac{E_W}{k_B T}) \qquad \text{(B,1)}$$

, where $A_c = \frac{4\pi m_e k_B e}{h^3} = 120.2\ \text{A/cm}^2K^2$, Richardson's constant, is a constant for all thermionic emitters, T is the absolute temperature, and k_B is Boltzmann's Constant. To reduce evaporation of the electron gun's filament, it's desirable to operate the filament at lower temperatures. This is achieved through using a filament material with a lower work function.

(b) Cold field emission, CFE, refers to the fact that the filament in the instrument's electron gun operates at room temperature, limiting the energy spread of the electron beam to about 0.5 eV. Such a low energy spread coupled with the small diameter of the electron source generates the highly coherent beam needed for recording high-quality electron holograms.

(c) Schottky field emission (SFE) has largely replaced earlier source technologies based on either thermionic tungsten and LaB_6 emission or cold field emission. Schottky and cold-field emission are superior to thermionic sources in terms of source size, brightness, and lifetime. Both are up to 1000 times smaller and up to 100 times brighter than thermionic emitters. Schottky emission is preferred over cold field emission because it provides higher stability and is easier to operate. Schottky emission's greater stability and usability are interrelated. Schottky emitters have a lower work function than cold field emitters, meaning the Schottky emitter requires less electrical field than the cold field emitter to achieve the same emission brightness. The electric field at the emitter is determined by the extraction voltage applied, the spacing between emitter and extraction element, and the sharpness and size of the emitter. The smaller and sharper the emitter, the stronger the electric field for a given voltage. For practical reasons, the extraction voltage used in an electron beam instrument is limited, as is the range of emitter to extractor spacing. Because of these practical limitations to achieve usable emission brightness, the higher work

function cold field emitter inevitably has a smaller radius (typically 0.1 μm) compared to the Schottky emitter (typical radius: 0.4 - 1.0 μm).

Beam noise is the time-dependent fluctuation in beam current. Describing the relationship simply, beam noise is inversely proportional to the emission area. Emission area is dependent on emitter radius. If all conditions are the same, the smaller the emission area, the higher the noise. Cold field emission is more noisy than Schottky emission simply because of the emission area (i.e. radius) size differences.

Another contributing factor to noise is emitter temperature. Schottky emission noise is caused by the surface Brownian motion of the W and Zr emitter atoms at 1800 ºC. The CFE is operated at room temperature, and one might think the noise caused by the surface Brownian motion of the W emitter atoms at 25 degrees C would be less. Unfortunately, in all real vacuum systems, residual gas adsorbs onto the CFE. It is the surface Brownian motion (which can be significant at room temperature) of these absorbed gases that is partly responsible for the noise in cold field emission.

Deformation of the emission area is another factor affecting long-term emission stability and usability. In all electron columns, residual gases are present. When a high energy electron hits a residual gas molecule, a positive ion can be created. This ion is accelerated back to the emitter and bombards the emission area. Ion bombardment will mechanically deform an emitter's surface. Because Schottky field emitters operate at 1800 ºC, the surface mobility is high enough to anneal such deformations in a reasonable time. The room temperature CFE will not anneal such deformations. To repair the CFE, it is necessary to periodically "flash" the emitter. The flashing process is simple heating of the emitter to allow deformations to be annealed and to remove the adsorbed molecules, just as occurs automatically with Schottky emitter use. The CFE flashing process not only interrupts work in progress, it eventually leads to end-of-life for the cold field emitter. Each time a CFE is flashed in the absence of an electric field, the emitter radius grows slightly. Ultimately, the tip radius grows so large to the extent that sufficient electric field cannot be achieved. Schottky emitters do not grow at these elevated temperatures because the Schottky emitter end-form is in thermal-field equilibrium.

Schottky emission vacuum requirements are less stringent than cold field emission vacuum requirements, reducing equipment and maintenance costs. Also, Schottky emitter lifetimes are very long compared to other sources, meaning a reduction in time-consuming and expensive source replacement. The table below reviews the key properties of the various electron sources. Schottky emission most closely matches ideal source properties.

Appendix C

Following is the Monte Carlo code used in this research. It is programmed to do the needed calculations for two layer materials. The code was written in Visual Basic 6.0.

```
'(c) DCJ & Mehdi Bolorizadeh November 2003
'complaints, bug reports etc to mbolori@utk.edu
'Version 1-1
'This is a modified version of DCJ April 2003 code. Except "Energy Plot 1", which is
'based on plural scattering for one layer material. The rest of the commands are based
'on single scattering for two layer materials.

Option Explicit        'declare all variables
Dim a_step, b_step, inc_energy, tilt, range, b, ga
Dim al, al_a(1 To 2), ak, er, lam_a(1 To 2), sg(1 To 2), sg_a(1 To 2)
' al_a is the screening factor (In Rutherford elastic cross section)
Dim X, Y, z, xn, yn, zn
Dim center, BS_coeff, e_min, Transmit_coeff
Dim two_pi, beam_range, the_top
Dim ca, cb, cc, cx, cy, cz
Dim nu, cp, sp, an, an_m, an_n, s_tilt, c_tilt
Dim h, i, j, k, l, click  As Integer
Dim plot_test, r_val, z_val, color_value, transmit As Integer
Dim traj_num, bs_yield, num As Long
Dim at_num(1 To 2), at_wht(1 To 2), density(1 To 2), mn_ion_pot(1 To 2),
m_t_step(1 To 2)
Dim Mass_abs, thick, thicksub, thicktotal, sp_rad, s_en, del_E, se_yield
Dim LH_edge, RH_edge, bottom
Dim se_gen, m_f_p, SE_coeff
Dim plot_scale, center_x, center_y, radial, r_step, z_step
Dim E(1 To 51) As Single
Dim radius(0 To 99) As Single
Dim data_Z(1 To 15) As Single
Dim data_A(1 To 15) As Single
Dim data_rho(1 To 15) As Single
Dim data_Ec(1 To 15) As Single
Dim data_MABS(1 To 15) As Single
Dim data_lm(1 To 15) As Single  'se mfp
Dim data_en(1 To 15) As Single  'see generation energy
Dim E_deposit(0 To 300, 0 To 300) As Single 'the data array for energy deposition
convolution
```

```
Dim BS_energy(0 To 1000) As Single
Dim no_color, hi_value, PEL, FSE_count
Dim Mottlambdai As Single
Dim NmbPixTotThick As Integer
Dim PercentOverThirty, PercentBetweenTenThirty, PercentBetweenThreeTen,
PercentBetweenOneThree, PercentBetweenPointsixOne
Dim Total_Energy_Deposited
Dim Total_Energy_Density_Deposited, cell_volume, peak_energy
Dim cells_exposed

Dim lambdai As Single



Public Sub hkbs()
'compute Rutherford scattering parameter b
'using the Hunger-Kuchler fit for BSE yields
Dim hkbs_val, hkc, hkm, dum
   hkm = (0.1382 - 0.9211 / Sqr(at_num(l)))
   dum = Log(at_num(l))
   hkc = 0.1904 - 0.2236 * dum + 0.1292 * dum ^ 2 - 0.01491 * dum ^ 3
   hkbs_val = hkc * inc_energy ^ hkm
'and the Love Scott model
   b = 0.016697 + 0.55108 * hkbs_val - 0.96777 * hkbs_val ^ 2 + 1.8864 * hkbs_val
^ 3
End Sub
Private Sub Form_MouseMove(Button As Integer, Shift As Integer, X As Single, Y
As Single)
Text4.Text = "Monte Carlo Development -(c) DCJ & MB November 2003"
End Sub
Private Sub Command1_Mousemove(Button As Integer, Shift As Integer, X As
Single, Y As Single)
Text4.Text = "Single scattering for 2 layer material and the energy distribution of
BSE"
End Sub

Private Sub Command1_Click()
'SS - a single scattering Monte Carlo model
'to determine the energy distribution of BSE

Dim the_value, transmit As Integer   'index
Dim beam_x           'beam center point
Dim ll, dum, dummy1, LowLoss
Dim FileName As String
Dim aa, bb
```

```
Picture1.Cls        'clear the screen
Form1.Show
List3.Clear

'Announce the program
       click = 1 'It means we are in Command1
    Text4.Text = " Single Scattering Monte Carlo Model"
       bs_yield = 0        'reset BS counter
       LowLoss = 0          ' reset LowLoss counter
        num = 0           'reset trajectory counter
        hi_value = 0      'maximum BS count

        For j = 0 To 54
          BS_energy(j) = 0 'reset energy array
        Next j

    ScaleMode = 3   'set scale to pixels
    Picture1.BackColor = QBColor(15) 'white background
'set up the screen for plotting the display
    center_x = Picture1.ScaleWidth / 2
    LH_edge = center_x * 0.1
     RH_edge = center_x * 1.95
      center_y = Picture1.ScaleHeight / 2
     the_top = center_y * 0.15
    bottom = center_y * 1.85

'set up the screen for plotting the display

'calculate the plotting scale
     thick = Val(Text5.Text) 'the resist thickness in Angstroms
     thicksub = Val(Text7.Text) 'the substrate thickness in Angstroms
     thicktotal = thicksub + thick 'the total thickness in Angstroms

     plot_scale = (((bottom - the_top) * 1#) / thicktotal) 'pixels/A
'plot the top surface
    Picture1.DrawWidth = 2
    Picture1.Line (LH_edge, the_top)-(RH_edge, the_top), QBColor(4)


'plot the bottom of the substrate
    Picture1.Line (LH_edge, bottom)-(RH_edge, bottom), QBColor(4)

'plot the boundary between the resist and the substrate
    Picture1.Line (LH_edge, the_top + thick * plot_scale)-(RH_edge, the_top + thick *
plot_scale), QBColor(5)
```

```
'hold beam normal to surface
   tilt = 0
      Text2.Text = 0
      s_tilt = 0
   c_tilt = 1
'plot the beam position
   beam_x = center_x
    Picture1.Line (beam_x, 10)-(center_x, the_top), QBColor(4)
   Picture1.DrawWidth = 1
'get the element to use for the substrate
   the_value = List2.ListIndex
    If the_value < 1 Then the_value = 1
   If the_value > 15 Then the_value = 15
'and assign the values for the substrate
   l = 2
   at_num(2) = data_Z(the_value)
    at_wht(2) = data_A(the_value)
   density(2) = data_rho(the_value)
   Call Berger_Selzer      'get value for J
      'get the necesary constants
       get_constants

'get the element to use for the resist
   the_value = List1.ListIndex
    If the_value < 1 Then the_value = 1
   If the_value > 15 Then the_value = 15
'and assign the values for the resist
   l = 1
   at_num(1) = data_Z(the_value)
    at_wht(1) = data_A(the_value)
   density(1) = data_rho(the_value)
   Call Berger_Selzer      'get value for J
      'get the necesary constants
       get_constants

   'set up parameters
   inc_energy = Val(Text1.Text)

'allow color trajectory plotting
      no_color = 0
      e_min = 0.5   '500V cut-off

Randomize            'reset generator
```

```
   traj_num = Val(Text3.Text)   'get number to run


'*****************************************
'****** the Monte Carlo loop **************
'*****************************************
   While ((num < traj_num))

      X = 0             'reset to starting values
       Y = 0
      z = 0
      cx = 0
       cy = 0
      cz = 1
      xn = 0
       yn = 0
      zn = 0
    s_en = inc_energy
    color_value = 14
    l = 1   'Resist

    'initial entry of the electron
     a_step = -lambda(s_en) * Log(Rnd)
     zn = a_step

     'test this coordinate
     If zn > thicktotal Then    'it is transmitted
        Call xyplot(0, 0, 0, 999)  'plot this line
        radius(0) = radius(0) + 1#
        transmit = transmit + 1#
     GoTo jump:              'end this trajectory
     End If

       Call xyplot(0, 0, 0, zn) 'show the trajectory step

        X = 0       'and reset the coordinates
        Y = 0
        z = zn

'now start the single scattering loop
     While (s_en > e_min)

     a_step = -lambda(s_en) * Log(Rnd)
     Call s_scatter(s_en)          'the Rutherford model
     Call new_coordinates     'get new position
```

```
    color_value = 6 + Int(7.55 - 6 * (inc_energy - s_en))

    'now decide what happens next depending on
    'the current position of the electron

     If zn < 0 Then                'this one is backscattered
       bs_yield = bs_yield + 1     'count it
        Call xyplot(Y, z, yn, 99)  'plot it
        ll = -z / cc               'exit vector

  'and compute the energy loss on the final step
     del_E = ll * Stop_Pwr(s_en) * density(l) * 0.00000001
       s_en = (s_en - del_E)  'exit energy
       the_value = Int(54 * s_en / inc_energy)
       BS_energy(the_value) = BS_energy(the_value) + 1
     GoTo jump:                    'and end the trajectory
     End If



    If zn > thicktotal Then
       ll = (thicktotal - z) / cc 'length of exit vector
        xn = X + ll * ca    'exit x coordinate
         yn = Y + ll * cb    'exit y coordinate
         Call xyplot(Y, z, yn, 999)
         transmit = transmit + 1#

       GoTo jump:  'finish this trajectory
    End If

'or go round again

      Call reset_data

Wend       'end of the while (energy) loop
jump:          'exit point
'*********************************************
'********* end of Monte Carlo loop ************
'*********************************************
  num = num + 1       'increment counter
  If (num Mod 100 = 0) Then Randomize  'reset RND generator
  Wend          'end of counter loop
   'get the BSE yield
   BS_coeff = Int(1000 * bs_yield / traj_num) / 1000
```

```
    LowLoss = Int(1000 * (BS_energy(19) + BS_energy(20)) / traj_num) / 1000
    Form1.List3.AddItem "BS = " & BS_coeff & "  LowLoss = " & LowLoss

   'now plot up the BSE energy data
    For j = 0 To 54
     If BS_energy(j) > hi_value Then hi_value = BS_energy(j)
    Next j

      'plot this data up
       Plot_BSE (hi_value)

   'and allow the data to be saved to disk
   If Check2 = 1 Then  'it will be saved
     FileName = "C:\" & Text6.Text 'give path and name
       Debug.Print "this file was " & FileName
       Debug.Print "  "
   'now write the file
      Open FileName For Output As #1
   'save the data
    For aa = 0 To 20
     Write #1, (aa * inc_energy / 20), (BS_energy(aa) / hi_value)
    Next aa
      Close #1


    End If
End Sub
Private Sub Command2_Mousemove(Button As Integer, Shift As Integer, X As
Single, Y As Single)
Text4.Text = "Single scattering for a sphere material and the energy distribution of
BSE"
End Sub
Private Sub Command2_Click()
'SPHERE - a single scattering Monte carlo model
'to determine the BSE energy distribution for a spherical particle
Form1.Show
Dim the_value, transmit As Integer   'index
Dim beam_x             'beam center point
Dim ll, dum, hi_value, dummy1
Dim origin_X, origin_Y As Integer
Dim plot_X, plot_Y, radius, cx, cy
Dim FileName As String
Dim aa, bb
Picture1.Cls       'clear the screen
List3.Clear
```

```
'Announce the program
      click = 2 'It means we are in Command2
   Text4.Text = " Single Scattering Monte Carlo Model"
      bs_yield = 0       'reset BS counter
       num = 0          'reset trajectory counter
       hi_value = 0     'maximum BS count
       For j = 0 To 54
        BS_energy(j) = 0 'reset energy array
       Next j

      'Draw the sphere
      Picture1.ScaleMode = 3      'Set scale to pixels
      Picture1.DrawWidth = 2
        cx = Picture1.ScaleWidth / 2
        cy = Picture1.ScaleHeight / 2
         two_pi = 710 / 113
          radius = cy * 0.85 'convenient value=97.325 pixels

          Picture1.Cls       'Clear screen
         Picture1.BackColor = QBColor(15) 'white background
     Picture1.Circle (cx, cy), radius, QBColor(4)  'Draw the circle
        'mark in the incident beam
              Picture1.DrawWidth = 1
               beam_x = center_x
    Picture1.Line (beam_x, 10)-(center_x, the_top), QBColor(4)

    'start the set up
    'hold beam normal to surface
   tilt = 0
      Text2.Text = 0
      s_tilt = 0
   c_tilt = 1

   'get the material to use
     the_value = List1.ListIndex
     If the_value < 1 Then the_value = 1
     If the_value > 15 Then the_value = 15
'and assign the values
   l = 1 'The sphere is only made from one material
   at_num(1) = data_Z(the_value)
    at_wht(1) = data_A(the_value)
   density(1) = data_rho(the_value)
   'set up parameters
   inc_energy = Val(Text1.Text)
```

```
    thick = Val(Text5.Text) 'sphere diameter in Angstroms
    sp_rad = thick / 2

    'allow color trajectory plotting
         no_color = 0

     Call Berger_Selzer      'get value for J

    'calculate the plotting scale
     plot_scale = (2 * radius / thick) 'pixels/A


    'get the necesary constants
       get_constants
        e_min = 0.5   '500V cut-off

Randomize            'reset generator
    traj_num = Val(Text3.Text)   'get number of trajectories to run

'*****************************************
'****** the Monte Carlo loop ***************
'*****************************************
    While num < traj_num
       X = 0             'reset to starting values
        Y = 0
       z = 0
       cx = 0
        cy = 0
       cz = 1
       xn = 0
        yn = 0
       zn = 0
      s_en = inc_energy
      color_value = 14

      'initial entry of the electron
       a_step = -lambda(s_en) * Log(Rnd)
       zn = a_step

       'test this coordinate
       If zn > thick Then    'it is transmitted
          Call xyplot(0, 0, 0, 999)  'plot this line
          transmit = transmit + 1#
         GoTo jump:              'end this trajectory
        End If
```

```
        Call xyplot(0, 0, 0, zn) 'show the trajectory step

        X = 0       'and reset the coordinates
        Y = 0
        z = zn

'now start the single scattering loop
      While s_en > e_min
        color_value = 6 + Int(7.55 - 6 * (inc_energy - s_en))
        a_step = -lambda(s_en) * Log(Rnd)
      Call s_scatter(s_en)          'the Rutherford model
      Call new_coordinates     'get new position

      'now decide what happens next depending on
      'the current position of the electron

       If Inside(xn, yn, zn) Then    'this one is outside and counts as backscattered
            'count it
          Call xyplot(Y, z, yn, zn)   'plot it
          If cc < 0 Then 'the detector can collect it
            the_value = Int(54 * s_en / inc_energy)
            BS_energy(the_value) = BS_energy(the_value) + 1
             bs_yield = bs_yield + 1 'count only detectable electrons
          End If
          GoTo jump:                  'and end the trajectory
       End If



'or go round again

        Call reset_data

     Wend       'end of the while (energy) loop
jump:           'exit point
'*********************************************
'********* end of Monte Carlo loop ************
'*********************************************
   num = num + 1       'increment counter

   If (num Mod 100 = 0) Then Randomize  'reset RND generator
   Wend          'end of counter loop
```

```
    'get the BSE yield
    BS_coeff = Int(1000 * bs_yield / traj_num) / 1000
    Form1.List3.AddItem "Computed BS yield = " & BS_coeff

     For j = 0 To 54
      If BS_energy(j) > hi_value Then hi_value = BS_energy(j)
     Next j



    'now plot up the BSE energy data
'           Plot_BSE (hi_value)

    'and allow the data to be saved to disk
   If Check2 = 1 Then  'it will be saved
     FileName = "C:\" & Text6.Text 'give path and name
       Debug.Print "this file was "; FileName
        Debug.Print "  "
   'now write the file
      Open FileName For Output As #1
   'save the data
    For aa = 0 To 54
     Write #1, (aa * inc_energy / 54), (BS_energy(aa) / hi_value)
    Next aa
     Close #1

    End If

End Sub
Private Sub Command3_Mousemove(Button As Integer, Shift As Integer, X As
Single, Y As Single)
Text4.Text = "Plural scattering for a layer material and plot the energy distribution"
End Sub

Private Sub Command3_Click()
'the Plural Scatter program
'used to compute the energy deposition profile
Dim the_value As Integer    'index
Dim beam_x                  'the beam position
Form1.Show
Picture1.Cls       'clear the screen
List3.Clear
'announce the program
   click = 3 'It means we are in Command3
   Text4.Text = " Monte Carlo Trajectory simulation"
```

```
    bs_yield = 0        'reset BS counter
    num = 0             'reset trajectory counter
    For j = 0 To 50
     For k = 0 To 50
      E_deposit(j, k) = 0
     Next k
    Next j
       Picture1.ScaleMode = 3   'set scale to pixels
       Picture1.BackColor = QBColor(15) 'white background

'set up the screen for plotting the display
    center_x = Picture1.ScaleWidth / 2
     LH_edge = center_x * 0.1
     RH_edge = center_x * 1.95
     center_y = Picture1.ScaleHeight / 2
    the_top = center_y * 0.15
'plot the top surface
    Picture1.DrawWidth = 2
    Picture1.Line (LH_edge, the_top)-(RH_edge, the_top), QBColor(4)

'set up parameters
    inc_energy = Val(Text1.Text)
     tilt = Val(Text2.Text)
     s_tilt = Sin(tilt / 57.4)
    c_tilt = Cos(tilt / 57.4)
'plot the beam position
    beam_x = center_x - (the_top - 10) * s_tilt / c_tilt
    Picture1.Line (beam_x, the_top - 20)-(center_x, the_top), QBColor(4)
    Picture1.DrawWidth = 1

'get the element to use for the resist
    the_value = List1.ListIndex
     If the_value < 1 Then the_value = 1
    If the_value > 15 Then the_value = 15
'and assign the values for the resist
    l = 1   'There is just one material
    at_num(1) = data_Z(the_value)
     at_wht(1) = data_A(the_value)
    density(1) = data_rho(the_value)

       'get the necesary constants
    Call Berger_Selzer      'get value for J
    Call Get_the_Range      'find Bethe range
    Call Profile            ' get E() array
Call hkbs               'get the scattering parameter
```

```
   Call micron_marker      'show the scale width
Randomize            'reset generator
   traj_num = Val(Text3.Text)   'get number to run
    no_color = 0   'use color plot

'*****************************************
'****** the Monte Carlo loop ***************
'*****************************************
   While num < traj_num
      X = 0
       Y = 0
      z = 0
      cx = 0
       cy = s_tilt
     cz = c_tilt
      For k = 1 To 50
        color_value = 6 + Int((55 - k) / 6)  'current value
         Call Scatter
      'test for the electron position
         Call new_coordinates
      'calculate the energy dump
       Call Energy_deposition
      'test for the electron position
         If zn < 0 Then
         bs_yield = bs_yield + 1
                    num = num + 1
                      Call xyplot(Y, z, yn, 99)
                    GoTo Back_Scatter
                 Else
                  Call xyplot(Y, z, yn, zn)
                  cx = ca
                   cy = cb
                     cz = cc
                    X = xn
                   Y = yn
                  z = zn
                 End If
    Next k
'*********************************************
'********* end of Monte Carlo loop ************
'*********************************************
   num = num + 1       'increment counter

Back_Scatter:       'end of branch
   If (num Mod 100 = 0) Then Randomize  'reset RND generator
```

```
   Wend          'end of counter loop
   'display the computer backscattering coefficient
   BS_coeff = Int(100 * bs_yield / traj_num)
   BS_coeff = BS_coeff / 100 'round off the number
   'put result in the text box
   Form1.List3.AddItem " computed BS yield = " & BS_coeff
   'and show the radial energy profile
    plot_energy_deposition


End Sub
Private Sub Command4_Mousemove(Button As Integer, Shift As Integer, X As
Single, Y As Single)
Text4.Text = "Single scattering for 2 layer material and plots the FSE energy
distribution"
End Sub
Private Sub Command4_Click()
'FSE - a program to compute and plot fast secondary electrons
Dim the_value, transmit As Integer   'index
Dim beam_x           'beam center point
Dim ll, dum, dummy1
Dim aa, bb, Test_for_FSE, zoom
Dim FileName As String
Form1.Show
List3.Clear
Picture1.Cls       'clear the screen

'Announce the program
      Text4.Text = "Using Mott cross section"
      bs_yield = 0       'reset BS counter
      transmit = 0       'reset transmit counter
      num = 0            'reset trajectory counter
      FSE_count = 0
      Total_Energy_Deposited = 0

  NmbPixTotThick = 299 ' ****Remember to change the arrray range at the
                ' beginning of the program
                ' **** This is different than plot_scale
                ' Defines the grid size (b_step) for the energy deposition

 'and clear the energy storage array
      For j = 0 To NmbPixTotThick
       For k = 0 To NmbPixTotThick
        E_deposit(j, k) = 0
       Next k
```

```
        Next j

    ScaleMode = 3   'set scale to pixels
    Picture1.BackColor = QBColor(15) 'white background
'set up the screen for plotting the display
    center_x = Picture1.ScaleWidth / 2
    LH_edge = center_x * 0.1
     RH_edge = center_x * 1.95
      center_y = Picture1.ScaleHeight / 2
     the_top = center_y * 0.15
    bottom = center_y * 1.85

'set up the screen for plotting the display
'plot the top surface
    Picture1.DrawWidth = 2
    Picture1.Line (LH_edge, the_top)-(RH_edge, the_top), QBColor(4)

'and plot the bottom surface
    Picture1.Line (LH_edge, bottom)-(RH_edge, bottom), QBColor(4)

'set up the screen for plotting the display

'calculate the plotting scale
     thick = Val(Text5.Text) 'the resist thickness in Angstroms
     thicksub = Val(Text7.Text) 'the substrate thickness in Angstroms
     thicktotal = thicksub + thick 'the total thickness in Angstroms

     plot_scale = (((bottom - the_top) * 1#) / thicktotal) 'pixels/A

'plot the boundary between the resist and the substrate
    Picture1.Line (LH_edge, the_top + thick * plot_scale)-(RH_edge, the_top + thick *
plot_scale), QBColor(5)

'hold beam normal to surface
    tilt = 0
        s_tilt = 0
    c_tilt = 1
'plot the beam position
    beam_x = center_x
     Picture1.Line (beam_x, 10)-(center_x, the_top), QBColor(4)
    Picture1.DrawWidth = 1

'get the element to use for the substrate
    the_value = List2.ListIndex
     If the_value < 1 Then the_value = 1
```

```
   If the_value > 15 Then the_value = 15
'and assign the values for the substrate
   l = 2
   at_num(2) = data_Z(the_value)
    at_wht(2) = data_A(the_value)
   density(2) = data_rho(the_value)
   Call Berger_Selzer      'get value for J
      'get the necesary constants
       get_constants

'get the element to use for the resist
   the_value = List1.ListIndex
    If the_value < 1 Then the_value = 1
   If the_value > 15 Then the_value = 15
'and assign the values for the resist
   l = 1
   at_num(1) = data_Z(the_value)
    at_wht(1) = data_A(the_value)
   density(1) = data_rho(the_value)
   Call Berger_Selzer      'get value for J
      'get the necesary constants
       get_constants

   'set up parameters
   inc_energy = Val(Text1.Text)
   zoom = Val(Text2.Text)

'calibrate the grid size for energy deposition
      b_step = thicktotal / NmbPixTotThick

'allow color trajectory plotting
      no_color = 0


'allow for zoom in plot
      If zoom = 0 Then zoom = 1

'get the necesary constants

    e_min = 0.1   '100V cut-off

Randomize           'reset generator
   traj_num = Val(Text3.Text)   'get number to run
```

```
'*****************************************
'****** the Monte Carlo loop ***************
'*****************************************
'Trajectory LoopTrajectory LoopTrajectory LoopTrajectory LoopTrajectory Loop
   While num < traj_num
      X = 0            'reset to starting values
       Y = 0
        z = 0
         cx = 0
          cy = 0
         cz = 1    'Electron's perpendicularly hit the target.
        xn = 0
       yn = 0
      zn = 0
    s_en = inc_energy
    color_value = 9          'light blue
    l = 1 'Resist

    'initial entry of the electron
     a_step = -Mott_Lambda(s_en) * Log(Rnd)

'now start the single scattering loop
'Energy LoopEnergy LoopEnergy LoopEnergy LoopEnergy LoopEnergy Loop
     While s_en > e_min

        Call s_scatter(s_en)          'the Rutherford model
        Call new_coordinatesCommand4     'get new position
'-------------------------------------------------------------------------------
      'This section will determine if the electron has been
      'backscattered or transmitted.

      If zn < 0 Then                'this one is backscattered
         bs_yield = bs_yield + 1      'count it
          Call xyplot(Y, z, yn, 99)   'plot it
           GoTo jump:                 'and end the trajectory
      End If

      If zn > thicktotal Then
         ll = (thicktotal - z) / cc 'length of exit vector
          xn = X + ll * ca    'exit x coordinate
           yn = Y + ll * cb    'exit y coordinate
            Call xyplot(Y, z, yn, 999)
             transmit = transmit + 1
              Form2.List1.AddItem num & "  " & s_en
            GoTo jump:  'finish this trajectory
```

```
      End If
'-------------------------------------------------------------------------------

        Call xyplot(Y, z, yn, zn)  'plot it
    'and compute the energy loss on that step
        del_E = a_step * Stop_Pwr(s_en) * density(l) * 0.00000001
        s_en = s_en - del_E

'   Form2.List1.AddItem num & del_E
    If del_E < 0 Then
    Form1.List4.AddItem "NEGATIVE J"
    End If

       Test_for_FSE = Rnd
       If Test_for_FSE > PEL Then 'an inelastic event has occurred
          Track_the_FSE        'follow FSE till it dies or escapes
'not necessary ???          GoTo reentry:
       End If

'reentry:
        'return point after tracking FSE
        color_value = 9
       a_step = -Mott_Lambda(s_en) * Log(Rnd)

     Call FSE_Energy_deposition(a_step) 'get the energy dump



'or go round again

       Call reset_data

     Wend      'end of the while (energy) loop
'Energy LoopEnergy LoopEnergy LoopEnergy LoopEnergy LoopEnergy Loop
jump:          'exit point
'*****************************************
'********* end of Monte Carlo loop ************
'*****************************************
   num = num + 1      'increment counter

   If (num Mod 100 = 0) Then Randomize  'reset RND generator ****
   Wend          'end of counter loop
'Trajectory LoopTrajectory LoopTrajectory LoopTrajectory LoopTrajectory Loop
```

```
    FileName = "C:\Documents and Settings\Me Myself\Desktop\Visual Basic\Energy
deposited.txt"

   'now write the file
    Open FileName For Output As #2
        'This is file is for the energy deposition for EVERY cell

       FileName = "C:\Documents and Settings\Me Myself\Desktop\Visual
Basic\Energy deposited nonzeros.txt"
    Open FileName For Output As #3
        'This is file is for the energy deposited (Not zero Energy)

    cells_exposed = 0
      For h = -(NmbPixTotThick) To NmbPixTotThick
        For k = 0 To NmbPixTotThick

          Total_Energy_Deposited = Total_Energy_Deposited + E_deposit(Abs(h),
k)
          If E_deposit(Abs(h), k) <> 0 Then
          cells_exposed = cells_exposed + 1
          Print #3, (h * b_step) & vbTab & (k * b_step) & vbTab &
(E_deposit(Abs(h), k) / E_deposit(0, 0))
          End If

        'lengthscale = (bottom - the_top) / (NmbPixTotThick)
        Print #2, (h * b_step) & vbTab & (k * b_step) & vbTab & (E_deposit(Abs(h),
k) / E_deposit(0, 0))

        Next k
      Next h

        'Form1.Hide
        'Form2.Show

   Close 2
   Close 3

    cell_volume = (b_step * b_step * b_step) ' Angstrom cube
    Total_Energy_Density_Deposited = (Total_Energy_Deposited * 1E+24 /
(cell_volume * cells_exposed))

    plot_FSE_energy_deposition
    Form1.Show
    Form1.List3.AddItem "Computed FSE  = " & FSE_count
    BS_coeff = Int(1000 * bs_yield / traj_num) / 1000
```

```
    Form1.List3.AddItem "BS Yield = " & BS_coeff
    Form1.List3.AddItem "BS Yield = " & bs_yield
    Transmit_coeff = (transmit / traj_num)
    Form1.List3.AddItem "Transmit Yield = " & Transmit_coeff

    Form1.List3.AddItem "Total Energy Deposited in the Sample= " &
Total_Energy_Deposited & " KeV"
    Form1.List3.AddItem "Total Energy Density Deposited in the Sample= "
    Form1.List3.AddItem Total_Energy_Density_Deposited & " KeV/cc"
    Form1.List3.AddItem Total_Energy_Density_Deposited / traj_num & "
KeV/cc/el"

    'Compute the maximum energy deposition per electron
     peak_energy = E_deposit(0, 0) / cell_volume / traj_num
     peak_energy = peak_energy * 1E+24  '1cm=10E8 Angstrom
    Form1.List3.AddItem " Peak Value = " & peak_energy & " KeV/cc/el" 'E is in
Kev
    'Form2.Show

End Sub

Private Sub Form_Load()
'color the form to look nice
FadeForm Me, False, False, True
'load the data table
data_Z(1) = 6: data_A(1) = 12.01: data_rho(1) = 2.3: data_Ec(1) = 0.284:
data_MABS(1) = 2147: data_lm(1) = 125: data_en(1) = 125
data_Z(2) = 13: data_A(2) = 26.98: data_rho(2) = 2.7: data_Ec(2) = 1.56:
data_MABS(2) = 397.5: data_lm(2) = 35: data_en(2) = 55
data_Z(3) = 14: data_A(3) = 28.09: data_rho(3) = 2.3: data_Ec(3) = 1.84:
data_MABS(3) = 347.2: data_lm(3) = 30: data_en(3) = 70
data_Z(4) = 22: data_A(4) = 47.9: data_rho(4) = 4.5: data_Ec(4) = 4.965:
data_MABS(4) = 107.7: data_lm(4) = 125: data_en(4) = 125
data_Z(5) = 24: data_A(5) = 52#: data_rho(5) = 7.1: data_Ec(5) = 7.111:
data_MABS(5) = 71.1: data_lm(5) = 13: data_en(5) = 50
data_Z(6) = 24: data_A(6) = 52#: data_rho(6) = 7.1: data_Ec(6) = 7.111:
data_MABS(5) = 71.1: data_lm(6) = 125: data_en(6) = 125
data_Z(7) = 29: data_A(7) = 64.55: data_rho(7) = 8.96: data_Ec(7) = 8.98:
data_MABS(7) = 63.5: data_lm(7) = 25: data_en(7) = 125
data_Z(8) = 42: data_A(8) = 95.94: data_rho(8) = 10.2: data_Ec(8) = 2.52:
data_MABS(8) = 673.3: data_lm(8) = 12: data_en(8) = 50
data_Z(9) = 47: data_A(9) = 107.9: data_rho(9) = 10.5: data_Ec(9) = 3.35:
data_MABS(9) = 517: data_lm(9) = 35: data_en(9) = 180
data_Z(10) = 46: data_A(10) = 106.4: data_rho(10) = 12#: data_Ec(10) = 10.26:
data_MABS(10) = 154.1: data_lm(10) = 10: data_en(10) = 50
```

```
data_Z(11) = 79: data_A(11) = 197: data_rho(11) = 19.3: data_Ec(11) = 2.22:
data_MABS(11) = 127.3: data_lm(11) = 7: data_en(11) = 40
data_Z(12) = 10: data_A(12) = 20.5: data_rho(12) = 1.74: data_Ec(12) = 0.284:
data_MABS(12) = 2373: data_lm(12) = 60: data_en(12) = 60
data_Z(13) = 6.5: data_A(13) = 13#: data_rho(13) = 1#: data_Ec(13) = 0.192:
data_MABS(13) = 74180: data_lm(13) = 50: data_en(13) = 70
data_Z(14) = 39.3: data_A(14) = 80: data_rho(14) = 1.84: data_Ec(14) = 2.142:
data_MABS(14) = 2840: data_lm(14) = 125: data_en(14) = 125
data_Z(15) = 46.6: data_A(15) = 95: data_rho(15) = 4.38: data_Ec(15) = 3.608:
data_MABS(15) = 57.3: data_lm(15) = 125: data_en(15) = 125
'set up the Materials lists
   List1.AddItem "Choose one"
   List1.AddItem "Carbon"        '#1
   List1.AddItem "Aluminum"      '#2
   List1.AddItem "Silicon"       '#3
   List1.AddItem "Titanium"      '#4
   List1.AddItem "Chromium"      '#5
   List1.AddItem "Iron"          '#6
   List1.AddItem "Copper"        '#7
   List1.AddItem "Molybdenum"    '#8
   List1.AddItem "Silver"        '#9
   List1.AddItem "Palladium"     '#10
   List1.AddItem "Gold"          '#11
   List1.AddItem "SiO2"          '#12
   List1.AddItem "PMMA"          '#13
   List1.AddItem "Cs2O"          '#14
   List1.AddItem "Ce2O3"         '#15
'set up the Substrate list

   List2.AddItem "Choose one"
   List2.AddItem "Carbon"        '#1
   List2.AddItem "Aluminum"      '#2
   List2.AddItem "Silicon"       '#3
   List2.AddItem "Titanium"      '#4
   List2.AddItem "Chromium"      '#5
   List2.AddItem "Iron"          '#6
   List2.AddItem "Copper"        '#7
   List2.AddItem "Molybdenum"    '#8
   List2.AddItem "Silver"        '#9
   List2.AddItem "Palladium"     '#10
   List2.AddItem "Gold"          '#11
   List2.AddItem "SiO2"          '#12
   List2.AddItem "PMMA"          '#13
   List2.AddItem "Cs2O"          '#14
   List2.AddItem "Ce2O3"         '#15
```

```
'default values for error trap (PMMA)
   at_num(1) = 6.5
   at_wht(1) = 13#
   density(1) = 1#
s_tilt = 0
c_tilt = 1
'set up the constant
two_pi = 710 / 113
'initialize text windows
Text1.Text = 5     'default inc_energy
Text2.Text = 0    'default tilt
Text3.Text = 1000      'default trajectory number
Text4.Text = "Monte Carlo Development -(c) DCJ & MB November 2003"
Text5.Text = 50
Text6.Text = "Will save in drive C:"
Text7.Text = 1200
center_x = Picture1.ScaleWidth / 2
LH_edge = center_x * 0.1
RH_edge = center_x * 1.95
center_y = Picture1.ScaleHeight / 2
the_top = center_y * 0.15
bottom = center_y * 1.55
plot_test = 0

End Sub




Public Sub FadeForm(frm As Form, Red%, Green%, Blue%)
Dim SaveScale%, SaveStyle%, SaveRedraw%
Dim i&, j&, X&, Y&, pixels%

'save current settings
SaveScale = frm.ScaleMode
SaveStyle = frm.DrawStyle
SaveRedraw = frm.AutoRedraw

'paint screen
frm.ScaleMode = 3
pixels = Screen.Height / Screen.TwipsPerPixelY
X = pixels / 64# + 0.5
frm.DrawStyle = 5
```

```
frm.AutoRedraw = True
For j = 0 To pixels Step X
  Y = 240 - 245 * j / pixels
    'can tweak if required
    If Y < 0 Then Y = 0
    'error trap
    frm.Line (-2, j - 2)-(Screen.Width + 2, j + X + 3), RGB(-Red * Y, -Green * Y, -
Blue * Y), BF
Next j

'reset previous settings
frm.ScaleMode = SaveScale
frm.DrawStyle = SaveStyle
frm.AutoRedraw = SaveRedraw



End Sub



Public Sub Berger_Selzer()
'calculates the mean ionization potential
'using the Berger-Selzer fit with atomic number, eq. (3.18)
    mn_ion_pot(l) = (9.768 * at_num(l) + (58.5 / at_num(l) ^ 0.19)) * 0.001
End Sub

Public Sub get_constants()
'computes constants needed by the program. Look at eq.(3.2)
'al_a(l)is the screeing factor in the Rutherford Cross Section for material l

al_a(l) = 0.00343 * at_num(l) ^ 0.667

'relativistically correct the beam energy. Look at Rutherford cross section (eq 3.8)and
(3.1)
er = (inc_energy + 511#) / (inc_energy + 1022#)
er = er * er

lam_a(l) = at_wht(l) / (density(l) * 6E+23) 'lambda in cm eq.(3.3)
lam_a(l) = lam_a(l) * 100000000# 'put into angstroms

sg_a(l) = at_num(l) * at_num(l) * 12.56 * 5.21E-21 * er  'Look at eq. (3.8)
End Sub

Public Function lambda(Energy)
```

```
'calculates the elastic MFP
al = al_a(l) / Energy
ak = al * (1# + al)
'giving the cross-section in cm^2 as
sg(l) = sg_a(l) / (Energy * Energy * ak)
'and lambda in angstroms is
lambda = lam_a(l) / sg(l)

End Function

Public Sub micron_marker()

'draws a scaled marker on the screen
Dim value, screenscale
Dim the_scale, micron_bar, scale_string
Dim kk As Integer
   For kk = 1 To 20
   value = 3000 / (range * kk)
   If value < 1000 Then GoTo Do_It
   Next kk
'now get the set up information
Do_It:
   plot_scale = (Picture1.ScaleWidth * 0.75) / range 'pixels/um
   the_scale = 1 / kk   'length of micron bar in um
   'tidy up this display
   If kk = 6 Then the_scale = 0.15
   If kk = 7 Then the_scale = 0.15
   If kk = 9 Then the_scale = 0.1
   If kk = 11 Then the_scale = 0.1
   If kk = 12 Then the_scale = 0.1
   If kk = 13 Then the_scale = 0.1
   If kk = 14 Then the_scale = 0.07
   If kk = 16 Then the_scale = 0.07
   If kk = 17 Then the_scale = 0.07
   If kk = 18 Then the_scale = 0.05
   If kk = 19 Then the_scale = 0.05
   If the_scale < 0.05 Then GoTo Forget_it
   micron_bar = the_scale * plot_scale
'now plot it on the screen
   Picture1.DrawWidth = 2
   Picture1.Line (10, 560)-(10 + micron_bar, 560), QBColor(12)
   Picture1.DrawWidth = 1
   Picture1.CurrentX = 3 + (micron_bar / 2)
   Picture1.CurrentY = 562
   Picture1.Print the_scale; "um"
```

```
Forget_it:
End Sub



Public Sub new_coordinates()
'computes the new coordinates for the electron
'using the scattering angles found earlier
'transforms coordinates back to laboratory frame
'Eqs (3.12)-(3.15)
Dim v1, v2, v3, v4, s, sstar
If cz = 0 Then cz = 0.000001 'error trap
   an_m = -cx / cz
   an_n = 1# / Sqr(1 + (an_m * an_m))
'get the transformation terms
   v1 = an_n * sp
   v2 = an_m * an_n * sp
   v3 = Cos(ga)
   v4 = Sin(ga)
'get the new direction cosines
   ca = (cx * cp) + (v1 * v3) + (cy * v2 * v4)
   cb = (cy * cp) + (v4 * (cz * v1 - cx * v2))
   cc = (cz * cp) + (v2 * v3) - (cy * v1 * v4)
'hence the new coordinates are
   xn = X + a_step * ca
   yn = Y + a_step * cb
   zn = z + a_step * cc


If ((thick - zn) = 0) Then
zn = zn + 0.0000001 * ((zn - z) / Abs(zn - z))
End If


   If (thick - zn) * (thick - z) < 0 Then
Form1.Show
'Form1.List3.AddItem "passed border1"
   lambdai = lambda(s_en)

   s = Sqr((zn - thick) * (zn - thick) + (a_step * ca) * (a_step * ca) + (a_step * cb) *
(a_step * cb))
                  ' length penetrated into the other material
                  ' without any corrections
   del_E = (a_step - s) * Stop_Pwr(s_en) * density(l) * 0.00000001
```

```
   s_en = s_en - del_E
'------------------------------------Assumption---------------------------------
      'now decide what happens next depending on
      'the current position of the electron
      If zn < thick Then
      l = 1
      Else
      l = 2
      End If

   sstar = s * (lambda(s_en) / lambdai)  ' length penetrated into the other
                                 ' material with corrections
'-------------------------------------------------------------------------------
'hence the new coordinates are
   xn = xn + (sstar - s) * ca
   yn = yn + (sstar - s) * cb
   zn = thick + sstar * cc
   a_step = sstar

         If zn < thick Then
          l = l
         Else
          l = 2
         End If
         s_en = s_en + del_E  ' s-en will be recalculated in reset_data

   End If


End Sub
Public Sub new_coordinatesCommand4()
'computes the new coordinates for the electron
'using the scattering angles found earlier
'transforms coordinates back to laboratory frame
'Eqs (3.12)-(3.15)
Dim v1, v2, v3, v4, s, sstar

If cz = 0 Then cz = 0.000001 'error trap
   an_m = -cx / cz
   an_n = 1# / Sqr(1 + (an_m * an_m))
'get the transformation terms
   v1 = an_n * sp
   v2 = an_m * an_n * sp
   v3 = Cos(ga)
   v4 = Sin(ga)
```

```
'get the new direction cosines
   ca = (cx * cp) + (v1 * v3) + (cy * v2 * v4)
   cb = (cy * cp) + (v4 * (cz * v1 - cx * v2))
   cc = (cz * cp) + (v2 * v3) - (cy * v1 * v4)
'hence the new coordinates are


   xn = X + a_step * ca
   yn = Y + a_step * cb
   zn = z + a_step * cc

If ((thick - zn) = 0) Then
zn = zn + 0.0000001 * ((zn - z) / Abs(zn - z)) 'Move the electron to the other side
'of the border by an infinitesimal number
End If


   If (thick - zn) * (thick - z) < 0 Then
Form1.Show
'Form1.List3.AddItem "passed border4"
   Mottlambdai = Mott_Lambda(s_en)

   s = Sqr((zn - thick) ^ 2 + (a_step * ca) * (a_step * ca) + (a_step * cb) * (a_step *
cb))
                    ' length penetrated into the other material
                    ' without any corrections
   del_E = (a_step - s) * Stop_Pwr(s_en) * density(l) * 0.00000001
   s_en = s_en - del_E
'----------------------------------------Assumtion---------------------------------
     'now decide what happens next depending on
     'the current position of the electron
     If zn < thick Then
     l = 1
     Else
     l = 2
     End If

   sstar = s * (Mott_Lambda(s_en) / Mottlambdai)  ' length penetrated into the other
                              ' material with corrections
'-------------------------------------------------------------------------------------
'hence the new coordinates are
   xn = xn + (sstar - s) * ca
   yn = yn + (sstar - s) * cb
   zn = thick + sstar * cc
   a_step = sstar
```

```
      If zn < thick Then
      l = 1
      Else
      l = 2
      End If
    s_en = s_en + del_E  ' s-en will be recalculated in reset_data

End If

End Sub



Public Sub reset_data()
'resets everything for the next step

 'first plot the last step
    Call xyplot(Y, z, yn, zn)
    'reset the local variables
     cx = ca
      cy = cb
       cz = cc
       X = xn
      Y = yn
     z = zn

'and compute the energy loss on that step
'  ALREADY IN COMMAND 4  del_E = a_step * Stop_Pwr(s_en) * density(l) *
0.00000001
'      s_en = s_en - del_E
End Sub

Public Sub reset_next_step()
'resets everything for the next step and
'computes the energy deposited
Dim radius, depth

 'first plot the last step
    Call xyplot(Y, z, yn, zn)
'and compute the energy loss on that step
    del_E = a_step * Stop_Pwr(s_en) * density(l) * 0.0001
      s_en = s_en - del_E
'get the r,z coordinates
      radius = Sqr((X + xn) * (X + xn) + (Y + yn) * (Y + yn))
```

```
      r_val = Int(radius / (2 * r_step))
       depth = (z + zn) / 2
      z_val = Int(depth / z_step)
'so the energy deposited in the annulus is
     E_deposit(r_val, z_val) = E_deposit(r_val, z_val) + del_E
 'reset the local variables
    cx = ca
     cy = cb
      cz = cc
      X = xn
     Y = yn
    z = zn
End Sub
Public Sub s_scatter(Energy)
'calculates the scattering angles using
'the screened Rutherford model
Dim R1, al(1 To 2)
     al(l) = al_a(l) / Energy
      R1 = Rnd
    cp = 1# - ((2# * al(l) * R1) / (1# + al(l) - R1))
   sp = Sqr(1# - cp * cp)
   'and get the azimuthal scattering angle
   ga = two_pi * Rnd
End Sub

Public Function Stop_Pwr(Energy)

'computes stopping power using modified Bethe law
'the result is in keV/gm/cm^2
If Energy < 0.05 Then Energy = 0.05
Stop_Pwr = 78500 * at_num(l) * (Log(1.166 * (Energy + 0.85 * mn_ion_pot(l)) /
mn_ion_pot(l))) / (at_wht(l) * Energy)
End Function



Public Sub xyplot(a, b, c, d)

'plots the trajectory step
Dim px, py, pxn, pyn
Dim show_energy 'plot color

   'determine the plotting color
    If no_color Then color_value = 0 'plot in black
```

```
    If color_value > 15 Then color_value = 15
    If color_value < 6 Then color_value = 0

  'start coordinates
   px = Int(center_x + a * plot_scale)
   py = Int(the_top + b * plot_scale)
  'finish coordinates
     pxn = Int(center_x + c * plot_scale)
     pyn = Int(the_top + d * plot_scale)
  If d = 99 Then pyn = the_top - 5          'BS case
  If d = 999 Then pyn = Int(bottom + 2) 'transmitted case
  'now plot this line segment
  Picture1.Line (px, py)-(pxn, pyn), QBColor(color_value)



End Sub

Public Sub Plot_BSE(maximum)
'plots the BSE energy distribution

Dim origin_X, origin_Y As Integer
Dim plot_X, plot_Y
    hi_value = maximum
    Picture1.Cls
   ScaleMode = 3   'set scale to pixels
   Picture1.BackColor = QBColor(11) 'light cyan background
'set up the screen for plotting the display
      origin_X = LH_edge
      origin_Y = the_top
'plot the axes
      Picture1.CurrentX = origin_X
      Picture1.CurrentY = origin_Y
         Picture1.DrawWidth = 2
      'first mark in the major axes
      Picture1.Line (LH_edge, 4)-(RH_edge, 4), QBColor(0)
      Picture1.Line (LH_edge, 4)-(LH_edge, 220), QBColor(0)
      'then complete the box
      Picture1.Line (LH_edge, 220)-(RH_edge, 220), QBColor(0)
      Picture1.Line (RH_edge, 220)-(RH_edge, 4), QBColor(0)
      'finally some horizontal scale markers
         Picture1.DrawWidth = 1
      Picture1.Line (LH_edge, 58)-(RH_edge, 58), QBColor(0)
      Picture1.Line (LH_edge, 112)-(RH_edge, 112), QBColor(0)
      Picture1.Line (LH_edge, 166)-(RH_edge, 166), QBColor(0)
```

```
        'plot the BSE energy distribution
          Picture1.DrawWidth = 4
        For k = 0 To 54
          plot_X = LH_edge + 12 * (k + 1)
          plot_Y = 220 - 205 * (BS_energy(k)) / hi_value
         Picture1.Line (plot_X, 220)-(plot_X, plot_Y), QBColor(1)
       Next k

End Sub

Public Function Inside(a, b, c)
'determines if this point is inside the sphere
      Inside = 1 'outside
      If (a * a + b * b + (c - sp_rad) * (c - sp_rad) - sp_rad * sp_rad) <= 0 Then 'its
inside
          Inside = 0
      End If
End Function

Public Sub plot_dot(a, b, c, d)
'plots a dot to indicate X-ray photon generation
Dim px, py
    px = center_x + (a + c) * plot_scale / 2
       py = the_top + (b + d) * plot_scale / 2
    Picture1.PSet (px, py), QBColor(12)
End Sub

Public Sub plot_energy_deposition()

'plots the energy deposition profile
Dim LH_edge, RH_edge, the_value
Dim the_color As Integer
Dim px, py As Integer
Picture1.Cls    'tidy up the screen
ScaleMode = 3   'set scale to pixels
Picture1.BackColor = QBColor(15) 'white background
 center_x = Picture1.ScaleWidth / 2
    LH_edge = center_x * 0.1
    RH_edge = center_x * 1.95
    center_y = Picture1.ScaleHeight / 2
   the_top = center_y * 0.15
'plot the top surface
   Picture1.DrawWidth = 2
   Picture1.Line (LH_edge, the_top)-(RH_edge, the_top), QBColor(4)
'now plot the data
```

```
   For h = -(NmbPixTotThick) To NmbPixTotThick
    For k = 0 To NmbPixTotThick
      i = Abs(h)
     the_value = E_deposit(i, k) / E_deposit(0, 0)
   'color code the data
      If the_value > 0.3 Then
         the_color = 13
         GoTo continue
        End If
      If the_value > 0.1 Then
         the_color = 11
         GoTo continue
        End If
      If the_value > 0.03 Then
         the_color = 12
         GoTo continue
        End If
      If the_value > 0.01 Then
         the_color = 10
         GoTo continue
        End If
      If the_value > 0.006 Then
         the_color = 9
         GoTo continue
        End If
        the_color = 14   'fade into the background
continue:
      px = center_x + h * a_step * plot_scale   'same scale as trajectories
      py = the_top + k * a_step * plot_scale
      Picture1.DrawWidth = 8
   Picture1.PSet (px, py), QBColor(the_color)
    Next k
   Next h
'Label the result in the text box
  Text4.Text = " Contours of Iso-Energy Deposition "
'and put up a marker
      Picture1.DrawWidth = 4
      Picture1.Line (10, 560)-(30, 560), QBColor(13)  '>30%
      Picture1.Line (31, 560)-(50, 560), QBColor(11)  '>10%
      Picture1.Line (51, 560)-(70, 560), QBColor(12)  '>3%
      Picture1.Line (71, 560)-(90, 560), QBColor(10)  '>1%
      Picture1.Line (91, 560)-(110, 560), QBColor(9)  '>0.6%
      Picture1.Line (111, 560)-(130, 560), QBColor(14) '<0.6%
      Picture1.DrawWidth = 1
      Picture1.CurrentX = 7
```

```
    Picture1.CurrentY = 561
    Picture1.Print "30%  10% 3%  1% 0.6% <"
End Sub

Public Sub Energy_deposition()
'computes the energy dump from the step
Dim mean_x, mean_y, mean_z
Dim radius, delta_E
Dim r_val, z_val As Integer
mean_x = (X + xn) / 2#
mean_y = (Y + yn) / 2#
mean_z = (z + zn) / 2#
   If mean_z < 0 Then mean_z = z / 2# 'error trap for BSE
'compute the indices for the array
   radius = Sqr((mean_x * mean_x) + (mean_y * mean_y))
   r_val = Int(radius / a_step)
   z_val = Int(mean_z / a_step)
'the energy deposited on this step is
   delta_E = E(k) - E(k + 1)
'so the array is incremented
   E_deposit(r_val, z_val) = E_deposit(r_val, z_val) + delta_E

 End Sub

Public Sub Get_the_Range()
'calculates the range assuming Bethe continuous
'energy loss. Uses Simpson's rule for integration
Dim f, fs, mass_thick, R_energy, the_range
Dim lll, m As Integer

   fs = 0
   For m = 1 To 21
    R_energy = (m - 1) * inc_energy / 20
    f = 1 / Stop_Pwr(R_energy)
   lll = 2      'default value
    If (m Mod 2 = 0) Then lll = 4 'm is even
    If (m = 1) Then lll = 1
    If (m = 21) Then lll = 1
     fs = fs + lll * f 'Simpson's rule
   Next m
   'now get the range and step length
   mass_thick = fs * inc_energy / 60#
   m_t_step(l) = mass_thick / 50#
   range = m_t_step(l) * 500000# / density(l)
   the_range = Int(1000 * range)
```

```
   the_range = the_range / 1000
   'report the result to the screen
   Form1.Show
   Form1.List1.AddItem "Electron range is " & the_range & " um"
   a_step = range / 50#


End Sub

Public Sub Profile()
'computes a 50 step energy profile for the beam
'using a 4-th order Runge-Kutter method
Dim A1, A2, A3, A4
Dim em
Dim m As Integer
E(1) = inc_energy
 For m = 2 To 51
 A1 = m_t_step(l) * Stop_Pwr(E(m - 1))
 A2 = m_t_step(l) * Stop_Pwr(E(m - 1) - A1 / 2)
 A3 = m_t_step(l) * Stop_Pwr(E(m - 1) - A2 / 2)
 A4 = m_t_step(l) * Stop_Pwr(E(m - 1) - A3)
 E(m) = E(m - 1) - (A1 + 2 * A2 + 2 * A3 + A4) / 6#
 Next m
 E(51) = 0      'set end value
 'and smooth the profile out a little
 For m = 2 To 50
  E(m) = (E(m) + E(m + 1)) / 2#
 Next m
 End Sub

Private Sub not_hkbs()


End Sub

Public Sub Scatter()
'computes the scattering angles
nu = Sqr(Rnd)       'the random generator
nu = ((1 / nu) - 1#)
an = nu * b * inc_energy / E(k)
'hence the scattering angles are
sp = (an + an) / (1 + (an * an))
cp = (1 - (an * an)) / (1 + (an * an))
'and the azimuthal angle is
ga = two_pi * Rnd
```

```
End Sub

Public Function Mott_Lambda(Energy)
'computes elastic and inelastic MFP
'mfp1 is the elastic MFP
'mfp2 is the inelastic MFP
'mfp3 is the total Mott Lambda MFP
'Definitions are made in Sub get_constants and General

Dim al, ak, sg(1 To 2), mfp1, mfp2, mfp3


    al = al_a(l) / Energy
    ak = al * (1# + al)
  'giving the cross-section in cm^2 as
     sg(l) = sg_a(l) / (Energy * Energy * ak)
  'and lambda in angstroms is
       mfp1 = lam_a(l) / sg(l)

  'for the FSE the MFP in A is
  mfp2 = at_wht(l) * Energy * Energy * 2.55 / (density(l) * at_num(l))

  'so the total MFP is
  mfp3 = (1 / mfp1) + (1 / mfp2)
  mfp3 = 1 / mfp3
  'and the decision ratio for elastic inelastic scattering
  PEL = mfp3 / mfp1

  'and the final result is
  Mott_Lambda = mfp3

End Function

Public Function FSEmfp(Energy)
'computes the MFP of the FSE during its subsequent scattering
'the MFP is the same the mfp1 value
Dim qk, ql, qm, qn, FSEEnergy
  FSEEnergy = Energy * 0.99
 ql = (0.00343 * (at_num(l) ^ 0.667)) / FSEEnergy
 qk = ql * (1# + ql)
'giving the cross-section in cm^2 as
  qm = (at_num(l) * at_num(l) * 1.6359E-20) / (FSEEnergy * FSEEnergy * qk)
'and lambda in angstroms is
  qn = at_wht(l) / (density(l) * 6E+23) 'lambda in cm
  qn = qn * 100000000# 'put into angstroms
```

```
  FSEmfp = qn / qm


End Function

Public Sub Track_the_FSE()
'follows the FSE and then returns control to main program
Dim FSEnergy, eps, sp, cp, ga, FSE_step
Dim s1, s2, s3, s4, s5, s6, s7, v1, v2, v3, v4, an_m, an_n, s, sstar
Dim deltaE, al, escape, p_escape, ll, radius
Dim r_val, z_val As Integer
Dim FSEmfpi As Single


      FSE_count = FSE_count + 1   'count the FSE production
      'find the energy with which the FSE is produced
       eps = 1 / (1000 - 998 * Rnd)
       FSEnergy = eps * s_en
       color_value = 12 'Red color for FSEs
       'Now store the primary coordinates to use later
       s1 = X
        s2 = Y
         s3 = z
         s4 = cx
         s5 = cy
        s6 = cz
       s7 = s_en - FSEnergy 'primary has lost this much energy

      If FSEnergy < e_min Then 'it is not tracked
'compute the indices for the array
         radius = Sqr((X * X) + (Y * Y))
         r_val = Int(radius / b_step)
         z_val = Int(z / b_step) '********

'so the array is incremented by an amount
            If (r_val <= NmbPixTotThick) Then
            If (z_val >= 0) Then
            If (z_val <= NmbPixTotThick) Then
            E_deposit(r_val, z_val) = E_deposit(r_val, z_val) + FSEnergy
            End If
            End If
            End If

         GoTo set_up_reentry:
```

```
        End If


    'If z_val > NmbPixTotThick Then z_val = NmbPixTotThick
    'If z_val < 0 Then z_val = -z_val

'get the initial scattering angles for FSE
          sp = (1 - eps)
          cp = Sqr(1 - sp)
          sp = Sqr(sp)

FSEloop:
         'first find the FSE step length
          FSE_step = -FSEmfp(FSEnergy) * Log(Rnd)
          ga = two_pi * Rnd
           If cz = 0 Then cz = 0.0001 'avoid overflow
           an_m = (-cx / cz)
           an_n = 1 / Sqr(1 + (an_m * an_m))

         'collect the transcendentals
           v1 = an_n * sp
           v2 = an_n * an_m * sp
            v3 = Cos(ga)
             v4 = Sin(ga)

         'find the new direction cosines
            ca = (cx * cp) + (v1 * v3) + (cy * v2 * v4)
            cb = (cy * cp) + (v4 * (cz * v1 - cx * v2))
             cc = (cz * cp) + (v2 * v3) - (cy * v1 * v4)

         'and get the new coordinates
            xn = X + FSE_step * ca
             yn = Y + FSE_step * cb
              zn = z + FSE_step * cc

If ((thick - zn) = 0) Then
zn = zn + 0.0000001 * ((zn - z) / Abs(zn - z))
End If


   If (thick - zn) * (thick - z) < 0 Then
Form1.Show
'Form1.List3.AddItem "passed border FSE"
```

```
   Mottlambdai = Mott_Lambda(FSEnergy)

   s = Sqr((zn - thick) * (zn - thick) + (FSE_step * ca) * (FSE_step * ca) + (FSE_step
* cb) * (FSE_step * cb))
                    ' length penetrated into the other material
                    ' without any corrections
   deltaE = (FSE_step - s) * Stop_Pwr(FSEnergy) * density(l) * 0.00000001


            FSEnergy = FSEnergy - deltaE
'-----------------------------------Assumtion---------------------------------
     'now decide what happens next depending on
     'the current position of the electron
     If zn < thick Then
     l = 1
     Else
     l = 2
     End If

   sstar = s * (Mott_Lambda(FSEnergy) / Mottlambdai)  ' length penetrated into the
other
                              ' material with corrections
'-------------------------------------------------------------------------------
'hence the new coordinates are
   xn = xn + (sstar - s) * ca
   yn = yn + (sstar - s) * cb
   zn = thick + sstar * cc
   FSE_step = sstar

     If zn < thick Then
     l = 1
     Else
     l = 2
     End If

     FSEnergy = FSEnergy + deltaE ' Because E( , ) would be calculated later
                         ' in FSE_Energy_deposition(FSE_step)
End If


         'now test the position and act accordingly

         If zn > thicktotal Then  'this FSE is transmitted

         transmit = transmit + 1
```

```
            ll = (thicktotal - z) / cc 'length of exit vector
            xn = X + ll * ca    'exit x coordinate
            yn = Y + ll * cb    'exit y coordinate
            Call FSE_Energy_deposition(ll)  'E_deposit(r_val, z_val) is evaluated
            Call xyplot(Y, z, yn, 999)
             GoTo set_up_reentry:  'finish this trajectory
           End If

            If zn <= 0 Then 'this FSE escapes

            bs_yield = bs_yield + 1
             Call FSE_Energy_deposition(FSE_step) 'E_deposit(r_val, z_val) is
evaluated
              Call xyplot(Y, z, yn, 99)
               GoTo set_up_reentry
             End If

             'otherwise plot the FSE trajectory
               Call FSE_Energy_deposition(FSE_step) 'E_deposit(r_val, z_val) is
evaluated
               Call xyplot(Y, z, yn, zn)
               deltaE = FSE_step * Stop_Pwr(FSEnergy) * density(l) * 0.00000001
               ' so the FSE energy is now
               FSEnergy = FSEnergy - deltaE

             If FSEnergy < e_min Then 'exit from the loop
             ' deposit the FSE energy at xn,yn,zn
'compute the indices for the array
               radius = Sqr((xn * xn) + (yn * yn))
                r_val = Int(radius / b_step)
                 z_val = Int(z / b_step) '********

'so the array is incremented by an amount
               If (r_val <= NmbPixTotThick) Then
               If (z_val >= 0) Then
               If (z_val <= NmbPixTotThick) Then
               E_deposit(r_val, z_val) = E_deposit(r_val, z_val) + FSEnergy
               End If
               End If
               End If
             GoTo set_up_reentry:
             End If


              'or go round again
```

```
            X = xn
             Y = yn
              z = zn
              cx = ca
             cy = cb
            cz = cc

          'scatter the FSE again
             al = al_a(l) / FSEnergy
             cp = 1 - ((2 * al * Rnd) / (1 + al - Rnd))
             sp = Sqr(1 - cp * cp)
             GoTo FSEloop:



set_up_reentry:
          X = s1
           Y = s2
            z = s3
            cx = s4
           cy = s5
          cz = s6
          s_en = s7

        'and get the scattering angles from the inelastic event
        sp = (eps + eps) / (2 + (s_en / 511) - (s_en * eps / 511))
        cp = Sqr(1 - sp)
        sp = Sqr(sp)
        ga = two_pi * Rnd
        'reset the color plot
         color_value = 9
        'and we are back in the main program



End Sub

Public Sub FSE_Energy_deposition(stepsize)
'computes the energy dump from the step
Dim mean_x, mean_y, mean_z
Dim radius, delta_E
Dim r_val, z_val As Integer
mean_x = (X + xn) / 2#
mean_y = (Y + yn) / 2#
mean_z = (z + zn) / 2#
```

```
   If mean_z < 0 Then
      mean_z = z / 2# 'error trap for BSE
   End If
   If mean_z >= 0 Then
'compute the indices for the array
   radius = Sqr((mean_x * mean_x) + (mean_y * mean_y))
   r_val = Int(radius / b_step)
   z_val = Int(mean_z / b_step)
         If (r_val <= NmbPixTotThick) Then
         If (z_val >= 0) Then
         If (z_val <= NmbPixTotThick) Then
'the energy deposited on this step is
         delta_E = stepsize * Stop_Pwr(s_en) * density(l) * 0.00000001
'so the array is incremented
         E_deposit(r_val, z_val) = E_deposit(r_val, z_val) + delta_E

         End If
         End If
         End If
   End If

End Sub

Public Sub plot_FSE_energy_deposition()
'plots the energy deposition profile
Dim LH_edge, RH_edge, the_value, pix_step, peak_energy
Dim OverThirty, BetweenTenThirty, BetweenThreeTen, BetweenOneThree,
BetweenPointsixOne
Dim PercentOverThirty, PercentBetweenTenThirty, PercentBetweenThreeTen,
PercentBetweenOneThree, PercentBetweenPointsixOne
Dim the_color As Integer
Dim px, py As Integer
Picture1.Cls    'tidy up the screen
ScaleMode = 3   'set scale to pixels
Picture1.BackColor = QBColor(15) 'white background
 center_x = Picture1.ScaleWidth / 2
' pix_step = Picture1.ScaleWidth / 101 'pixels to fill range
    LH_edge = center_x * 0.1
    RH_edge = center_x * 1.95
    center_y = Picture1.ScaleHeight / 2
   the_top = center_y * 0.15
'--------------------------------------------------------------------------------
' The quantities OverThirty, BetweenTenThirty,
' BetweenThreeTen , BetweenOneThree, BetweenPointsixOne are defined to find out
' the percentage of the area with a range dose
```

```
            OverThirty = 0
            BetweenTenThirty = 0
            BetweenThreeTen = 0
            BetweenOneThree = 0
            BetweenPointsixOne = 0
'-------------------------------------------------------------------------------
'now plot the data
   For h = 0 To NmbPixTotThick
    For k = 0 To NmbPixTotThick
     ' i = Abs(h)

     the_value = E_deposit(h, k) / E_deposit(0, 0)
   'color code the data

      If the_value > 0.3 Then
         the_color = 13
            OverThirty = OverThirty + 1
         GoTo continue
        End If
      If the_value > 0.1 Then
         the_color = 11
            BetweenTenThirty = BetweenTenThirty + 1
         GoTo continue
        End If
      If the_value > 0.03 Then
         the_color = 12
            BetweenThreeTen = BetweenThreeTen + 1
         GoTo continue
        End If
      If the_value > 0.01 Then
         the_color = 10
            BetweenOneThree = BetweenOneThree + 1
         GoTo continue
        End If
      If the_value > 0.006 Then
         the_color = 9
            BetweenPointsixOne = BetweenPointsixOne + 1
         GoTo continue
        End If
        the_color = 14   'fade into the background
continue:
      'px = center_x + h * (RH_edge - LH_edge) / 201

      'px = center_x + h * (bottom - the_top) / (NmbPixTotThick + 1)
      'py = the_top + k * (bottom - the_top) / (NmbPixTotThick + 1)
```

```
      px = Abs(center_x + h * (bottom - the_top) / (NmbPixTotThick + 1))
      py = Abs(the_top + k * (bottom - the_top) / (NmbPixTotThick + 1))
      Picture1.DrawWidth = 6
   'Plots the point on the right
   Picture1.PSet (px, py), QBColor(the_color)
      'px = center_x - h * (bottom - the_top) / (NmbPixTotThick + 1)
      px = Abs(center_x - h * (bottom - the_top) / (NmbPixTotThick + 1))
   'Plots the point on the left (with the same energy deposition as the point in the
right
   Picture1.PSet (px, py), QBColor(the_color)
    Next k
   Next h

         PercentOverThirty = (OverThirty) * 100 / ((NmbPixTotThick + 1) ^ 2)
         PercentBetweenTenThirty = (BetweenTenThirty) * 100 / ((NmbPixTotThick
+ 1) ^ 2)
         PercentBetweenThreeTen = (BetweenThreeTen) * 100 / ((NmbPixTotThick +
1) ^ 2)
         PercentBetweenOneThree = (BetweenOneThree) * 100 / ((NmbPixTotThick
+ 1) ^ 2)
         PercentBetweenPointsixOne = (BetweenPointsixOne) * 100 /
((NmbPixTotThick + 1) ^ 2)
'-------------------------------------------------------------------------
'plot the top surface
   Picture1.DrawWidth = 2
   Picture1.Line (LH_edge - 10, the_top)-(RH_edge, the_top), QBColor(4)
'plot the bottom of the substrate
   Picture1.Line (LH_edge - 10, bottom)-(RH_edge, bottom), QBColor(4)

'plot the boundary between the resist and the substrate
   Picture1.Line (LH_edge - 10, the_top + thick * plot_scale)-(RH_edge, the_top +
thick * plot_scale), QBColor(4)
'-------------------------------------------------------------------------
'Compute the maximum energy deposition per electron
' Moved this to FSE section
    'peak_energy = E_deposit(0, 0) / (b_step * b_step * b_step) / traj_num
    'peak_energy = peak_energy * 1E+24  '1cm=10E8 Angstrom
    'Form1.List3.AddItem " Peak Value = " & peak_energy & " KeV/cc/el" 'E is in
Kev
'and put up a marker
      Picture1.DrawWidth = 4

      Picture1.Line (111, 560)-(130, 560), QBColor(13)  '>30%
      Picture1.Line (131, 560)-(150, 560), QBColor(11)  '>10%
      Picture1.Line (151, 560)-(170, 560), QBColor(12)  '>3%
```

```
    Picture1.Line (171, 560)-(190, 560), QBColor(10)  '>1%
    Picture1.Line (191, 560)-(210, 560), QBColor(9)  '>0.6%
    Picture1.Line (211, 560)-(230, 560), QBColor(14) '<0.6%
    Picture1.DrawWidth = 1
    Picture1.CurrentX = 7
    Picture1.CurrentY = 561
    Picture1.Print "                          30%  10% 3%  1% 0.6% <"
End Sub
```

Vita

Mehdi Bolorizadeh was born on August 28, 1976 in Yazd, Iran. For the first eight years of his life he lived in Lincoln, Nebraska while his parents were pursuing their degrees in the US. In 1990, after returning to Iran, he was one of only 22 students chosen to attend the gifted high school in Kerman, Iran, Allameh Helli High School. In 1995 he was admitted to the Electrical Engineering program at Isfahan Uinversity of Technology, but changed his major to Physics in 1997. In June 1998 he was chosen as one of the top 20 Physics students in Iran, as a result of which he was invited to attend the prestigious Physics summer school held at Zanjan's Center for Graduate Studies. He obtained his Bachelor of Science in Physics in August 1999.

In 1999 he started his graduate studies at Old Dominion University (ODU) in the U.S. He passed both the General Physics exam and the Advanced Qualifier exams with the highest grade in the department's history. In December 2000, he earned his Master of Science in Physics from O.D.U. and in the fall of 2001 was admitted to the Physics Ph.D. program at the Physics and Astronomy Department of the University of Tennessee, Knoxville (UTK).

He began his Ph.D. research with Professor E. Ward Plummer in the field of Surface Physics. He studied the charge density wave phase transition of Pb/Ge (111), temperature dependent studies of transition metal oxide such as Sr_2RuO_4, and measurement of the interplanar thermal expansion coefficients of open faces like Al (210). However, in 2003, he joined Dr. David C. Joy's research team, and has since been conducting research in the field of electron beam lithography, electron beam microscopy, CD metrology, nanofabrication, and the development of other scanning electron microscope techniques applicable for semiconductor industry.

Currently he is a member of the American Physical Society, Materials Research Society, Microscopical Society of America, and Canada, Sigma Pi Sigma, The National Physics Honor Society, and The American Scholars National Honor Society.

5874 8922 12
04/04/07 VR
IFGroup